STATIC FRICTION AND JUNCTION GROWTH OF CONTACTING THREE-DIMENSIONAL SINUSOIDAL ASPERITIES AND ROUGH SURFACES

by

Xianzhang Wang

A dissertation submitted to the Graduate Faculty of
Auburn University
in partial fulfillment of the
requirements for the Degree of
Doctor of Philosophy

Auburn, Alabama
December 16, 2017

Keywords: Static Friction, Sinusoidal Asperity, Rough Surfaces,
Elastic-Plastic, Multi-scale Model, Finite Element Model

Approved by

Robert L. Jackson, Chair, Professor of Mechanical Engineering
Dan Marghitu, Professor of Mechanical Engineering
Ali Abdel-Hadi, Assistant Professor of Mechanical Engineering
Bertram Zinner, Associate Professor of Mathematics and Statistics

Abstract

It is reported that about one third of the primary energy is consumed by friction all over the world [1], and about 55% of the machine parts failed due to wear and tear [2]. For example, about one third of the fuel energy is used to overcome the various frictions in a passenger car [3]. In general, friction is undesirable, such as in gears, bearings and cylinder and piston systems. However, sometimes it is desirable, such as in belt drives, brakes, clutches, and even small compartments like electrical connectors and screws. Therefore, it is important to understand the process involved in friction and to obtain accurate models that predict the friction. Unfortunately, due to the complexity of friction mechanisms, it has been extremely difficult to obtain universal friction models. Modeling friction contacts becomes a challenge due to the complicated multiple scales of features on surfaces. Many researchers have developed different kinds of models to solve this problem. If researchers are successful, engineers could use the results predicted by the models, to increase or decrease the desirable friction in a controlled manner.

There are many methods describing the contact of rough surfaces, such as statistical models, multi-scale models and deterministic models. Statistical models use the solution of the contact of an elastic or elastic-plastic asperity to stochastically model an entire contacting surface of asperities with a postulated height distribution. The multi-scale model considers that a rough surface profile can be decomposed into smaller asperities stacked on top of larger asperities. A profile can consist of the superposition of sinusoidal waves with different amplitudes and

wavelengths. Therefore, in this work, the sinusoidal shaped asperity is considered instead of considering the spherical shaped asperity considered in most of the existing statistical models.

A study of the sinusoidal surface contact is investigated comprehensively. First, the contact behaviors of a single three-dimensional sinusoidal asperity under normal loading were investigated for elastic contact. The complete contact pressure, general stress distribution, maximum von Mises and critical amplitude under the full stick condition are derived analytically. The results show that these values have the same trend as the corresponding values in the perfect slip condition. It is shown that the complete contact pressure in the full stick condition increases as Poisson's ratio increases, and it is lower than the corresponding valued under the perfect slip condition. It is also found that the maximum von Mises stress can locate either on the surface or below it, depending on the Poisson's ratio. When the Poisson's ratio is less than $\frac{1}{8}$, the maximum von Mises stress locates on the surface; otherwise, the maximum von Mises stress locates beneath the surface. The dimensionless critical amplitude is also derived, and it is larger than the corresponding value under the perfect slip condition. It increases as the Poisson's ratio increases, and approaches to the perfect slip value.

For the elastic-plastic contact under normal loading, the average contact pressure required to cause complete contact between the deformable sinusoidal surface and a rigid flat under the full stick condition is examined. Complete contact is defined as when there are no gaps between the contacting surfaces. the effect of contact conditions (perfect slip, full stick) on the complete contact pressure was investigated by using the finite element method (FEM). This study confirms the previous studies about sinusoidal contact. From the results, the effect of contact conditions on complete contact pressure does not apparent to be significant for this case. The dimensionless complete contact pressure is independent of material properties, except for Poisson's ratio.

Then, the contact behavior of a single elastic-plastic sinusoidal asperity under combined normal and tangential loading was investigated. The effects of the following parameters on the effective static friction coefficient and junction growth of a single sinusoidal asperity were investigated: material properties (elastic modulus, Poison's ratio, yield strength), geometric parameter (amplitude/wavelength), contact pressure and the critical interfacial shear strength. It was found that the effective static friction coefficient of a single sinusoidal asperity decreases with increasing contact pressure, elastic modulus, Poisson's ratio, and the ratio of amplitude to wavelength, and increases with increasing yield strength and critical shear strength. Empirical equations of the effective static friction coefficient and junction growth due to tangential load were provided. These equations then can be used in spectral and fast Fourier transform (FFT) based methods for modeling the contact and friction between rough surfaces.

Most of the existing models use the measured surface data directly and consider the shape between the measured surface data to be straight lines. This might not be realistic, because the surface is more continuous. The sharp peaks generated by neighboring lines may cause stress concentrations, which should be influence the accuracy of the results in simulations. Then questions then arise: what is the real shape between the measured surface data, and what is the appropriate resolution to represents the real rough surfaces?

Therefore, the effect of sampling resolution on the contact behaviors is investigated in this study. The spectral interpolation method is proposed to smooth the surface and reduce the resolution in the FE model. This method is based on the FFT interpolation, and assumes that the original surfaces and interpolation surfaces have the same spectrum. The elastic-plastic contact between deformable rough surfaces and a rigid flat under combined normal and tangential loading is the studied. The first loading step, in which a normal load is applied on the rigid flat is initially studied. During this normal load step, the effects of sampling resolution on the contact area ratio, dimensionless displacement, dimensionless average gap, and maximum von Mises stress were investigated. It was found that: as the resolution decreases, the contact area ratio and dimensionless displacement decreases, while the dimensionless average gap and dimensionless contact pressure both increase under normal preload and at sliding inception. During the second step, in which the normal load remains constant and a tangential load is applied and increases gradually, the static friction coefficient is investigated. The effect of tangential load on the contact behaviors are studied as well. It was found that the tangential force can increase the contact area ratio, dimensionless displacement and dimensionless maximum von Mises stress, and decrease the dimensionless average gap and dimensionless contact pressure.

Next, the contact and friction behavior between rough surfaces and a rigid flat is studied using FEM. Three kinds of rough surfaces (generated fractal rough surfaces, generated gaussian distribution rough surfaces, and real measured rough surfaces) are used in the FE model. The effects of the following parameters on contact area ratio and static friction coefficient of rough surfaces were investigated: plasticity index, normal force and tangent modulus. It is observed that the static friction coefficient decreases as the dimensionless normal load and plasticity index increases. The FEM results are then compared to the existing statistical models. The overall trends of both the FEM results and statistical models are the same. However, the FEM friction results are always greater than the values predicted by the statistical models. This might be because of either the assumptions of the statistical models or the insufficient surface data. It was also found that the tangent modulus can decrease the static friction coefficient by hardening the surface.

The results of contact area predicted by the multi-scale model is confirmed initially. The FEM results of single asperity sinusoidal is used within the multi-scale frame work in for the

normal loading step to predict real contact area. The FEM simulations with different real rough surfaces are conducted. The results show that the multi-scale contact model and the FEM data show a reasonable agreement. Since the existing friction models have some limits, such as did not consider heavy loads, and the surfaces with very large plasticity indices. A friction model considering these conditions (heavy loads and the surfaces with very large plasticity indices) is still needed. Hence, a new stacked multi-scale friction model is developed to predict the static friction for the rough surfaces in this work. The multi-scale contact model then is extended to a friction model. The predictions are compared with FEM results and a statistical model. They show the same trend, however, they show some differences, the friction coefficient predicted by the multi-scale friction model is greater than the statistical model predictions and lower than the FEM results. This is probably because one or more of the following reasons: the rough surface is not so istropic, the asperity summits have different radii, there is a uncertain interaction between asperities and bulk deformation, the distribution of the asperity are not Gaussian, and the measured nominal contact area is anistropic and not large enough. This still needs further investigating.

Acknowledgments

First of all, I would like to express my sincere appreciation to my advisor, Dr. Robert L. Jackson, for his supervision, guidance, support, and patience throughout my Ph.D. Studies. The experience of working with him over the last six years in Auburn has left me wonderful memories to appreciate for the rest of my life.

Besides, I would like to express my warmest gratitude to my committee members, Dr. Dan Marghitu, Dr. Ali Abdel-Hadi, Dr. Bertram Zinner and my dissertation outside reader Dr. W. Robert Ashurst for providing unconditional support and valuable suggestions during the studies. I feel fortunate that I met them and had a chance to work with them. I would like to thank Dr. Andres Carrano and Mr. Ali Khoshkhoo for their help on measuring rough surfaces. I would like to thank Mr. Shannon Price and HPC administrators at Auburn University for their assistance and support in computer. Special thanks are extended to Mr. Yang Xu for his help in both academic and daily life. I also thanks to all my fellow students in multi-scale tribology laboratory at Auburn University: Ms. Xiaohan Zhang, Ms. Swarna Saha, Mr. Hamid Ghaednia, Mr. Bowen An, Mr. Alex Locker, Mr. Nolan Chu and Mr. Geetanj Bhandari for their friendship, help, research advice and for creating a supportive environment.

Finally, I should also mention the support of the most important people in my life, my parents. Without their invaluable help and generous encouragement, the present thesis would not have been accomplished. I will try my best to be a person that will make them proud.

Table of Contents

List of Figures

List of Tables

List of Abbreviations

A	Area of contact
$\bar{A}$	Contact area for single asperity
A_r	Real contact area
A_0	Contact area under normal loading
A_n	Nominal contact area
BKE	From model of Brizmer, Kilgerman and Etsion [6]
CKE	From model of Cohen, Kilgerman and Etsion [11]
COF	Coefficient Of Friction
E	Elastic modulus
E'	Effective elastic modulus, $E/(1-\nu^2)$
$\bar{F}$	Contact force for single asperity
f	Spatial frequency (reciprocal of wavelength)
F_c	Critical force (full stick condition)
F_{cs}	Critical force (perfect slip condition)
F_n	Normal force
F_t	Tangential force
G	Shear modulus of solid body, $E/(2(1-\nu))$
g	Surface separation
h	The height of the surface

JGH	From model of Johnson, Greenwood and Higginson [43]
KE	From model of Kogut and Etsion [1]
KJ	From model of Krithivasan and Jackson [54]
L	Length
LET	From model of Li, Etsion and Talke [12]
N	Total number of asperities
$\bar{p}$	Average pressure over the entire surface
p^*	Average pressure to cause complete contact (Elastic)
p_{ep}^*	Average pressure to cause complete contact (Elastic-plastic)
$p_{11}, p_{12}, p_{21}, p_{22}$	Normal stress constant
q	Shear stress
q_x^*, q_y^*	Amplitude of shear stress
S_y	Yield strength
u_x, u_y, u_z	displacement component
$\mathrm{x, y, z}$	Cartesian coordinates on the surface (z is normal to the surface)
z_0	The position where the maximum von Mises stress locates at

Greek symbols

α	Stress spatial frequency in x direction
β	Stress spatial frequency in y direction
η	Area density of asperities
Δ	Amplitude of sinusoidal surface
Δ_c	Critical asperity amplitude
ϵ_x, ϵ_z	Strain components

ζ	$\sqrt{\alpha^2 + \beta^2}$
λ	Wavelength of sinusoidal surface (*1/f*)
ν	Poisson’s ratio
τ_c	Critical shear strength
ω_c	Critical interference (full stick condition)
ω_{cs}	Critical interference (perfect slip condition)
μ_s	Static friction coefficient for asperity or rough surface
σ	Standard deviation of surface heights
$\sigma_x, \sigma_y, \sigma_z$	Normal stress component
$\tau_{x11}, \tau_{x12}, \tau_{x21}, \tau_{x22}$	Shear Stress constant
$\tau_{xy}, \tau_{yz}, \tau_{xz}$	Shear stress component
$\tau_{y11}, \tau_{y12}, \tau_{y21}, \tau_{y22}$	Shear Stress constant
φ	Sinusoidal parameter
Ψ	Plasticity index
ϕ	Distribution of surface height
$\Phi(i,j)$	Airy stress function
Φ_x, Φ_x, Φ_z	A first partial derivative to Φ
$\Phi_{xx}, \Phi_{xy}, \Phi_{xz}, \Phi_{zz}$	A second partial derivative to Φ
$\Phi_{xxz}, \Phi_{xyz}, \Phi_{xzz}$	A third partial derivative to Φ

Subscripts

ave	Average value
c	Critical value at the onset of plastic deformation (full stick condition)
cs	Critical value at the onset of plastic deformation (perfect slip condition)

ep	Elastic-plastic
max	Maximum value
r	real
stick	Under the full stick condition
slip	Under the perfect slip condition
vm	von Mises
x	In x direction
y	In y direction

Operator symbols

$\partial^2/\partial \mathrm{x}, \partial^2/\partial \mathrm{y}, \partial^2/\partial \mathrm{z}$	First partial derivative
$\partial^2/\partial \mathrm{x}\,\partial \mathrm{z}, \partial^2/\partial x^2, \partial^2/\partial z^2$	Second partial derivative

CHAPTER 1. INTRODUCTION

1.1. Background

Friction plays an important role in everyday life, especially for engineering components. Friction is the force resisting the relative motion of solid surfaces in contact sliding against each other. There are several types of friction, one of the most common type is dry friction. Dry friction arises from a combination of interface adhesion, surface roughness, surface deformation, and so on. It is subdivided into static friction between non-moving surfaces, and kinetic friction between moving surfaces.

The so-called “Laws of friction” were provided by Amonton, although Davinci may have also been responsible.

- Amonton’s first law: the friction force, F_f, is directly proportional to the applied normal force, F_n.
- Amonton’s second law: the friction force, F_f, is independent of the apparent area, A_0.
- Coulomb’s law: Kinetic friction is independent of sliding velocity.

Then, Euler summarized these laws, and provided an equation:

$$F_f = \mu F_n \tag{1.1}$$

where, μ is the coefficient of friction.

However, none of these ‘Laws’ hold universally. The friction force required to start sliding is usually greater than the force require maintaining sliding, and this has given rise to the notion that there are two coefficients of friction: static friction coefficient (for the surfaces at rest) and kinetic (for surfaces in motion). Euler is also the first person to present that friction behaves different for two surfaces initially at rest then two surfaces in relative sliding motion. That is, the dry friction is subdivided into static friction between non-moving surfaces, and kinetic friction between moving surfaces.

From the second of Amonton's friction laws, friction is independent of apparent area of contact. While these laws provide a general guideline of the sensitivity of the coefficient of friction to the materials in contact, they may not necessarily be representative of friction that results between actual contact pairs [4]. Although some surfaces look very smooth, they are rough to some degree at the microscale or nanoscale. When two rough surfaces are pressed together, a contact is made by the asperities or peaks on either surface. These small values contacts make up the real contact area. For rough surfaces, the friction force becomes independent of the load, but proportional merely to the real contact area. Bowden and Tabor [5] later made a critical insight into the cause of friction and the physical reason behind the laws. Bowden and Tabor were perhaps the first to theorize about friction and the real area of contact between surfaces. They presented a different approach, which considered the sliding inception and static friction as failure mechanism related to the material properties. Therefore, when two rough surfaces are pressed together only isolated asperities on the surface are in contact. They then assumed that when the sliding occurs the average shear stress over the real contact area of contact has the value of, τ_{Av}. The expression for the total friction force, F_f, then can be given as:

$$F_f = \tau_{Av} \cdot A_r \tag{1.2}$$

To understand the friction, it is important to understand the effect of surface morphology and load on the tribological performance of different rough surfaces. Hence, numerous models that predict at the asperity-scale (10 nm-100 micros) static friction were developed by many researchers [6]. This includes asperity contact under combined normal and tangential loads.

The three main criteria that have been used to theoretically determining the sliding inception are:

1.) Local yield criterion

Based on Bowden and Tabor's work, Chang et al. [7] treated the sliding inception as a plastic yield failure mechanism using the von Mises yield strength. They found that the maximum tangential load that can be supported by a single sphere asperity before plastic yield first occurs either below or at the asperity contact interface. They employed the stress field to calculate the allowable maximum tangential load of a single spherical asperity contact. Later, similar to the CEB friction model [7], Kogut and Etsion [8] investigated the contact between a deformable sphere in contact with a rigid flat under combined normal and tangential loading, and presented a semi-analytical approximate solution that treated sliding inception as a plastic yield failure mechanism using the von Mises yield criterion. They found the yield can occur either on the contact area or below it, depending on the plastic status of normal loading. A plastic volume was found to evolve and expand to the sphere surface prior to full sliding inception.

2.) Contact stiffness criterion

Brizmer et al. [9] analyzed an elastic-plastic contact between a deformable sphere and a rigid flat under combined normal and tangential loading under the full stick condition, and proposed a stiffness criterion to find the initiation of full sliding. They assume that when the instantaneous tangential stiffness become zero, the surface starts sliding. For convenience, they treated the sliding inception as when the instantaneous tangential stiffness becomes less than a small defined function of the initial tangential stiffness. It is given as:

$$\frac{(K_T)_i}{(K_T)_1} \leq \alpha \tag{1.3}$$

where $(K_T)_i$ is the instantaneous tangential stiffness, and given by:

$$(K_T)_i = \left(\frac{\partial F_t}{\partial u_x}\right)_i \approx \frac{(F_t)_i - (F_t)_{i-1}}{(u_x)_i - (u_x)_{i-1}} \tag{1.4}$$

and i is loading step number, the $(K_T)_1$ is the initial tangential stiffness corresponding to the first tangential loading step, α is the predefined number, and it is set to 0.1.

3.) Maximum friction shear stress criterion

This criterion assumes that the sliding initiates at the interface. When the computed shear stresses reach the upper local shear stress limit, local sliding takes place at this point. Once all the points in the contact area slide, the entire surface starts sliding. There are two methods to set the upper local shear stress limit, the first one is using the “Local Coulomb Friction law”. Mindlin [10] implemented the “Local Coulomb Friction Law” by imposing an upper limit on the local shear stress equal to the local contact pressure times an assumed local static friction coefficient. Eriten et al. [11] developed a physics-based friction model for the spherical contact by applying the “Local Coulomb Friction law” on the contact interface. The other method [12] is to set a maximum shear strength as the upper local shear stress limit, then the maximum shear stress was set to $S_y/\sqrt{3}$ based on von Mises theory, where S_y is the yield strength of the soft material in contact.

Based on these criteria, numerous studies are carried out on the presiding static friction by many researchers. Most commonly the roughness is considered using a statistical model: This model incorporates the results of the finite element method and sliding inception of a single asperity in a statistical representation of the surface roughness. In this kind of model, the surfaces are assumed to consist of a certain number of spherical asperities, whose heights above the mean level are modeled with a probability function, such as an exponential or Gaussian distribution.

Chang, Etsion, and Bogy [2] developed a statistical model, in which the von Mises yield criterion is used to calculate the tangential force that causes failure of contacting asperities. They found that the static friction coefficient is affected by material properties, surface topography and normal contact load. Kogut et al. [4] developed a model that shows the strong effect of the external force and nominal contact area and found that the main parameters affecting the static friction coefficient are the plasticity index and the adhesion parameter. Cohen et al. [13] found the static friction is strongly affected by normal load, nominal contact area, mechanical properties, and surface roughness. Cohen et al. [14] investigated the effect of surface roughness on the static friction of an elastic-plastic spherical contact with a low plasticity index. Li et al. [15] extended the consideration of the plasticity index to a higher range. It should be noted however that in all of these papers the asperities were modeled as spheres.

Due to the multi-scale nature of rough surfaces, there are many other methods to model the contact of rough surfaces. Archard [16] developed the first multi-scale contact model between rough surfaces. The rough surfaces used in Archard's model are described as "protuberances on protuberances". By using a concept of multiple scales of the asperities, the model considers smaller spheres layered upon larger spheres. Ciavarella et al. [17] solved the contact problem of a 2D Weierstrass–Mandelbrot fractal surface in contact with a rigid flat using the same stacked asperity assumption. They modeled the surface deformation using the two-dimensional elastic sinusoidal solution given by Westergaard [18]. Jackson and Streator [19] developed a multi-scale rough surface contact model which considers smaller asperities located on top of larger asperities. In addition to their work, Gao and Bower [20] also extended the multi-scale stacked contact model by including plastic deformation for 2-D sinusoidal asperities. Based upon the model in [19], Wilson et al. [21] used stacked 3D elastic-plastic sinusoids to model the multiple scales of roughness. However, a multi-scale stacked model predicting the static friction between rough surfaces is still missing.

1.2. Organization

The key research objectives of this work are to: 1) investigate the contact and friction behaviors for a single sinusoidal asperity for both the elastic and elastic-plastic case; 2) investigate static friction for rough surfaces. This work is focused on the further development of the sinusoidal based multi-scale modeling contact technique. Most of the previous models of contact between rough surfaces assume a sphere or elliptical shape for the geometry of the asperities on the surfaces. Hence, both single sinusoidal asperities and rough surfaces are analyzed.

Chapter 1 gives a general introduction of the background and outlines the objectives of this dissertation.

The first section, covered in Chapter 2, 3 and 4, formulates the details of contact and friction for a single asperity. In Chapter 2, the contact behaviors under full stick contact considering sinusoidal geometry were analyzed. In this chapter, an elastic contact between a deformable sinusoidal surface and rigid flat is studied. In Chapter 3, a finite element analysis, for an elastic-plastic sinusoidal surface normally loaded by a rigid flat is analyzed, and the effect of contact conditions and interfacial strength on the contact area and complete contact pressure is investigated. In Chapter 4, the behavior of an elastic-plastic contact between a deformable sinusoidal surface and a rigid flat under combined normal and tangential loading is investigated.

In the second section, covered in Chapter 5, 6 and 7, an elastic-plastic contact and friction between a rough surface and a rigid flat are investigated. In Chapter 5, the effect of resolution on the behaviors of contact and friction. In Chapter 6, the static friction coefficient is studied, and the

FEM results are compared with the existing theoretical models. Three kinds of rough surface models (generated fractal rough surfaces, generated Gaussian distribution rough surfaces, and real measured rough surfaces) are used in the FE model. The effects of roughness, normal load and plasticity on static friction coefficient are investigated. In Chapter 7, the generated and real measured surface data are used to characterize the rough surface. A multi-scale friction model is developed to predict the static friction coefficient.

In Chapter 8, all the conclusions of these topics in this dissertation are summarized, and the future work is recommended.

CHAPTER 2. ELASTIC SINUSOIDAL CONTACT UNDER NORMAL LOADING IN FULL STICK

2.1. Introduction

The normal contact of linear, isotropic, homogeneous linear elastic bodies is a fundamental problem in contact mechanics. For this kind of problem, the solutions (e.g., the contact and interfacial shear stress) strongly rely on the types of boundary conditions at the interface which can be generally divided into two categories: normal and tangential ones. This work will consider a non-adhesive contact case. The normal boundary condition for the non-adhesive contact is characterized by the Kuhn-Tucker inequality [22]. Different cohesive models might be applied together with the Kuhn-Tucker inequality to the interface when adhesion is introduced. The three main commonly used tangential boundary conditions in the analytical and numerical models are: 1.) Perfect slip condition: Interfacial shear stress is not considered, i.e. there is no friction existing between the two surfaces in contact. 2.) Full stick condition: The interfacial shear stress is sufficient to prevent any slip between the contact interfaces of the elastic bodies. 3.) Partial slip condition: The contact area is divided into two regions: the stick region and the slip region. In the stick region, the friction at the interface is sufficient to prevent any slip; in the slip region, the relative displacement can take place.

The full stick condition is considered in the current work. When contact interfaces are under the full stick condition, the mating points from both interfaces have zero relative displacement along their tangent direction. This type of boundary condition occurs in many situations. Experimental results of a glass lens in torsional [23, 24] and sliding contact [25] confirmed the existence of the stick region before the onset of the global rotation and sliding. Recently, a delicate experiment done by Svetlizky and Fineberg [26] showed that the stick and slip result in pre-sliding can be modeled as the propagation of the interfacial crack. This clearly indicates that the contact region is under the full stick condition right before being penetrated by the slip region. Due to the complex nature of the contact problem under the full stick condition, very little work was done on analytically solving the interfacial states for plane (2D) and spatial (3D) contact problems.

For the elastic contact under the plane stress/strain condition, several researchers have focused on the indenter with simple geometries and some of the results are summarized in Johnson's classic book [27]. Johnson [27] gave the interfacial normal and shear stress between the rigid flat end punch and an elastic half-space under the full-stick condition. The solutions were solved based on the integral governing equation developed by Galin [28]. Since all the points on the flat end come into contact simultaneously, the punch results do not rely on the loading history. Johnson [27] also gave a solution for the sliding contact of the cylindrical punch under full stick assuming that the interaction between the interfacial normal and shear stresses are decoupled. Adhesive plane contact between a cylinder and a stretched flat of similar materials where the substrate was stretched was studied by Chen and Gao [29] and later they solved the similar contact problem between dissimilar materials [30]. A similar contact between a rigid cylinder and an elastic half-space was studied by Zhupanska [31]. In Zhupanska’s model, the half-space is not pre-stretched. Block and Keer [32] applied Galin's formulation [28] for the non-periodic contact problem to the periodic contact problem based on the periodic Green's function. The solution [32] to the rigid periodic flat end punches in contact with an elastic half-space was given by analytically solving the coupled integral equations. The Goodman's approximation [33] was applied to the problem where the punch profile is a periodically sinusoidal profile and closed-form solutions were obtained for the interfacial normal and shear stresses.

Most works on the analytical modeling of three dimensional full-stick contact belong to the axisymmetric case. Mossakovskii [34, 35] was the first to solve the axisymmetric normal contact problem under the full stick condition. Mossakovskii [35] presented the solutions for an elastic half space in contact with a rigid indenter of different shapes: a flat-end cylinder, a parabolic shaped punch and a power law shaped punch. Because the interfacial normal and shear stresses are dependent on the loading history, Mossakovskii [34, 35] modeled the interfacial state of stresses incrementally. Goodman [33] gave an approximate solution of the Hertzian contact between dissimilar materials under the full stick condition. The interfacial normal stress is found by Hertzian contact based on Goodman's approximation. Goodman [33] also used the incremental formulation to solve the interfacial shear stress. A more efficient analysis to the axisymmetric contact under the full-stick condition was given by Spence [36]. He found similar interfacial states of stresses are yielded at each step during the progressive loading and this behavior is usually referred to as self-similarity. He pointed out that the solution to the self-similar problem can be obtained directly without the application of the incremental technique. Solving the governing dual integral equations by the Wiener-Hopf technique [37] yields the interfacial normal and shear stresses. Based on the self-similarity technique, Borodich [38] solved the Hertzian contact between two nonlinear elastic anisotropic bodies under the full stick condition. Based on Mossakovskii's analysis, Borodich and Keer [39] considered a contact between a rigid, axisymmetric punch and an isotropic elastic half space under the adhesive (full stick) condition, and found a relation between the contact stiffness, the contact area and the elastic modulus.

Numerical simulation is an effective approach for investigating the situation for both elastic and elastic plastic contact. This method was used to find the stress distribution and displacement for elastic contact by Conway [40]. He considered that an elastic strip was compressed by a punch with the shapes of cylindrical and circular rollers in the full stick condition. Kosior et al. [41] used a numerical method to analysis the contact problem with friction between two elastic bodies. They used a domain decomposition method coupled with the boundary element method (BEM) to solve the contact problem of two elastic bodies. In an additional paper [42], they solved the same problem numerically by the finite element method (FEM) considering the contact between both a deformable spherical indenter and a deformable support. Chen and Wang [43] developed a three dimensional numerical model for the contact of elastic dissimilar materials. A simulation was performed for a ball against a half space contact under normal loading and tangential loading. The effects of shear tractions on the contact area, the stick zone, pressure and so on were considered. An incremental algorithm which assumed that the loading history are considered was used to analyze the coupled elastic contact by Gallego et al. [44]. They used this algorithm to solve the stick-slip contact problem under both normal and tangential loading.

All the previous work assumed a spherical shaped asperity. Recently, Greenwood [45] at the 2015 Leeds-Lyon tribology Symposium suggested that more realistic asperity models similar to wavy surfaces should be considered. Several researchers have also investigated the elastic contact between a rigid flat and a sinusoidal or wavy geometry. Sinusoidal contact has been studied since the works of Westergaard [18] and Johnson, Greenwood, Higginson (1985) [46]. The two dimensional elastic sinusoidal contact was first solved by Westergaard [18]. Johnson, Greenwood and Higginson (JGH) [46] developed asymptotic solutions for the elastic contact of a three dimensional sinusoidal profile. In their work, they presented the average contact pressure that causes complete contact, p^*. It implies that if the average pressure is equal to or greater than the value of p^*, then the contact is complete, i.e. there are no gaps remaining between the surfaces. They also provided a relationship between pressure and contact area for two limiting regimes: at the early stages of contact and near complete contact. Jackson and Streator [19] provided an empirical equation based on the experimental and numerical data, linking the two regimes. Recently, a two-dimensional symmetric sinusoidal contact model was developed by Saha et al. [47]. In their work, an empirical expression for the average contact pressure that causes complete contact was provided. All the literatures introduced above only consider the sinusoidal contact under the perfect slip condition.

As can be seen from the above literature review, most of the existing literature are about either spherical contact under full stick condition or sinusoidal contact under the perfect slip condition. Very little work was done so far on the sinusoidal contact under the full stick condition, and an analytical solution for complete contact pressure is still missing for elastic contact under the full stick condition. The main goal of this chapter is to analyze the behavior of sinusoidal contact under the full stick condition. Therefore, the effects of contact conditions (perfect slip or full stick) is investigated in the present study for an elastic sinusoidal contact.

2.2. Methodology

2.2.1. Problem Statement

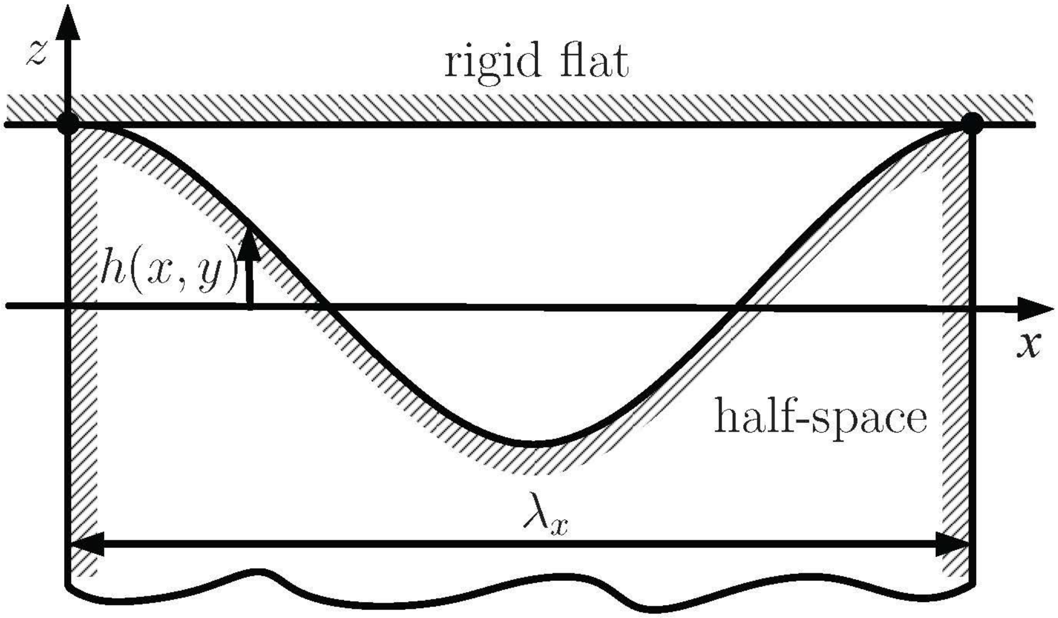

Fig. 2.1. Schematic representation of a half-space with bi-sinusoidal waviness in contact with a rigid flat surface. Only the *xz* cross-section is shown.

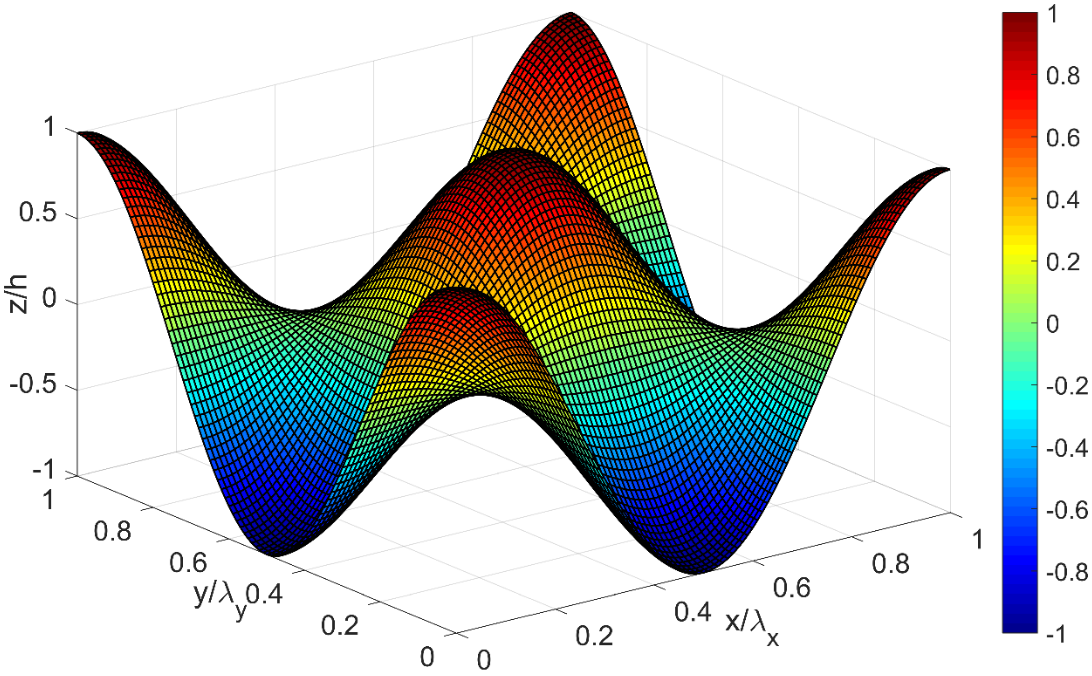

Fig. 2.2. Three-dimensional plot of bi-sinusoidal waviness surface.

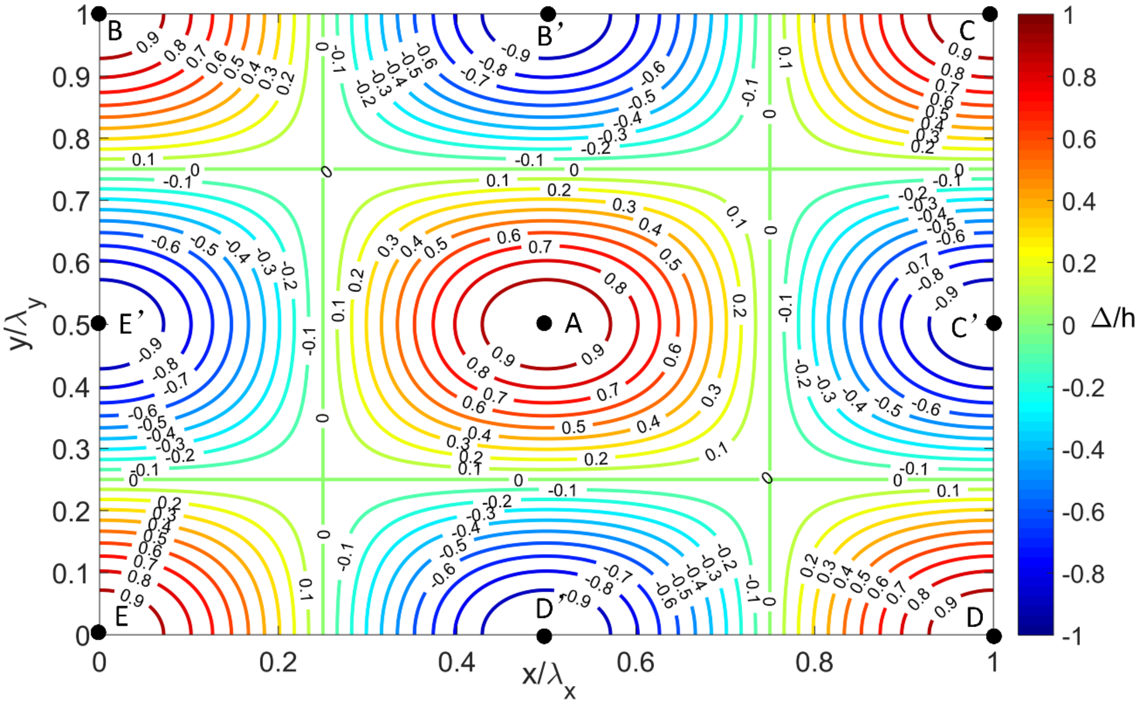

Fig. 2.3. Schematic representation bi-sinusoidal waviness. Points A, B, C, D and E are the peaks. Points B', C', D' and E' are the valleys.

A half-space with a bi-sinusoidal waviness contour is in purely normal contact with a rigid flat. The half-space is homogeneous, isotropic and linear elastic. The periodic bi-sinusoidal surface has the following expression:

$$h = \Delta \cos(\alpha x) \cos(\beta y) \tag{2.1}$$

where only one period is considered: $\{(x, y) | x \in [0, \lambda_x), y \in [0, \lambda_y)\}$. The wavelengths are $\lambda_x = 2\pi/\alpha$ and $\lambda_y = 2\pi/\beta$. The 3-dimensional view and the contour of the surface are shown in Fig. 2.2 and Fig. 2.3, respectively. In order to compare the results with the Equations in [46] and [48], in which the geometry are described as:

$$h = \Delta\,(1 - \cos(\alpha x) \cos(\beta y)) \tag{2.2}$$

a special case $\alpha = \beta$ will be considered in the section 2.3. The only difference is a constant term, the amplitude, Δ. It should be much less than the wavelengths, i.e. $\Delta \ll \lambda_x(\lambda_y)$, in order to exclude large deflections. The small ratio of amplitude to wavelength was also observed experimentally by Jackson [49] and Zhang and Jackson [50]. The contacting interface is under the full-stick condition. Since the interfacial normal and shear stresses depend on the loading stage [33, 35], generally, the contact problem should be formulated incrementally [33, 35]. In some special cases, (e.g., spherical contact), self-similarity can be used to simplify the formulation [37]. In order to avoid the complexity brought by the load-dependency, the contacting points are assumed to be achieved simultaneously, i.e., $u_x(x,y,0) = u_y(x,y,0) = 0$.

Tangential loading and adhesion are not considered. Consider the special stage where the bi-sinusoidal waviness is initially in contact with the rigid flat everywhere. This stage is referred to as complete contact. At complete contact and under full stick, the contact problem belongs to the second type boundary value problem where the surface displacement components in [27] at the boundary are prescribed by:

$$\begin{aligned} u_x(x,y,0) &= 0 \\ u_y(x,y,0) &= 0 \\ u_z(x,y,0) &= -h(x,y) \end{aligned} \tag{2.3}$$

2.2.2. Displacements for Plane Contact (2D)

The periodic semi-infinite elastic body can be treated as a plane strain problem, and the stress field can be calculated by using the Airy stress function [51]. The general form is given as:

$$\sigma_x(x,z) = \frac{\partial^2 \Phi(x,z)}{\partial z^2} \tag{2.4a}$$

$$\sigma_z(x,z) = \frac{\partial^2 \Phi(x,z)}{\partial x^2} \tag{2.4b}$$

$$\tau_{xz}(x,y) = \frac{\partial^2 \Phi(x,y)}{\partial x \partial z} \tag{2.4c}$$

To calculate the strain and displacement in generalized plane stress, we employ Hooke's law. The components of strain are given by:

$$\varepsilon_x = \frac{1}{E}[(1-v^2)\sigma_x - v(1+v)\sigma_z] \tag{2.5a}$$

$$\varepsilon_z = \frac{1}{E}[(1-v^2)\sigma_z - v(1+v)\sigma_x] \tag{2.5b}$$

From the strain-displacement relations

$$u_x(x,z) = \int_0^x \varepsilon_x(x,z)\,\mathrm{dx} \tag{2.6a}$$

$$u_z(x,z) = \int_\infty^z \varepsilon_z(x,z)\,\mathrm{dx} \tag{2.6b}$$

The two traction conditions at the surface $z = 0$ are each discussed separately.

2.2.2.1. Normal Stress Condition

The body is subject to the periodic normal stress and free of shear stress. The periodic normal stress imposed on the semi-infinite elastic body used in [52] is

$$\sigma_z(x,0) = p_0 cos(\alpha x) \tag{2.7}$$

Tripp et al. [52] provided the Airy Stress function

$$\Phi(x,z) = -\left(\frac{p_0}{\alpha^2}\right)(1+\alpha z)e^{-\alpha z}cos(\alpha x) \tag{2.8}$$

Substitute equation (2.6) and (2.8) into (2.4),

$$\epsilon_x = p_0\,\frac{1+v}{E}(1-2v-\alpha z)\,e^{-\alpha z}\,cos(\alpha x) \tag{2.9a}$$

$$\epsilon_z = p_0\frac{1+v}{E}\,(1-2v+\alpha z)\,e^{-\alpha z}cos(\alpha x) \tag{2.9b}$$

The components of strain are from the Eqs. (2.5a) and (2.9b), then substituting Eqs. (2.9a) and (2.9b) into Eqs. (2.6a) and (2.6b) respectively, we can calculate the displacement tangent and normal to the boundary respectively from:

$$u_x(x,z) = p_0 \frac{(1+v)}{\alpha E}(1-2v-\alpha z)e^{-\alpha z}\, sin(\alpha x) \tag{2.10a}$$

$$u_z(x,z) = p_0 \frac{(1+v)}{\alpha E}(\alpha z-2v+2)e^{-\alpha z}\, cos(\alpha x) \tag{2.10b}$$

Next, letting $z = 0$, the interfacial displacement components under the plane strain condition at the surface are given as:

$$u_x(x,z=0) = p_0 \frac{(1+v)(1-2v)}{\alpha E} sin(\alpha x) \tag{2.11a}$$

$$u_z(x,z=0) = -p_0 \frac{2(1-v^2)}{\alpha E} cos(\alpha x) \tag{2.11b}$$

2.2.2.2 Shear Stress Condition

On the contrary, the body is subject to the periodic shear stress and free of normal stress. Similarly, Tripp et al. [52] provided the stress distribution for a stress applying at the interference:

$$\tau_{xz}(x,0) = q_0 cos(\alpha x) \tag{2.12}$$

and the Airy stress function:

$$\Phi(x,y) = -\left(\frac{q_0}{\alpha}\right) z\, e^{-\alpha z} sin(\alpha x) \tag{2.13}$$

Substituting Eq. (2.6) and (2.13) into Eq. (2.4), the components of strain are obtained:

$$\epsilon_x = q_0\, \frac{1+v}{E}(2-2v-\alpha z)\, e^{-\alpha z}\, sin(\alpha x) \tag{2.14a}$$

$$\epsilon_z = q_0 \frac{1+v}{E}\, (-2v+\alpha z)\, e^{-\alpha z} sin(\alpha x) \tag{2.14b}$$

Substituting Eq. (2.14) into Eq. (2.5), the components of displacement are obtained:

$$u_x(x,z) = q_0 \frac{(1+v)}{\alpha E}(2-2v-\alpha z)e^{-\alpha z}\,[1-cos(\alpha x)] \tag{2.15a}$$

$$u_z(x,z) = -q_0 \frac{(1+v)}{\alpha E}(\alpha z-2v+1)e^{-\alpha z}\,sin(\alpha x) \tag{2.15b}$$

Letting $z = 0$, the interfacial displacement components under the plane strain condition are given as:

$$u_x(x,z=0) = q_0 \frac{2(1-v^2)}{E\alpha}\,[1-cos(\alpha x)] \tag{2.16a}$$

$$u_z(x,z=0) = -q_0 \frac{(1+v)(1-2v)}{E\alpha} sin(\alpha x) \tag{2.16b}$$

The sign of the normal stress follows the convention common in contact mechanics, i.e., compressive stress is positive and tensile stress is negative.

2.2.3. Displacements for Spatial Contact (3D)

Similarly, we calculate the displacement components for the normal stress and shear stress condition, respectively.

2.2.3.1. Normal Stress Condition

The elastic displacements due to a bi-sinusoidal distribution of surface pressure, p_{11}, is used instead of p_0, because the amplitude of contact pressure might be different. The pressure is given as:

$$p = \sigma_z(x,y,0) = p_{11}\cos(\alpha x)\cos(\beta y) \tag{2.17}$$

The normal elastic displacements of the surface for Eq. (2.17) is given by Johnson [46]:

$$u_z(x,y) = \left[2p_{11}\,\frac{(1-v^2)}{\zeta E}\right]\cos(\alpha x)\cos(\beta y) \tag{2.18}$$

Eq. (2.17) can be extended to three different cases:

$$p = \sigma_z(x, y, 0) = p_{12} cos(\alpha x) sin(\beta y) \quad (2.19a)$$

$$p = \sigma_z(x, y, 0) = p_{21} sin(\alpha x) cos(\beta y) \quad (2.19b)$$

$$p = \sigma_z(x, y, 0) = p_{22} sin(\alpha x) sin(\beta y) \quad (2.19c)$$

Since the amplitudes may be different, p_{12}, p_{21} and p_{22} was used here.

Following the method in [52], the displacements caused by the pressure in equations (2.19a) to (2.19c) are obtained:

From Eq. (2.19a)

$$u_x(x, y) = -\left[p_{12} \frac{(1+v)(1-2v)}{\zeta E}\right] cos(\gamma)\ sin(\alpha x) sin(\beta y) \quad (2.20a)$$

$$u_y(x, y) = \left[p_{12} \frac{(1+v)(1-2v)}{\zeta E}\right] cos(\gamma)\ [1 - cos(\alpha x) sin(\beta y)] \quad (2.20b)$$

$$u_z(x, y) = \left[2p_{12} \frac{(1-v^2)}{\zeta E}\right] \cos(\alpha x) \sin(\beta y) \quad (2.20c)$$

From Eq. (2.19b)

$$u_x(x, y) = \left[p_{21} \frac{(1+v)(1-2v)}{\zeta E}\right] cos(\gamma)\ [1 - cos(\alpha x) sin(\beta y)] \quad (2.21a)$$

$$u_y(x, y) = \left[p_{21} \frac{(1+v)(1-2v)}{\zeta E}\right] sin(\gamma)\ sin(\alpha x) sin(\beta y) \quad (2.21b)$$

$$u_z(x, y) = \left[2p_{21} \frac{(1-v^2)}{\zeta E}\right] \sin(\alpha x) \cos(\beta y) \quad (2.21c)$$

From Eq. (2.19c)

$$u_x(x, y) = \left[p_{22} \frac{(1+v)(1-2v)}{\zeta E}\right] cos(\gamma)\ sin(\alpha x) cos(\beta y) \quad (2.22a)$$

$$u_y(x, y) = -\left[p_{22} \frac{(1+v)(1-2v)}{\zeta E}\right] sin(\gamma)\ cos(\alpha x) sin(\beta y) \quad (2.22b)$$

$$u_z(x,y) = \left[2p_{22}\ \frac{(1-v^2)}{\zeta E}\right] \sin(\alpha x)\sin(\beta y) \tag{2.22c}$$

2.3.2.2 Shear Stress Condition

For the shear stress on the surface or the traction distributions in the *x* direction, the corresponding Airy potential function and displacement components were found by Tripp et al. [52]:

$$\tau_{xz}(x,y,0) = \tau_{x_{11}}\, cos(\alpha x) cos(\beta y) \tag{2.23}$$

and

$$\phi(x,y,z) = -\left(\frac{2\pi\tau_x}{\zeta^3}\right) e^{-\zeta z}\, cos(\alpha x) cos(\beta y) \tag{2.24}$$

and

$$u_x = \frac{1}{4\pi G}(2\Phi_{zz} + 2v\Phi_{xx} - z\Phi_{xxz}) \tag{2.25a}$$

$$u_y = \frac{1}{4\pi G}\left(2v\Phi_{xy} - z\Phi_{xyz}\right) \tag{2.25b}$$

$$u_z = \frac{1}{4\pi G}[(1-2v)\Phi_{xz} - z\Phi_{xzz}] \tag{2.25c}$$

Substituting Eq. (2.24) into Eq. (2.25), the displacement components are obtained:

$$u_x = -\frac{1}{2G}\frac{1}{\zeta}\left[2 - 2v\left(\frac{\alpha}{\zeta}\right)^2 - \left(\frac{\alpha}{\zeta}\right)\alpha z\right] e^{-\zeta z}\tau_{x_{11}}\, cos(\alpha x) cos(\beta y) \tag{2.26a}$$

$$u_y = -\frac{1}{2G}\frac{\alpha\beta}{\zeta^3}[2v + \zeta z]e^{-\zeta z}\, \tau_{x_{11}}\ sin(\alpha x) sin(\beta y) \tag{2.26b}$$

$$u_z = \frac{1}{2G}\frac{\alpha}{\zeta^2}[1 - 2v + \zeta z]e^{-\zeta z}\, \tau_{x_{11}}\, cos(\alpha x) sin(\beta y) \tag{2.26c}$$

Following Tripp’s formulation, Eq. (2.23) can be extended to:

$$\tau_{xz}(x,y,0) = \tau_{x_{12}}\, cos(\alpha x) sin(\beta y) \tag{2.27a}$$

$$\tau_{xz}(x,y,0) = \tau_{x_{21}}\, sin(\alpha x)\, cos(\beta y) \tag{2.27b}$$

$$\tau_{xz}(x,y,0) = \tau_{x_{22}}\, sin(\alpha x) sin(\beta y) \tag{2.27c}$$

and the corresponding Airy stress function:

$$\phi(x,y,z) = -\left(\frac{2\pi\tau_x}{\zeta^3}\right) e^{-\zeta z}\, cos(\alpha x) sin(\beta y) \tag{2.28a}$$

$$\phi(x,y,z) = -\left(\frac{2\pi\tau_x}{\zeta^3}\right) e^{-\zeta z}\, sin(\alpha x)\, cos(\beta y) \tag{2.28b}$$

$$\phi(x,y,z) = -\left(\frac{2\pi\tau_x}{\zeta^3}\right) e^{-\zeta z}\, sin(\alpha x) sin(\beta y) \tag{2.28c}$$

The displacement components for the 3 cases given by the distributions in Eq. (2.27) are derived:

$$u_x = -\frac{1}{2G}\frac{1}{\zeta}\left[2 - 2v\left(\frac{\alpha}{\zeta}\right)^2 - \left(\frac{\alpha}{\zeta}\right)\alpha z\right] e^{-\zeta z}\tau_{x_{12}}\, cos(\alpha x) sin(\beta y) \tag{2.29a}$$

$$u_y = \frac{1}{2G}\frac{\alpha\beta}{\zeta^3}[2v + \zeta z] e^{-\zeta z}\, \tau_{x_{12}}\ \ sin(\alpha x) cos(\beta y) \tag{2.29b}$$

$$u_z = -\frac{1}{2G}\frac{\alpha}{\zeta^2}[1 - 2v + \zeta z] e^{-\zeta z}\, \tau_{x_{12}}\, sin(\alpha x) cos(\beta y) \tag{2.29c}$$

$$u_x = -\frac{1}{2G}\frac{1}{\zeta}\left[2 - 2v\left(\frac{\alpha}{\zeta}\right)^2 - \left(\frac{\alpha}{\zeta}\right)\alpha z\right] e^{-\zeta z}\tau_{x_{21}}\, s\ in(\alpha x) cos(\beta y) \tag{2.30a}$$

$$u_y = \frac{1}{2G}\frac{\alpha\beta}{\zeta^3}[2v + \zeta z] e^{-\zeta z}\, \tau_{x_{21}}\ \ cos(\alpha x) sin(\beta y) \tag{2.30b}$$

$$u_z = \frac{1}{2G}\frac{\alpha}{\zeta^2}[1 - 2v + \zeta z] e^{-\zeta z}\, \tau_{x_{21}}\, cos(\alpha x) cos(\beta y) \tag{2.30c}$$

$$u_x = -\frac{1}{2G}\frac{1}{\zeta}\left[2 - 2v\left(\frac{\alpha}{\zeta}\right)^2 - \left(\frac{\alpha}{\zeta}\right)\alpha z\right] e^{-\zeta z}\tau_{x_{22}}\, sin(\alpha x)sin(\beta y) \tag{2.31a}$$

$$u_y = -\frac{1}{2G}\frac{\alpha\beta}{\zeta^3}[2v + \zeta z]e^{-\zeta z}\,\tau_{x_{22}}\; sin(\alpha x)sin(\beta y) \tag{2.31b}$$

$$u_z = \frac{1}{2G}\frac{\alpha}{\zeta^2}[1 - 2v + \zeta z]e^{-\zeta z}\,\tau_{x_{22}}\, cos(\alpha x)sin(\beta y) \tag{2.31c}$$

Likewise, the displacement components are given by the traction of the surface stress distributions $\tau_{y_{11}}\, cos(\alpha x)cos(\beta y)$, $\tau_{y_{12}}\, cos(\alpha x)cos(\beta y)$, $\tau_{y_{21}}\, cos(\alpha x)cos(\beta y)$, and $\tau_{y_{22}}\, cos(\alpha x)cos(\beta y)$. This displacement components are then derived as:

$$u_x = -\frac{1}{2G}\frac{\alpha\beta}{\zeta^3}[2v + \alpha z]\; e^{-\zeta z}\tau_{y_{11}}\, sin(\alpha x)sin(\beta y) \tag{2.32a}$$

$$u_y = -\frac{1}{2G}\frac{1}{\zeta}\left[2 - 2v\left(\frac{\beta}{\zeta}\right)^2 - \left(\frac{\alpha}{\zeta}\right)\alpha z\right] e^{-\zeta z}\,\tau_{y_{11}}\; cos(\alpha x)cos(\beta y) \tag{2.32b}$$

$$u_z = -\frac{1}{2G}\frac{\beta}{\zeta^2}[1 - 2v + \zeta z]e^{-\zeta z}\,\tau_{y_{11}}\, cos(\alpha x)sin(\beta y) \tag{2.32c}$$

$$u_x = \frac{1}{2G}\frac{\alpha\beta}{\zeta^3}[2v + \alpha z]\; e^{-\zeta z}\tau_{y_{12}}\, sin(\alpha x)cos(\beta y) \tag{2.33a}$$

$$u_y = -\frac{1}{2G}\frac{1}{\zeta}\left[2 - 2v\left(\frac{\beta}{\zeta}\right)^2 - \left(\frac{\alpha}{\zeta}\right)\alpha z\right] e^{-\zeta z}\,\tau_{y_{12}}\; cos(\alpha x)sin(\beta y) \tag{2.33b}$$

$$u_z = \frac{1}{2G}\frac{\beta}{\zeta^2}[1 - 2v + \zeta z]e^{-\zeta z}\,\tau_{y_{12}}\, cos(\alpha x)cos(\beta y) \tag{2.33c}$$

$$u_x = \frac{1}{2G}\frac{\alpha\beta}{\zeta^3}[2v + \alpha z]\; e^{-\zeta z}\tau_{y_{21}}\, cos(\alpha x)sin(\beta y) \tag{2.34a}$$

$$u_y = -\frac{1}{2G}\frac{1}{\zeta}\left[2 - 2v\left(\frac{\beta}{\zeta}\right)^2 - \left(\frac{\alpha}{\zeta}\right)\alpha z\right] e^{-\zeta z}\,\tau_{y_{21}}\; sin(\alpha x)cos(\beta y) \tag{2.34b}$$

$$u_z = -\frac{1}{2G}\frac{\beta}{\zeta^2}[1-2v+\zeta z]e^{-\zeta z}\,\tau_{y_{21}}\,sin(\alpha x)sin(\beta y) \tag{2.34c}$$

$$u_x = -\frac{1}{2G}\frac{\alpha\beta}{\zeta^3}[2v+\alpha z]\,e^{-\zeta z}\tau_{y_{22}}\,cos(\alpha x)cos(\beta y) \tag{2.34a}$$

$$u_y = -\frac{1}{2G}\frac{1}{\zeta}\left[2-2v\left(\frac{\beta}{\zeta}\right)^2-\left(\frac{\alpha}{\zeta}\right)\alpha z\right]e^{-\zeta z}\,\tau_{y_{22}}\;sin(\alpha x)sin(\beta y) \tag{2.34b}$$

$$u_z = -\frac{1}{2G}\frac{\beta}{\zeta^2}[1-2v+\zeta z]e^{-\zeta z}\,\tau_{y_{22}}\,sin(\alpha x)cos(\beta y) \tag{2.34c}$$

2.3. Results and Discussion

2.3.1. Interfacial State of Stress

Generally, the unknown contact pressure, $p(x,y)$, and the interfacial shear stresses, $q_x(x,y)$, and $q_y(x,y)$, can be expressed by the Fourier series with an infinite number of terms. Since the normal displacement, $u_z(x,y,0)$, only contains a single sinusoidal term, a simplified form of the boundary stresses may be written as:

$$\begin{aligned} p(x,y) &= p_{11}\,cos(\alpha x)\,cos(\beta y) + p_{12}\,cos(\alpha x)\,sin(\beta y) \\ &\quad + p_{21}\,sin(\alpha x)\,cos(\beta y) + p_{22}\,sin(\alpha x)\,sin(\beta y) \end{aligned} \tag{2.35a}$$

$$\begin{aligned} q_x(\mathrm{x,y}) &= \tau_{x11}\cos(\alpha x)\cos(\beta y) + \tau_{x12}\cos(\alpha x)\,sin(\beta y) \\ &\quad + \tau_{x21}\,sin(\alpha x)\,cos(\beta y) + \tau_{x22}\,sin(\alpha x)\,sin(\beta y) \end{aligned} \tag{2.35b}$$

$$\begin{aligned} q_y(\mathrm{x,y}) &= \tau_{y11}\cos(\alpha x)\cos(\beta y) + \tau_{y12}\cos(\alpha x)sin(\beta y) \\ &\quad + \tau_{y21}\,sin(\alpha x)\,cos(\beta y) + \tau_{y22}\,sin(\alpha x)\,sin(\beta y) \end{aligned} \tag{2.35c}$$

where the normal stress constants $p_{11}, p_{12}, p_{21}, p_{22}$ and shear stress constants τ_{x11}, τ_{x12}, τ_{x21}, τ_{x22}, τ_{y11}, τ_{y12}, τ_{y21}, τ_{y22}, are initially unknown. Note that the mean value of $q_x\,(x,y)$ and $q_y\,(x,y)$ over each period are zero. The average value of $p\,(x,y)$ is $\bar{p}$ and is the minimum of the value which can exclude all the negative values in $p\ (x, y)$. The addition of $\bar{p}$ would be achieved by the application of a sufficient normal load.

Similarly to the calculation of displacement components on the sinusoidal surface of the plane contact in Appendix A, the elementary solutions of the interfacial displacement components due to different bi-sinusoidal/cosinusoidal stress boundaries are listed in subsection 2.2.3. The resultant interfacial displacement components, $u_x\ (x, y, 0)$, $u_y\ (x, y, 0)$, and $u_z\ (x, y, 0)$, due to the stress boundaries in Eq. (2.3) are the superposition of the corresponding elementary solutions. Substituting the interfacial displacement components into the boundary conditions for complete contact under full stick (see Eq. (2.3)) and combining the same bi-sinuosidal/cosinusoidal terms, then the above boundary conditions can be decomposed into 12 linear equations. After solving this linear system, only three out of the twelve unknowns are non-zero:

$$p_{11} = p^* = \frac{2\Delta E\zeta(1-v)}{(1+v)(8v^2-12v+5)} \tag{2.36a}$$

$$\tau_{x21} = q_x^* = \frac{\Delta E\alpha(1-2v)}{(1+v)(8v^2-12v+5)} \tag{2.36b}$$

$$\tau_{y12} = q_y^* = \frac{\Delta E\beta(1-2v)}{(1+v)(8v^2-12v+5)} \tag{2.36c}$$

where $\zeta = \sqrt{\alpha^2+\beta^2}$

Note the complete contact pressure is reached when the average contact pressure is equal to p^* in the full stick condition. It is now denoted p_{stick}^*, Eq. (2.36a) becomes for $\alpha = \beta = 2\pi/\lambda$:

$$p_{stick}^* = \frac{4\sqrt{2}\pi E\Delta f(1-v)}{(1+v)(8v^2-12v+5)} \tag{2.37}$$

In contrast, the complete contact pressure for a special case ($\alpha = \beta = 2\pi/\lambda$) in the perfect slip condition is given by Johnson et al. [46]:

$$p_{slip}^{*} = \sqrt{2}\pi E'\Delta\mathrm{f} \tag{2.38}$$

where $E' = \frac{E}{1-\upsilon^2}$

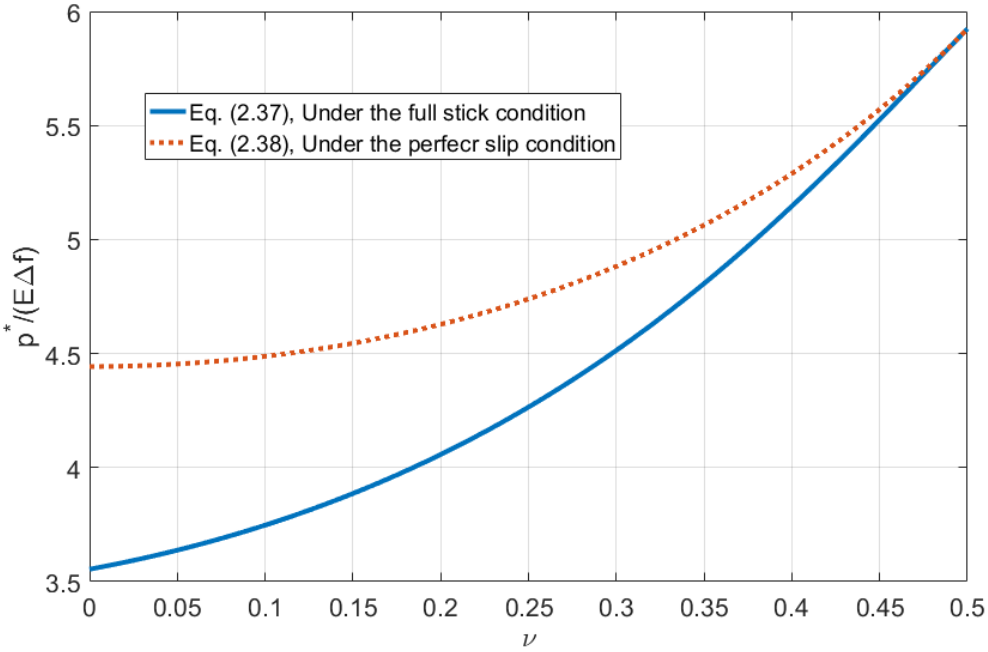

Fig. 2.4. Dimensionless complete contact pressure in full stick and prefect slip condition.

Since both Eqs. (2.37) and (2.38) have a $E\Delta f$ term, the complete contact pressure in the perfect slip condition, p_{slip}^{*}, and in the full stick condition, p_{stick}^{*} are normalized using $E\Delta f$. Then the normalized complete contact pressure is plotted versus Poisson's ratio (see Fig. 2.4.). It can be seen from Fig. 2.4. that as the Poisson's ratio increases, the dimensionless complete contact pressure also increases in both stick and slip. The complete contact pressure is also much lower in stick than it is in slip. This is because the addition of traction in the stick case increases the overall stress in the contact and therefore lowers the pressure needed to cause strain to compress the surface. The difference between the two curves decreases as ν increases, and they converge to the same value at $\nu = 0.5$. This is because the influence of tangential traction on the normal pressure is small for high values of Poisson's ratio, and the tangential stress under the full stick condition are low enough to make the complete contact pressure in stick and in slip similar. This observation was also found for the rigid flat punch indentation case as found in Johnson's book [27]. For the compressible material ($\nu < 0.5$), the complete contact pressures in stick are lower than their corresponding value in slip; For the incompressible material ($\nu = 0.5$), the complete contact pressure in stick is exactly equal to the value in slip.

Dividing Eq. (2.37) by Eq. (2.38), then the ratio is given by the following function of ν :

$$\frac{p^*_{stick}}{p^*_{slip}} = \frac{4(1-\nu)^2}{(8\nu^2 - 12\nu + 5)} \tag{2.39}$$

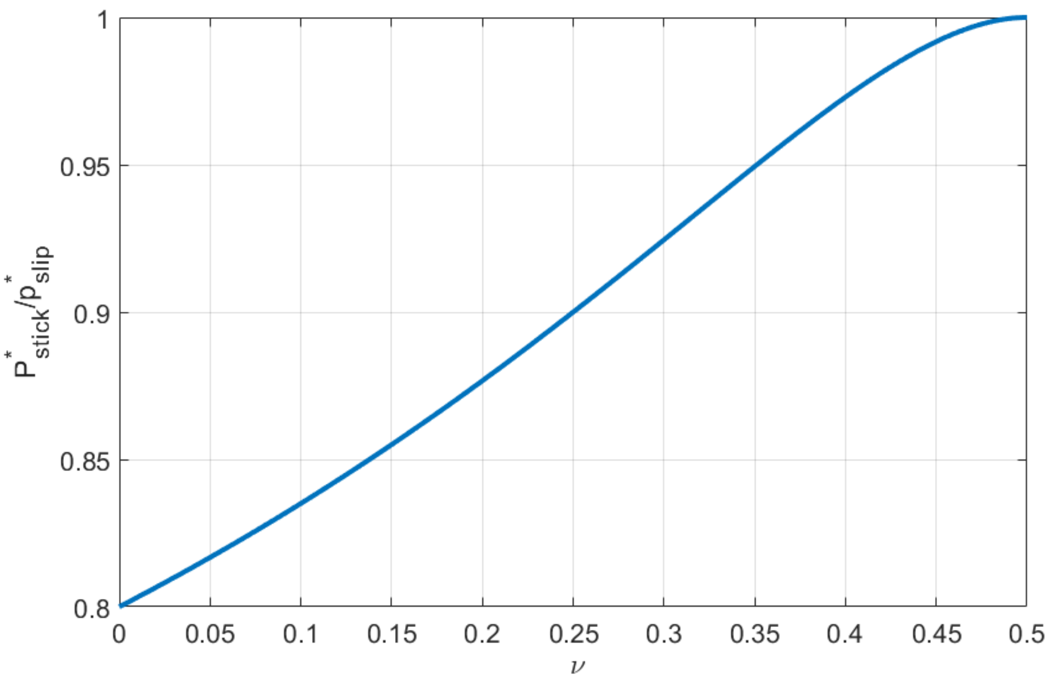

Fig. 2.5. The ratio of complete contact pressure in full stick over perfect slip.

Fig. 2.5. presents the ratio of the complete contact pressure in full stick over that in perfect slip. The ratio was found to be independent of the geometry and material properties except for Poisson's ratio. From Eq. 2.39, $p^*_{stick}/p^*_{slip} = 0.8$ when $\nu = 0$, and $p^*_{stick}/p^*_{slip} = 1$

when $\nu = 0.5$. Therefore the ratio increases as Poisson's ratio increases. That is because the tangential traction does not affect the ratio or Eq. (2.39) so much at the high values of Poisson's ratio.

Consequently, the final forms of the contact pressure and the interfacial shear stresses under the full stick condition are:

$$p(\mathrm{x},\mathrm{y}) = p^*_{stick}\cos(\alpha x)\cos(\beta y) + \bar{p} \tag{2.40a}$$

$$q_x(\mathrm{x},\mathrm{y}) = q^*_x\, sin(\alpha x)\cos(\beta y) \tag{2.40b}$$

$$q_y(\mathrm{x},\mathrm{y}) = q^*_y\, cos(\alpha x)\sin(\beta y) \tag{2.40c}$$

Note that the complete contact is initially reached when $\bar{p} = p^*_{stick}$.

2.3.2. General State of Stresses at Complete Contact

In order to determine the state of stresses of the half-space under the action of the boundary stresses, Eq. (2.37) can be decomposed into three sub-states for each surface traction $p(\mathrm{x},\mathrm{y})$, $q_x(\mathrm{x},\mathrm{y})$ and $q_y(\mathrm{x},\mathrm{y})$ individually. Then they can be superposed to find the complete solution. First, we will neglect the final $\bar{p}$ in Eq. (2.40a). Tripp et al. [52] provided the state of stresses of the half-space due to the application of a bi-cosinusoidal normal stress distribution, $\mathrm{p}(\mathrm{x},\mathrm{y}) = p^*_{stick}\cos(\alpha x)\cos(\beta y)$ on the boundary of a half-space:

$$\sigma_x = p^*_{stick}\left[\frac{\alpha^2}{\zeta^2} - \frac{\alpha^2 z}{\zeta} + 2\nu(\beta/\zeta)^2\right] e^{-\zeta z}\cos(\alpha x)\cos(\beta y) \tag{2.41a}$$

$$\sigma_y = p^*_{stick}\left[\frac{\beta^2}{\zeta^2} - \frac{\beta^2 z}{\zeta} + 2\nu(\alpha/\zeta)^2\right] e^{-\zeta z}\cos(\alpha x)\cos(\beta y) \tag{2.41b}$$

$$\sigma_z = p^*_{stick}(1 + \zeta z)\, e^{-\zeta z}\cos(\alpha x)\cos(\beta y) \tag{2.41c}$$

$$\tau_{xy} = -p^*_{stick}\left(\frac{\alpha\beta}{\zeta^2}\right)(1 - 2\nu - \zeta \mathrm{z})e^{-\zeta z}\sin(\alpha x)\sin(\beta y) \tag{2.41d}$$

$$\tau_{yz} = p^*_{stick}\,\beta \mathrm{z}\, e^{-\zeta z}\cos(\alpha x)\sin(\beta y) \tag{2.41e}$$

$$\tau_{xz} = p^*_{stick}\,\alpha \mathrm{z}\, e^{-\zeta z}\cos(\alpha x)\sin(\beta y) \tag{2.41f}$$

In addition, Tripp et al. [52] also gave the closed-form solution of the state of stress of the half-space due to the action of a bi-cosinusoidal shear stress distribution, $q_x(\mathrm{x},\mathrm{y}) = q^*_x\sin(\alpha x)\cos(\beta y)$, on the boundary. This boundary problem is solved by a known potential function. Following the same methodology, the state of stresses due to the boundary stress $q_x(\mathrm{x},\mathrm{y}) = \mathrm{q}^*_x sin(\alpha x)\cos(\beta y)$ are

$$\sigma_x = -q^*_x\alpha/\zeta[2 + 2\upsilon(\beta/\zeta)^2 - (\alpha/\zeta)(\alpha z)]\, e^{-\zeta z}\cos(\alpha x)\cos(\beta y) \tag{2.42a}$$

$$\sigma_y = -q^*_x\alpha\left[\frac{\beta^2}{\zeta^2} - \frac{\beta^2 z}{\zeta} + 2\upsilon(\alpha/\zeta)^2\right]e^{-\zeta z}\cos(\alpha x)\cos(\beta y) \tag{2.42b}$$

$$\sigma_z = -q^*_x\alpha z\, e^{-\zeta z}\cos(\alpha x)\cos(\beta y) \tag{2.42c}$$

$$\tau_{xy} = q^*_x\beta/\zeta\left(1 - \frac{2\mathrm{v}\alpha^2}{\zeta^2} - \frac{\alpha^2\mathrm{z}}{\zeta}\right)e^{-\zeta z}\,\sin(\alpha x)\sin(\beta y) \tag{2.42d}$$

$$\tau_{yz} = -q^*_x\frac{\alpha\beta}{\zeta}\mathrm{z}\, e^{-\zeta z}\cos(\alpha x)\sin(\beta y) \tag{2.42e}$$

$$\tau_{xz} = q^*_x(1 - \alpha^2 z/\zeta)\, e^{-\zeta z}\sin(\alpha x)\cos(\beta y) \tag{2.42f}$$

Similarly, a boundary stress distribution, $q_y(\mathrm{x},\mathrm{y}) = q^*_y sin(\alpha x)\cos(\beta y)$ will result in the following state of stress:

$$\sigma_x = -q^*_y\beta/\zeta\left(2\nu\frac{\beta^2}{\zeta^2} - \frac{\alpha^2 z}{\zeta}\right)\, e^{-\zeta z}\cos(\alpha x)\cos(\beta y) \tag{2.43a}$$

$$\sigma_y = q^*_y\,\beta/\zeta[2 + 2\upsilon(\alpha/\zeta)^2 - (\beta/\zeta)(\beta z)]\, e^{-\zeta z}\cos(\alpha x)\cos(\beta y) \tag{2.43b}$$

$$\sigma_z = -q^*_y\beta z\, e^{-\zeta z}\cos(\alpha x)\cos(\beta y) \tag{2.43c}$$

$$\tau_{xy} = q_y^*\alpha/\zeta\left(1-\frac{2\mathrm{v}\beta^2}{\zeta^2}-\frac{\beta^2\mathrm{z}}{\zeta}\right)e^{-\zeta z}\sin(\alpha x)\sin(\beta y) \tag{2.43d}$$

$$\tau_{yz} = q_y^*(1-\beta^2 z/\zeta)\,e^{-\zeta z}\cos(\alpha x)\sin(\beta y) \tag{2.43e}$$

$$\tau_{xz} = -\,q_y^*\left(\frac{\alpha\beta}{\zeta}\right)\mathrm{z}\;e^{-\zeta z}\sin(\alpha x)\cos(\beta y) \tag{2.43f}$$

Then the state of stress due to the mutual action of the boundary tractions, $p(x,y)$, $q_x(x,y)$, and $q_y(x,y)$ in Eq. (2.40), are the superposition of the contributions listed above:

$$\sigma_x = \left\{p_{stick}^*\left[\frac{\alpha^2}{\zeta^2}-\frac{\alpha^2 z}{\zeta}+2\upsilon(\beta/\zeta)^2\right]-q_x^*\alpha/\zeta\left[2+2\upsilon\left(\frac{\beta}{\zeta}\right)^2-(\alpha/\zeta)(\alpha z)\right]\right.$$
$$\left.-\,q_y^*\beta/\zeta\left(2\upsilon\frac{\beta^2}{\zeta^2}-\frac{\alpha^2 z}{\zeta}\right)\right\}e^{-\zeta z}\cos(\alpha x)\cos(\beta y) \tag{2.44a}$$

$$\sigma_y = \left\{p_{stick}^*\left[\frac{\beta^2}{\zeta^2}-\frac{\beta^2 z}{\zeta}+2\upsilon(\alpha/\zeta)^2\right]-q_x^*\alpha\left[\frac{\beta^2}{\zeta^2}-\frac{\beta^2 z}{\zeta}+2\upsilon\left(\frac{\alpha}{\zeta}\right)^2\right]\right.$$
$$\left.+\,q_y^*\,\beta/\zeta[2+2\upsilon(\alpha/\zeta)^2-(\beta/\zeta)(\beta z)]\right\}e^{-\zeta z}\cos(\alpha x)\cos(\beta y) \tag{2.44b}$$

$$\sigma_z = \left\{p_{stick}^*(1+\zeta z)-q_x^*\alpha z-q_y^*\beta z\right\}e^{-\zeta z}\cos(\alpha x)\cos(\beta y) \tag{2.44c}$$

$$\tau_{xy} = \left[-p_{stick}^*\left(\frac{\alpha\beta}{\zeta^2}\right)(1-2\mathrm{v}-\zeta\mathrm{z})+\;q_x^*\frac{\beta}{\zeta}\left(1-\frac{2\nu\alpha^2}{\zeta^2}-\frac{\alpha^2\mathrm{z}}{\zeta}\right)\right.$$
$$\left.+\;q_y^*\frac{\alpha}{\zeta}\left(1-\frac{2\mathrm{v}\beta^2}{\zeta^2}-\frac{\beta^2\mathrm{z}}{\zeta}\right)\right]e^{-\zeta z}\sin(\alpha x)\sin(\beta y) \tag{2.44d}$$

$$\tau_{yz} = \left[p_{stick}^*\,\beta\mathrm{z}-q_x^*\frac{\beta}{\zeta}(\alpha z)+q_y^*\left(1-\frac{\beta^2 z}{\zeta}\right)\right]\;e^{-\zeta z}\cos(\alpha x)\sin(\beta y) \tag{2.44e}$$

$$\tau_{yz} = \left\{p_{stick}^*\,\alpha\mathrm{z}+q_x^*(1-\alpha^2 z/\zeta)-q_y^*\left(\frac{\alpha\beta}{\zeta}\right)\mathrm{z}\right\}e^{-\zeta z}\sin(\alpha x)\cos(\beta y) \tag{2.44f}$$

After algebraic manipulation by instituting of p_{stick}^*, Eq. (2.44) yields the following simplified forms of the state of stress:

$$\sigma_x = \frac{\Delta\, E\ (-\alpha^2 + 2\nu\zeta)}{(1+\nu)(8v^2 - 12v + 5)} e^{-\zeta z} \cos(\alpha x)\cos(\beta y) \tag{2.45a}$$

$$\sigma_y = \frac{\Delta\, E\ (-\beta^2 + 2\nu\zeta)}{(1+\nu)(8v^2 - 12v + 5)} e^{-\zeta z} \cos(\alpha x)\cos(\beta y) \tag{2.45b}$$

$$\sigma_z = \frac{\Delta\, E\ (\zeta^2 z + 2z - 2v\zeta)}{(1+\nu)(8v^2 - 12v + 5)} e^{-\zeta z} \cos(\alpha x)\cos(\beta y) \tag{2.45c}$$

$$\tau_{xy} = \frac{\Delta\, E\alpha\beta z\ (\zeta^2 z + 2z - 2v\zeta)}{(1+\nu)(8v^2 - 12v + 5)} e^{-\zeta z} \sin(\alpha x)\sin(\beta y) \tag{2.45d}$$

$$\tau_{yz} = \frac{\Delta\, E\ \beta(\zeta z + 1 - 2v)}{(1+\nu)(8v^2 - 12v + 5)} e^{-\zeta z} \cos(\alpha x)\sin(\beta y) \tag{2.45e}$$

$$\tau_{xz} = \frac{\Delta\, E\ \beta(\zeta z + 1 - 2v)}{(1+\nu)(8v^2 - 12v + 5)}\ e^{-\zeta z} \sin(\alpha x)\cos(\beta y) \tag{2.45f}$$

In addition to the sinusoidal stresses, there is an average uniform pressure given in the last term in Eq. (2.40). Due to this uniform pressure, $\bar{p} = p^*_{stick}$, and by employing Hooke's law, the stress on the half space is derived by:

$$\sigma_x = p^*_{stick}\left(\frac{v}{1-v}\right) \tag{2.46a}$$

$$\sigma_y = p^*_{stick}\left(\frac{v}{1-v}\right) \tag{2.46b}$$

$$\sigma_z = p^*_{stick} \tag{2.46c}$$

Note that the sign of the stresses in Eq. (2.46) follows the convention in contact mechanics, i.e. compressive stress is positive and tensile stress is negative. Carrying out the superposition, the stress field can be recombined from the Eqs. (2.45) and (2.46) with the following results:

$$\sigma_x = \frac{\Delta\, E}{(1+\nu)(8v^2 - 12v + 5)}\left[\,(-\alpha^2 + 2\nu\zeta)\, e^{-\zeta z}\cos(\alpha x)\cos(\beta y) + 2v\right] \tag{2.47a}$$

$$\sigma_y = \frac{\Delta\, E}{(1+\nu)(8v^2 - 12v + 5)}\left[\,(-\beta^2 + 2\nu\zeta)\, e^{-\zeta z}\cos(\alpha x)\cos(\beta y) + 2v\right] \tag{2.47b}$$

$$\sigma_z = \frac{\Delta\, E}{(1+\nu)(8\upsilon^2-12\upsilon+5)}\left[\,(\zeta^2 z+2\zeta-2\upsilon\zeta)\, e^{-\zeta z}\cos(\alpha x)\cos(\beta y)+\ 2-2\upsilon\right] \tag{2.47c}$$

$$\tau_{xy} = \frac{\Delta\, E\alpha\beta z}{(1+\nu)(8\upsilon^2-12\upsilon+5)}\, e^{-\zeta z}\sin(\alpha x)\sin(\beta y) \tag{2.47d}$$

$$\tau_{yz} = \frac{\Delta\, E\ \beta(\zeta z+1-2\upsilon)}{(1+\nu)(8\upsilon^2-12\upsilon+5)}\, e^{-\zeta z}\cos(\alpha x)\sin(\beta y) \tag{2.47e}$$

$$\tau_{xz} = \frac{\Delta\, E\ \alpha(\zeta z+1-2\upsilon)}{(1+\nu)(8\upsilon^2-12\upsilon+5)}\ e^{-\zeta z}\sin(\alpha x)\cos(\beta y) \tag{2.47f}$$

2.3.3. The Maximum von Mises Stress

When considering the initiation of the plastic deformation, the von Mises (or distortion energy) criteria is considered to be a very effective method. It is given by:

$$\sigma_{vm} = \sqrt{\frac{1}{2}\left[(\sigma_x-\sigma_y)^2+(\sigma_y-\sigma_z)^2+(\sigma_x-\sigma_z)^2+6\left(\tau_{xy}^2+\tau_{yz}^2+\tau_{xz}^2\right)\right]} \tag{2.48}$$

By substituting σ_x, σ_y, σ_z, τ_{xy}, τ_{yz}, and τ_{xz} from Eq. (2.47) into Eq. (2.48). Since for the current case, wavelengths in the *x* and *y* directions are equal ($\alpha = \beta$), the equation becomes

$$\begin{aligned}\sigma_{vm} = \frac{\Delta\, E\ \zeta}{(1+\nu)(8\upsilon^2-12\upsilon+5)}\Bigg\{&\left[\left(\frac{3}{2}\zeta z-4\upsilon+2\right)e^{-\zeta z}\cos(\alpha x)\cos(\alpha y)-4\upsilon+2\right]^2\\ &+\frac{3}{4}\zeta^2 z^2 e^{-2\zeta z}\ sin^2(\alpha x) sin^2(\alpha y)\\ &+\frac{3}{2}(\zeta z+1-2\upsilon)^2 e^{-2\zeta z}\left[cos^2(\alpha x) sin^2(\alpha y)+sin^2(\alpha x) cos^2(\alpha y)\right]\Bigg\}^{\frac{1}{2}}\end{aligned} \tag{2.49}$$

In order to find the location of the maximum von Mises stress in the *xy* plane, the maximum of Eq. (2.49) will occur at the inflection point or where the gradient is nil. Therefore, carrying out the second order derivation, and letting $\frac{\partial\sigma_{vm}^2}{\partial \mathrm{x}\,\partial \mathrm{y}} = 0$, the location of the peak points, i.e. $(0{,}0)$,

$(0, \lambda)$, $(\lambda, 0)$, (λ, λ), and $(\frac{\lambda}{2}, \frac{\lambda}{2})$. of σ_{vm} are determined. Substituting the 5 points results in the same equation:

$$\sigma_{vm0} = \frac{\Delta\, E\, \zeta}{(1+\nu)(8\upsilon^2 - 12\upsilon + 5)} \left|\left[\left(\frac{3}{2}\zeta z - 4\upsilon + 2\right) e^{-\zeta z} - 4\upsilon + 2\right]\right| \tag{2.50}$$

The differential of Eq. (2.50) is then

$$\frac{d\sigma_{vm0}}{dz} = \frac{\Delta\, E\, \zeta^2}{(1+\nu)(8\upsilon^2 - 12\upsilon + 5)} \left|-\frac{3}{2}\zeta z + 4\upsilon - \frac{1}{2}\right| \tag{2.51}$$

The maximum von Mises stress is obtained by solving for the location *z* where $d\sigma_{vm0}/dz = 0$. Hence, we can find the value of *z* where the von Mises reaches the maximum value. It is:

$$z_0 = \frac{8\nu - 1}{3\zeta} \tag{2.52}$$

since $\zeta = \sqrt{2}\alpha$, $z_0 = \frac{8\nu-1}{6\sqrt{2}\pi}\,\lambda$

The location z_0 is dependent only on the geometry parameter of wavelength, λ, and the material parameter Poisson's ratio, ν. Most of the Poisson's ratios of typical engineering materials are in the range of $0 \le \nu \le 0.5$. Considering this range, $z_0 < 0$, when $0 \le \nu < \frac{1}{8}$ and $z_0 \ge 0$ when $\frac{1}{8} \le \nu \le 0.5$. By definition, z_0 should be always greater than zero, and therefore we need to discuss these two cases: When $0 \le \nu \le \frac{1}{8}$, there is no solution for the Eq. (2.52) on $[0, +\infty)$. Considering that Eq. (2.51) is a decreasing function, when $z_0 < 0$, it should be set to $z_0 = 0$. This physically means that the maximum stress is on the surface. When $\frac{1}{8} \le \nu \le 0.5$, z_0 is at $[0, +\infty)$ and then found to be: $z_0 = \frac{8\nu-1}{6\sqrt{2}\pi}\,\lambda$. The values of $z_0 = \frac{8\nu-1}{6\sqrt{2}\pi}\,\lambda$ and $z_0 = 0$ are then substituted back into Eq. (2.50) to find the maximum value of the von Mises stress:

$$When\ \nu < \frac{1}{8}, \qquad (\sigma_{vm})_{max} = \frac{8\sqrt{2}\pi\,(1-2v)}{(1+v)(8v^2-12\nu+5)}\frac{\Delta}{\lambda}\,E$$

$$When\ \nu \geq \frac{1}{8}, \qquad (\sigma_{vm})_{max} = \frac{3\sqrt{2}\pi\,e^{(1-8v)/3} - 8\sqrt{2}v + 4\sqrt{2}}{(1+v)(8v^2-12\nu+5)}\frac{\Delta}{\lambda}\,E \tag{2.53}$$

In contrast, the corrected maximum von Mises stress expression for the slip condition in [48] is given as:

$$(\sigma_{vm})_{max} = \sqrt{2}\pi E'\Delta f\left[\frac{3}{2}e^{-2/3(v+1)} + \left(\frac{1-2v}{1-v}\right)\right] \tag{2.54}$$

The dimensionless maximum von Mises stress is plotted in Fig. 2.6. It is shown that the ratio will decrease as the Poisson's ratio increases for both in stick and slip. The maximum von Mises stress under the full stick condition is lower than or equal to the corresponding value in slip. From the previous discussion, the maximum von Mises stress can occur either on the surface, (z_0 = 0), or somewhere under the surface, ($z_0 = \frac{8\nu-1}{6\sqrt{2}\pi}\,\lambda$), depending on the value of Poisson's ratio. This is similar to that found in cylindrical contact. The transition is at $\nu = \frac{1}{8}$, while the transition found in [53] was at $\nu = 0.1938$, for the cylindrical contact.

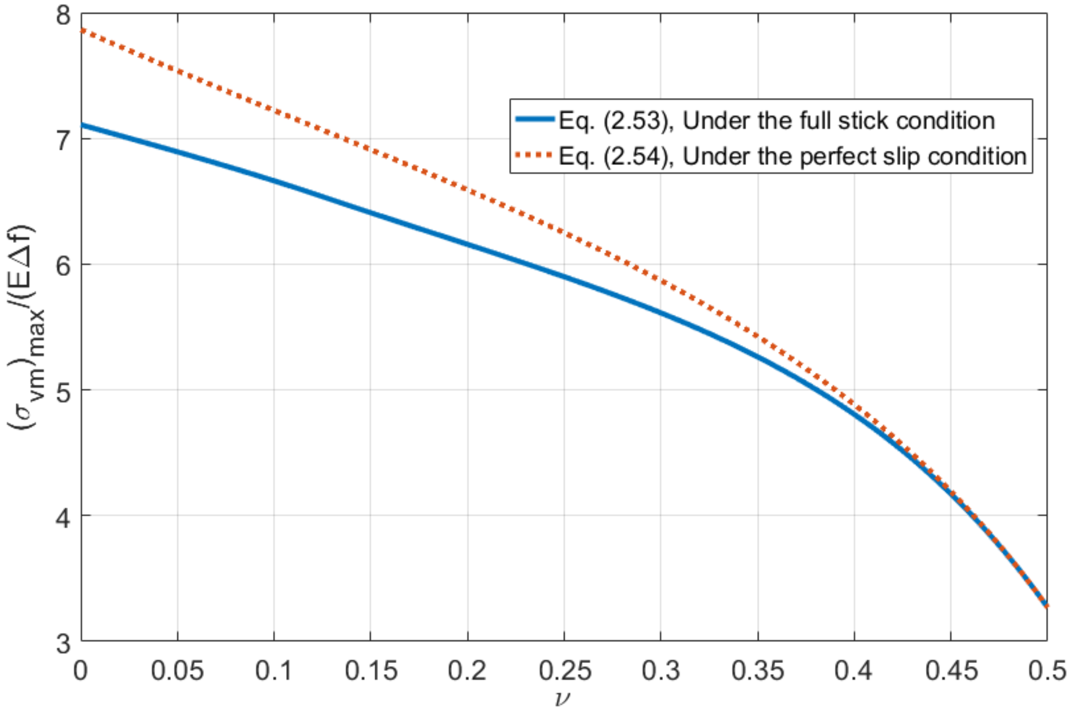

Fig. 2.6. Dimensionless maximum von Mises stress as a function of Poisson's ratio.

2.3.4. Critical Value of Amplitude

The value of σ_{vm} is valid in the elastic deformation range, and is used to calculate the critical amplitude during complete contact denoted as Δ_c, defined by Jackson et al. [48]. The definition of the critical amplitude is: when $\Delta \leq \Delta_c$ the sinusoidal contact will deform purely elastically for all loads, even until the sinusoidal surface geometry has completely flattened out. However, when $\Delta > \Delta_c$, plastic deformation may occur before complete contact is reached. By setting the von Mises stress σ_{vm} equal to the yield strength, S_y, and solving for Δ, the critical amplitude during complete contact, Δ_c, is given as [54]:

$$When\ \nu < \frac{1}{8}, \Delta_c = \frac{(1+\upsilon)(8\upsilon^2 - 12\nu + 5)}{8\sqrt{2}\pi\ (1-2\upsilon)} \frac{\mathrm{Sy}}{E}\ \lambda \tag{2.55}$$

$$When\ \nu \geq \frac{1}{8}, \Delta_c = \frac{(1+\upsilon)(8\upsilon^2 - 12\upsilon + 5)}{3\sqrt{2}\pi\, e^{(1-8\upsilon)/3} - 8\sqrt{2}\upsilon + 4\sqrt{2}} \frac{\mathrm{Sy}}{E}\, \lambda$$

In addition, the critical amplitude during complete contact for the perfect slip given in [48] is incorrect and the corrected equation is given as [55]:

$$\Delta_c = \frac{\sqrt{2} S_y \lambda}{\pi E' \left[3\, e^{-2(\upsilon+1)/3} + 2\left(\frac{1-2\nu}{1-\nu}\right)\right]} \tag{2.56}$$

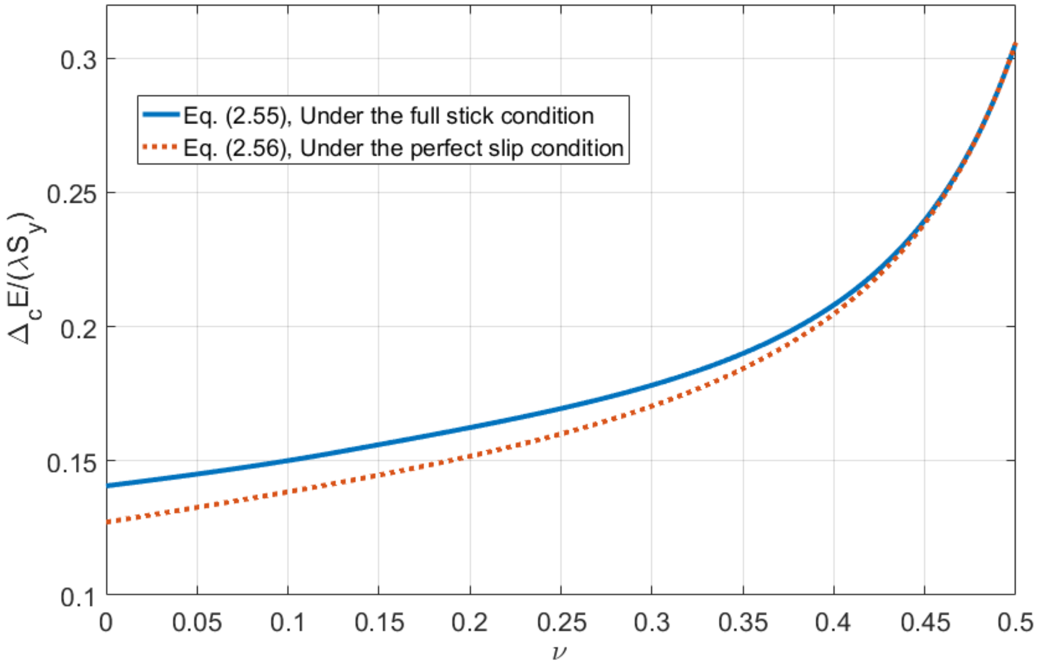

Fig. 2.7. Dimensionless critical amplitude as a function of Poisson’s ratio

The critical value of amplitude, Δ_c, for the perfect slip and full stick conditions are plotted in Fig. 2.7. It is noted that the value of the critical amplitude under the full stick is greater than the one in the perfect slip condition. This is because the tangential stresses in the contact interface under the full stick condition are nonexistent in the perfect slip condition. The additional tangential stresses result in higher von Mises stresses in the material below a non-slip (i.e. full stick) surface compared to the slip case.

2.4. Conclusion

An analytical, closed-form solution was provided to make predictions of the average pressure required to obtain complete contact between elastic wavy or sinusoidal surfaces in full stick. The value of the complete contact pressure in stick is lower than the value in slip. The ratio of the average complete contact pressure between perfect slip and full stick conditions are mostly affected by Poisson's ratio.

This work also determines the location of the maximum von Mises stress in sinusoidal contact based upon the distortion energy theory as well. Similar to the cylindrical contact, the maximum von Mises stress occurs on the axis of symmetry, and it can occur either on the surface or under the surface, depending on Poisson's ratio. For $0 \leq \nu < \frac{1}{8}$, the maximum von Mises stress occurs on the surface; for $\frac{1}{8} \leq \nu < 0.5$, the maximum von Mises stress occurs beneath the surface.

A critical amplitude of the sinusoidal surface is also derived. When the amplitude of the sinusoidal surface is less than the critical value, the deformation is always in the elastic range up to the initiation of complete contact; when the amplitude is greater than the critical value, the deformation will be able to enter the elastic-plastic range prior to complete contact. The critical value of amplitude is higher in stick than in slip.

CHAPTER 3. ELASTIC-PLASTIC SINUSOIDAL CONTACT UNDER NORMAL LOADING IN FULL STICK

3.1. Introduction

The behavior of an elastic-plastic contact between a deformable single asperity and a rigid flat under normal loading in full stick have been investigated by many researchers. As we discussed in Chapter 2, the three main commonly used tangential boundary conditions are perfect slip, full stick and partial slip condition. The slip condition assumes that there is no friction on the surface in the contact area. Since this ideal assumption of perfect slip may not be realistic, several researchers have considered the full stick condition, in which the surfaces and the flat are bonded together and there is no relative displacement. Brizmer et al. [56] analyzed the effect of contact conditions and material properties on the yield inception of a spherical contact. They found that the normalized yield inception is independent of the geometric parameters and material properties except for Poisson's ratio. The yield inception always occurs on the circle of the sphere surface for brittle materials, while it occurs at the single point on the axis of symmetry for ductile materials. For the ductile materials, the critical interference, critical load and yield inception depth in full stick are lower than the corresponding values in slip with lower values of Poisson's ratio. The unloading process of an elastic–plastic spherical contact under the stick contact condition was analyzed for various material properties using the FE method by Zait et al. [57]. There is no difference was between the two contact conditions for the interference load behavior, however a substantial difference was noticed for the area load curves.

The asperities of rough surfaces are typically described by spherical or parabolic geometries in most rough surface contact models. However, the geometry of actual asperities is much different than this, especially at the base of the asperity. This is especially important when an asperity is under a heavy load. Therefore, wavy or sinusoidal surface models are important for the consideration of rough surface contact. The elastic-plastic contact problem between sinusoidal surfaces has been investigated by many researchers. Gao et al. [20] used the finite element method (FEM) to investigated the two-dimensional elastic plastic solid body with a sinusoidal surface. Krithivasan and Jackson [58] provided empirical equations for the contact area as a function of contact pressure considering elastic-plastic contact. Later, Jackson et al. [48] confirmed their work in [58] by using an analytical solution, and provided an expression for the critical interference during complete contact. Rostami et al. [59] provided a model to predict the average surface separation between a sinusoidal surface and a rigid flat as well as the contact stiffness. Some fast Fourier transforms (FFT) based models [19, 49] were presented using the relationships from sinusoidal asperity contact. These models can be used to predict electrical and thermal contact resistance [21, 60, 61].

It can be seen from the above introduction, very little work was done on the sinusoidal contact in the full stick condition. The main goal of this chapter is to find the difference in behaviors of sinusoidal contact between the perfect slip and the full stick condition. We analyze the elastic-plastic contact under the full stick condition with different material properties, and to compare the results with the results of an existing semi-analytical model of perfect slip [48].

3.2 Modeling Approach

3.2.1 Theoretical Model

The schematic of the deformable sinusoidal surface with a rigid plat under normal loading is shown in Fig. 3.1. In Fig. 3.1, Δ is the amplitude of the sinusoidal surface, λ is the wavelength of the sinusoidal surface contact, and h_b is the substrate depth for the sinusoidal surfaces.

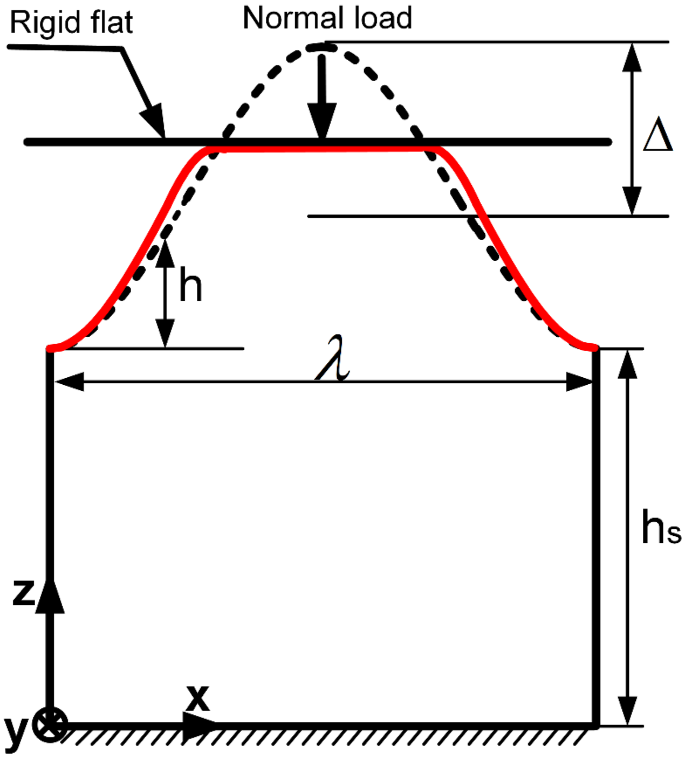

Fig. 3.1. The schematic of the deformable sinusoidal surface with a rigid flat under normal loading.

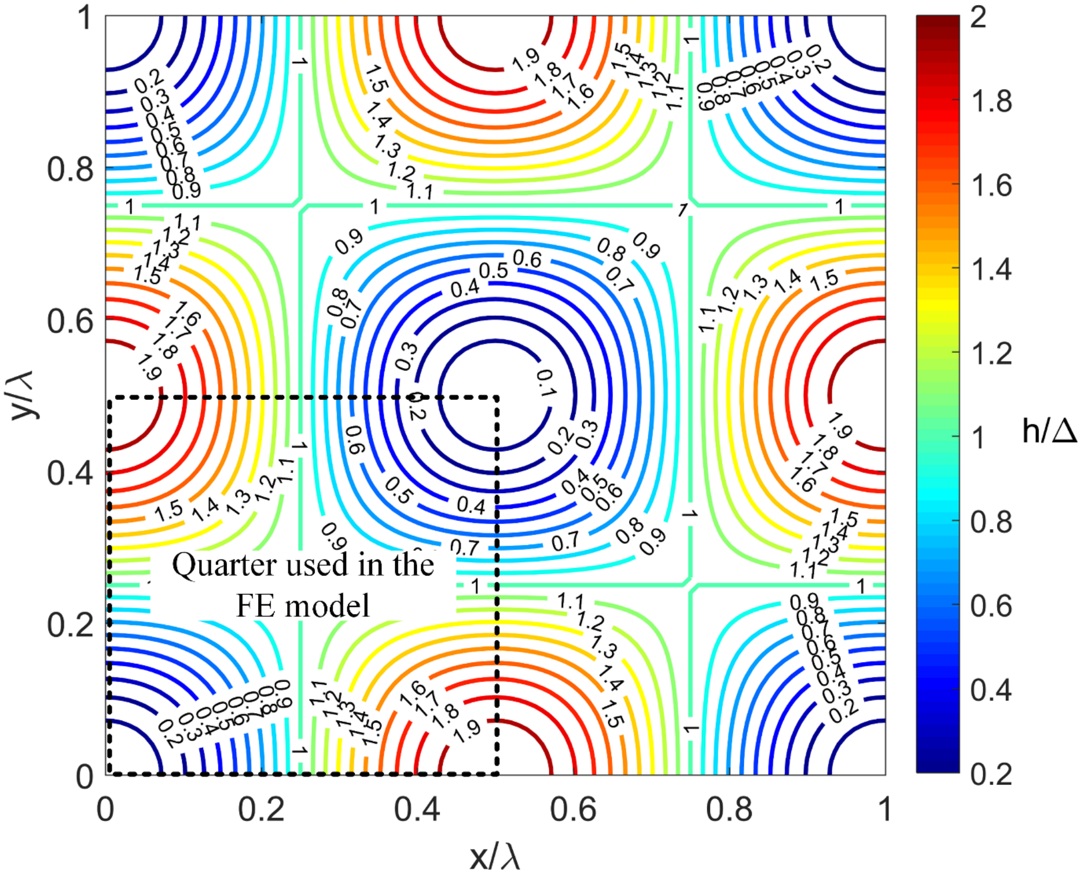

Fig. 3.2. The sinusoidal surface geometry considered in the FE model.

Three-dimensional elastic-plastic contact between sinusoidal surfaces has been investigated by Krithivasan and Jackson [58] and Jackson et al. [62]. The geometry is given by:

$$h = \Delta\left(1 - cos\left(\frac{2\pi x}{\lambda}\right)cos\left(\frac{2\pi y}{\lambda}\right)\right) \tag{3.1}$$

where h is the height of the sinusoidal surface, Δ is the amplitude of the sinusoidal surface, and λ is the wavelength of the sinusoidal surface, and the contour of the sinusoidal surface is shown in Fig. 3.2.

Johnson et al. [46] provided two asymptotic solutions to the elastic contact of a sinusoidal shaped surface

$$When\ \bar{p} \ll p^*: \qquad \left(A_{JGH}\right)_1 = \frac{\pi}{f^2}\left(\frac{3}{8\pi}\frac{\bar{p}}{p^*}\right)^{2/3} \tag{3.2}$$

$$When\ \bar{p} \to p^*: \qquad \left(A_{JGH}\right)_2 = \frac{1}{f^2}\left[1 - \frac{3}{2\pi}\left(1 - \frac{\bar{p}}{p^*}\right)\right] \tag{3.3}$$

Jackson and Streator [19] developed an empirical equation linking Eqs. (3.2) and (3.3) based on the experimental data provided by Johnson et al. [46]:

$$For\ \ \bar{p} < 0.8: \qquad A = \left(A_{JGH}\right)_1\left[1 - \left(\frac{\bar{p}}{p^*}\right)^{1.51}\right] + \left(A_{JGH}\right)_2\left(\frac{\bar{p}}{p^*}\right)^{1.04} \tag{3.4}$$

$$For\ \ \bar{p} \geq 0.8: \qquad A = \left(A_{JGH}\right)_2 \tag{3.5}$$

The critical values for sinusoidal contact under normal load in the perfect slip condition are given by [58]:

$$\omega_c = \left(\frac{CS_y}{4E'f}\right)^2 \frac{1}{\Delta} \tag{3.6}$$

$$F_c = \frac{1}{6\pi}\left(\frac{1}{\Delta f^2 E'}\right)^2\left(\frac{C}{2}S_y\right)^3 \tag{3.7}$$

$$\mathrm{A}_c = \frac{2}{\pi}\left(\frac{CS_y}{8\Delta f^2 E'}\right)^2 \tag{3.8}$$

where the constant C is related to the Poisson's ratio by:

$$C = 1.295exp(0.736\nu) \tag{3.9}$$

and ω_c is the critical interference, F_c is the critical force, and A_c is the critical area under the perfect slip condition. Note that the above equations are based on spherical contact, but adapted to a sinusoidal shaped surface. In these equations, the critical values for the sinusoidal contact are based on spherical contact. The effect of contact conditions and material properties on the termination of elasticity in spherical contact was investigated by Brizmer et al. [56]. They found that the ratios of critical interference and load in the full stick condition over that in the perfect slip condition are independent of material properties except for the Poisson's ratio. The relationship between the critical values for spherical contact with ductile materials in full stick and slip conditions is given by [56]

$$\frac{(\omega_{cs})_{stick}}{\omega_c} = 6.82\nu - 7.83(\nu^2 + 0.0586) \tag{3.10}$$

$$\frac{(F_c)_{stick}}{F_c} = 8.88\nu - 10.13(\nu^2 + 0.089) \tag{3.11}$$

where $(\omega_{cs})_{stick}$ and $(F_c)_{stick}$ are the critical interference and force under the full stick condition respectively.

Since the sinusoidal contact in the initial contact is similar to the spherical contact, Eqs. (3.10) and (3.11) can be used to calculate the critical values of sinusoidal contact in the full stick. By substituting Eq. (3.6) and (3.7) into Eq. (3.10) and (3.11), the expressions for the critical interference and force under the full stick condition are obtained:

$$(\omega_{cs})_{stick} = [6.82\nu - 7.83(\nu^2 + 0.0586)]\left(\frac{CS_y}{4E'f}\right)^2 \frac{1}{\Delta} \tag{3.12}$$

$$(F_c)_{stick} = [8.88\nu - 10.13(\nu^2 + 0.089)]\ \frac{1}{6\pi}\left(\frac{1}{\Delta f^2 E'}\right)^2 \left(\frac{C}{2}S_y\right)^3 \tag{3.13}$$

Ghaednia et al. [55] present an empirical equation for the average pressure that causes complete contact for the elastic-plastic case. The equation is given as:

$$\frac{p_{ep}^*}{p^*} = 0.992^{\left\{\left(\frac{\Delta}{\Delta_c}\right)^{\left[\frac{10}{3}\left(\frac{\Delta}{\Delta_c}\right)^{-0.39} + \frac{9}{4}\nu^4 + 0.64\right]_{-1}}\right\}} \tag{3.14}$$

where Δ_c is the analytically derived critical amplitude. When the amplitude is less than this value, the sinusoidal surface deforms elastically. When the amplitude is greater than this value, it deforms plastically. Δ_c is given by:

$$\Delta_c = \frac{\sqrt{2}S_y}{\pi E' f\left[3e^{-2/3(\nu+1)} + 2\left(\frac{1-2\nu}{1-\nu}\right)\right]} \tag{3.15}$$

And C_ν is a function of Poisson's ratio, and given by

$$C_\nu = 0.0017\exp(8.09\nu) - 0.0567 \tag{3.16}$$

Note that when $\Delta = \Delta_c$, $p^*_{ep} = p^*$. Eq. (3.14) results is the same overall prediction as given in [48]. Ghaednia et al. [55] also provide an correct version of critical ratio of amplitude to wavelength, B_c, which was original presented in [48].

$$B_c = \frac{\sqrt{2}S_y}{\pi E'\left[3e^{-2/3(\nu+1)} + 2\left(\frac{1-2\nu}{1-\nu}\right)\right]} \tag{3.17}$$

If the ratio of amplitude to wavelength of sinusoidal surface, B, is less than B_c, it will deform elastically. Likewise, when $B$is greater than B_c, the surfaces deforms elastic-plasticly.

Using Eq. 3.6, an equation to the finite element results to predict contact area as a function of average contact pressure [58]

$$A = A_p\left[1 - \left(\frac{\bar{p}}{p^*_{ep}}\right)^{1.51}\right] + \left(A_{JGH}\right)_2\left(\frac{\bar{p}}{p^*_{ep}}\right)^{1.04} \tag{3.18}$$

Where

$$A_p = 2\left(\frac{A_c}{2}\right)^{\frac{1}{1+d}}\left(\frac{3\bar{p}}{4CS_y}\lambda^2\right)^{\frac{d}{1+d}} \tag{3.19}$$

$$\mathrm{d} = 3.8\left(\frac{E'}{S_y}\frac{\Delta}{\lambda}\right)^{0.11} \tag{3.20}$$

However, for many applications it is also important to be able to predict the separation.

Asymptotic solutions of the surface separation for elastic contact was given by [46]

$$when\ \bar{p}/p^* \rightarrow 0: \qquad G_1 = 1 - \frac{1}{2}\left(3\pi^2 \frac{\bar{p}}{p^*}\right)^{\frac{2}{3}} + \left[4ln\left(\sqrt{2}+1\right)\right]\left(\frac{\bar{p}}{p^*}\right) \tag{3.21}$$

$$when\ \bar{p}/p^* \rightarrow 1: \qquad G_2 = \frac{16}{15\pi^2}\left(\frac{3}{2}\right)^{3/2}\left[\left(1 - \frac{\bar{p}}{p^*}\right)^{5/2}\right] \tag{3.22}$$

An equation was fitted at the total range by Rostami and Jackson. [59]

$$G = \Delta\left(1 - \frac{\bar{p}}{p^*}\right)^{5/2} \tag{3.23}$$

Rostami and Jackson [59] also provides an equation of the surface separation for elastic-plastic contact

$$G = \Delta\left[1 - \left(\frac{\bar{p}}{p_{ep}^*}\right)^{A_1 p_{ep}^* + A_2}\right]^{5/2} \tag{3.24}$$

Where A_1 and A_2 are given by:

$$A_1 = -0.08\ \ln(B/B_c) \tag{3.25}$$

$$A_2 = \frac{1}{15}(B/B_c - 1)^{0.44} + 0.99^{0.41(B/B_c - 1)} - \frac{1}{2} \tag{3.26}$$

Note that**,** The Eqs. (3.2) - (3.9) and Eqs. (3.14) - (3.26) are all for the perfect slip condition.

3.2.2 Finite Element Model

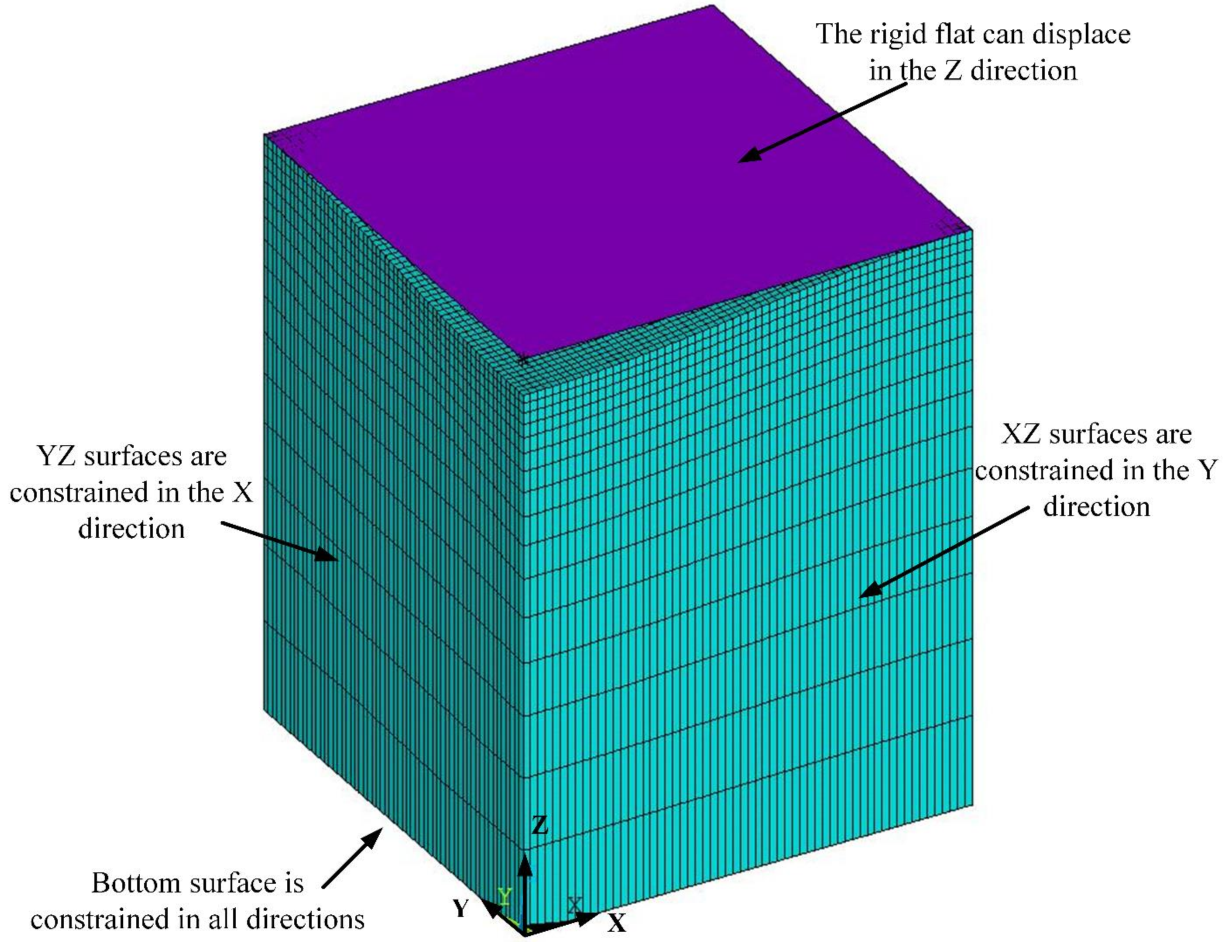

Fig. 3.3. The element plot and boundary conditions used for the FE model under normal loading.

A three-dimensional model was developed in commercial ANSYS^{TM} 17.0 Since the sinusoidal surface is symmetric, it is sufficient to consider only a quarter section of the whole problem. The twenty-node brick element (solid 186) is used to mesh the solid body. Conta 174 and Targe 170 elements are used to form the contact pair. A single element Targe 170 was used to model the rigid surface, and a pilot node, which governs the motion of rigid flat, was created to associate with the rigid target surface. The sinusoidal surface consisted of a 60×60 array of elements. The uniform mesh on the rigid surface is used to predict the ratio of real contact area. In all, there are 57,600 elements in the model. The force method was employed to simulate the contact problem. The force was applied on the pilot node in the *z* direction, by determining the contact force of each element in each substep. The normalized contact area, which is the ratio of the real contact area over apparent area, was obtained by the ratio of the number of the element in contact to the total number. In order to compare the results in this paper to other works, the current analysis uses the same geometry used in Johnson et al. [46] and Krithivasan and Jackson [58].

3.2.3 Verification of Model Accuracy

In order to verify the accuracy of the FE model, comparisons were performed for both elastic and elastic-plastic contact considering the contact area.

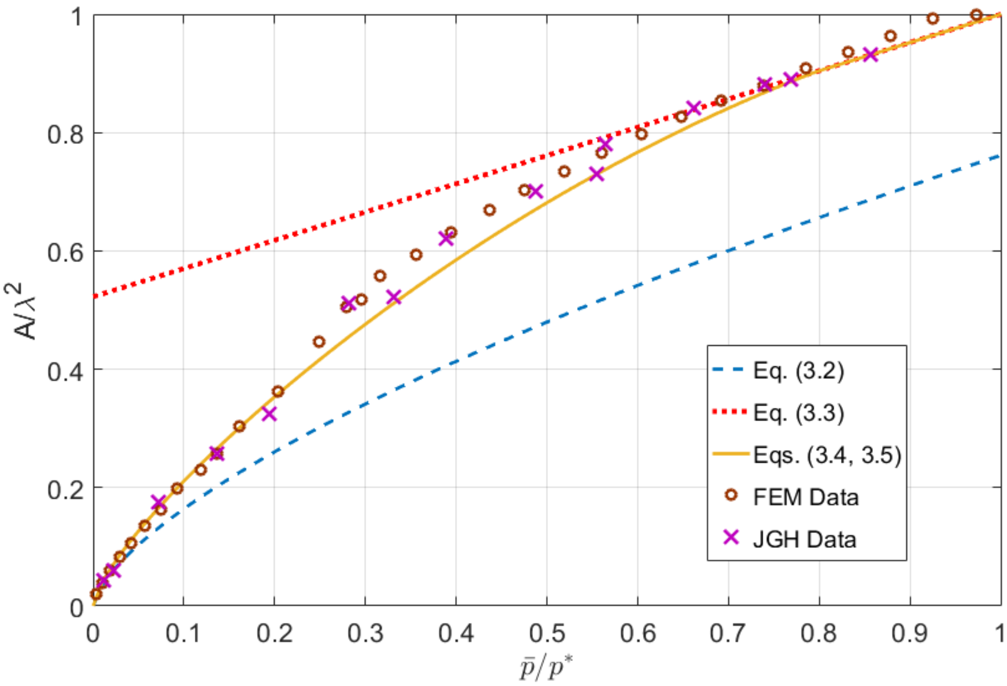

Fig. 3.4. Comparison of the elastic FEM contact area results with JGH data and JS equation.

For the elastic case, the comparison is achieved by comparing the FEM results with the Johnson et al. data [46] and the Jackson et al. fit [19]. For this case, the material properties of a typical steel are used, $E = 200\ GPa$ and $\nu = 0.3$ and the geometrical ratio $\Delta/\lambda = 0.02$ are used in the FE model. As shown in Fig. 3.4, the FEM results and the equations have the same trend. Although the FEM data differ from the empirical equation slightly, they are in overall good agreement. An average error of only 5% was found between the FEM data and the empirical Eqs. (3.4) and (3.5), but it appears that the FEM results are closer to the JGH data. Note that the variation may change with Δ/λ.

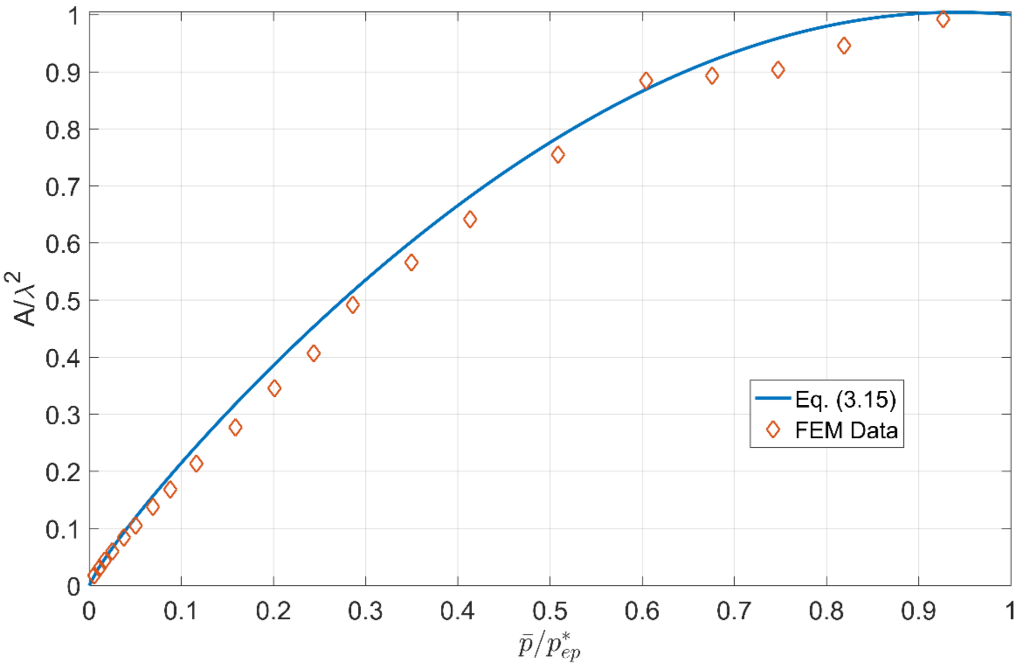

Fig. 3.5. Comparison of the elastic-plastic FEM contact area results with KJ equation.

For the elastic-plastic contact, the results are compared to the empirical equation provided by Krithivasan and Jackson (KJ). The material of the sinusoidal surface is assumed to be bilinear isotropic solid body. The material used is as following: elastic modulus, $E = 200\ GPa$, the Poisson's ratio, $\nu = 0.3$, the yield strength, $S_y = 1GPa$ and the tangential modulus, $E_t = 2\%\ E$, which has an effect on the results. The geometry is described by the ratio of the amplitude to wavelength and assigned, $\Delta/\lambda = 0.02$. Again, this comparison considers the real contact area. As shown, the FEM data and the empirical equation have the same trend, and the average error between them is less than 4%.

3.3. Results and Discussion

3.3.1. Real Contact Area under The Full Stick Condition

Table 3.1. Overview of the parameter ranges used for the FE simulation for normal loading

Parameter Name	Symbol	Range
Elastic Modulus	E	$150-450\ GPa$
Poisson's Ratio	ν	$0.10-0.45$
Yield Strength	S_y	$0.10-2.25\ GPa$
Geometric Ratio	Δ/λ	$0.001-0.05$

In order to investigate the behaviors of elastic-plastic sinusoidal contact under the full stick condition, a parametric analysis of contact area that is similar to the work in [58] is conducted. The material properties and geometric parameters are varied, and the overall ranges for each parameter are list in the Table 3.1. For convenience, a benchmark case was set to analyze the contact problem. The material properties used for the benchmark case are $E = 200\ GPa$, $\nu = 0.3$, $S_y = 1GPa$, and $E_t = 4\ GPa$. The dimensionless geometric ratio Δ/λ is set to 0.02. When conducting the simulations, only the parameter being analyzed and is varied, all other parameters are fixed to the benchmark values.

First, a range of elastic moduli are considered in the model (see Fig. 3.6). The elastic modulus, E, was varied from $100\ GPa$ to 450 GPa. The average contact pressure, $\bar{p}$, resulting from the elastic-plastic model is normalized using p^*(elastic case). Then the normalized contact area A/λ^2 versus $\bar{p}/p^*$ for different elastic modulus values is plotted in Fig. 3.6.

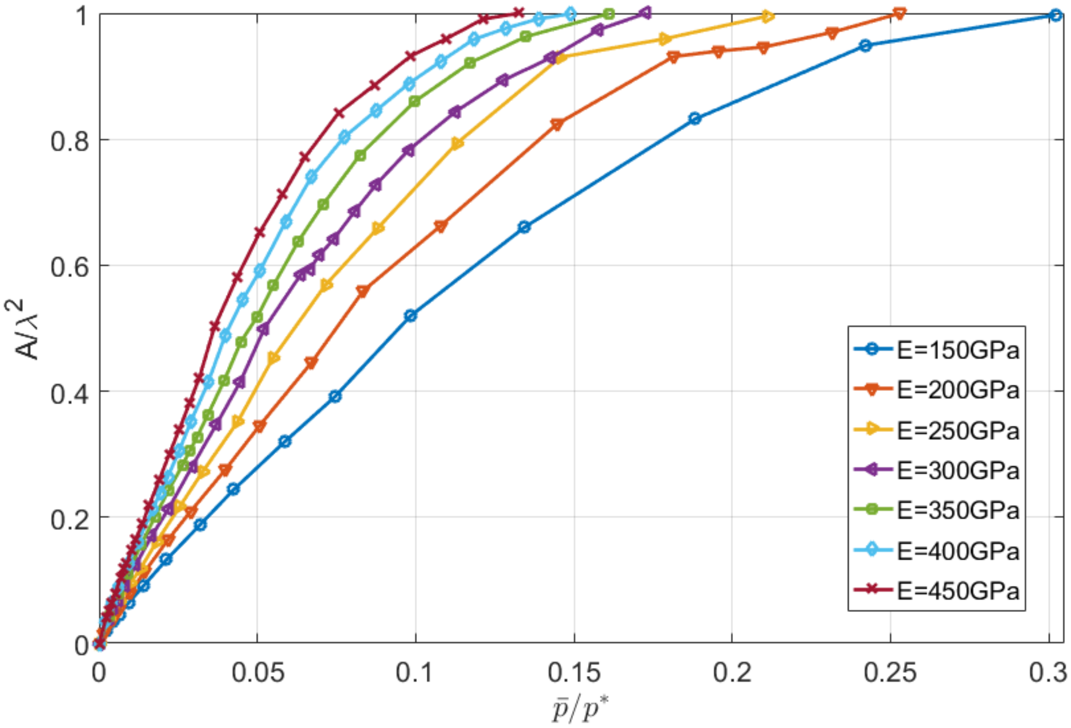

Fig. 3.6. Contact area ratio, A/λ^2 versus $\bar{p}/p^*$ for different values of elastic modulus.

Eq. 2.37 is used to normalize $\bar{p}$ by p^*. It can be seen from Fig. 3.6, under the same dimensionless contact pressure, $\bar{p}/p^*$, as the elastic modulus increases, the contact area, A/λ^2, increases, (i.e. the contact becomes more complete). For each case, when the normalized contact area ratio is equal to 1 (the contact is complete), $\bar{p}/p^*$ is less than one. Thus, for the elastic-plastic cases, complete contact occurs much earlier than when it occurs in elastic contact. This behavior is very similar to the sinusoidal contact under the slip condition [58].

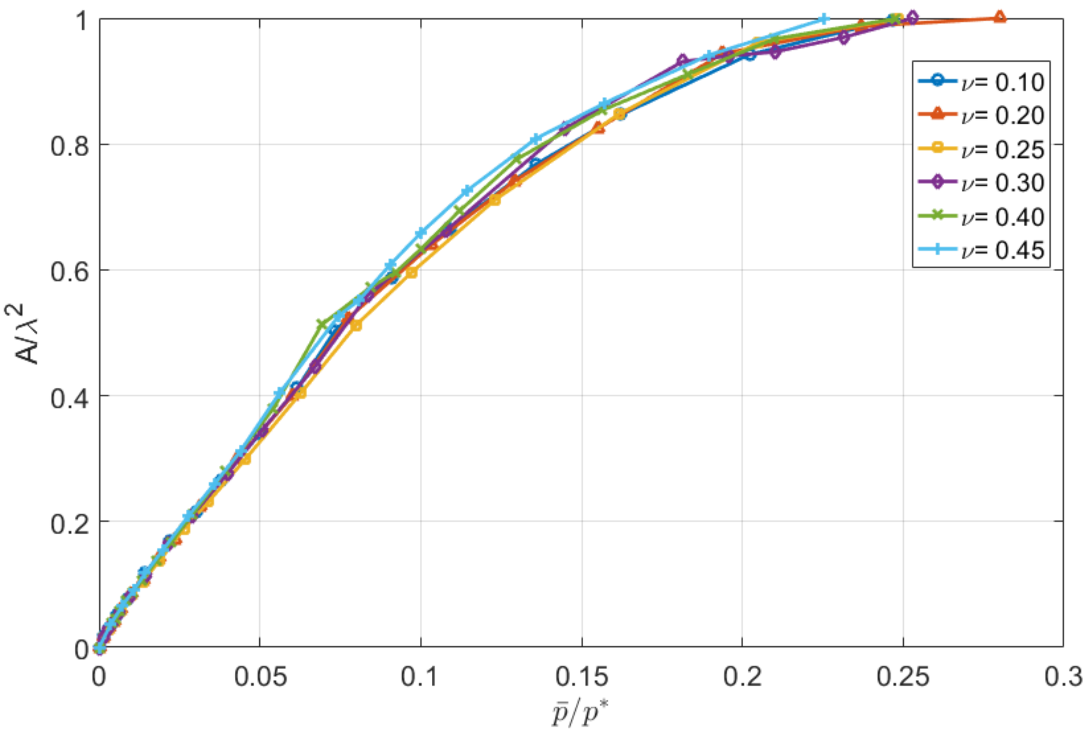

Fig. 3.7. Contact area ratio, A/λ^2 versus $\bar{p}/p^*$ for different values of Poisson's ratio.

Similarly, the normalized contact area A/λ^2 versus $\bar{p}/p^*$ for different Poisson's ratio values is plotted in Fig. 3.7. As can be seen from Fig. 3.7, a very little difference between each case is founded. Under the same dimensionless contact pressure, $\bar{p}/p^*$, as the Poisson's ratio increases, the contact area, A/λ^2, increases (and the contact becomes more complete).

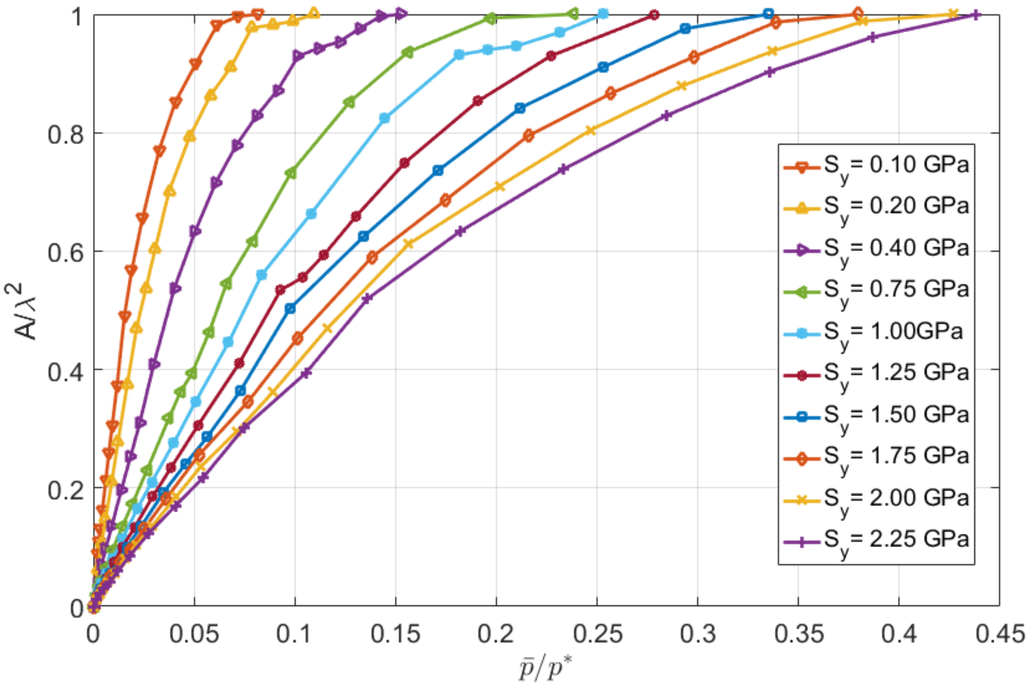

Fig. 3.8. Contact area ratio, A/λ^2 versus $\bar{p}/p^*$ for different values of yield strength.

Then the normalized contact area A/λ^2 versus $\bar{p}/p^*$ for different yield strength values are plotted in Fig. 3.8. It can be seen from Fig. 3.8, under the same dimensionless contact pressure, $\bar{p}/p^*$, as the yield strength increases, the contact area, A/λ^2, decreases (i.e. the contact becomes less complete). This agrees with our intuition, since increasing the strength will lower the amount of yielding and cause the contact to be more elastic.

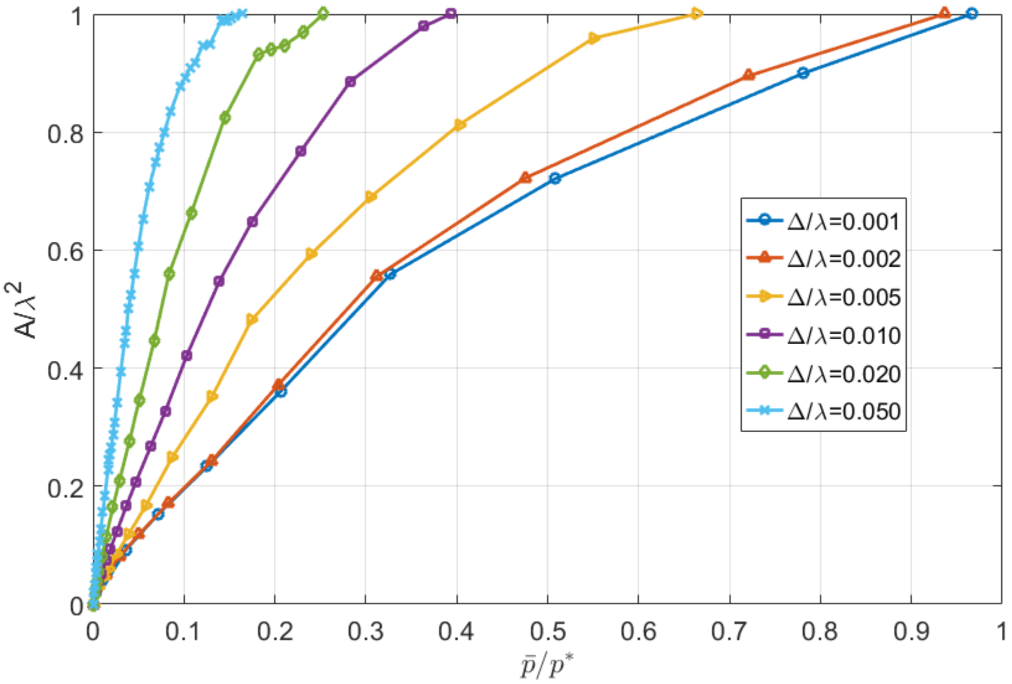

Fig. 3.9. Contact area ratio, A/λ^2 versus $\bar{p}/p^*$ for different values of Δ/λ.

Finally, the normalized contact area A/λ^2 versus $\bar{p}/p^*$ for different values of the dimensionless geometric parameter, Δ/λ, are plotted in Fig. 3.9. It can be seen from Fig. 3.9, under the same dimensionless contact pressure, $\bar{p}/p^*$, as the geometric ratio increases, the contact area, A/λ^2, increases, (i.e. the contact becomes more complete). It should be mentioned that the contact behavior in full stick is very similar to the one under the perfect slip condition. Therefore, this work in affect also confirms the model for the perfect slip condition.

3.3.2. The Effects of Contact Conditions and Parameters on Complete Contact Pressure

In this subsection, the average contact pressure required to cause complete contact is examined. The average pressure, p_{ep}^*, that causes complete contact is extracted from the finite element model data for each case. This value corresponds to the average pressure when the area ratio, A/λ^2 reaches one. When the complete contact occurs, there is no space between the rigid flat and the sinusoidal surface. Thus, the average pressure to cause complete under the full stick condition can be found. In order to compare the complete contact pressure between under the full stick condition and perfect slip condition, FEM data for the full stick condition and Eq. (3.14) for the contact model under the perfect slip are plotted in Figs. 3.10 - 3.13.

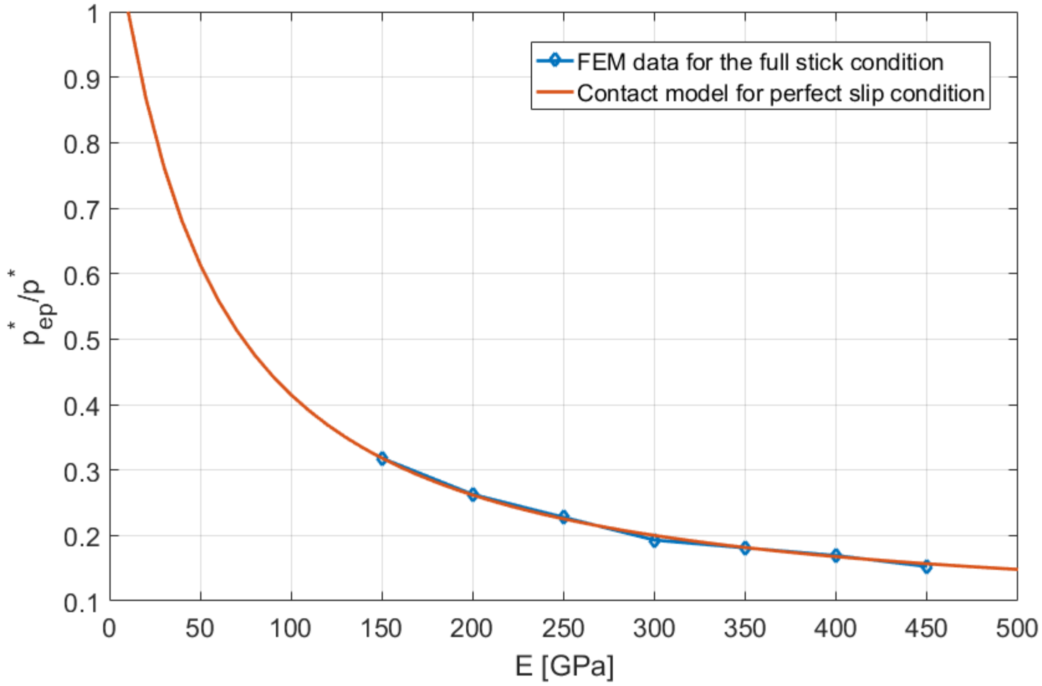

Fig. 3.10. The dimensionless complete contact pressure versus elastic modulus under different contact conditions.

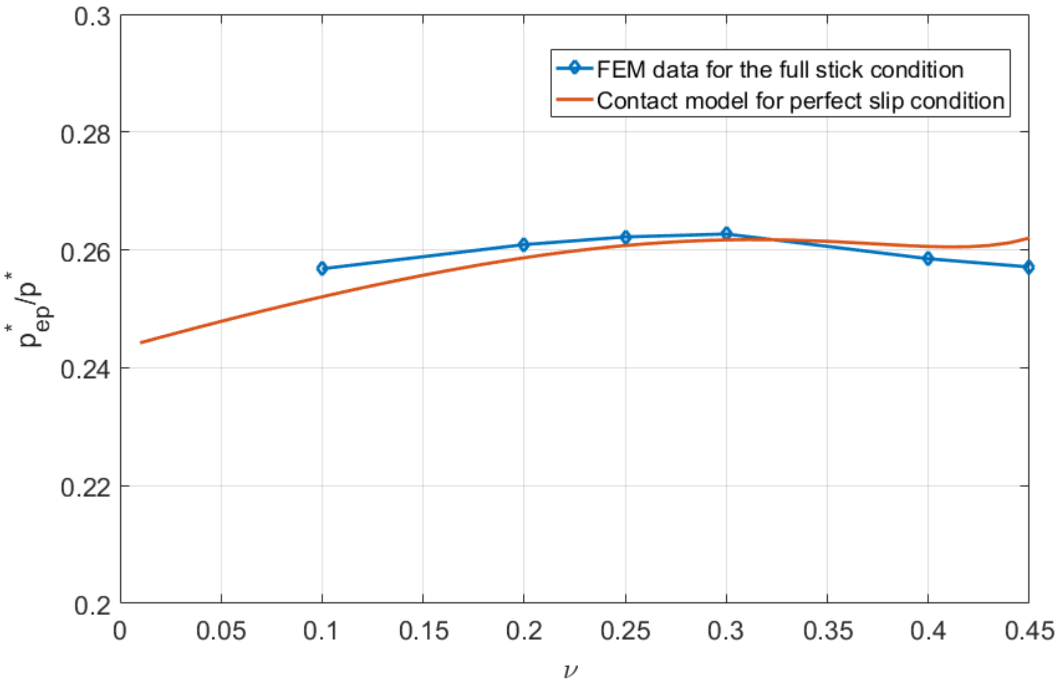

Fig. 3.11. The dimensionless complete contact pressure versus Poisson's ratio under different contact conditions.

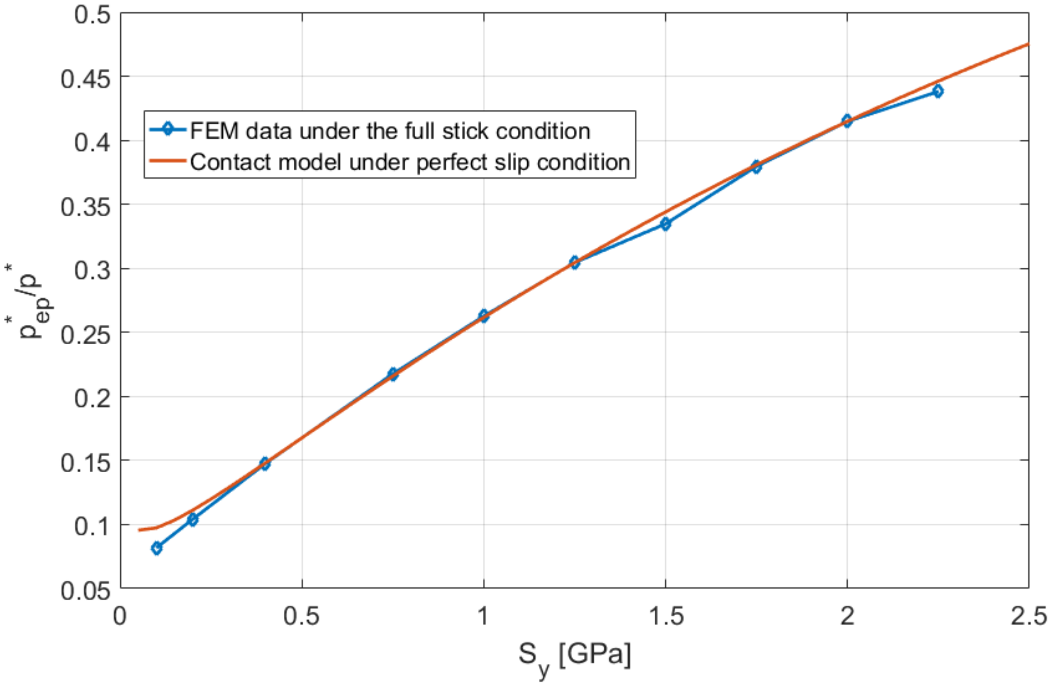

Fig. 3.12. The dimensionless complete contact pressure versus yield strength under different contact conditions.

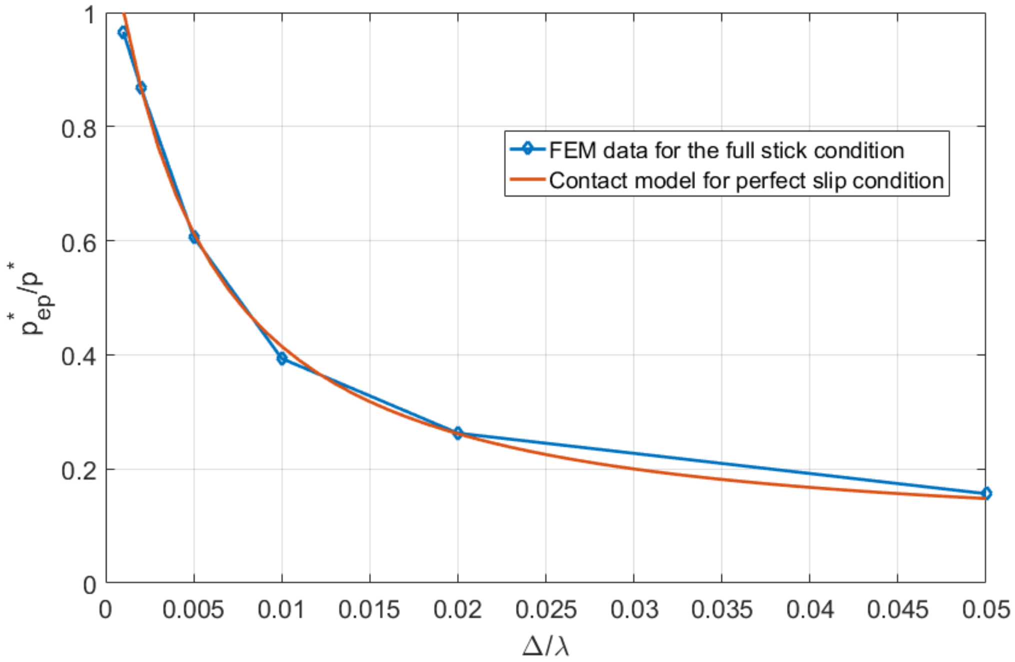

Fig. 3.13. The dimensionless complete contact pressure versus the ratio of amplitude to wavelength under different contact conditions.

First, the material properties are considered. For different values of elastic modulus, E, Poisson's ratio, ν, and the yield strength, S_y, the dimensionless complete contact pressure under different contact conditions are plotted in Figs. 3.10, 3.11, and 3.12. As it is shown in Fig. 3.10, as the elastic modulus increases, the dimensionless complete contact pressure decreases. Fig. 3.11. shows the complete contact pressure versus the dimensionless contact pressure with different Poisson's ratios. As shown in Fig. 3.11, as Poisson's ratio increases, the dimensionless complete contact pressure increases first, and then decreases, as does the model under the slip contact condition in [58]. For the materials with lower Poison's ratios, the values of p^*_{ep}/p^* under the full stick condition are greater than the responding values under the slip condition; For the materials with higher Poison's ratios, the values of p^*_{ep}/p^* under the full stick condition are less than the responding values under the slip condition. Fig. 3.12. shows the complete contact pressure versus the dimensionless contact pressure with different yield strengths. As shown in Fig. 3.12, as yield strength increases, the dimensionless complete contact pressure increases.

Next, the effect of the geometric ratio, Δ/λ , on the complete contact pressure is studied. The dimensionless complete contact pressure under different contact conditions with different geometric ratios is plotted (see Fig. 3.13). As shown in Fig. 3.13, As the geometric ratio increases, the dimensionless complete contact pressure increases. Again, there is no significant difference of the complete contact pressure between the slip, full stick and partial slip conditions, the results also agree with the existing the model under slip contact condition in [58].

Overall, from all the cases, one thing is observed, the dimensionless complete contact pressures under the full stick and perfect slip conditions show the same trend, and there is not too much difference between these two contact conditions (full stick and perfect slip). Hence, the equations for the perfect slip condition can be used for the full stick condition as well.

3.4. Conclusion

In this chapter, the elastic-plastic contact between a deformable sinusoidal surface and a rigid flat under the full stick condition was studied. First, the critical interference and critical force under the full stick condition were derived. Then, a comparison between the FEM results for full stick, and the model under perfect slip in [58] was performed. The effects of material properties, geometrical parameter and contact conditions on complete contact pressure are analyzed. We also found the differences for complete contact pressure among these contact conditions (full stick, perfect slip) were independent of the geometric parameter and material properties except for the Poisson's ratio, ν. For the sinusoidal contact, it is found that found the ratio of complete contact pressure in full stick condition over that in perfect slip is independent of geometry and it is only slightly affected by the material properties. especially the Poisson’s ratio, the average difference is less than 4%. Hence, the contact pressure that causes complete contact can be considered to be approximately equal to p_{ep}^{*} for the slip case. That is, the Eq. (3.14) also can be used in the full stick condition.

CHAPTER 4. ELASTIC-PLASTIC SINUSOIDAL CONTACT UNDER NORMAL LOADING IN FULL STICK

4.1. Introduction

The contact of spheres under combined normal and tangential loading has been studied quite extensively, from the classical works of Mindlin in 1949 [10] and Mindlin and Deresiewicz in 1953 [63]. Mindlin used a predefined friction coefficient to consider slip and stick between two surfaces. He set an upper limit on the local shear stress, which is equal to the local normal pressure multiplied by the coefficient of friction. Whenever the computed shear stress exceeds the upper limit, local slip takes place. This is known as the local Coulomb friction law. The sliding of the entire surface occurs when the shear stresses over the entire contact area reach the upper limit, satisfying the Coulomb friction law. Mindlin also obtained the surface shear stress distribution in the full stick and partial slip conditions. Keer et al. [64] followed Mindlin's approach, finding the criterion for complete sliding of elastic bodies in contact. Hamilton [65] found the yield inception of spherical sliding contact by using Hertz contact pressure and the Mindlin shear stress distribution. Hills et al. [66] modified the stress distribution by considering the effect of the shear stress on surface displacements for two dissimilar elastic cylinders.

Bowden and Tabor [67] presented a different approach, which considered the start of surface slip in relation to the mechanical properties rather than a local friction law as in [10]. They used a failure mechanism related to the material properties to determine the sliding inception. They suggested that the tangential load at sliding inception was equal to the real contact area times the material shear strength. Courtney-Pratt and Eisner [68] measured the contact area of a metallic sphere pressed normally and tangentially again a smooth flat. They observed an increase of the contact area when the tangential load was increased. Tabor [69] defined this phenomenon as "junction growth", explaining that a contact area that has already yielded plastically under a given preload must grow when it is subjected to an additional tangential loading. Junction growth occurs because the tangential loading can reduce the mean contact pressure in order to accommodate the additional shear stresses.

Chang et al. [7] treats sliding inception as a failure mechanism based on the failure of small junctions between contact surfaces. They gave an explicit formula to calculate the maximum tangential loads that a single spherical asperity can support for a given preload against a rigid flat before sliding inception. Then the total tangential load for the rough surface contact was obtained by using a statistical method. Improving Change et al. [7], Kogut and Etsion [8] presented a semi-analytical approximate solution for the sliding inception for both elastic and plastic cases. They treated the sliding inception as a failure mechanism, and failure occurs either on the contact area or below it, depending on the status of normal loading.

Brizmer et al. [9] presented a new approach using FEM to determine the sliding inception for the full stick condition, which is known as the stiffness criterion. They considered that the sphere starts sliding when the instantaneous tangential stiffness is equal to a small predefined value. By using this criterion. Brizmer et al. [9] investigated several parameters such as junction stiffness, static friction force and static friction coefficient. The evolution of the contact area was also investigated in [70] and an empirical relation between the contact area and the normal preload was found by fitting to the FEM results. The contact of a deformable sphere under combined normal and tangential loading by a rigid flat in the pre-sliding regime was also investigated by

Zolotarevskiy et al. [71], and they developed a model for the evolution of static friction force and stiffness in the pre-sliding regime.

Some researchers also considered the partial slip condition, which means there is some local slip even though gross slip does not happen. Eriten et al. [11] developed a physics based model considering this. In their FE based model, the local Coulomb’s law was used to govern the interfacial strength. They set the product of the friction coefficient and normal stress to a critical friction shear stress. Following this approach, Patil and Eriten [72] showed that the static friction coefficient strongly depends on the interfacial strength, a material property. Mulvihill et al. [73] set the interfacial adhesional shear strength equal to a few different values related to the bulk yield strength. Based on the von Mises theory, Wu et al. [12] fixed the strength equal to a constant value, and proposed a frictional model that transitioned from the KE model [8] to the BKE model [9] for the partial slip condition.

All of the previous works assumed a spherical asperity. However, real asperities on surfaces are not shaped like spheres, especially at their base. At lower loads where the asperity base does not influence the result, the sphere works well. However, at higher loads, the effect of the complete asperity geometry and interaction with adjacent asperities becomes important. Even though statistical models use the assumption that only the peaks of the asperities are in contact, the taller asperities can still be heavily loaded and deformed (practically crushed in some cases) [74].

Recently, Greenwood [45] at the 2015 Leeds-Lyon tribology Symposium suggested that more realistic asperity models similar to wavy surfaces should be considered. The current work uses a sinusoidal or wavy geometry. In addition, for spectral based and multiscale rough surface contact models it is logical to use sinusoidal shapes for the asperities because the surface is often treated as a series of superposed harmonic waves (i.e. Fourier Series or for fractals, the Mandelbrot Function). For either statistical or multiscale models, when the sinusoidal asperities are under heavy loads they behave much differently than spheres, due to the difference in geometry and also their periodic nature. Theoretically, a portion of the asperities will always be under higher pressures, no matter the load applied. This is because the pressure is magnified with decreasing scales, as predicted by the multi-scale models [49, 75, 76]. The periodicity may also capture the effect of adjacent asperities better than spheres. With the development of more multi-scale models between rough surfaces [20, 49], which could be applied to electrical [77] and thermal contact [60, 61], the contact problem of an elastic-plastic deformable sinusoidal surface and rigid flat was investigated by several researchers [48, 58, 59, 78] . Gao et al. [78] found a relationship between contact pressure, contact size, effective indentation depth and residual stress for the 2-D sinusoidal contact. Krithvasion and Jackson [58] provided an approximate solution for the elastic-plastic regimes and an empirical expression for predicting the contact area as a function of contact pressure. Jackson et al. [48] provided an analytical expression for critical amplitude that causes yield and the average pressure that causes complete contact. Rostami and Jackson [59] provided close form equations that predict surface separation and stiffness for both elastic and elastic-plastic cases.

As seen from the literature review above, most existing models considering the sinusoidal geometry are only under normal loading. Several researchers have investigated the case of deformable sinusoidal surface in contact with a flat. However, very little work was done on the sinusoidal contact under combined normal and tangential loading. The main goal of this Chapter is to use the FEM to investigate the contact performance parameters based on junction growth and the static friction coefficient for a deformable sinusoidal surface contacting a rigid flat. These relationships then might be used in spectral and fast Fourier transform (FFT) based methods for modeling the contact and friction between rough surfaces (along with other rough surface contact models).

4.2. Modeling Approach

4.2.1. Theoretical Model

The current analysis uses the same geometry used by Johnson et al [46], Krithivasan and Jackson [58] and Jackson et al.[48] , as shown in Fig. 4.1. The equation defining this sinusoidal surface was already given by Eq. (3.2).

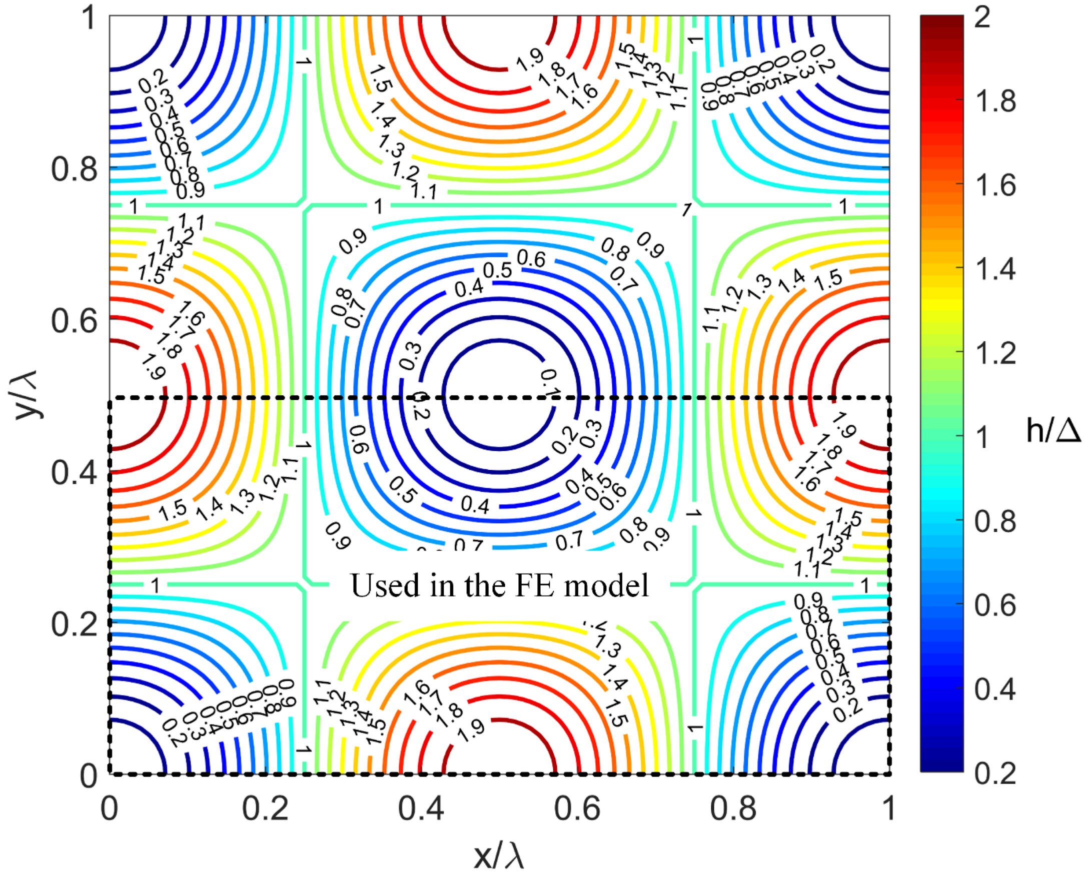

Fig. 4.1. Topographical depiction of the three-dimensional sinusoidal surface geometry.

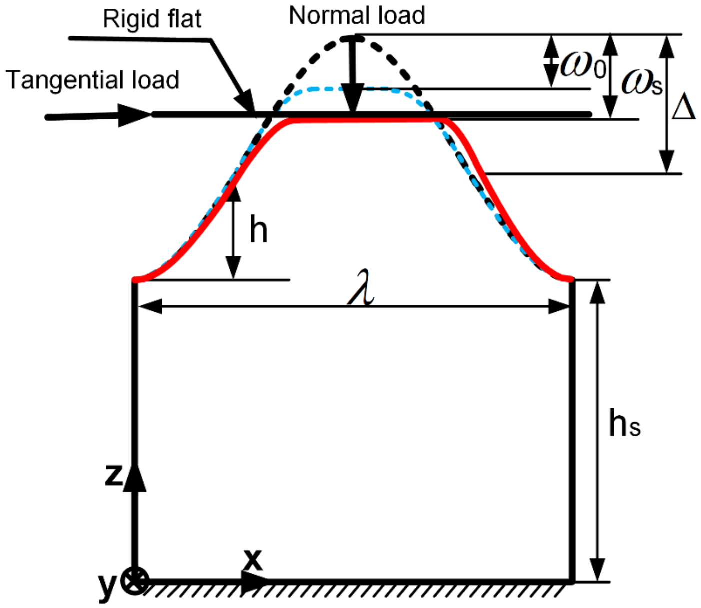

Fig. 4.2. The contact of a deformable sinusoidal surface and a rigid flat under combined normal and tangential loading.

The cross-section of a deformable sinusoidal asperity in contact with a rigid flat under combined normal and tangential loading is schematically shown in Fig. 4.2. The tangential load, F_t, is applied gradually, while the normal preload, F_n, remains constant. The thick and thin dashed lines show the contours of the sinusoidal asperity before and after applying the normal preload, respectively, while the solid line shows the final contour of sinusoidal asperity after the application of the tangential load. The normal load produces an initial interference, ω_0, while the additional tangential load combined with the normal preload produces the final interference, ω_s.

4.2.1.1 Normal Loading

Complete contact is defined as when there are no gaps remaining between the two surfaces. The average contact pressure that causes complete contact for the elastic case is given by Johnson et al. [48], the equation was introduced in Eq. (2.38), and they provided two asymptotic solutions to the real contact area as well. They are given in the Eqs. (3.2) and (3.3). Based on the experimental and numerical data, Jackson and Streator [19] provided an empirical fit in Eqs. (3.4) and (3.5).

For the elastic plastic case, Jackson et al. [48] defined a critical amplitude of a sinusoidal surface. When the amplitude is less than this value, the sinusoidal surface deforms elastically. When the amplitude is greater than this value, it deforms plastically. The critical amplitude is given in [48] and the equation was given in Eq. (3.13). The resulting fit equation for contact pressure to cause complete contact was given in Eq. (3.12). An empirical expression for the contact area in elastic-plastic sinusoidal contact is obtained by fitting the FEM results by Krithivasan and Jackson [58], and is given in Eq. (3.15). These previous results are all for perfect slip and without tangential load.

Three main contact conditions are generally considered: the perfect slip condition, the full stick condition, and the partial slip condition. The full stick condition implies that the contact points of the surface and the flat are prevented from further relative displacement once touching. While the perfect slip condition assumes no tangential stresses in the contact area. The effect of contact conditions and material properties on the termination of elasticity in spherical contact was investigated by Brizmer et al. [56]. They found that the ratios of critical interference and load in the full stick condition over that in the perfect slip condition are independent of material properties, except for Poisson’s ratio. Eriten et al. [79] investigated he influence of friction on the onset of plastic yielding in these three contact conditions for spherical contact.

As we discussed in Chapter 3, for the sinusoidal contact, we found the ratio of complete contact pressure in the full stick condition over that in perfect slip is independent of geometry and it is only slightly affected by the material properties, especially the Poisson’s ratio. Hence, the contact pressure that causes complete contact can be considered to be equal to p_{ep}^{*} [80].

4.2.2.1 Combined Normal and Tangential Loading

The behavior of a contact between a deformable elastic-plastic sphere and a rigid flat under normal and tangential loading was investigated by several researchers [8, 9, 70, 71] . The sliding inception is treated as a failure mechanism based on plastic yield in [8], and sliding might actually initiate in the yielded material below the surface in some cases. The static friction coefficient equation found by fitting to FEM results in [8] is given as:

$$\mu_s = \begin{cases} 0.516\left(\frac{F_n}{F_c}\right)^{-0.345}, & 0 \le \frac{\omega}{\omega_c} \le 1 \\ -0.007\left(\frac{F_n}{F_c}\right)^{2.104} + 0.083\left(\frac{F_n}{F_c}\right)^{1.405} - 0.380\left(\frac{F_n}{F_c}\right)^{0.701} + 0.822, & 1 \le \frac{\omega}{\omega_c} \le 6.2 \end{cases} \tag{4.1}$$

Considering the full stick contact condition, the contact stiffness criterion was used to determine the sliding inception in [9, 70, 71] such that

$$\frac{(K_T)_i}{(K_T)_1} \le \alpha \tag{4.2}$$

where $(K_T)_i$ is the corresponding instantaneous tangential stiffness of the i_{th} tangential loading step, and the $(K_T)_1$ is the initial tangential stiffness of the joint corresponding to the first tangential loading step. And α is a predefined number that was chosen to determine the sliding inception by the criterion, i.e. the spherical asperity initiated sliding when the tangential stiffness drops by a factor α, which is typically 0.1. The corresponding tangential force at the moment of initial sliding is the maximum static friction force, $(F_t)_{max}$.

From [9], the empirical equation of the static friction coefficient is given as a function of F_n/F_c or

$$\mu_s = 0.27coth\left(0.27\left(\frac{F_n}{F_c}\right)^{0.35}\right) \tag{4.3}$$

And as a function of $\frac{\omega}{\omega_c}$ given by

$$\mu_s = 0.26coth\left(0.27\left(\frac{\omega}{\omega_c}\right)^{0.46}\right) \tag{4.4}$$

Another method for determining slip between surfaces is the maximum shear stress criterion. There is some local slip even though the gross slip does not happen (i.e. partial slip). For partial slip, Patil and Eriten [72] used Coulomb friction to determine the contact interfacial strength, and proposed the phenomenological equation

$$\mu_s = \min\left(\mu_{local}, \max(0.167, \alpha\left(\frac{F_n}{F_c}\right)^{\lambda}\right) \tag{4.5}$$

where $\alpha = 0.0931\mu_{local}^{0.7153}$, and $\lambda = -0.223\mu_{local} + \left(-0.00002\frac{E}{S_y} + 0.0261\right)$, μ_{local} is the assumed local static friction coefficient.

Another model was proposed by Wu et al. [12], in which the critical friction shear stress, τ_c, was set by the shear strength of the weaker material. i.e. once the frictional shear stress in the contact area reaches the shear strength, the local sliding occurs at this element. Once all the elements in the contact slides, the whole surface start sliding. Considering the partial slip, the static friction coefficient is given by:

$$\mu_s = 0.3coth\left(0.57\left(\frac{\omega}{\omega_c}\right)^{0.41}\right) \tag{4.6}$$

Note that Eqs. (4.1) - (4.6) are for spherical contact, but these equations can still be used for formulating empirical equations for the sinusoidal contact. Eq. (4.1) and Eq. (4.3) are also used to compare with the results in the current work. Once the static friction coefficient is given, the maximum tangential load can be easily obtained by:

$$(F_t)_{max} = \mu_s \mathrm{F}_n \tag{4.7}$$

Note that the static friction coefficient predicted in Eq. (4.1) and Eqs. (4.3) - (4.6) and the static friction predicted by Eq. (4.7) are not the static friction coefficient or static friction measured between real surfaces but theoretical values for single point contact.

Brizmer et al. [70] developed a model for junction growth of a spherical contact under the full stick condition and gave an empirical expression that approximates the dimensionless contact area at sliding inception

$$\frac{A_s}{A_0} = 0.5\left(\frac{F_n}{F_c}\right)^{0.166} \coth\left[0.3\left(\frac{F_n}{F_c}\right)^{0.318}\right] \tag{4.8}$$

4.2.2. Finite Element Model

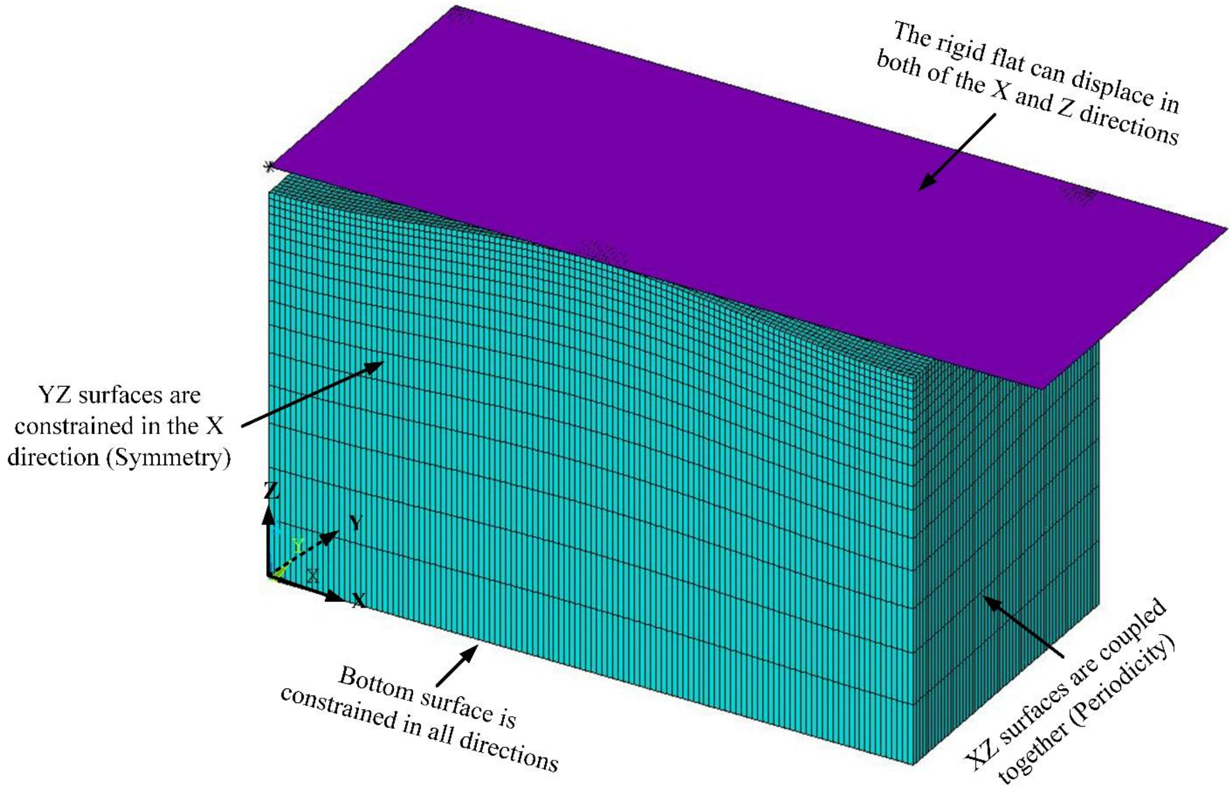

Fig. 4.3. The finite element model and boundary conditions.

In the current work, a three-dimensional model was developed and the commercial FEM software ANSYS^{TM} 17.0 was used to further analyze the combined normal and tangential loading of an elastic-plastic sinusoidal contact problem. Due to the symmetry about the xz plane, it is sufficient to consider only one half of the sinusoidal volume, (see Fig 4.3). The three-dimensional mesh consisted of more than 121,000 twenty-node brick elements (Solid 186). The sweep mesh option is selected. Conta 174 and Targe 170 elements formed the contact pair to model interaction between the surfaces. In order to make the simulation more efficient, the contacting surface of the rigid flat was modeled by a single element (Targe 170) with the size that can cover the largest contact area. The contact surface comprised of 174 elements arranged in a uniform mesh of 60×120 elements. The rigid target surface was associated with a "pilot node" which is an element with one node, whose motion governs the motion of the entire target surface. Forces and displacements for the entire target surface can be prescribed on just the pilot node. Note that this is still double the size needed for normal contact because the problem is no longer symmetrical in the sliding direction.

For the volume below the sinusoidal surface, the nodes on the bottom surface were constrained in all directions. All the nodes with the same *y, z* location on the outer *yz* plane were coupled to enforce periodicity, and the nodes on the out *xz* plane were constrained to the zero displacement in the y direction to apply the symmetric boundary condition (See Fig. 4.3).

The states of contact elements on the sinusoidal surface is used to predict the real contact area. An uniform mesh on the surface is used, and therefore the contact area is just the ratio of elements in contact to the total number of the elements. By checking the contact status of each element during post-processing. The sticking contact area ratio is the sticking contact area normalized by apparent contact area, and it is given by the number of sticking elements over the total number of elements in contact. Similarly, the sliding contact area ratio is defined as well. The total contact area ratio is equal to the sum of the contact area ratios of sticking and sliding. In other words, the real contact area normalized by the apparent area of contact was given by the ratio of the number of elements in contact to the total number of elements over the surface.

Verify the Three-dimensional FE Model

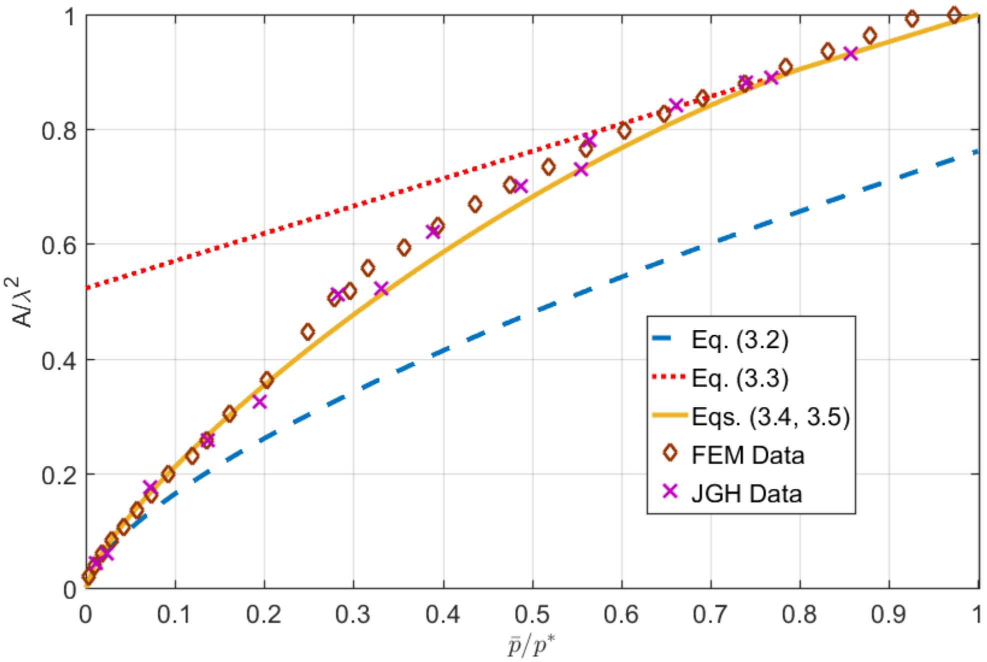

Fig. 4.4. Comparison of the elastic FEM contact area results with JGH for meshing in Fig. 4.3 data and JS equation.

In order to verify the accuracy of the three-dimensional FE model. The normal loading case is compared to existing data in [46]. As shown in Fig. 4.4, the FEM data differs from the empirical equation slightly, but is in overall good agreement. The FEM results and the equations have the same trend. An average error of only 5% was found between the FEM data and the empirical Eqs. (3.4) and (3.5), but it appears that the FEM results are closer to the JGH data [46]. Note that this is the case for the tangential load mesh in Fig. 4.3.

In order to verify the methodology of loading the surfaces, the complete contact case ($A_r = A_n$) was used. A critical interfacial shear strength, τ_c, was defined as $S_y/\sqrt{3}$, the static friction is calculated by: $(F_t)_{max} = \tau_c A_0$. As expected, the maximum tangential force extracted from the FEM results is exactly equal to the theoretical value when in complete contact.

A constant normal load, F_n, was applied as a single force at the pilot node, and then a step wide increase of the tangential displacement, u_x, of the flat was added to simulate the gradually increasing tangential load. The instantaneous tangential force, F_t, was obtained from the x-component of the reaction at the pilot node. The sliding inception occurs when all the contact elements are sliding. When this occurs, the static friction coefficient is $\mu_s = (F_t)_{max}/F_n$.

4.3. Results and Discussion

Before tangential loading, the sinusoidal surface and the rigid flat are assumed to be in the full stick condition. Once the tangential loading is applied, the maximum frictional shear stress criterion is used for governing the local sliding initiation. The local sliding occurs when the frictional shear stress at one element on the contact area reaches the critical interfacial shear strength value, τ_c. The sliding of the asperity occurs when all the elements on the contact area slide. At that moment, the average shear stress over the real area of contact is equal to the critical shear strength, i.e. $\tau_{ave} = \tau_c$.

The elastic plastic sinusoidal behavior was investigated over a wide range of material properties, geometry properties, dimensionless average contact pressures and dimensionless critical shear stresses. In order to formulate a fit for the FEM data, a bench mark case was set to analyze the problem between the deformable sinusoidal surface and a rigid flat. The material properties used for the benchmark case are: $E = 200$ GPa, $S_y = 1$ GPa, and $\nu = 0.3$. The material of the sinusoidal surface was assumed as elastic-plastic bilinear isotropic material with a tangent modulus $E_t = 2\% \, E$. The dimensionless geometry ratio Δ/λ was set to 0.02. The dimensionless average contact pressure $\bar{p}/p_{ep}^*$ was set as 0.05. Based on the distortion energy (von Mises) theory, the critical shear strength, τ_c, should satisfy the expression: $\tau_c \leq S_y/\sqrt{3} \approx 0.577 S_y$. Therefore, the dimensionless critical shear strength $\tau_c/S_y$was set as 0.577 for the benchmark case. When we are analyzing one specific parameter, all the other parameters are fixed, and only that one is varied in a certain range. The overall parameter ranges are listed in Table 4.1.

Table 4.1. Overview of the parameter ranges used for the FE simulation for under normal and tangential loading case

Parameter Name	Symbol	Range
Elastic Modulus	E	$150 - 450$ GPa
Poisson's Ratio	ν	$0.10 - 0.45$
Yield Strength	S_y	$0.05 - 2.25$ GPa
Geometric Ratio	Δ/λ	$0.001 - 0.1$
Dimensionless Contact Pressure	$\bar{p}/p_{ep}^*$	$0.001 - 0.1$
Dimensionless Critical Interfacial Shear Strength	τ_c/S_y	$0.1 - 0.577$

4.3.1. Junction Growth (Contact Area Increase Caused by Tangential Loading)

The contact status can be subdivided into three types: sticking state, sliding state and non-contact in ANSYS. When two separate elements first touch each other, they are in the sticking state, and they can carry some shear stress. While when the tangential shear stress exceeds the critical shear strength, the two elements slide relative to each other, and they are in sliding state. Both sticking and sliding belong to contact.

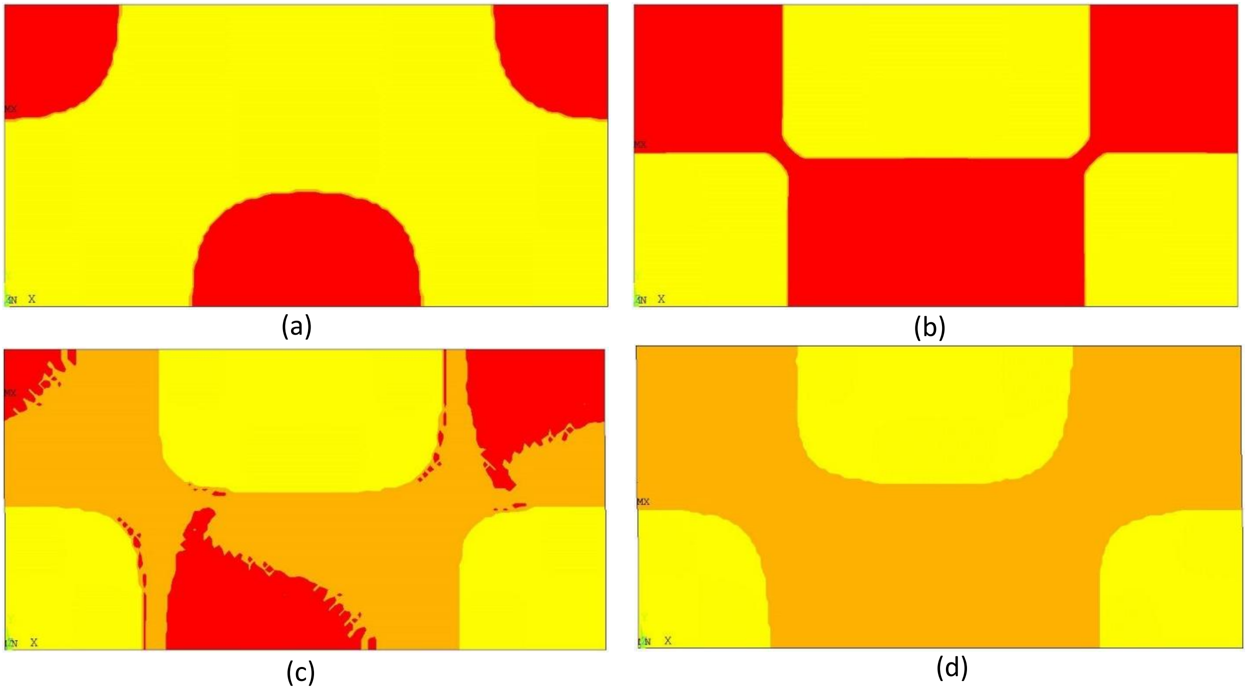

(a) (b)

(c) (d)

Fig. 4.5. Evolution of the contact area of the sinusoidal contact: (a) contact area under a small normal load only, (b) contact area under larger normal preload, (c) contact area under combined normal and a small tangential load and (d) contact area at sliding inception.

A typical contact area growth as predicted by FEM results for the benchmark case are presented in Fig. 4.5. The sliding direction is from left to right. Fig. 4.5 (a) presents the sinusoidal surface conduct when it is under a small normal load, and Fig. 4.5 (b) presents the sinusoidal surface when it is under the normal preload that is a heavier normal load than in Fig. 4.5 (a). From Fig. 4.5 (a) and Fig. 4.5 (b), the larger normal load results in a larger contact area. Fig. 4.5 (c) presents the sinusoidal surface is under a small normal tangential load, and Fig. 4.5 (d) presents the sinusoidal surface is at sliding inception, which is under the maximum tangetial load. Fig. 4.5 (c) shows that the loacal sliding occurs on the sinusoidal surface. The contact area of sinusoidal surface under normal preload only and at sliding inception are shown in Fig. 4.5 (b) and Fig. 4.5 (d). It should be clear that the contact area at sliding inception is greater than the contact area under normal load alone. Under the same normal preload, the tangential load can cause contact area growth. This is because the new points of the surface, which original outside of the initial contact area coming into the new contact area during the tangential loading. This penomennon was studied theoritically and experimentally in [14].

A range of $0.0001 \leq \bar{p}/p_{ep}^{*} \leq 1$ is considered by the model while keeping all other properties the same as the benchmark case (see Fig. 4.6). Therefore, only the dimensionless contact pressure $\bar{p}/p_{ep}^{*}$ is varied parametrically.

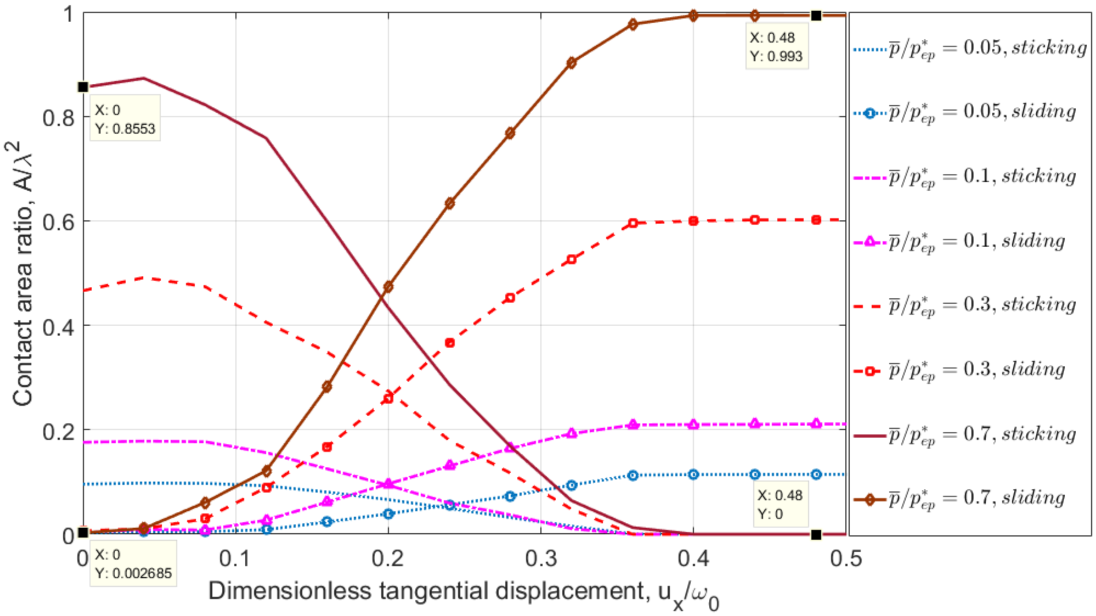

Fig. 4.6. The portion of surface that is in slip or stick

An example of the typical growth of the contact area is present in Fig. 4.6. Fig. 4.6 presents the numerical results for the evolving of both the sticking and sliding states of the contact area. The lines with no mark are the contact area ratio of the sticking contact area, while the lines with different marks are the contact area ratio of the sliding contact area. When $u_x/\omega_0 = 0$, the sticking contact area ratio is the sticking contact area before applying the tangential load. Then the sliding contact area ratio is very low but not zero. For different average contact pressures, the dimensionless contact area ratio for sliding increases with increasing normal tangential displacement. As the dimensionless tangential displacement further increases, the sliding contact area ratio reaches a constant value. At that moment, all the elements are sliding. The dimensionless contact area for sticking shows a different decreasing trend. As the dimensionless tangential displacement increases, the sliding contact area ratio increases slightly and then decreases until it reaches to a constant value at last. The increase is caused by junction growth. As seen from Fig. 4.6, at the same dimensionless tangential displacement, both the sticking and sliding contact area ratios of the higher contact pressures are higher than the values at the lower pressures. Another point that should be noted, is that the total contact area ratio at the sliding inception is much higher than the one before applying tangential loading. For example: when the $\bar{p}/p_{ep}^{*} = 0.7$ (but the tangential loading is $u_x/\omega_0 \ = 0$), the total contact area ratio is approximate 0.858 (obtained by adding both contact areas marked in Fig. 4.6, or 0.8553+0.002685), while the contact area ratio at the sliding inception ($u_x/\omega_0 \ = 0.48$) is approximately 0.9932 (almost complete contact). The increase is around 16%. This implies that an additional tangential load can cause the junction growth. That probably is because of the formation of the additional contact area by the normal contact pressure can support the additional loading.

4.3.2. Effect of Contact Pressure on Effective Static Friction Coefficient

The cases with changing dimensionless contact pressure cover the deformation range from elastic to deeply elastic-plastic. Fig. 4.7 presents typical results for the instantaneous dimensionless tangential load as a function of the normal dimensionless tangential displacement, as can be seen from Fig. 4.7. As the tangential loading progresses the slopes of the curves decrease and gradually diminish. The tangential stiffness (the slope) decreases as the dimensionless tangential load increases. When the tangential load no longer increases, the slope and the stiffness become nil, and gross slip occurs.

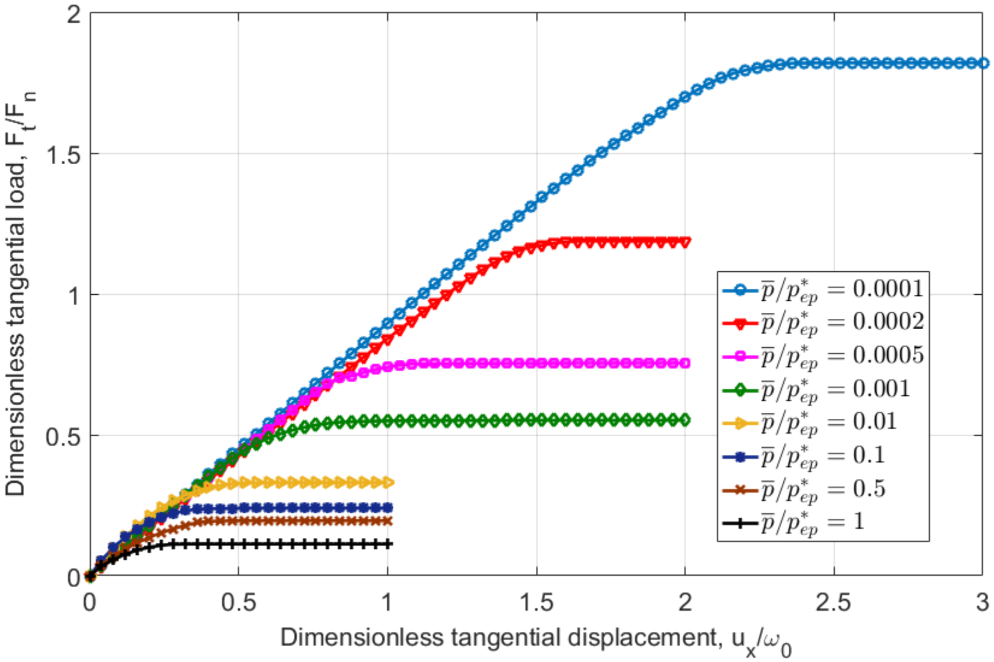

Fig. 4.7. The dimensionless tangential load F_t/F_n, versus the dimensionless tangential displacement u_x/ω_0, for different dimensionless contact pressures $\bar{p}/p^*_{ep}$.

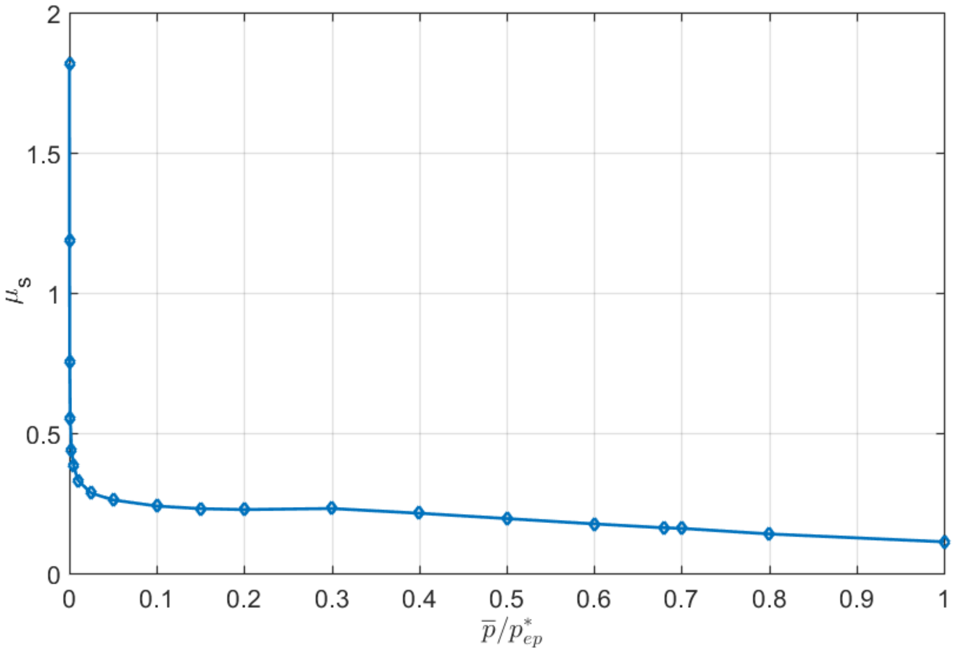

Fig. 4.8. Static friction coefficient $\mu_s$versus the dimensionless contact pressure.

Adding a tangential load to a given normal preload leads to an increase in the contact area, and as result, it can affect the coefficient of friction. The tangential load $(F_t)_{max}$ at the sliding inception is the static friction force for a single asperity. It is extracted from the finite element data for each case in Fig. 4.8. The static friction coefficient is obtained by $(F_t)_{max}/F_n$, however, again note that this is only for a single asperity. To predict the friction coefficient for an actual rough surface contact, the asperity model needs to be included in a rough surface contact model, which will be done in Chapter 8. It can be seen from Fig. 4.8, that the static friction coefficient is dependent on the average contact pressure. Hence the static friction coefficient is plotted versus the dimensionless contact pressure.

As seen from Fig. 4.8, at the low dimensionless contact pressure ($0.0001 \leq \bar{p}/p_{ep}^{*} \leq 0.05$), the static friction coefficient decreases sharply with increasing contact pressure. At the medium contact pressure ($0.05 \leq \bar{p}/p_{ep}^{*} \leq 0.3$), the static friction coefficient nearly approaches a constant value (around 0.23). As the contact pressure further increases, the static friction coefficient continues to reduce, and the relationship is nearly linear. One point should be noted; at the very low dimensionless contact pressures, such as $\bar{p}/p_{ep}^{*} = 0.0001$ or $\bar{p}/p_{ep}^{*} = 0.0002$, the coefficient is higher than one. This is because the deformation is in the elastic range, and the surface can support more shear stress. An interesting finding observed in Fig. 4.8 is that the static friction coefficient still follows a nearly linear relationship even as the compete contact is reached.

4.3.3. Effects of Material Properties on Effective Static Friction Coefficient

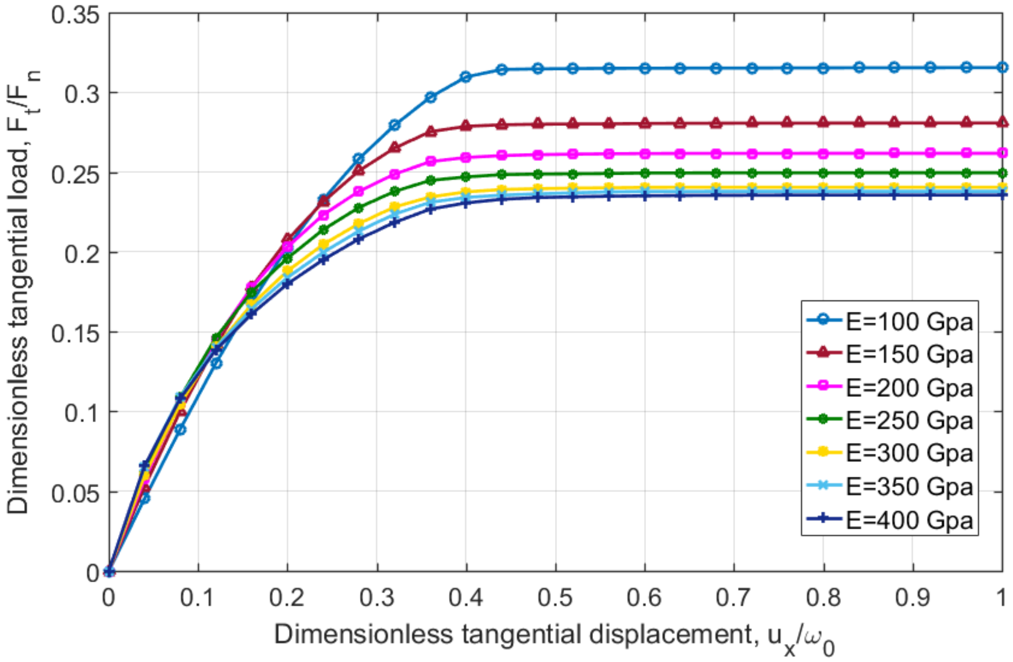

Fig. 4.9. The dimensionless tangential load F_t/F_n, versus the dimensionless tangential displacement u_x/ω_0, for different elastic moduli E.

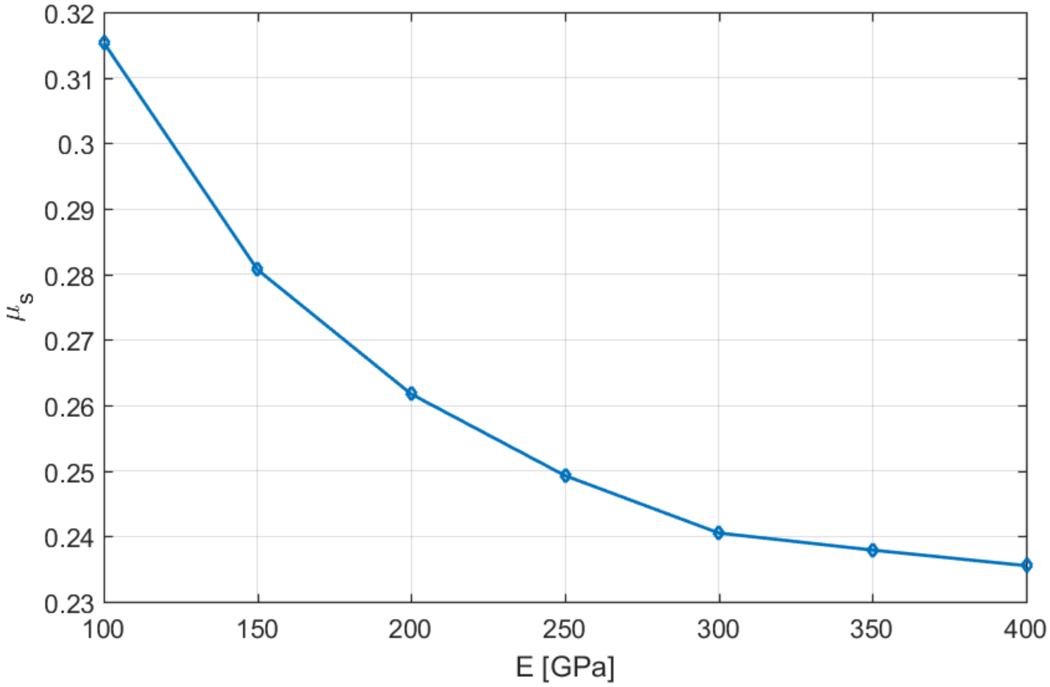

Fig. 4.10. Static friction coefficient versus elastic modulus.

A parametric analysis of the material properties is also considered. First, the elastic modulus, E, is varied from 100 GPa to 400 GPa, while the Poisson's ratio (v = 0.3), yield strength ($S_y = 1$ GPa), dimensionless contact pressure ($\bar{p}/p_{ep}^* = 0.05$), the critical interfacial strength ratio ($\tau_c/S_y = 0.577$) are all held constant. As shown in the Fig. 4.9, as the elastic modulus increases, the value of the curve decreases. At higher values of E, the curves seem to converge. The static friction is then plotted versus elastic modulus, as shown in Fig. 4.10. The static friction coefficient decreases with increasing elastic modulus. This is probably because as the elastic modulus decreases the amount of deformation increases and the contact becomes smaller. Under the same contact pressure, the contact area with the larger elastic modulus has a smaller value, and therefore the corresponding static friction coefficient is smaller.

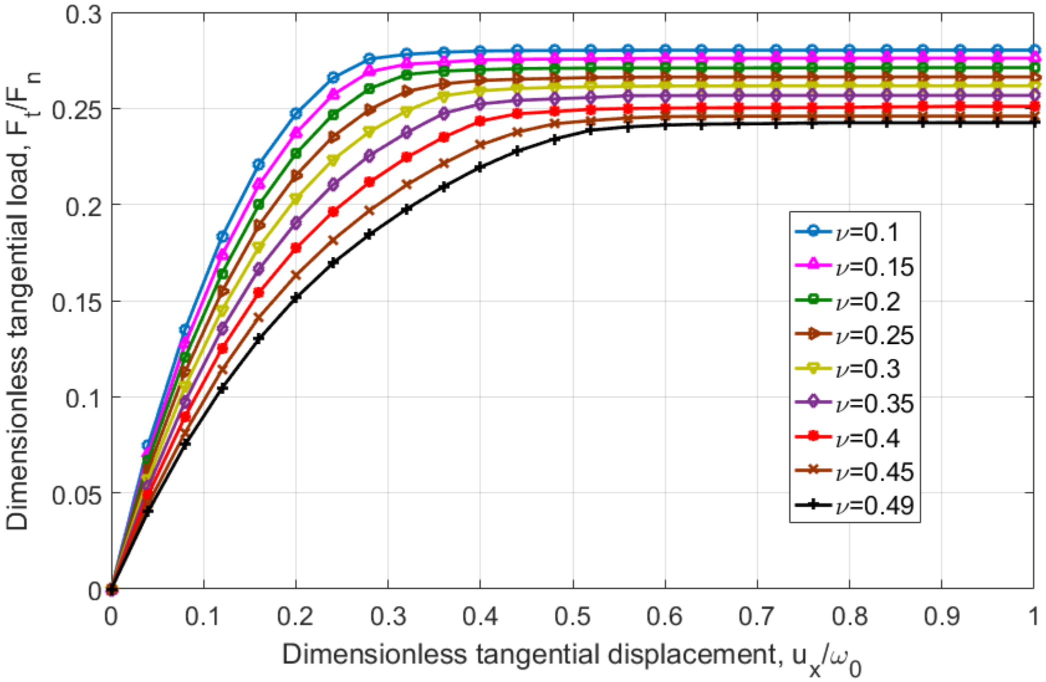

Fig. 4.11. The dimensionless tangential load F_t/F_n, versus the dimensionless tangential displacement u_x/ω_0, for different Poisson's ratio ν.

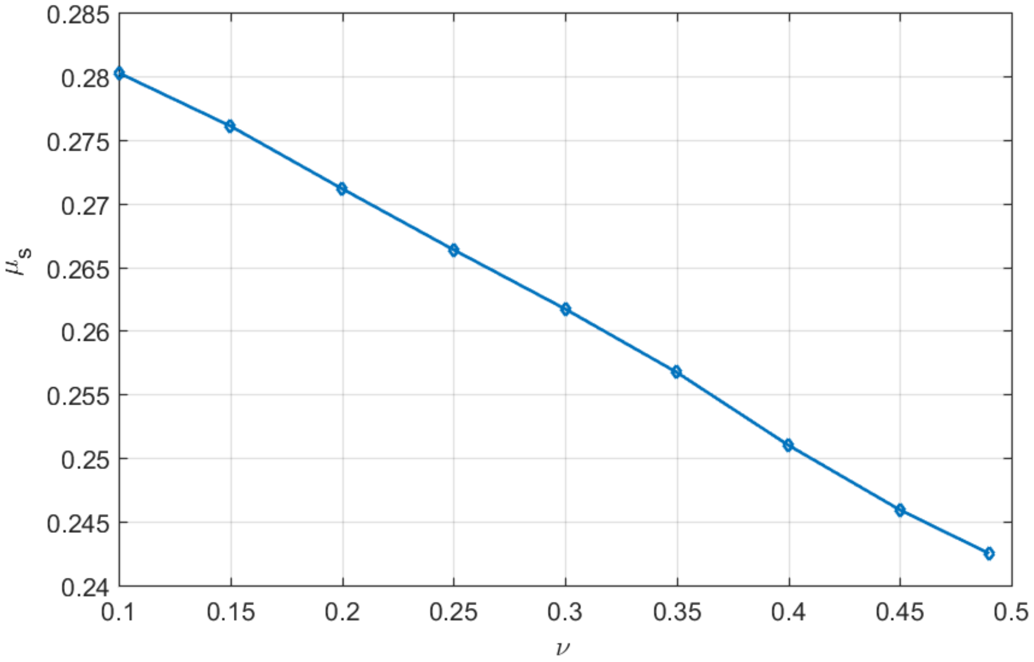

Fig. 4.12. Static friction coefficient versus Poisson's ratio.

Next, the Poisson's ratio, ν, is now varied from 0.1 to 0.49, while the elastic modulus ($E = 200\ \mathrm{GPa}$), yield strength ($S_y = 1\ \mathrm{GPa}$), dimensionless contact pressure ($\bar{p}/p^*_{ep} = 0.05$), the critical interfacial strength ratio ($\tau_c/S_y = 0.577$) are held constant. As shown in the Fig. 4.11 that as the Poisson's ratio increases, the curve decreases. It can be seen from Fig. 4.11, at each loading step, the dimensionless tangential load with a higher Poisson's ratio has a higher value. The static friction is then plotted versus Poisson's ratio, as can be seen in Fig. 4.12. The static friction coefficient decreases nearly linearly with increasing Poisson's ratio. When ν is small, it causes less expansion in the x and y direction, the surface separation is small, and the contact area therefore becomes smaller than when ν is large. Thus, the static friction coefficient increases with ν increasing.

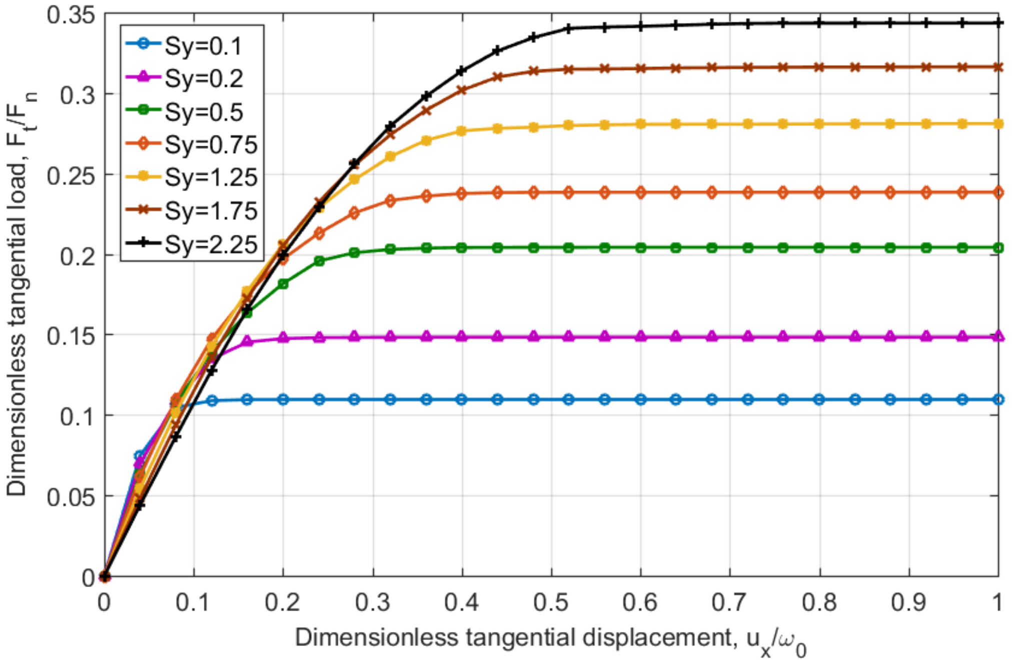

Fig. 4.13. The dimensionless tangential load F_t/F_n, versus the dimensionless tangential displacement u_x/ω_0, for different yield strength S_y.

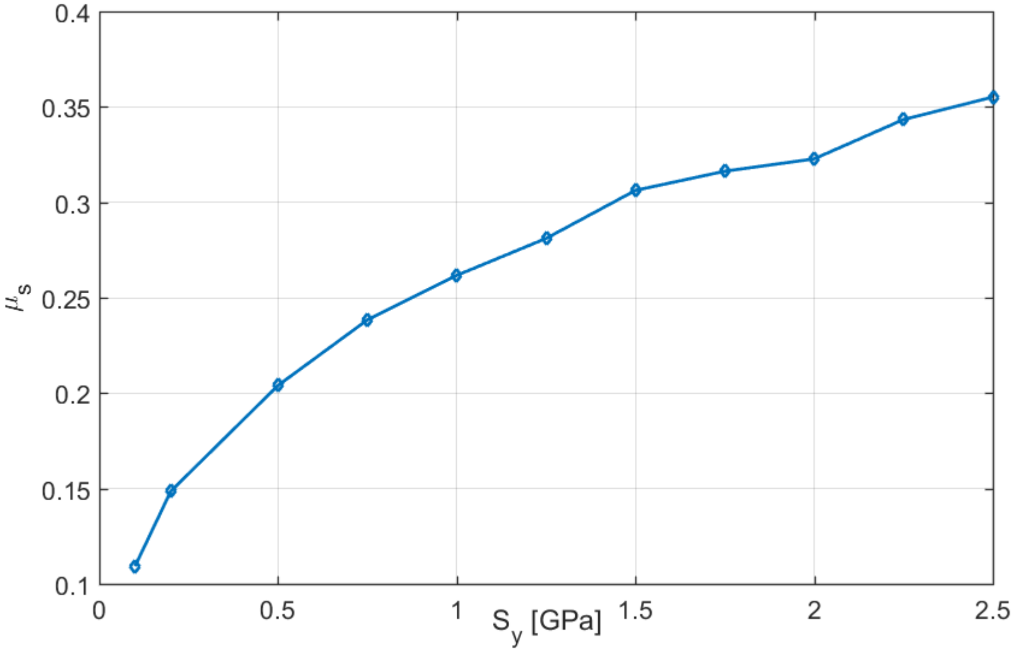

Fig. 4.14. Static friction coefficient versus yield strength.

Finally, the yield strength, S_y, is now varied from 0.1 GPa to 2.5 GPa, while the elastic modulus, ($E = 200$ GPa), the Poisson's ratio ($\nu = 0.3$), yield strength ($S_y = 1$ GPa), geometric parameter ($\Delta/\lambda = 0.02$), dimensionless contact pressure ($\bar{p}/p_{ep}^{*} = 0.05$), and the critical shear stress ratio ($\tau_c/S_y = 0.577$) are held constant. The results are shown in the Fig. 4.12. As the yield strength increases, the magnitude of the curve also increases. This is because the increase in yield strength causes the asperity to resist more tangential load before slipping. The static friction is then plotted versus yield strength. It can be seen from Fig. 4.13, that the static friction coefficient increases with increasing yield strength.

4.3.4. Effect of Geometric Ratio Δ/λ on Effective Static Friction Coefficient

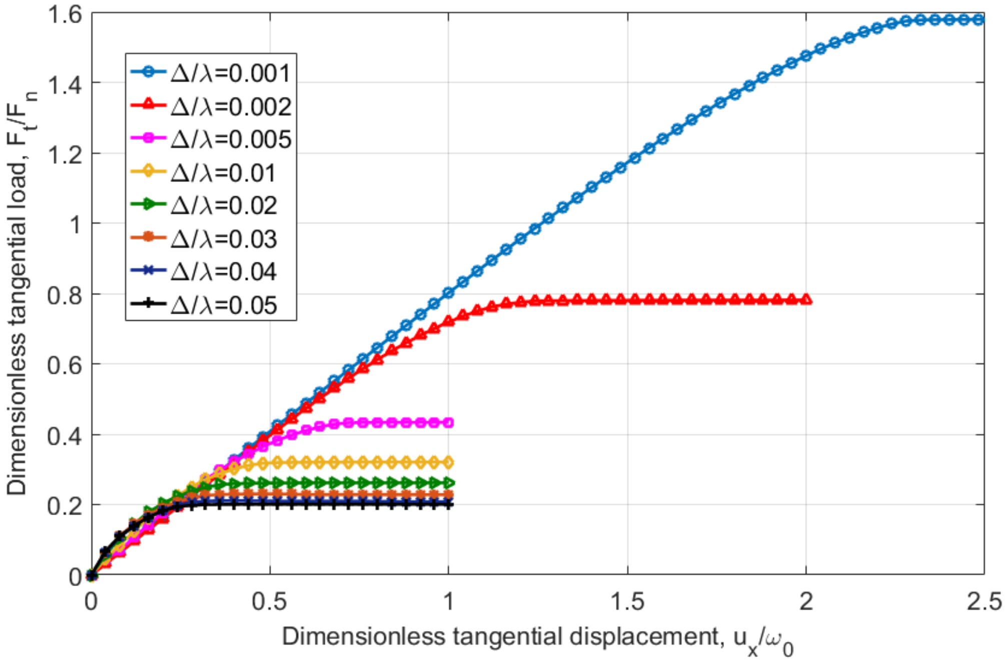

Fig. 4.15. The dimensionless tangential load F_t/F_n, versus the dimensionless tangential displacement u_x/ω_0, for different Δ/λ.

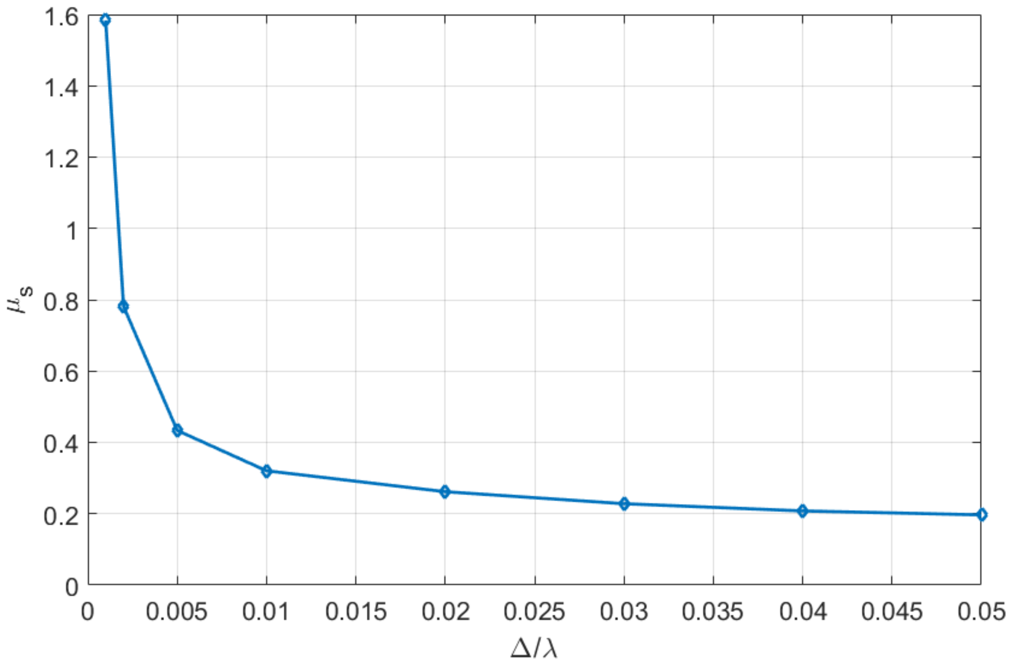

Fig. 4.16. Static friction coefficient versus geometric ratio.

Next, a range of $\varDelta/\lambda$ were considered. The geometry property $\varDelta/\lambda$ is now varied from 0.001 to 0.05, as shown in Fig. 4.14. All other properties are held to the benchmark case value. As shown in the Fig. 4.15, as $\varDelta/\lambda$ increases, the curve also decreases. This is because the contact area decreases by having a larger value of $\varDelta/\lambda$ (i.e. taller asperities).

The effect of Δ/λ on the static friction coefficient is shown by the plot in Fig. 4.15. It can be seen that the static friction coefficient decreases when the Δ/λ increases. Another point should be noted, that lower values of the ratio Δ/λ can cause vary large static friction coefficients. For example $\mu_s \approx 1.6$ when $\varDelta/\lambda = 0.001$ and $\bar{p}/p^*_{ep} = 0.05$, this is because the smooth surface results in a larger contact area and needs a large force to overcome the shear strength of the material. This also correlates to the observation that adhesive friction is larger for smoother surfaces [81]. The shear strength plays an important role in the contact problems.

4.3.5. Effect of Interfacial Shear Strength on Effective Static Friction Coefficient

Finally, a range of interfacial shear strength ratios were considered**.** The sliding is also governed by the critical interfacial shear strength τ_c. When the shear stress exceeds the critical interfacial shear strength, local slipping occurs. In [12], the critical interfacial shear strength was set as $S_y/\sqrt{3}$. However, the interfacial shear strength is not always equals to $S_y/\sqrt{3}$, because of contaminants, lubrication and changes in temperature. Hence, a wide range of the critical shear stress ratios, τ_c/S_y, are considered in the model (see Fig. 4.17). The interfacial shear strength ratio τ_c/S_y was varied from 0.1 to 0.577. The elastic modulus, (E= 200 GPa), Poisson's ratio, ($\nu = 0.3$), yield strength ($S_y = 1$ GPa), geometry ratio ($\Delta/\lambda = 0.02$), and dimensionless contact pressure ($\bar{p}/p^*_{ep} = 0.05$) are held constant.

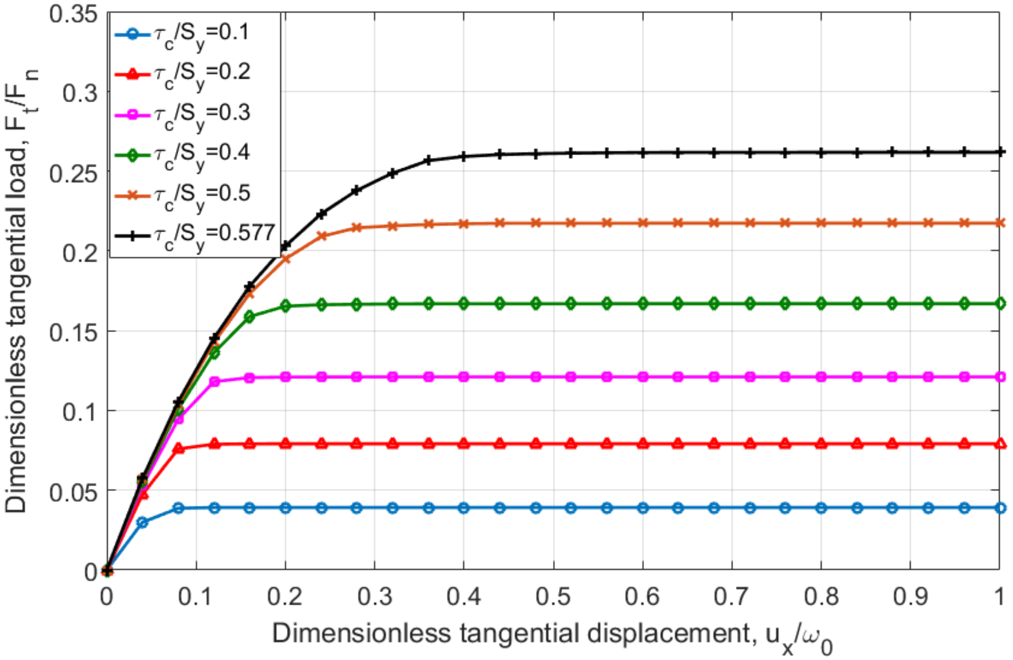

Fig. 4.17. The dimensionless tangential load F_t/F_n, versus the dimensionless tangential displacement u_x/ω_0, for different τ_c/S_y.

As can be seen from Fig. 4.17, as the interfacial shear strength ratio increases, the curve levels off at a higher dimensionless tangential load. The initial stiffness increases with τ_c/S_y as well.

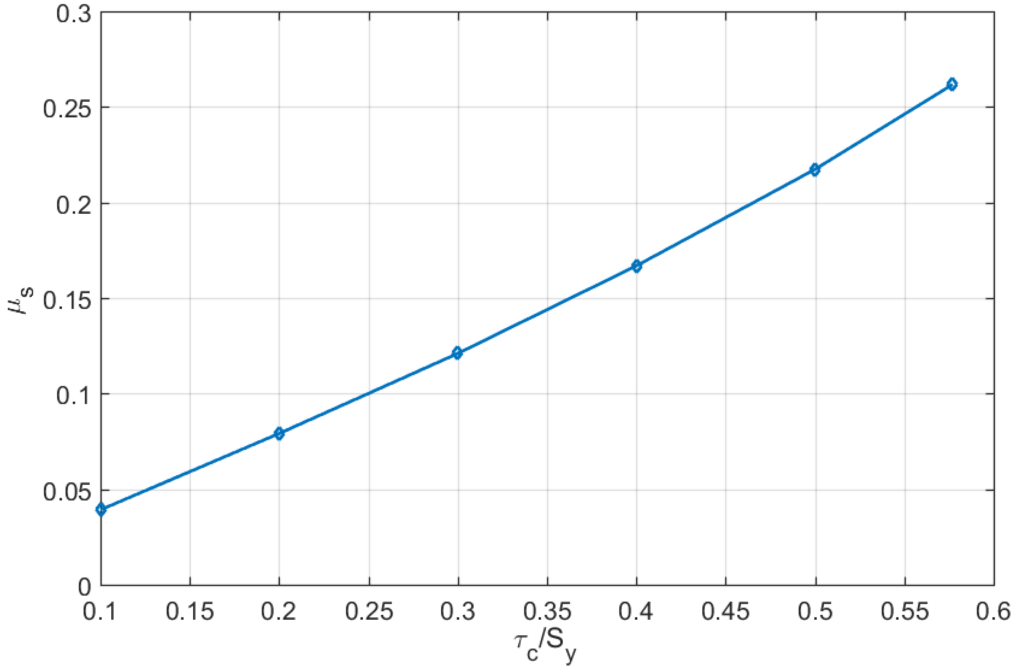

Fig. 4.18. Static friction coefficient versus interfacial shear strength ratio.

Fig. 4.18 presents the effect of critical interfacial shear strength on the static coefficient of friction. In this case, the dimensionless contact pressure, $\bar{p}/p_{ep}^{*}$, is chosen as 0.05. As can be seen from Fig. 4.18, the static friction coefficient increases with increasing dimensionless critical interfacial shear strength. Not surprisingly, the relationship is nearly linear. This occurs because the asperity needs a larger force to overcome the local strength when the material has a large critical shear strength.

4.3.6. Empirical Equations and Comparison

Since the material properties, geometry properties, dimensionless contact pressure, and dimensionless critical tangential stress, are each varied independently from the benchmark case, an equation can be fit for each trend. It is very convenient to use an additional parameter, φ , proposed by Gao et al. [20] to combine several of these parameters in one parameter. It can be expressed in the form:

$$\varphi = \frac{E'}{S_y} \frac{\Delta}{\lambda} \tag{4.8}$$

Effective Static Friction Coefficient

The static friction coefficient as a function of the parameter, φ , dimensionless normal contact pressure, $\bar{p}/p_{ep}^*$, and the dimensionless critical shear strength, τ_c/S_y, was fitted to all of the FEM data. And it is given by

$$\mu_s = \left[1.848\, coth\left(6.5\, \varphi^{2/3} \left(\frac{\bar{p}}{p_{ep}^*}\right)^{1/3}\right) - 0.184\, \varphi^{\frac{1}{4}} \left(\frac{\bar{p}}{p_{ep}^*}\right)^{\frac{1}{8}} - 1.482\right] \left[\left(\frac{\tau_c}{S_y}\right)^2 + 2\frac{\tau_c}{S_y}\right] \tag{4.9}$$

Again, note that Eq. (4.9) does not predict macro scale friction, but the local asperity friction, as is the case analyzed in this work.

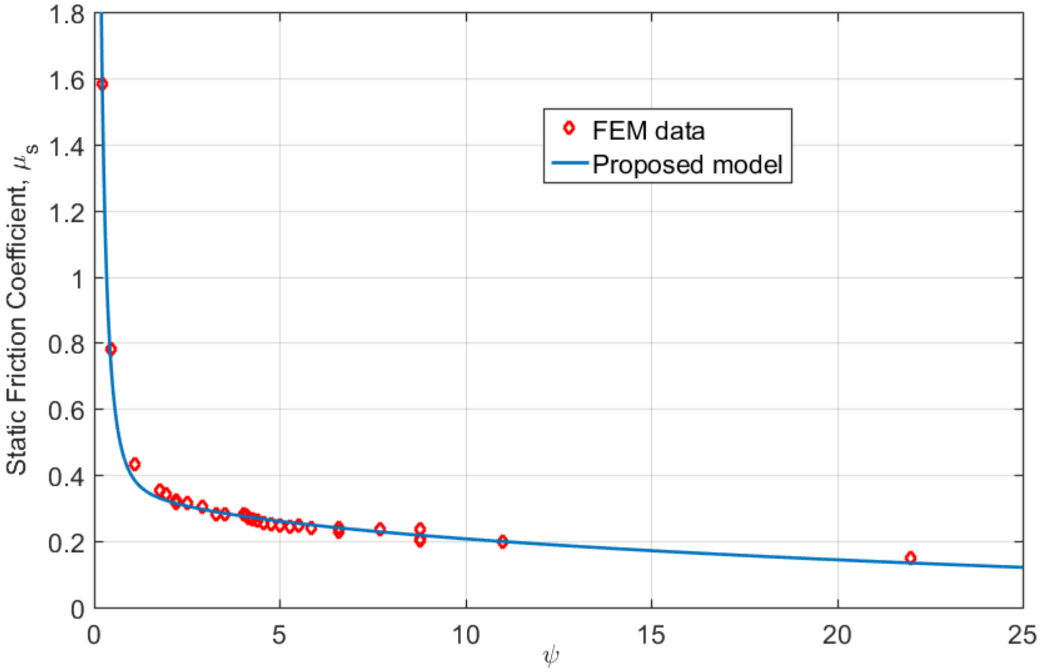

Fig. 4.19. Comparison of static friction coefficient between the FEM results and the proposed model for various values of φ.

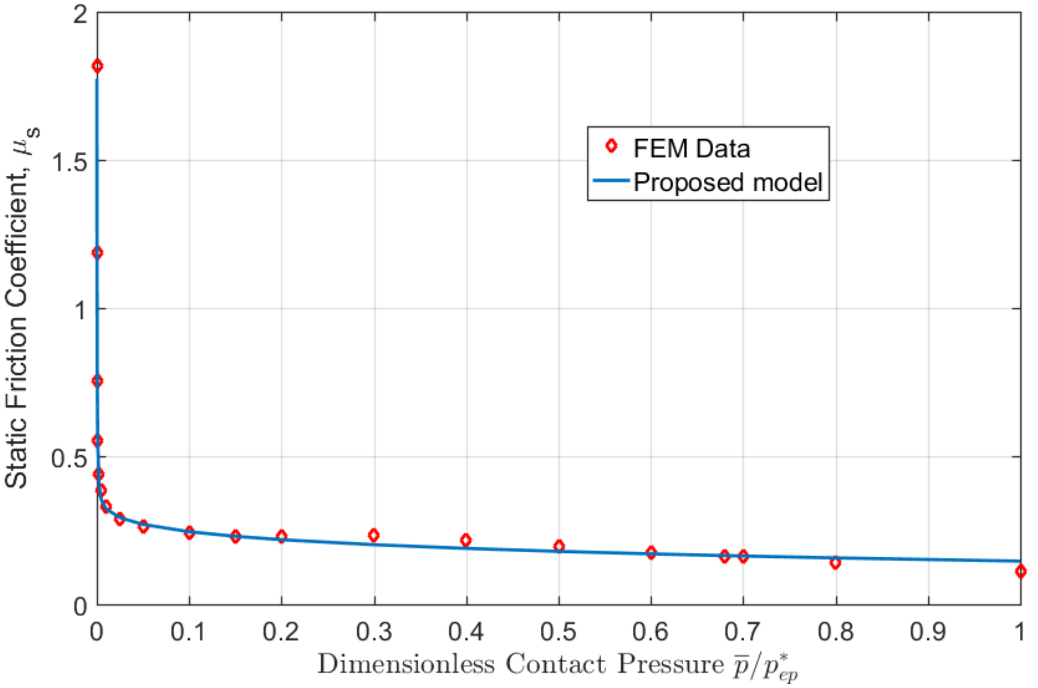

Fig. 4.20. Comparison of static friction coefficient between the FEM results and the proposed model for various values of $\bar{p}/p^*_{ep}$.

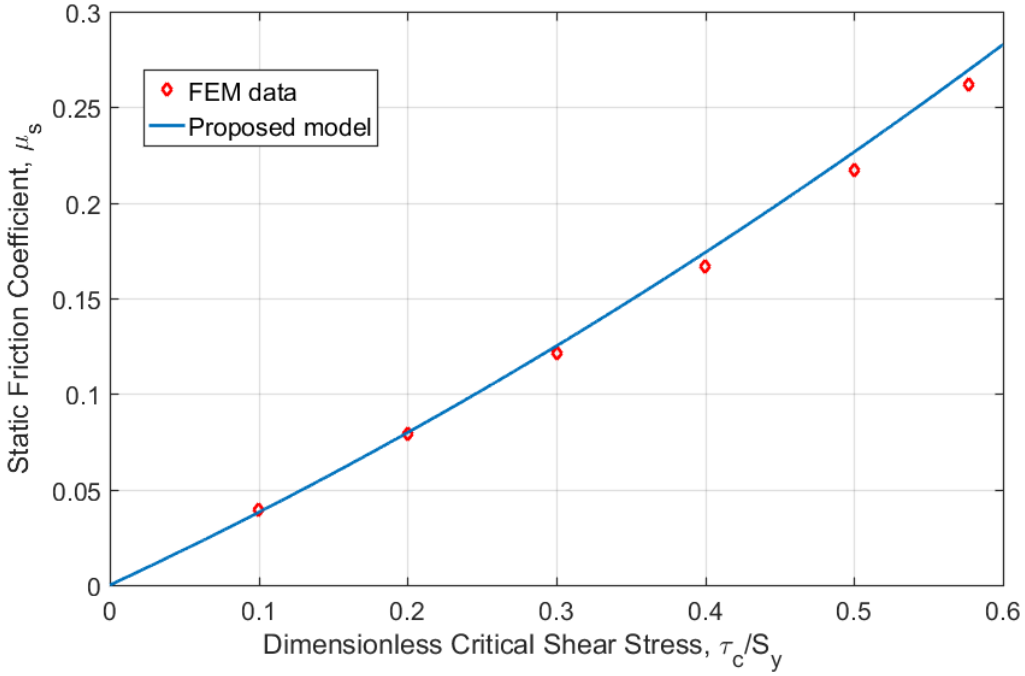

Fig. 4.21. Comparison of static friction coefficient between the FEM results and the proposed model for various values of τ_c/S_y.

A comparison between Eq. (4.9) and the FEM results of different case are shown in Figs 4.18 - 4.20. In Fig. 4.18 we can see the model for the static friction coefficient (Eq. 4.9) agrees fairly well with the FEM data based on the parameter φ. The average error between the new model given by Eq. (4.9), and the FEM results when the φ is varied independent is less than 2%. Likewise, the plots in Fig. 4.19 and Fig. 4.20 show that the model also compares well for the cases where the dimensionless contact pressure, $\bar{p}/p_{ep}^*$ and the dimensionless critical shear strength, τ_c/S_y, are also varied (the errors in these cases are less than 4%).

In order to compare the proposed model to the spherical contact models in [8, 9], it is necessary to present the expression of Eq. (4.9) in terms of F_n/F_c instead of $\bar{p}/p_{ep}^*$. The term $\bar{p}/p_{ep}^*$ in Eq. (4.9) can be exprssed as

$$\frac{\bar{p}}{p_{ep}^*} = \frac{\bar{p}\, A_n}{p_{ep}^*\, A_n} = \frac{F_n}{\left(p_{ep}^*\, A_n/F_c\right) F_c} = \left(\frac{F_c}{p_{ep}^*\, A_n}\right)\frac{F_n}{F_c} \tag{4.10}$$

And the new equation is given by:

$$\mu_s = \left[1.848\, coth\left(6.5\, \varphi^{2/3}\left(\left(\frac{F_c}{p_{ep}^*\, A_n}\right)\frac{F_n}{F_c}\right)^{1/3}\right) - 0.184\, \varphi^{\frac{1}{4}}\left(\left(\frac{F_c}{p_{ep}^*\, A_n}\right)\frac{F_n}{F_c}\right)^{\frac{1}{8}} - 1.482\right]\left[\left(\frac{\tau_c}{S_y}\right)^2 + 2\frac{\tau_c}{S_y}\right] \tag{4.11}$$

where p_{ep}^* can be calculated from Eq. (3.12).

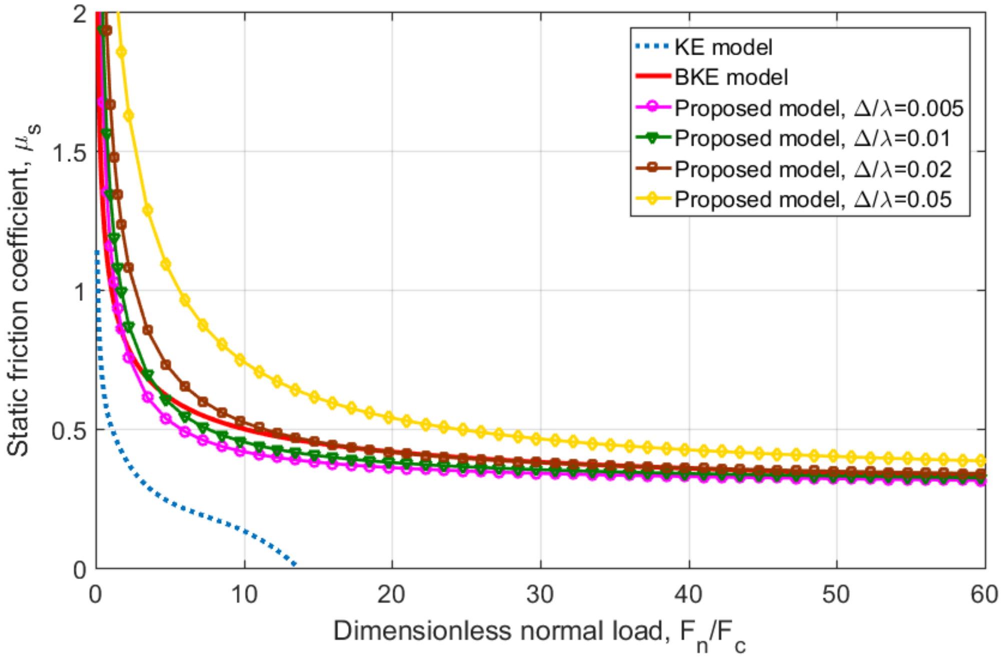

Fig. 4.22. Comparison of static friction coefficient between the KE, BKE model and the proposed model with different Δ/λ.

Since the geometry and contact condition assumption of the proposed model are different from the sphere used in [8, 9], the same material properties in these papers are used now to make a comparison. Reference [9] by Brizmer et al. is now referred to as the BKE model, while reference [8] by Kogut and Etsion is refered to as the KE model. First, typical amplitudes to wave length ratios (Δ/λ) are considered while keeping the critical shear stress ratio (τ_c/S_y) constant at 0.577. The effective static friction coefficient as a function of the dimensionless tangential load with different values of Δ/λ are plotted in Fig. 4.21. As seen from Fig. 4.21, the proposed model has the same trend as the BKE model and the difference depends on the values of Δ/λ. Both the proposed model and the BKE model have higher values of the effective static friction coefficient than the KE model.

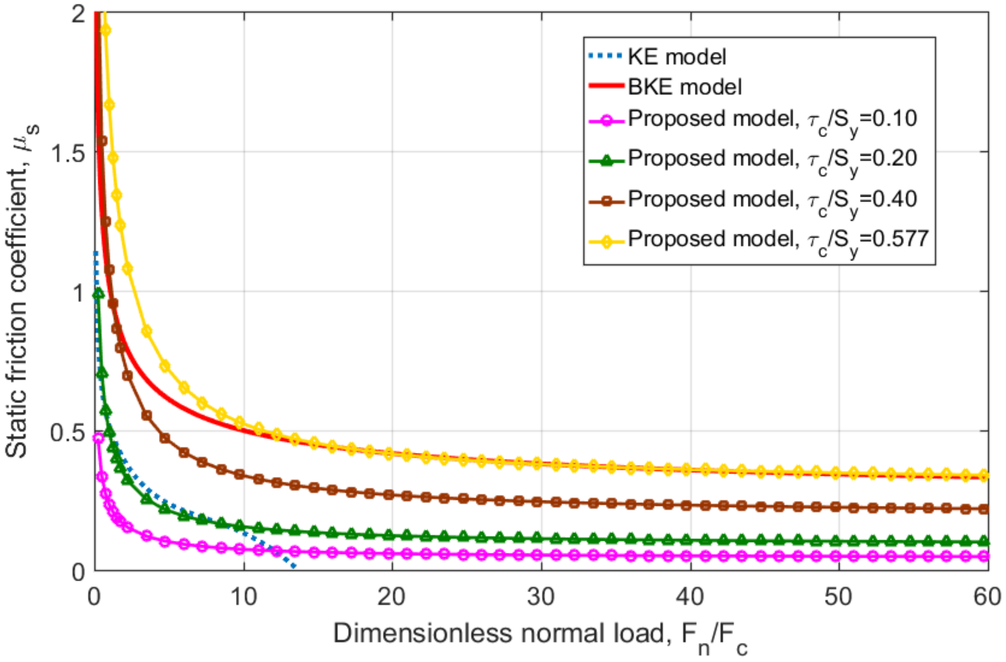

Fig. 4.23. Comparison of static friction coefficient between the KE, BKE model and the proposed model with different τ_c/S_y.

Next, several interfacial shear strengths (τ_c/S_y) are considered, while keeping the amplitude to wave length ratio (Δ/λ) constant at a value of 0.02 . The effective static friction coefficient is plotted as a function of the dimensionless tangential load with different τ_c/S_y values in Fig. 4.22. As seen from Fig. 4.22, the proposed sinusoidal model again has the same trend as the BKE model. As is introduced in [56], the BKE model is independent of contact radius of the sphere. The sinusoidal model is always close or lower than the BKE model, and differs quantitatively depending on the value of τ_c/S_y. One observation is that when $\tau_c/S_y = 0.2$, the value of the static friction coefficient is close to the value predicted by the KE model at low normal preloads.

Junction Growth

By using the same method, the dimensionless contact area at sliding inception as a function of the parameter, φ , dimensionless normal contact pressure, $\bar{p}/p_{ep}^{*}$, and the dimensionless critical shear strength, τ_c/S_y, was fitted to all of the FEM data. The FEM results are presented alongside the proposed model and are plotted in Figs. 4.24 - 4.26. The plots in Figs. 4.24 - 4.26 show that the contact area at sliding inception of the proposed model agree fairly well with FEM results (the average error in these cases is also than 6%).

$$\frac{A_s}{A_0} = 2.6\left\{coth\left[15.2\left(\frac{\bar{p}}{p_{ep}^{*}}\right)^{1/2}\right]\exp(-0.017\,\varphi - 3) - 0.03\,\varphi^{\frac{1}{4}}\left(\frac{\bar{p}}{p_{ep}^{*}}\right)^{4} + 0.1364\right\}\left[\left(\frac{\tau_c}{S_y}\right)^{2} + 2.13\right] \qquad (4.12)$$

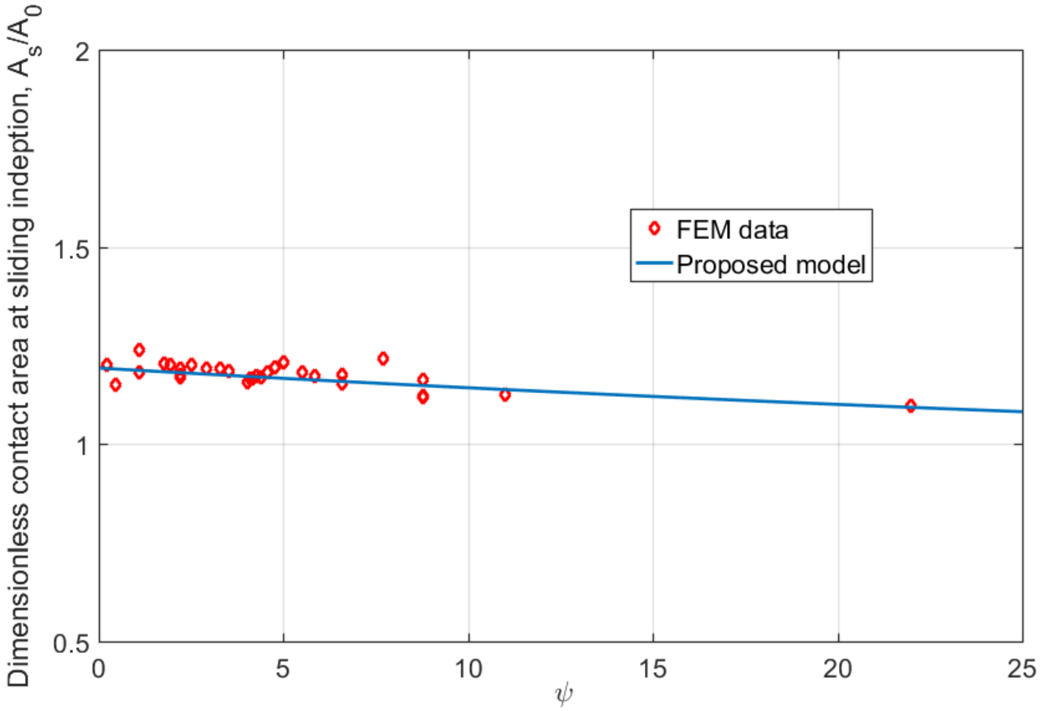

Fig. 4.24. Comparison of junction growth between the FEM results and the proposed model for various values of φ.

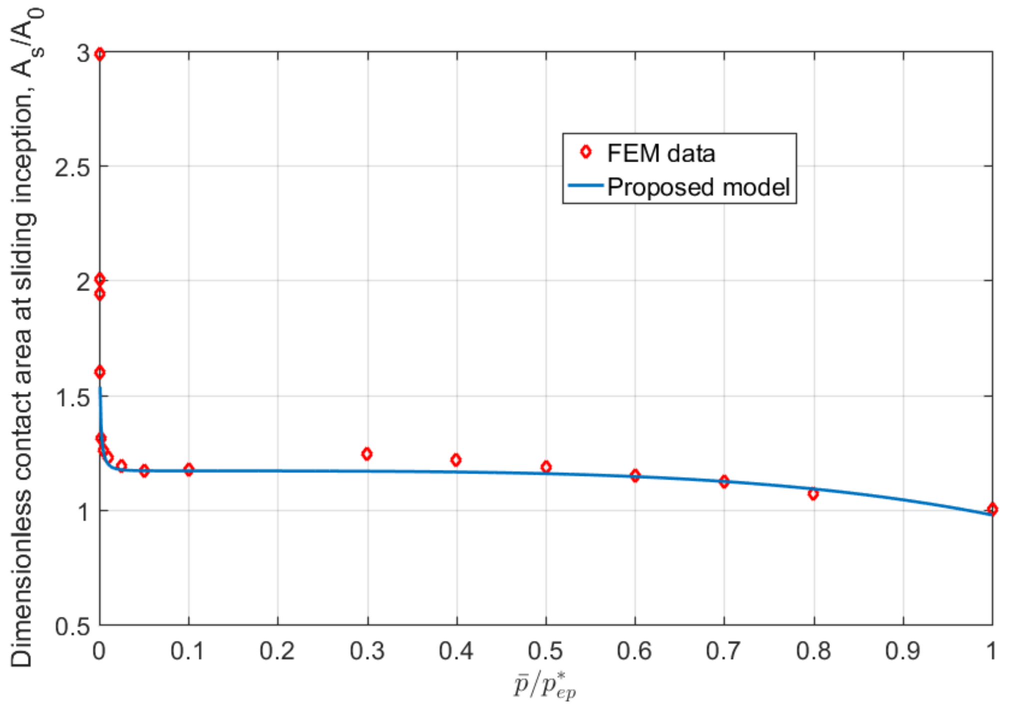

Fig. 4.25. Comparison of junction growth between the FEM results and the proposed model for various values of $\bar{p}/p^*_{ep}$.

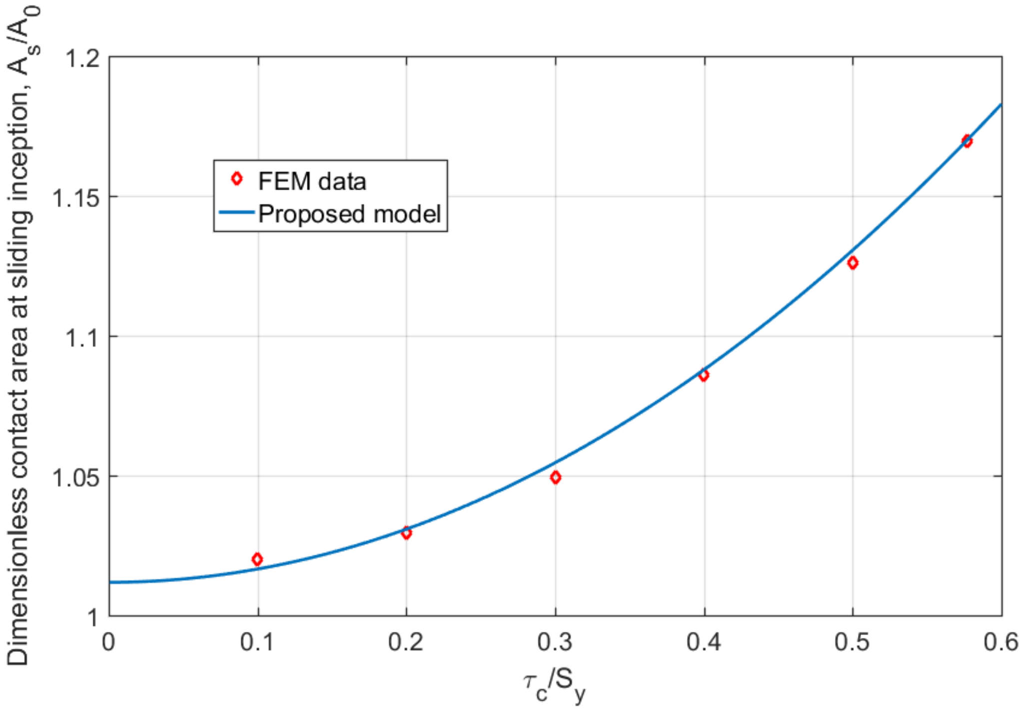

Fig. 4.26. Comparison of junction growth between the FEM results and the proposed model for various values of τ_c/S_y.

4.3.7. The Yield Inception Due to Tangential Loading

Since these previous works of Etsion's group showed that yielding can effectively separate the surface from the initial stick to sliding inception below the surface, this is investigated for sinusoidal contact. The plastic deformation is related to the normal preload or interference [8, 9, 12] for spherical contact, the same situation is also found for this study. For the sinusoidal contact, it is also related to the wave length ratio (Δ/λ). A typical metal is chosen with material properties $E = 200\ GPa, \nu = 0.3, S_y = 1\ GP$, dimensionless contact pressure, $\bar{p}/p^*_{ep} = 0.05$, and the critical interfacial shear strength ratio is chosen as $\tau_c/S_y = 0.577$.

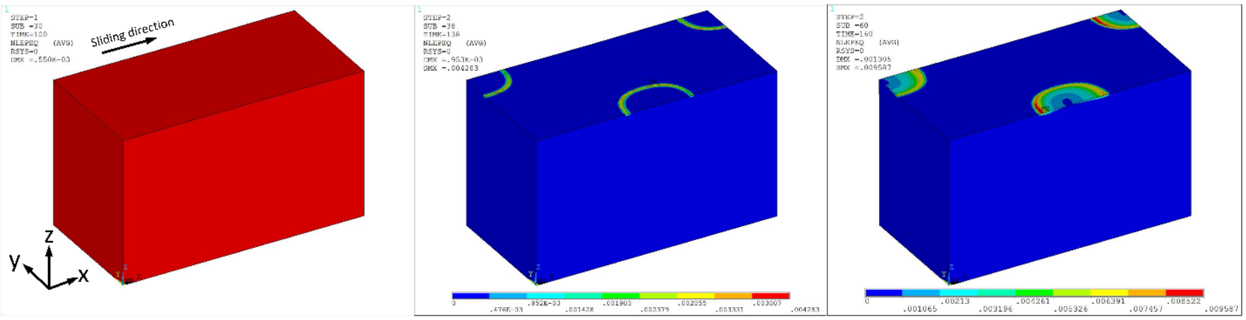

(a) Ft = 0 (b) Ft=0.75 Ftmax (c) Ft=Ftmax

Fig. 4.27. Equivalent Plastic strain during tangential loading ($\Delta/\lambda = 0.001$).

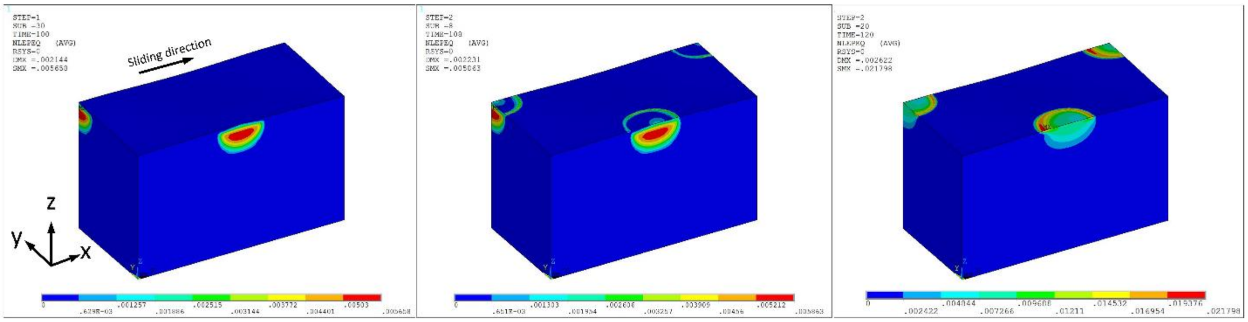

(a) Ft = 0 (b) Ft=0.625 Ftmax (c) Ft=Ftmax

Fig. 4.28. Equivalent Plastic strain during tangential loading ($\Delta/\lambda = 0.005$).

Fig. 4.27. presents the equivalent plastic strain during tangential loading. As shown in Fig. 4.27 (a), when the sinusoidal surface is only under the normal loading, there is no yield strain anywhere. As tangential load is increased, the yield occurs on the surface and underneath of the surface on the annulus of the contact area, as shown in Fig. 4.27 (b). Further tangential loading results in a larger yield area. The yield area extends from the plastically deformaed volume held to the surface to the edge of contact. At the sliding inception, an elastic area exist in the middle of the contact aea. As shown in Fig. 4.27 (c), for the case of $\Delta/\lambda = 0.005$, the yield first occurs at the solid body below the surface. There is no yield on the surace, and the plastic area on the surface becomes larger as the tangential load increases. At the sliding inception, the plastic area is extended to the whole contact area, and there is no elastic area in it, see Fig. 4.28.

Considering the sliding inception as a failure mechanism, both an FEM [8, 9] and experimental study [82] were carried out. They suggested that when the normal preload is less than the critical load, the failure occurs on the contact area. If the normal load exceeds the critical value, the failure occurs below the contact area. Etsion [83] revisited the Cattaneo-Mindlin concept of interfacial slip in tangentially loaded compliant bodies. He pointed out that sliding occurs under the surface for typical metallic materials, and interfacial slip can only occur in some special cases, such as when the interface is much weaker than any of the contacting bodies, or lubricated contact. Different from the full stick model, the sliding inception defined in the current work is when the gross relative displacement between the two surfaces in contact takes place. This may be different than the other definitions based on the plastic failure. However, the results show they have a reasonable agreement. For our cases the slipping always occurs on the surface. At high pressures, an elastic island of hydrostatic stress can form, but it appears to be restrained by the surrounding material, and slip still occurs on the surface. It might be possible that slip can occur below the surface for higher amplitude to wave length ratios (Δ/λ) not considered in this work. However, we choose a range that seems to be typical for rough surface asperities [60, 77, 84, 85].

4.4. Conclusion

Finite element simulations are carried out for a rigid flat on a deformable sinusoidal surface under combined normal and tangential loading at the asperity scale. This work used a finite element model to characterize the three-dimensional sinusoidal contact. A maximum shear stress criterion was used to determine the sliding inception. The static friction coefficient shows strong dependency on material properties, contact pressure and interfacial shear strength. The static friction coefficient of a single sinusoidal asperity decreases with increasing contact pressure, elastic modulus, Poisson's ratio, and the ratio of amplitude over wavelength. The static friction coefficient of a single sinusoidal asperity, increases with increasing yield strength and critical shear strength. An empirical expression of the static friction coefficient was given considering these effects. This equation could be used in a multi-scale or statistical model to predict the static friction coefficient for the rough surface. The phenomenon of junction growth of the interference and contact area are described briefly, and an empirical expression was given. How the plastic deformation of the sinusoidal surface caused by tangential loads relates to friction is also studied. For the cases considered in this work, slip initiates on the surface and not below it.

CHAPTER 5. THE EFFECT OF SAMPLING RESOLUTION ON CONTACT BEHAVIOR

Finite element models of contacting bodies are sensitive to the mesh resolution. Therefore, the effect of the sampling resolution on the FEM predicted contact behaviors has been studied by a few researchers. Demiric et al. [86] analyzed the contact behaviors for different scale levels by decomposing from the real measured rough surface. They also analyzed the effect of the scale of roughness on kinetic friction coefficient and found the fine scale of roughness has a strong influence on the full-film lubrication and mixed lubrication. Yastrebov et al. [87] analyzed the contact of rough surfaces with by decreasing the sampling points from the measured real surface data, and introduced a corrective function to compensate for errors in the contact area computations caused by mesh, i.e. this technique can be used to evaluate the true contact area using a coarse mesh. Both of them used an approach that filtered the measured surface data. We use an opposite approach by using Fourier interpolation to increase the sampling points between the measured points**.**

Most of the researchers use the measured surface data directly, and assume that the shape between two measured points is a straight line. If the data points are connected using straight lines, the surface will become discontinuous, and the sharp peaks will cause stress concentrations. It is possible to develop some techniques to create a continuous, smooth surface model. Kown et al. investigated the effect of surface smoothing and mesh density for real surfaces [88] and single asperities [89]. In their work, they also investigated several contact parameters by smoothing surfaces and changing the mesh density. The spline interpolation method was used to smooth the surfaces. Thompson [90] found that the spline smoothing surface method has a relatively small effect on the contact parameters of a rough surface contact, while it has a significant effect for a single asperity contact. In this study, we proposed another possible description for the shape between the measured points. We considered that the surfaces follow a harmonic structure between measured points based on the surface spectrum. Essentially, the surface resolution increased while the surface spectrum is preserved which may not be the cases for other methods.

5.1. Topography Measurements

Surface roughness is defined as the deviation of the actual surface topography. The rough surfaces embody a complex shape made of a series of peaks and troughs of varying heights, depths, and spacing. Surface roughness is greatly affected by the microscopic structure of the surface of each part. In this study, a standard micro-finish comparator was used for surface data (see Fig. 5.1). the micro-finish comparator contains machined surface finish specimens from different machining processes.

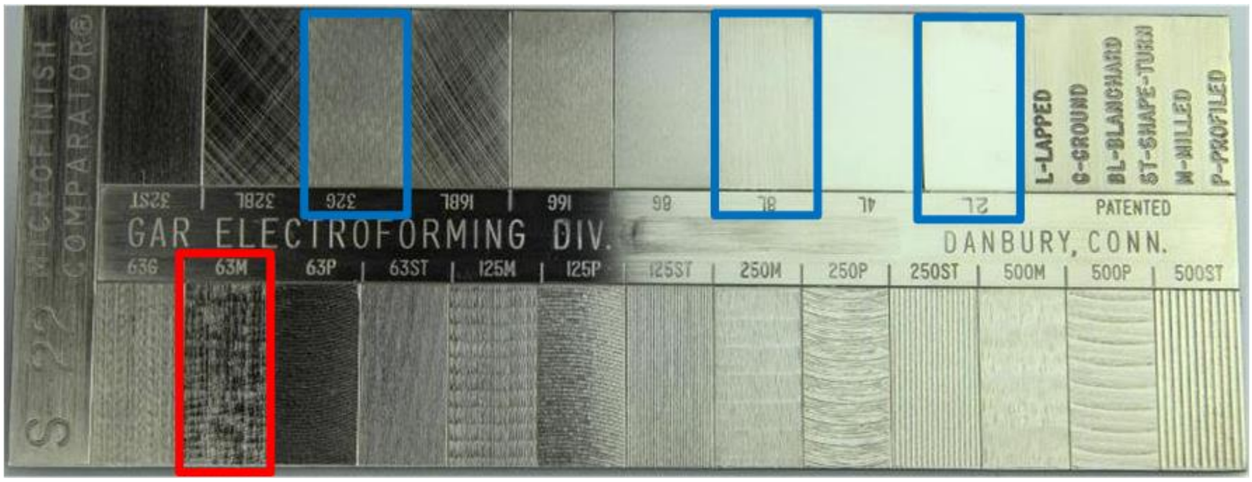

Fig. 5.1. S-22 Micro-finish comparator surface finish scale.

Surface measurement is a process used for obtaining the quantitative information about the individual or average surface heights. The two most commonly used techniques for roughness measurement are the stylus technique and the optical technique. The machines that make these measurements are usually known as profilometers or profilers. For the stylus profilometer, a sharp stylus with a very light load is drawn at a constant speed over the surface to be examined. The quantity of height is measured by the vertical position of the diamond stylus tip at a certain lateral position. The optical measurement technique uses an optical measurement principle called Axial Chromatism, and they use a white light source where light passes through an objective lens with a high degree of chromatic aberration. The objective lens' refractive index will vary with the wavelength of the light, and each separate wavelength of the incident white light will refocus at a different height. In this study, the NANOVEA ST400 white light optical profilometer (see Fig. 5.2) is used. The 63M surface (milled 63 $\mu\, inch$) is measured for use in this chapter. The lapped surfaces 2L, 8L and 32G are also measured and used in Chapter 5, 6 and 7.

Fig. 5.2. NANOVEA ST400 optical profilometer.

5.2. Methodology

5.2.1 Spectral Interpolation Method

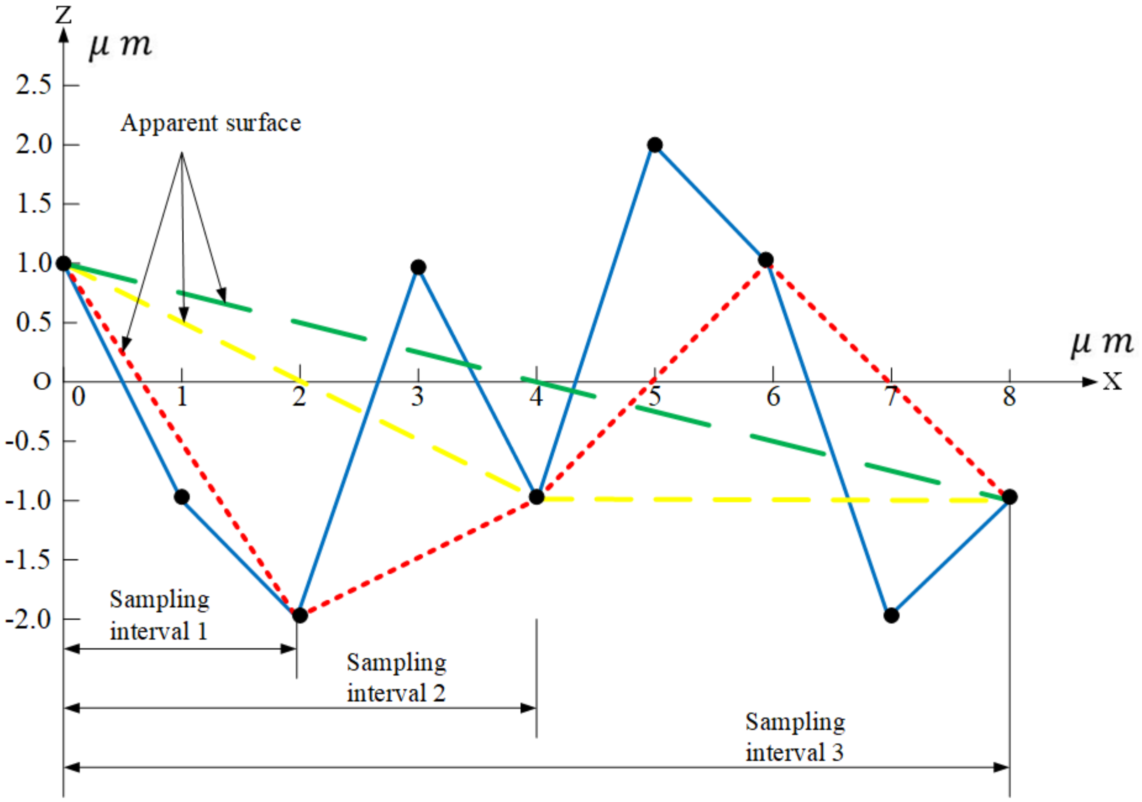

Fig. 5.3. A schematic of the effect of the sampling interval on the surface profile.

The choice of lateral resolution will determine whether the data is enough to represent the surface accurately or not. This becomes a challenge for surface characterization. Due to the precision of the measuring equipment, the surface may not be sampled often enough to describe the real rough surface. However, real surfaces are continuous, at least they can be considered that at scales above the atomic scales. Therefore, they have no lower sample interval. If the sampling intervals are not small enough, then it could not represent the same profile as the original data. Since surfaces are multi-scale in nature, reducing scale might introduce more roughness. As shown in Fig. 5.3, the blue line presents the real surface, the interval is 1.0 μm, and the amplitude is 2.0 μm and the location of the lowest valley is -2.0 μm. If the sampling resolution or sampling interval is set to 2 μm, the amplitude becomes 2.0 μm, and the location of the lowest valley is -2.0 μm. If the sampling resolution or sampling interval is set to 4 μm, the amplitude becomes 1.0 μm, and the location of the lowest valley is -1.0 μm. If the sampling resolution or sampling interval is set to 8 μm, the amplitude remains at 1.0 μm, and the location of the lowest valley is -1.0 μm. Therefore, the profiles changed significantly for different sampling intervals. This was studied and confirmed by Majumdar and Tien [91] and Kogut and Jackson [92] who made similar observations and how properties change with sampling length. Most of the researchers conducting FEM just use the measured data, and they inadvertently assume that the relation between two neighboring sampling points are linearly distributed. In this study, we present another possibility of the point distribution between two sampling points.

The discrete Fourier transform (DFT) can convert a signal from its original domain to the frequency domain. The equation is given by

$$F(k_x, k_y) = \frac{1}{N_x N_y} \sum_{n_x=0}^{N_x-1} \sum_{n_y=0}^{N_y-1} z(n_x, n_y) e^{-i2\pi(\frac{K_x n_x}{L_x} + \frac{K_x n_x}{L_x})} \tag{5.1}$$

and the inverse discrete Fourier transform (IDFT) is given by

$$z(n_x, n_y) = \sum_{n_x=0}^{N_x-1} \sum_{n_y=0}^{N_y-1} F(k_x, k_y) e^{i2\pi(\frac{K_x n_x}{L_x} + \frac{K_x n_x}{L_x})} \tag{5.2}$$

The Fast Fourier transform (FFT) algorithm, a fast way to perform a DFT, is widely used for many applications in engineering. In this study, we use the FFT command in MATLAB to transform the measured surface data (real numbers) into a sequence of complex numbers. After interpolation, the data was converted back by using an inverse Fast Fourier transform (IFFT). By changing the resolution of the surface by zero padding, intermediate points may be introduced. This is effectively a spectral interpolation.

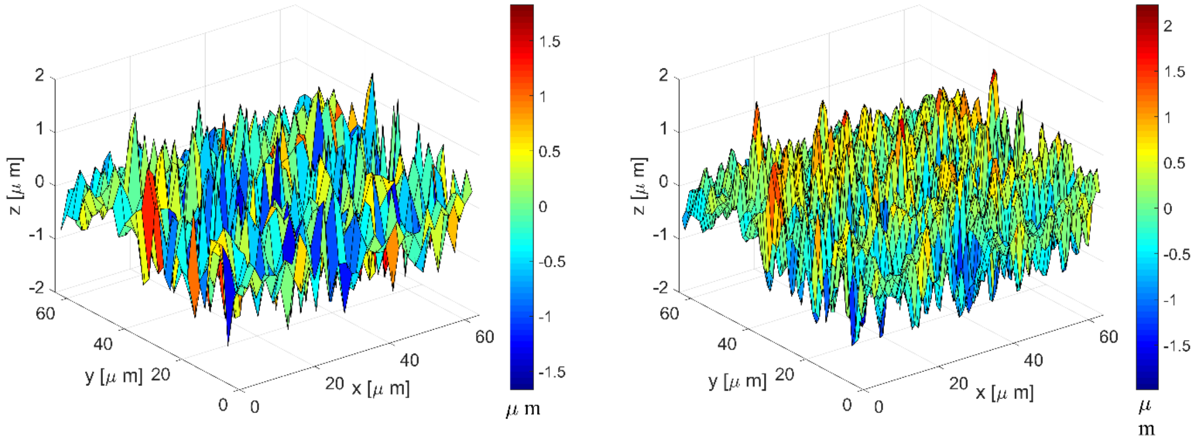

a. Original surface (32*32)

b. one-interpolation (64*64)

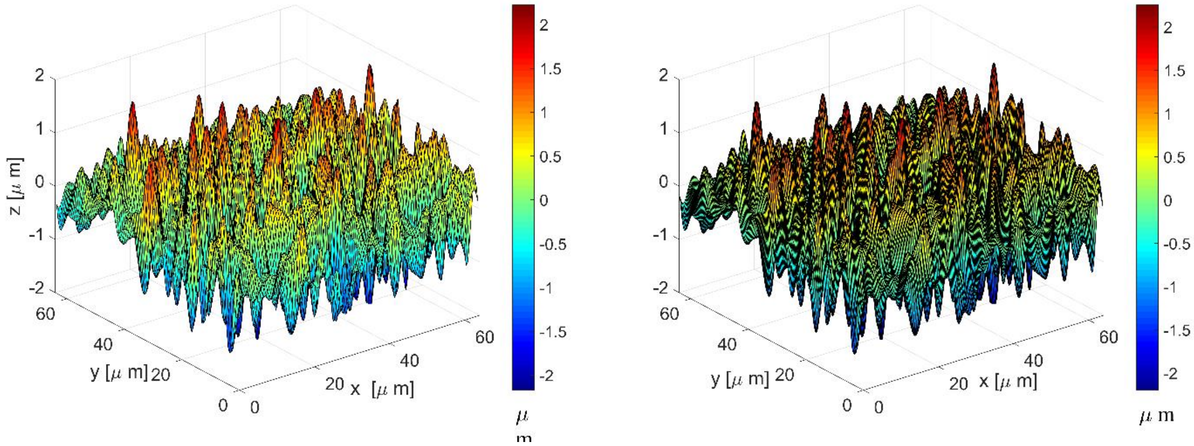

c. two-interpolation (128*128)

d. three-interpolation (256*256)

Fig. 5.4. The 3-D surface plots before and after interpolation.

First, a 32×32 points data was extracted from an entire measured data set (1024×1024) of M64 (64 μ inch milled). The profile shown in Fig. 5.4. a, is the original measured surface profile, and the data size is 32×32 data points. Then, we interpolate one point between each two adjacent points by using the FFT interpolation method. The size then repeating becomes 64×64, and by repeating the same procedure, the data size is increased to 128×128 and 256×256, whose profiles are shown in Fig. 5.4 c. and Fig. 5.4 d. The original surface resolution is 2 μm, but is reduced to 1 μm, 0.5 μm and 0.25 μm, respectively, after the spectral interpolations. It should be noted that the surfaces still all have exactly the same spectrum. The comparisons of an example profile between the interpolated surfaces and the original rough surface are presented in Figs. 5.5−5.7. Fig. 5.8 shows the detail of the interpolations for one interval. As can be seen, the shape between two measured points is a smooth harmonic curve after three interpolations, rather than the traditional assumed a straight line. This reduces the artificial sharp asperity points often seem as measured data.

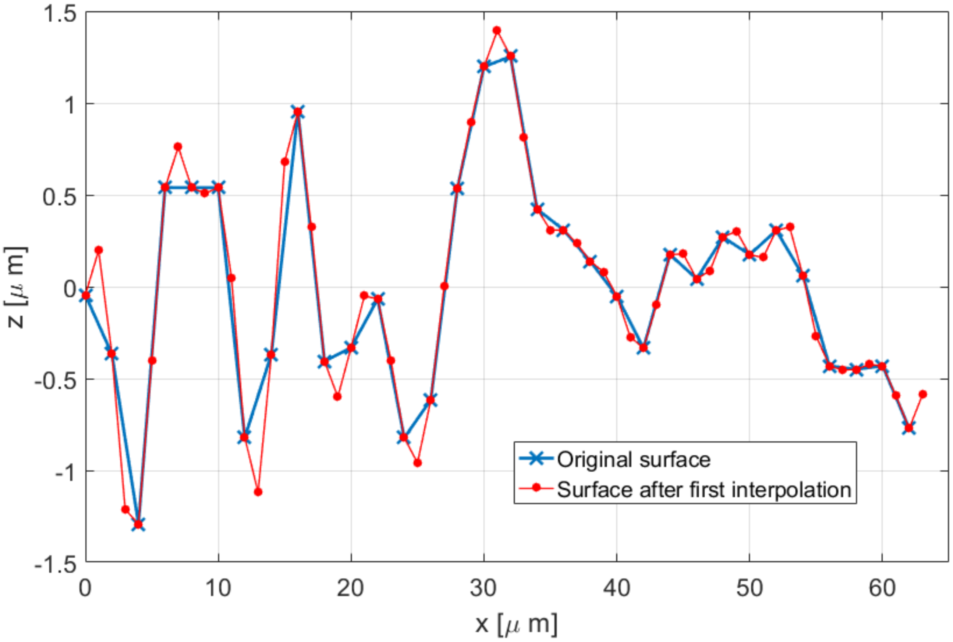

Fig. 5.5. Comparison of the original surface profile (32*32) and the one interpolation surface profile (64*64).

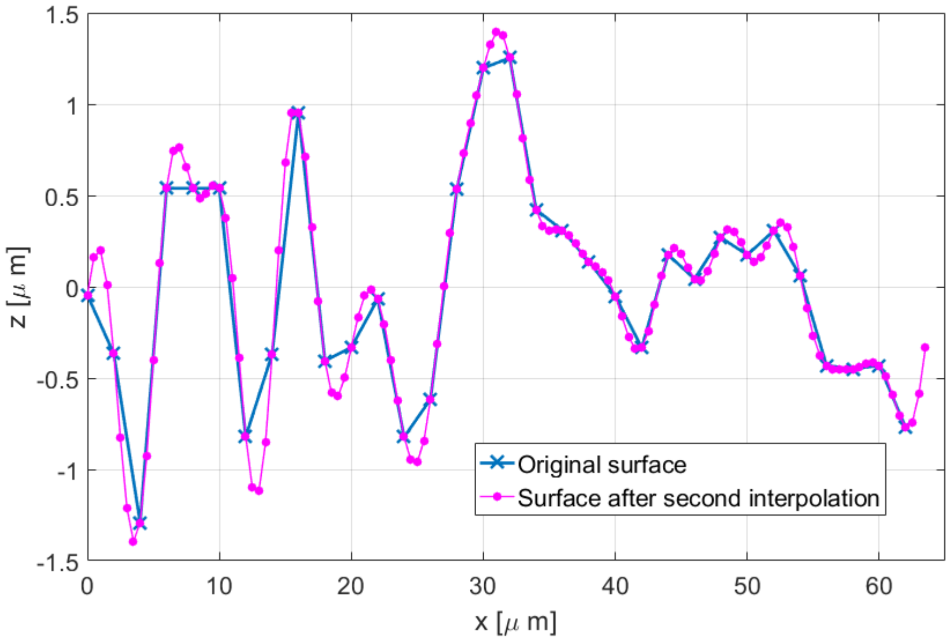

Fig. 5.6. Comparison of the original surface profile (32*32) and the two-interpolation surface profile (128*128).

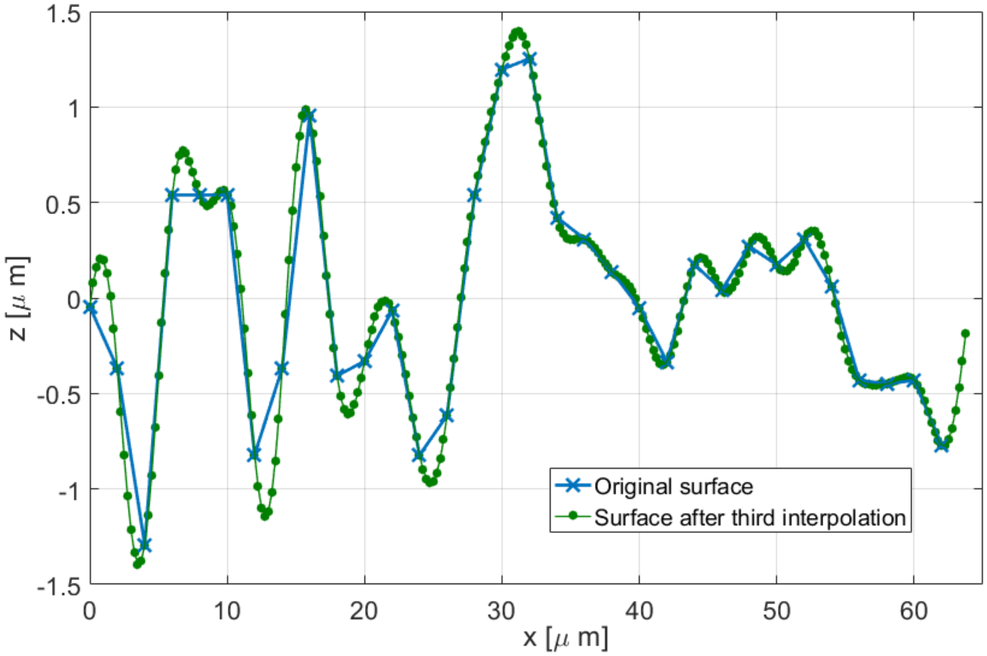

Fig. 5.7. Comparison of the original surface profile (32*32) and the three-interpolation surface profile (256*256).

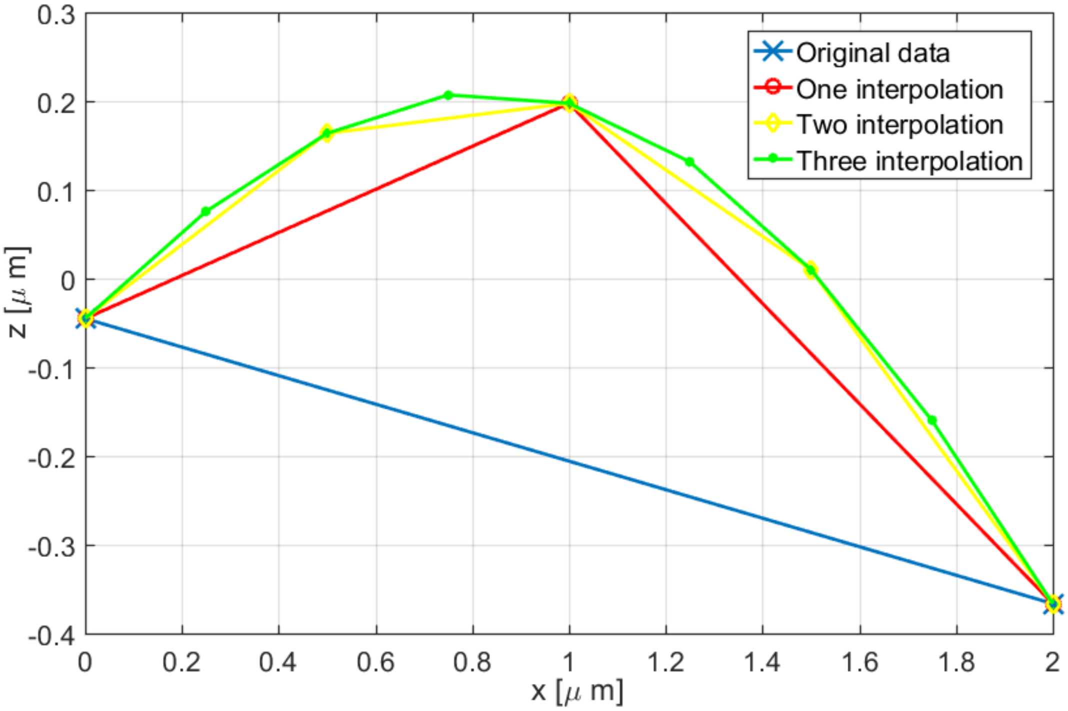

Fig. 5.8. The original surface profile for one interval and the interpolations surface profile.

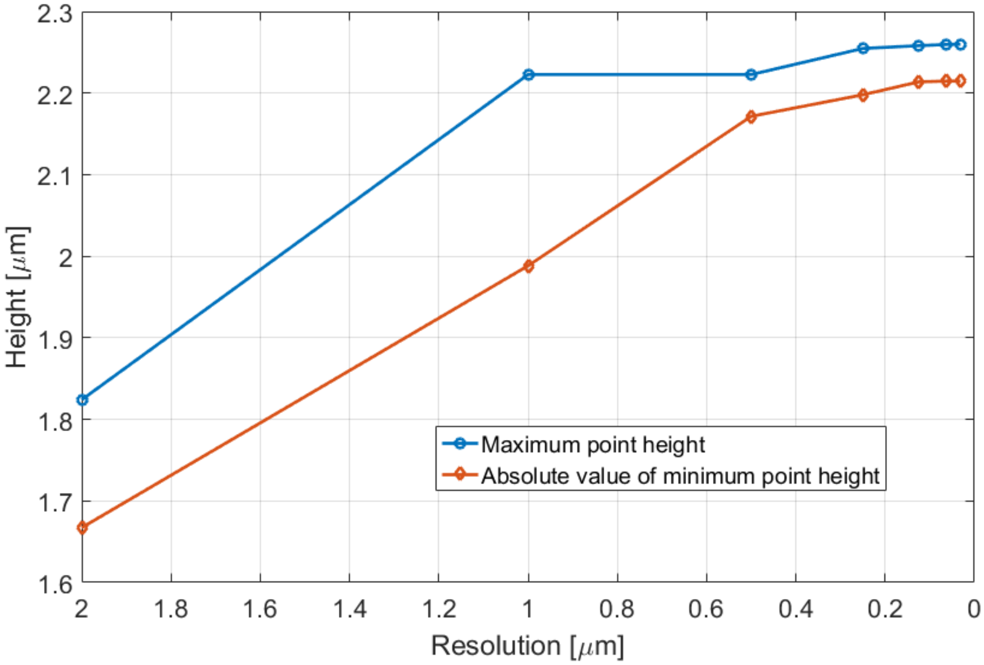

Fig. 5.9. The maximum and minimum value of the rough surface height versus resolution.

Fig. 5.9. presents the evolution of the value of the maximum height and the absolute value of the minimum height of the rough surface. As shown in Fig. 5.9, as the resolution increases, the value of maximum height of the rough surface increases until it reaches a nearly constant value. The absolute value of the minimum height increases, and then does not change significantly any more as well. When these two values reach the constant values, the surface topography will not change any more. For this case, the surface topography converges when the resolution equals to 0.125. Over the resolution considered, the maximum and minimum height changes by 23.9% and 32.8%, respectively, but the average value of surface heights does not change at all.

One of the most important parameters that describes rough surfaces is the root mean square (RMS) height, which is calculated by the following equation:

$$R_q = \sqrt{\frac{1}{N}\sum_{i=1}^{N}(z_i - \bar{z})^2} \tag{5.3}$$

where N is the total number of the measured points, z_i is the measured height at the ith point, and $\bar{z}$ is the average height of all the measured points.

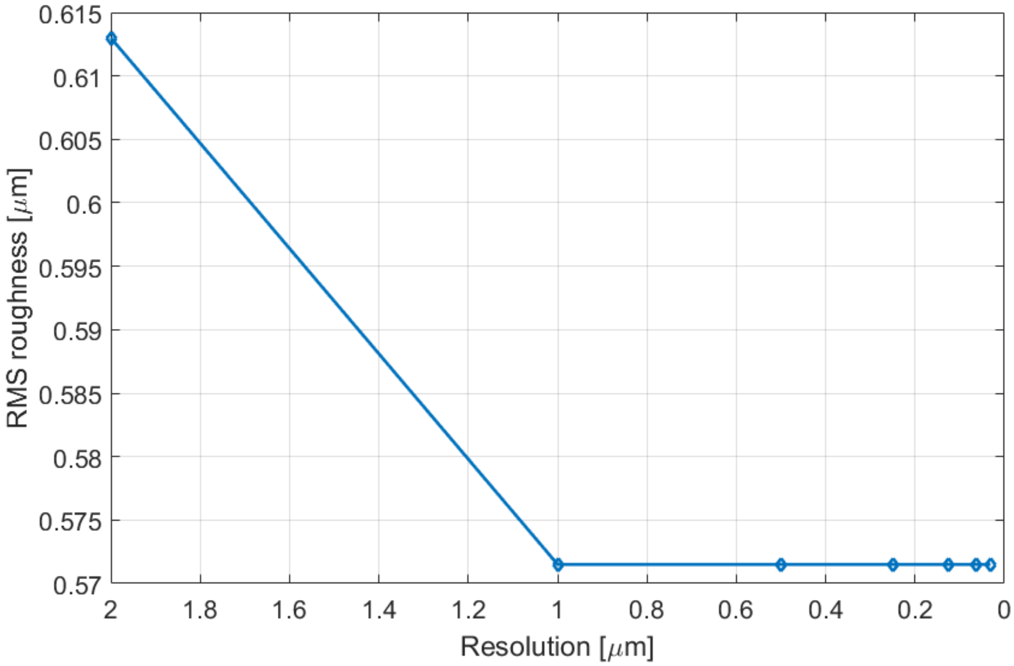

Fig. 5.10. The RMS roughness versus resolution.

The resolution is getting smaller and smaller as the number of interpolations increases. First, we analyze the effect of the resolution on the RMS roughness of the surfaces. As can be seen from Fig. 5.10, the roughness decrease becomes lower after the first interpolation, this means that the surface becomes slightly smoother, and then keeps a nearly constant roughness no matter what the resolution is. The roughness changes a relative small amount (7.26%). Note that in Figs. 5.9 and 5.10 that the values of the x-axis are reversed so that they decrease from left to right.

5.2.2. Finite Element Model

The commercial finite element ANSYS^{TM} package is used for the analysis. Finite element simulations are carried out for the three-dimensional elastic-plastic contact between a rigid flat and rough surface with the different resolutions produced from spectral interpolation. The same criterion for the initiation of slip in Chapter 4, which is characterized by loss of tangential stiffness, is used.

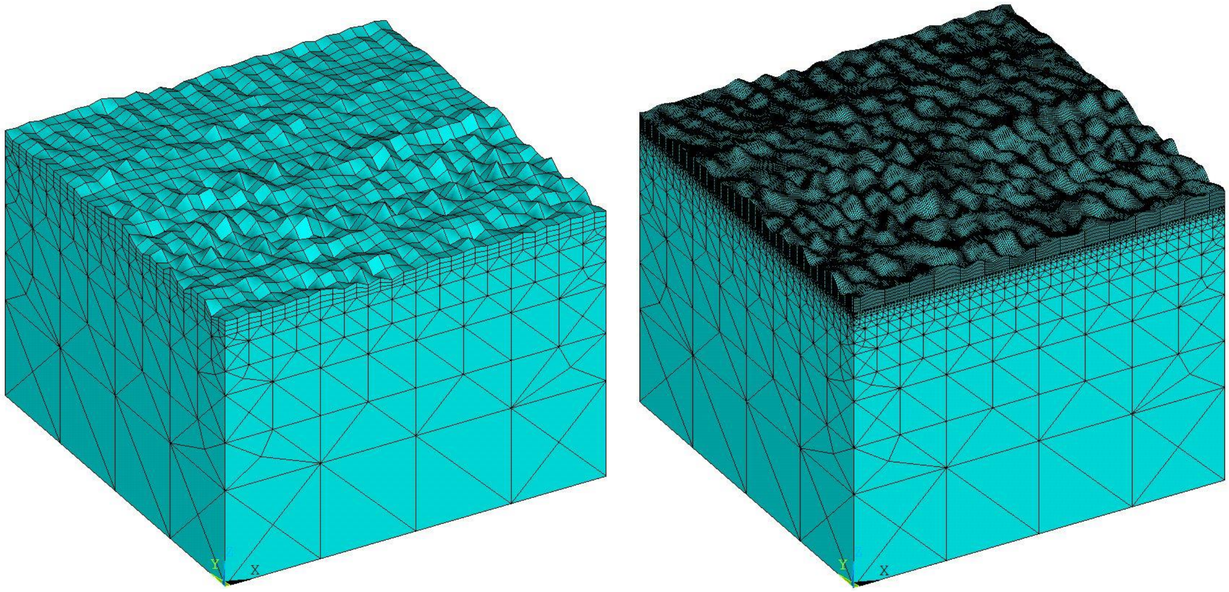

a. FEM model with Original surface **b.** FEM model with three interpolation surface

Fig. 5.11. The FEM mesh for the model with surfaces before and after interpolations.

Fig. 5.11 presents the mesh in FE model before and after interpolations. Fig. 5.11 (a) shows the mesh with original surface, some sharp peaks in the model can be seen. Fig. 5.11 (b) shows the mesh with the spectrally interpolated surface. The rough surface becomes smoother with spectral interpolation, which can reduce stress concentrations and single node contacts.

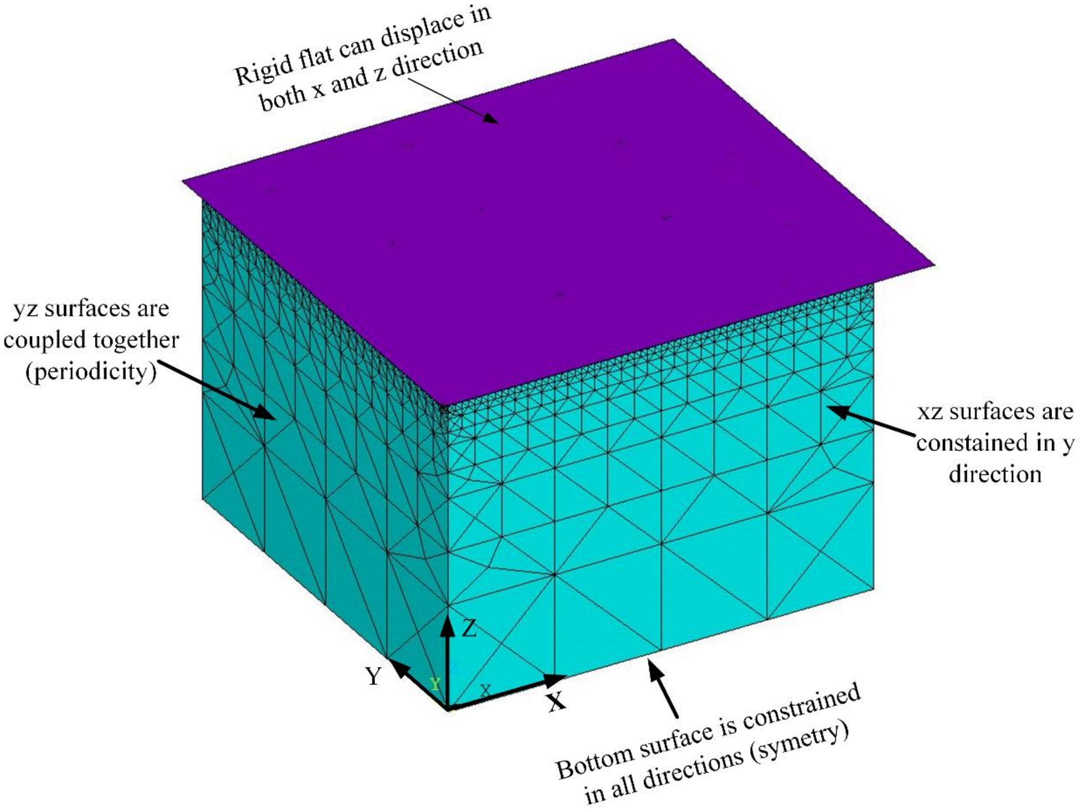

Fig. 5.12. Finite element model and boundary conditions for rough surface contact.

A three-dimensional FEM model and the boundary conditions are shown in Fig. 5.12. The contact elements use the augmented LaGrange method for enforcing contact and limiting penetration between the surfaces. The augmented LaGrange method is very similar to the pure penalty method, but it adjusts the contact force with a constant that is independent of the penetration stiffness. Conta 173 and Targe 170 are used to form the contact pair to model the interaction between the rigid flat and rough surface. In order to make the surface periodic, two lines are added to the last row and column respectively, so that the heights of coordinates of points at *z*(i, 1) and *z*(i, n+1), *z*(1, j) and z(n+1, j) have the same values, and they have the same displacements in the y direction. Hence, the contact surface is comprised with 33×33, 65×65, 129×129 and 257×257 nodes respectively, that results in 32×32, 64×64,128×128 and

256×256 elements. The moving node method is adapted to model the rough surface. In order to avoid producing badly distorted elements and negative Jacobians, several steps used to move the whole surface height from flat to rough, i.e. there are a few layers to model the rough surface heights, and it is meshed uniformly. Hexahedron elements are used to model these layers, and tetrahedra elements are used to model the base. How many layers are used depends on the resolution. The surfaces with higher resolutions and smaller sampling lengths have more layers. The Solid 185 element, which is an 8-nodes brick element, is used to model the solid substrate. The total number of elements is varied from 11,514 to 868,806 for different interpolations. Similar to the FEM model of the single sinusoidal rough surface contact (see Chapter 4), the bottom surface is fixed in all directions. The *xz* surfaces are restrained in the direction perpendicular to the plane (*y* direction), and the *yz* surfaces are coupled to enforce the periodicity. The rigid flat can displace in the *x* and *z* directions.

Computational time is an important factor that should be considered. As introduced in [90] , the largest number of elements in the FE models of rough surface contact using Ansys is 377,556, and the computation time is 105 hours in the literatures before 2010. For that case, it was only under normal loading. When the resolution is 0.25, the elements in the model is already 868,806, and we have two loading steps in the simulation, and so the computation time exceeds 20 days. If we interpolate one more time, the total elements would be around four billion, and the estimated running time would be around 3 months. Hence, the resolutions are only varied from 2.0 μm to 0.25 μm in this study. Note that 20 processor high performance cluster computer is used for the simulations. As noted above, the surface topography may converge at the resolution 0.125 μm, but this simulation is still running. However, the results have not been obtained. Only the results of these cases with the resolution 2.0 μm to 0.25 μm are used to show the trend and the effects of the resolution on the contact behavior before convergence.

5.3. Results and discussion

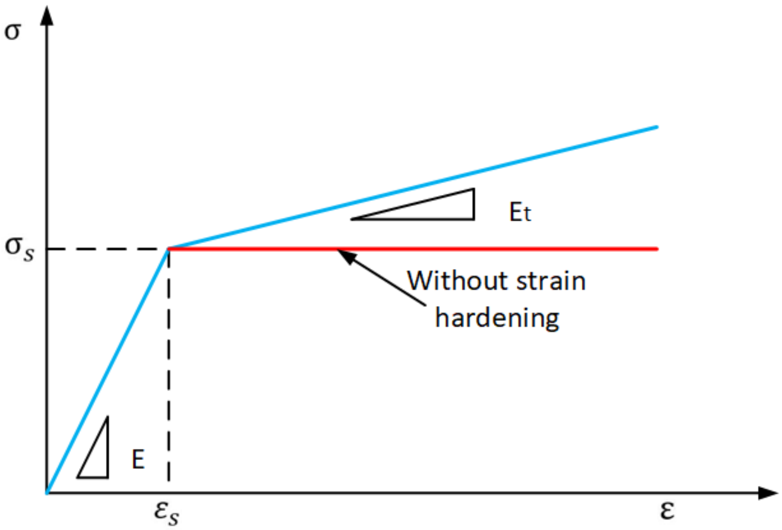

Fig. 5.13. Stress-strain diagram for material having bilinear isotropic and perfect plastic properties.

For all of the simulations, a typical steel was considered. The employed material properties are for elastic modulus, $E = 200$ GPa, Poisson's ratio, ν = 0.3, and yield strength, $S_y = 1GPa$. The material of the solid body with the rough surface are considered as elastic-plastic with linear isotropic hardening with a tangent modulus, E_t. The stress stain relationship for this material model is shown in Fig. 5.13. If the tangent modulus is equal to zero, which is without strain hardening, the material behavior is called perfect plastic. The bilinear strain hardening tangent modulus is set to 2% of the elastic modulus. Again, in the simulation, the normal load is applied firstly, and then the normal preload is held constant. The tangential displacement is next applied and increased gradually. In this study, the normal preload is 20 N, and the resulting nominal contact pressure is 4.883 MPa.

5.3.1. The Effect of Resolution under Normal Preload

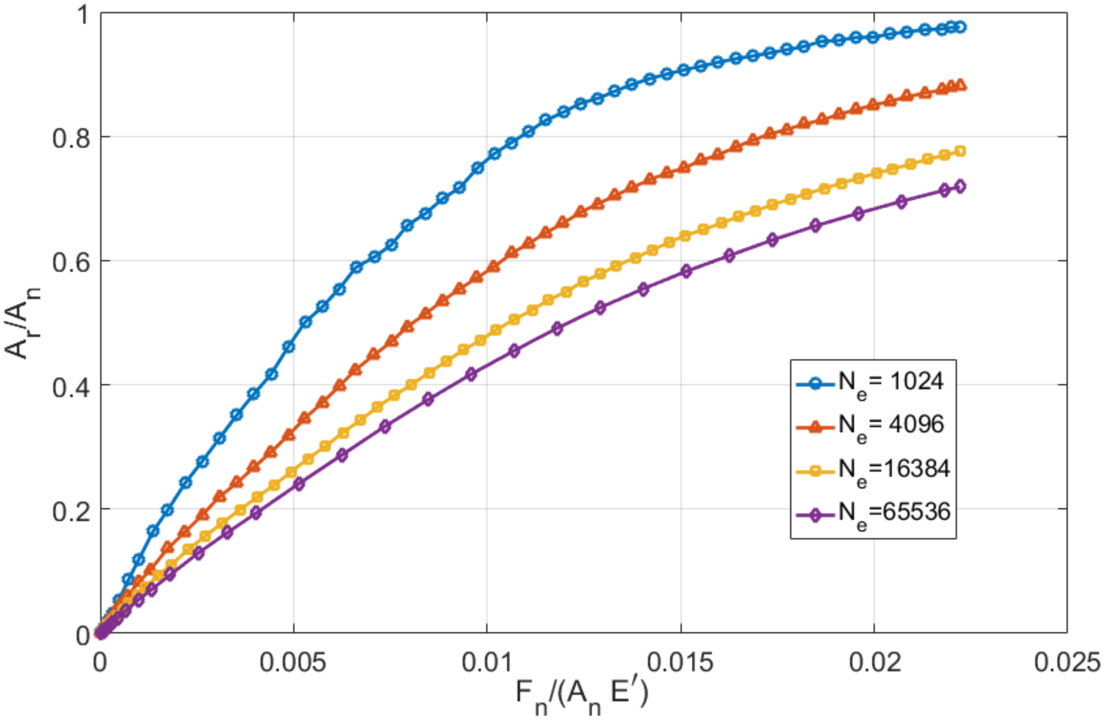

Fig. 5.14. The contact area ratio versus dimensionless normal load with different resolutions.

The resulting evolution of the FEM predicted contact area ratio for different resolutions are plotted in Fig. 5.14. Before reaching the normal preload, the contact area ratio increases as the dimensionless normal force increases. As the resolution decreases, the contact area ratio, A_r/A_n, decreases under the same load. This is probably because the spectral interpolation smooths the surfaces and reduces the stresses.

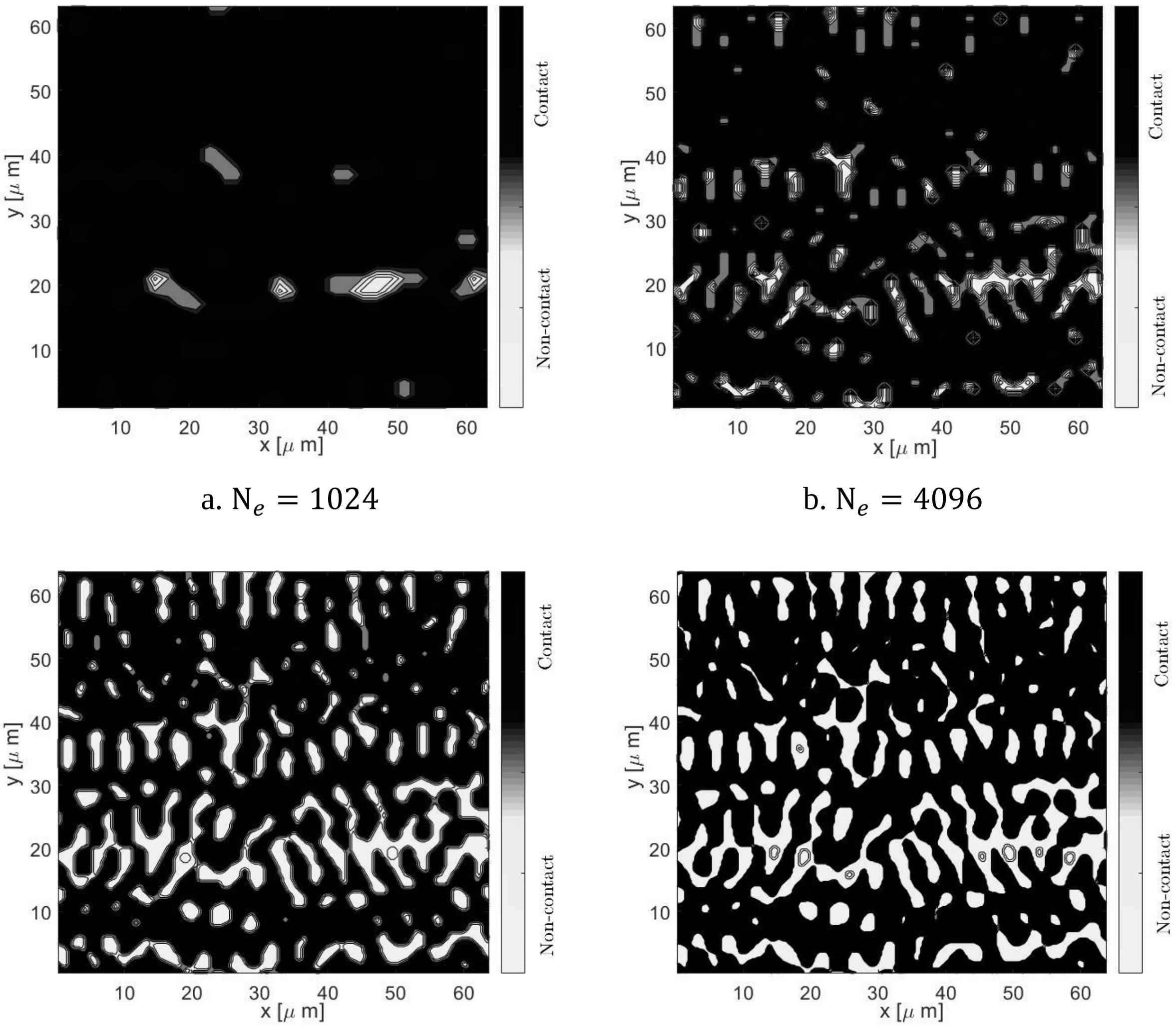

a. $N_e = 1024$ b. $N_e = 4096$

c. $N_e = 16384$ d. $N_e = 65536$

Fig. 5.15. The contact area for the surfaces with different resolution under a normal preload of 20N (contact pressure = 4.883 MPa).

The contact area under the normal preload (20N) for different resolutions are plotted in Fig. 5.15. In Fig. 5.15, the black color represents contact area, and the white color indicates the uncontacted area. It can be seen clearly from Fig. 5.15 (a-d) that as the resolution decreases, the contact area decreases. The contact area ratio as a function of resolution is plotted in Fig. 5.16. Fig. 5.16. shows the effect of resolution on the contact area ratio. It shows that as the resolution decreases, the contact area ratio decreases. This is mainly because that the Fourier interpolation can make the surface much smoother and lower the stresses (see Figs. 5.5 - 5.7).

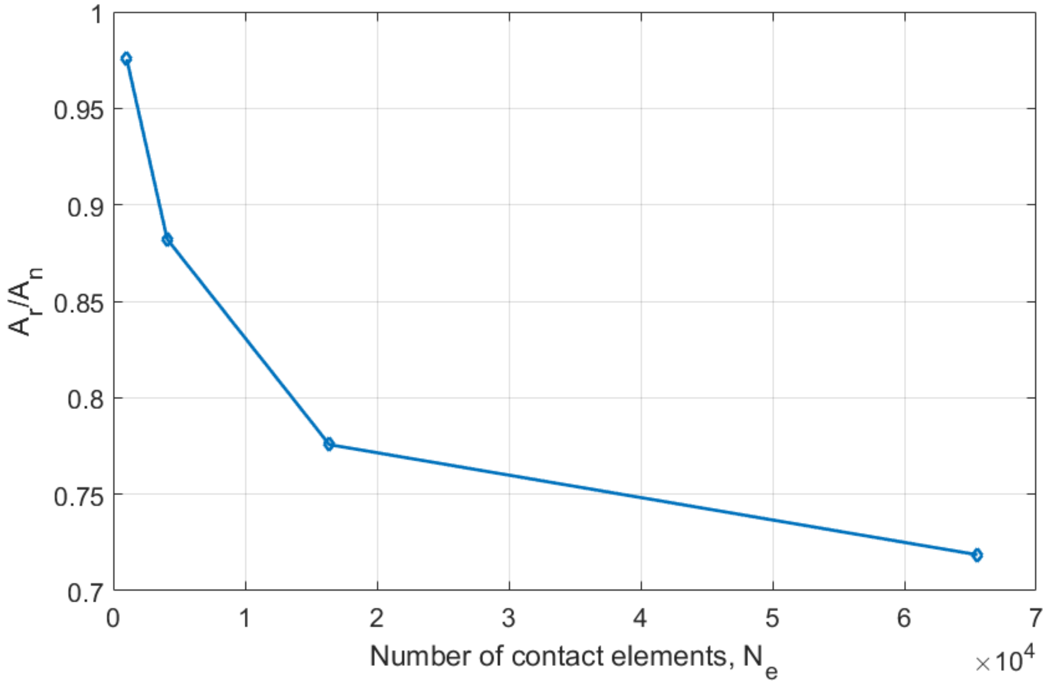

Fig. 5.16. Number of contact elements versus contact area ratio under a normal preload of 20N (contact pressure = 4.883 MPa).

The distance between the surface and rigid flat at each point is known as local surface separation, g. The average surface separation, $\bar{g}$, is given by averaging all the values of the local separation over the entire surface. In the following part, a parameter, z_{pv}, which presents the distance between the maximum peak to minimum valley is used for normalizing the displacement and average gap. The dimensionless displacement of the rigid flat, u_z/z_{pv}, the dimensionless average gap, $\bar{g}/R_q$, the dimensionless average contact pressure, p/S_y, and the dimensionless maximum von Mises stress, σ_{vm}/S_y are also investigated. Note that the value of u_z, g, and σ_{vm} are extracted from the FEM results.

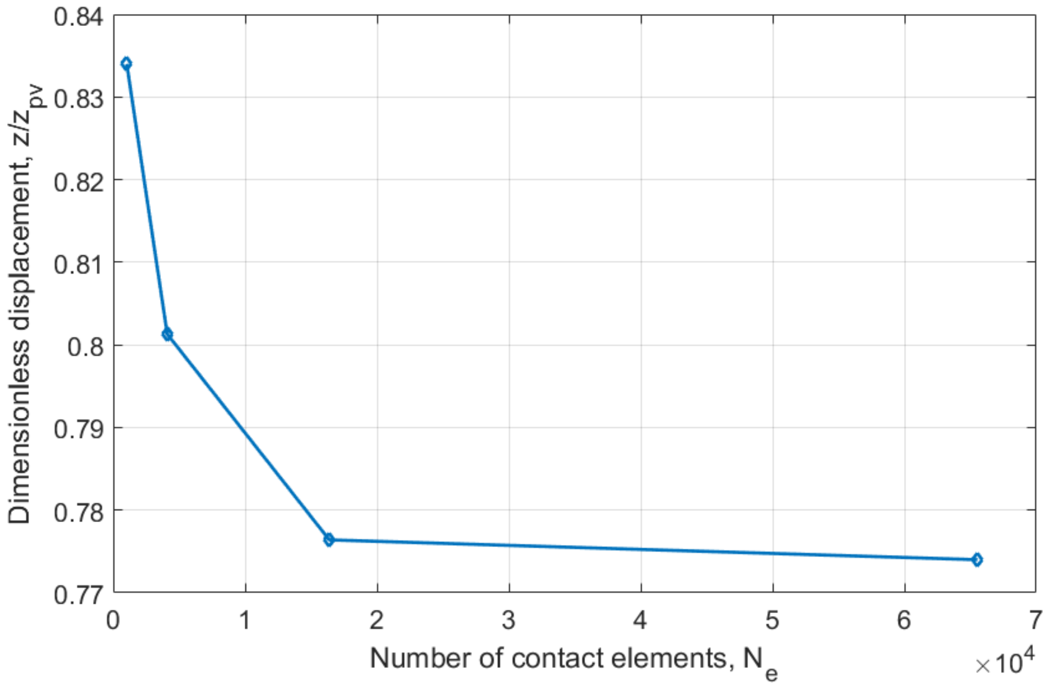

Fig. 5.17. Number of contact elements versus dimensionless displacement of the rigid flat under a normal preload of 20N (contact pressure = 4.883 MPa).

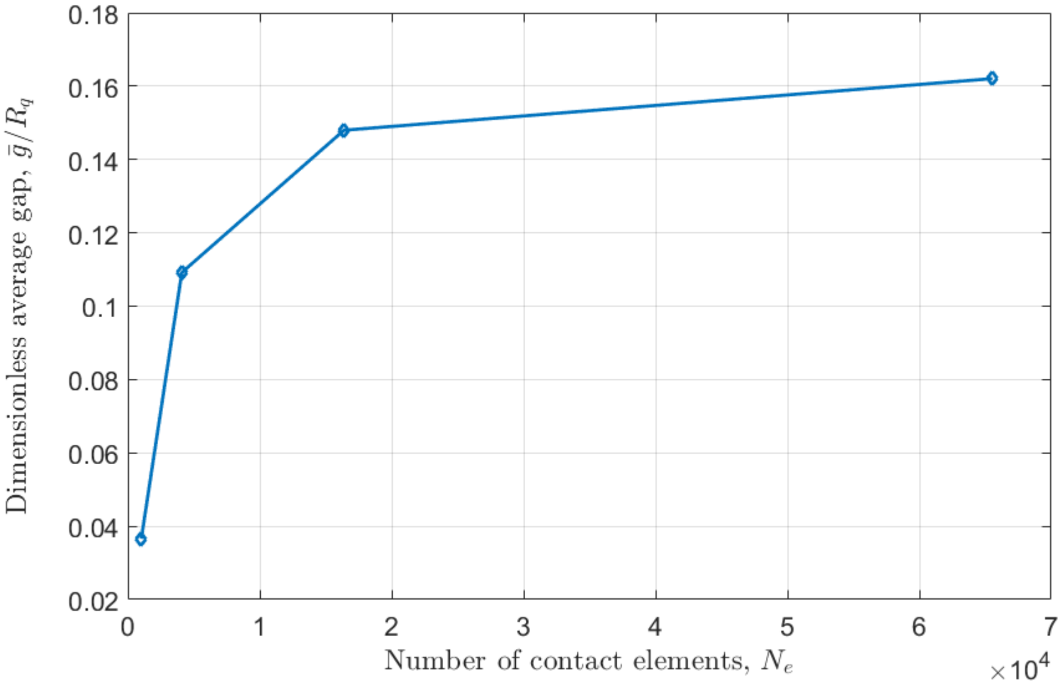

Fig. 5.18. Number of contact elements versus dimensionless average gap under a normal preload of 20N (contact pressure = 4.883 MPa).

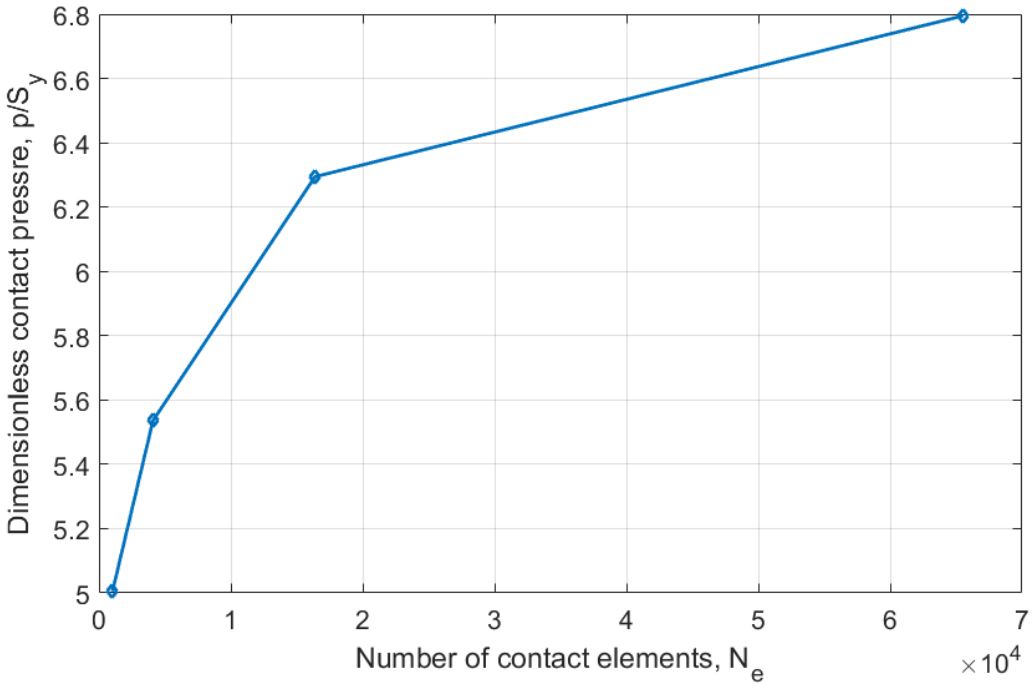

Fig. 5.19. Number of contact elements versus dimensionless average contact pressure a normal preload of 20N (contact pressure = 4.883 MPa).

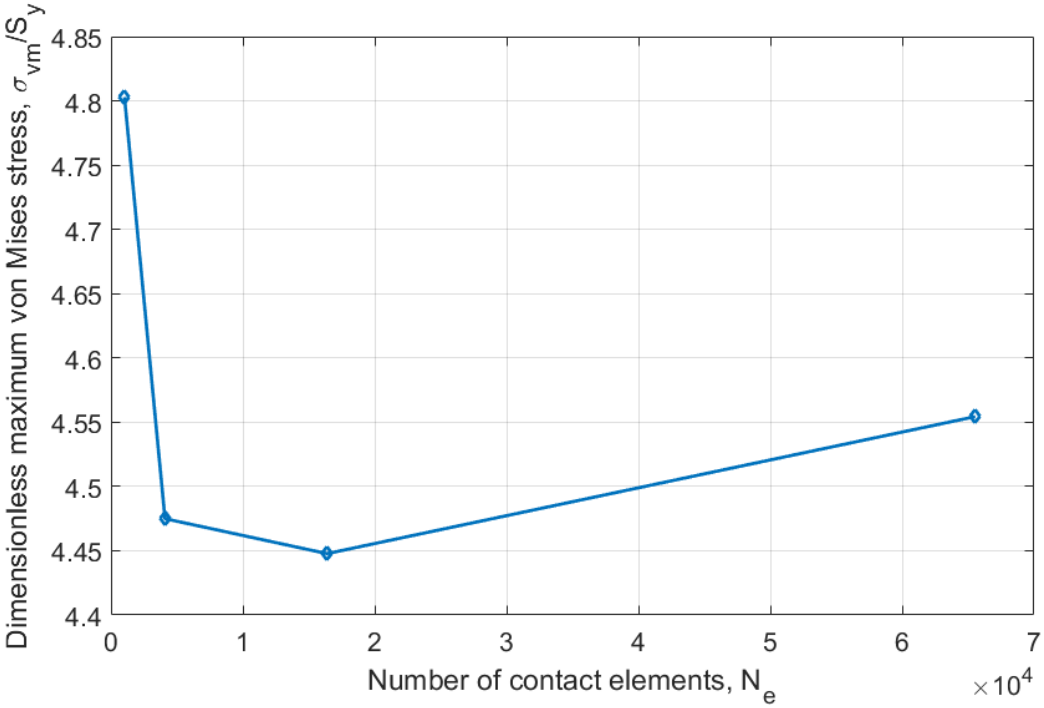

Fig. 5.20. Number of contact elements versus dimensionless maximum von Mises stress under a normal preload of 20N (contact pressure 4.883 MPa).

As can be seen from Fig. 5.17 and Fig. 5.18, that as the number of contact elements increases, the displacement of the rigid flat decreases, while the average gap increases. In Fig. 5.19, the dimensionless contact pressure increases with the increasing number of contact elements. It is also interesting that this pressure is well above the material hardness. Fig. 17 does not show a clearly trend for the maximum von Mises stress variation for the decreasing resolution, but we can see that all the interpolated surfaces have lower maximum von Mises stresses compared to the original surface. This may be because the asperities peaks are effectively smoothed by the spectral interpolation.

Table 5.1. Difference compare to the original surface with different resolutions under normal preload

Resolution(μm)	N_e	A_r/A_n	u_z/z_{pv}	$\bar{g}/R_q$	p/S_y	σ_{vm}/S_y
1	4096	9.57%	3.92%	198.5%	10.61%	6.83%
0.5	16384	20.48%	6.91%	304.5%	25.76%	7.39%
0.25	65536	26.34%	7.19%	343%	35.76%	5.17%

The differences of parameters between the interpolated surfaces with the original surface are listed in Table 5.1. From Table 5.1, the effects of resolution on the dimensionless displacement of the rigid flat and the dimensionless maximum von Mises stress turn out to be small (the differences are all under 7.39%). However, the resolution influences the dimensionless average gap significantly. This is probable because that the applied normal preload is so high that complete contact is almost reached. That results in the average gap being so small for the original surface. Then, even though the dimensionless gap changed a little, the differences would be very large in percent. Hence, the most significant effects of the resolution are on the dimensionless contact area ratio and dimensionless average contact pressure. For both of them, the difference increases as the number of contact elements increases (resolution decreases), and the decline becomes very slow. They are supposed to converge at more number of times of interpolation.

5.3.2. The Effect of Resolution at Sliding Inception

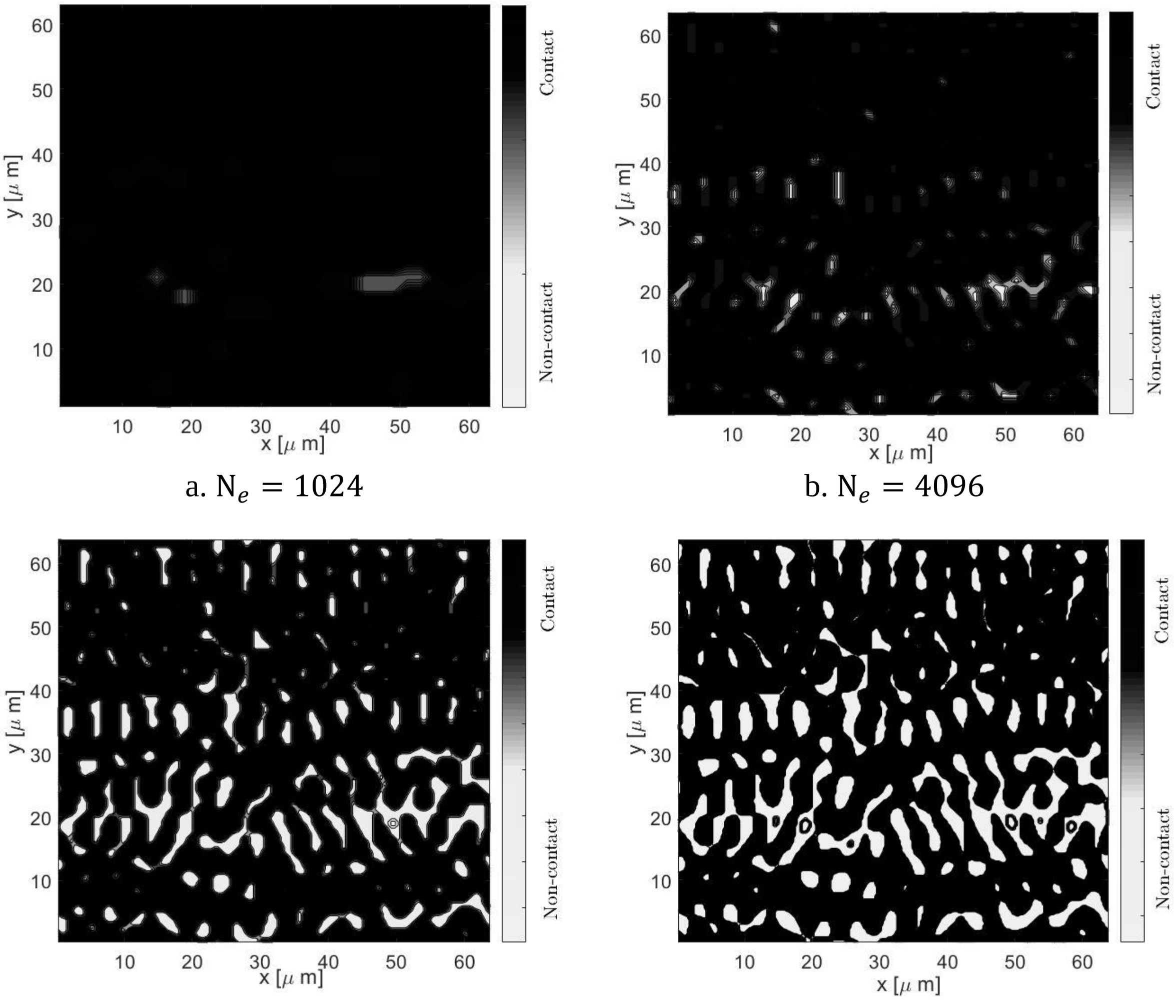

a. $\mathrm{N}_e = 1024$ b. $\mathrm{N}_e = 4096$

c. $\mathrm{N}_e = 16384$ d. $\mathrm{N}_e = 65536$

Fig. 5.21. The contact area of original and interpolation surfaces at sliding inception.

Fig. 5.21 presents the contact area with the different numbers of contact elements at the sliding inception. Similar to the case under normal preload (see Fig. 5.15), as the number of contact elements decreases, the contact area at the sliding inception decreases.

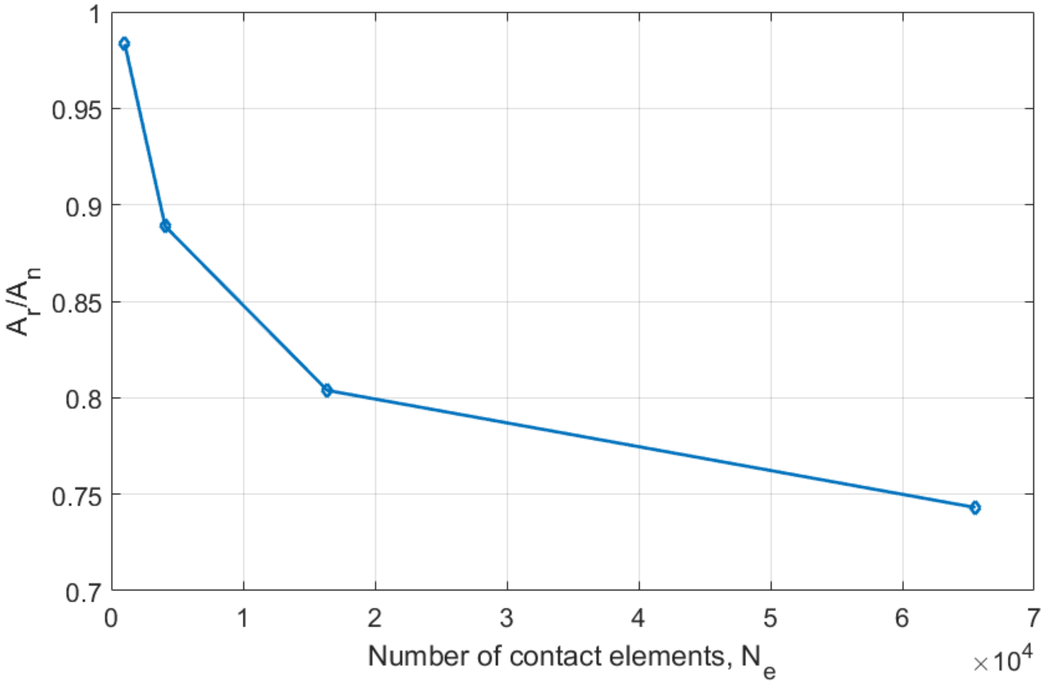

Fig. 5.22. Number of contact elements versus contact area ratio at sliding inception.

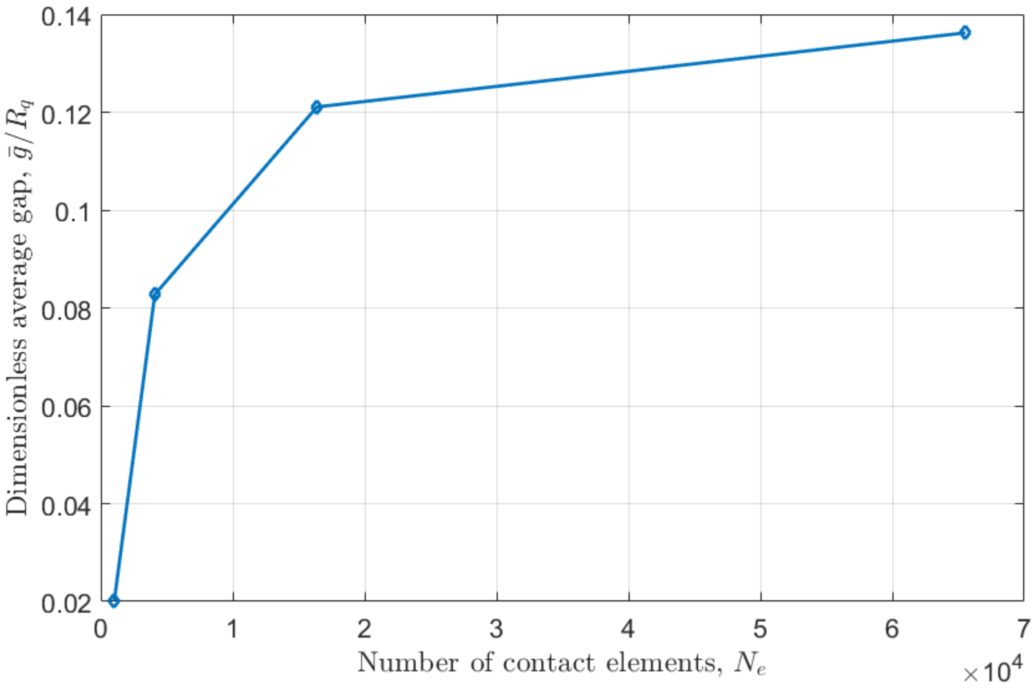

Fig. 5.23. Number of contact elements versus dimensionless displacement at sliding inception.

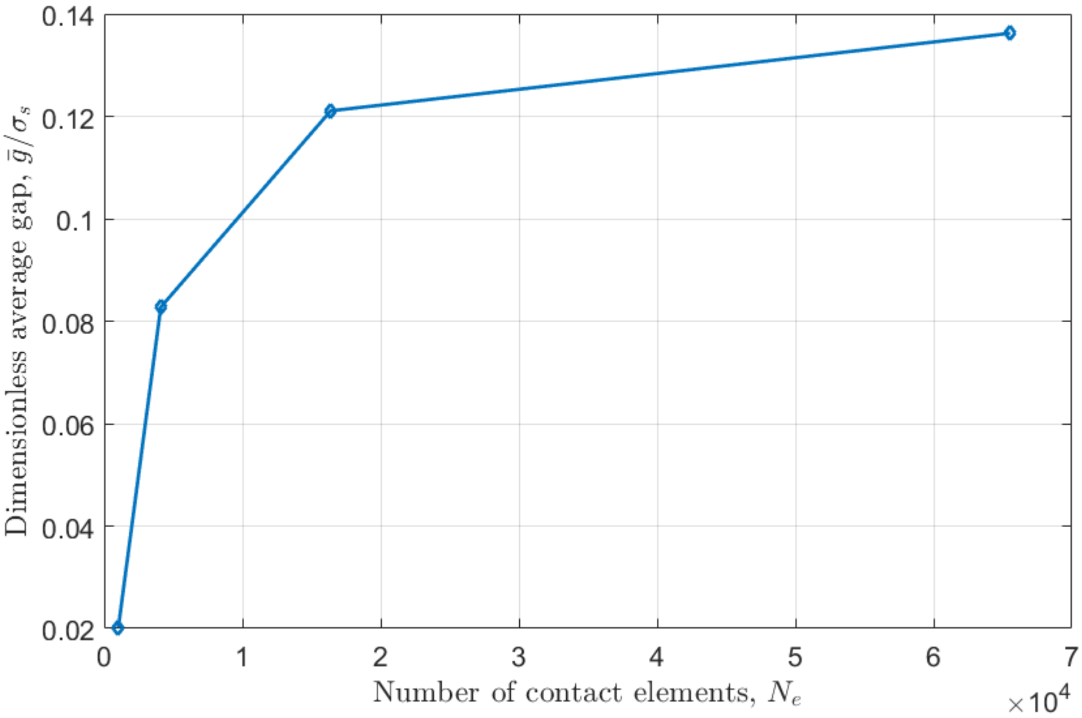

Fig. 5.24. Number of contact elements versus dimensionless average gap at sliding inception.

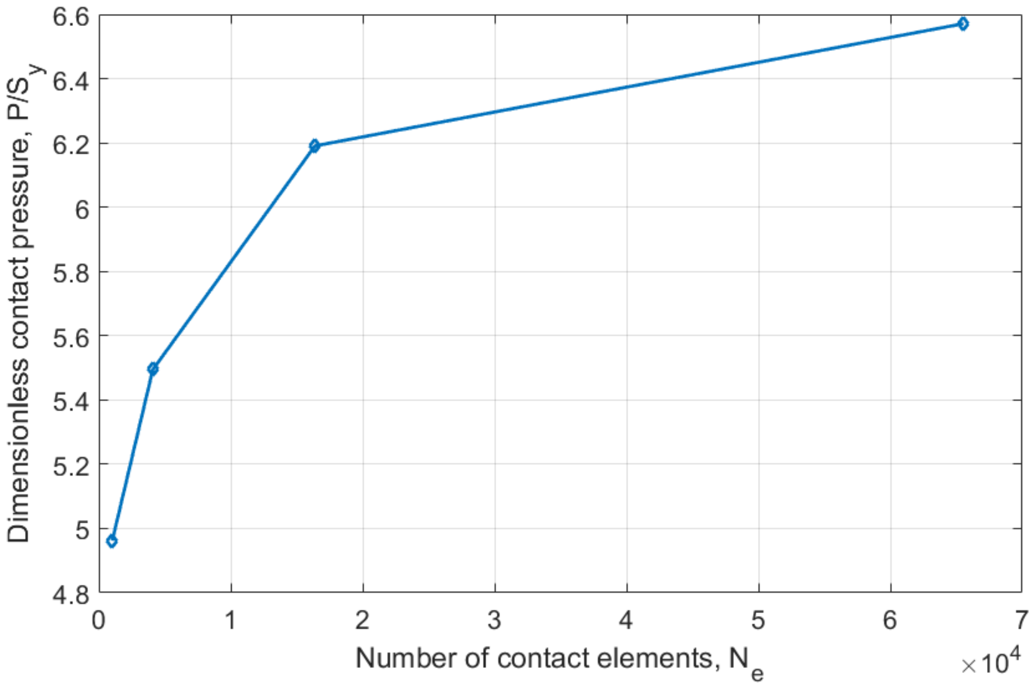

Fig. 5.25. Number of contact elements versus average contact pressure at sliding inception.

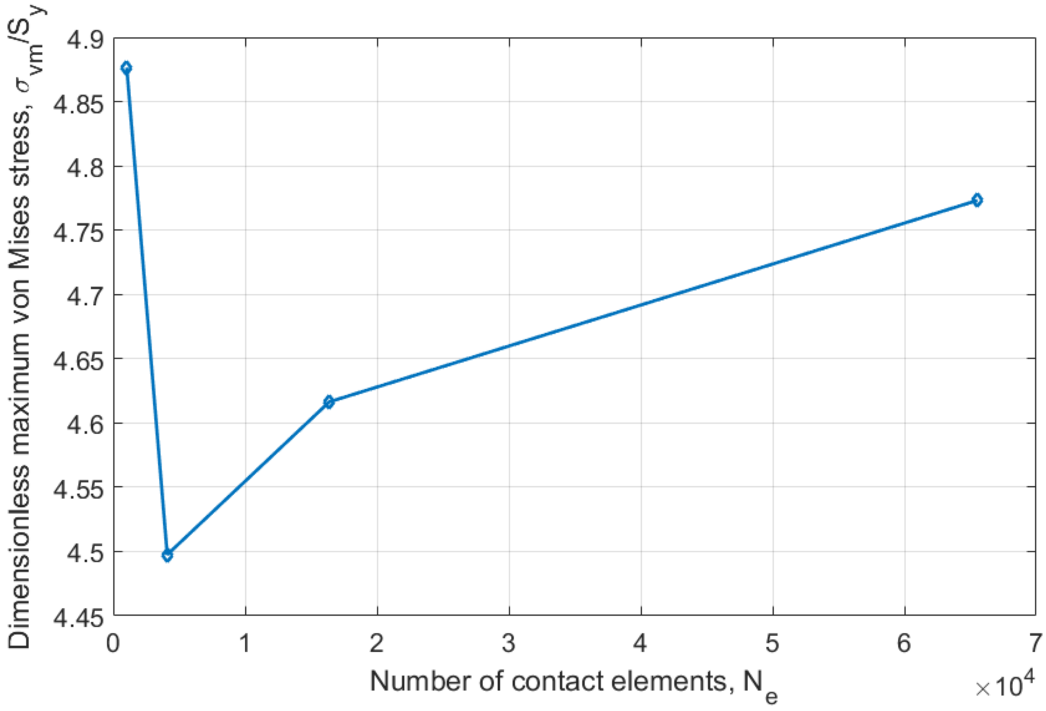

Fig. 5.26. Number of contact elements versus dimensionless maximum von Mises stress at sliding inception.

The effects of resolution on different parameters are plotted from Fig. 5.22 - 5.26. the behaviors are similar to the ones under only normal preload. Fig. 5. 22. shows the contact area ratio at sliding inception, A_s/A_n, versus resolution. The contact area ratio increases as the resolution decreases. As seen from Figs. 5.23 and 5.24, as the resolution decreases (i.e. the number of contact elements increases), the dimensionless displacement at sliding inception decreases, and the dimensionless average gap increases. Fig. 5.25. shows that the dimensionless contact pressure at sliding inception increases with decreasing resolution (i.e. increasing the number of contact elements). Fig. 5.26. shows that the dimensionless maximum von Mises stress at sliding inception becomes lower compared to the original surface. The differences of the parameters between interpolated surfaces and the original surface are listed in Table 5.2.

Table 5.2. Difference compare to the original surface with different resolutions at sliding inception

Resolution(**μm**)	N_e	A_s/A_n	u_z/z_{pv}	$\bar{g}/R_q$	p/S_y	σ_{vm}/S_y
1	4096	9.62%	4.58%	310%	10.72%	7.77%
0.5	16384	18.26%	7.92%	500%	24.75%	5.33%
0.25	65536	24.44%	8.44%	575%	32.42%	2.12%

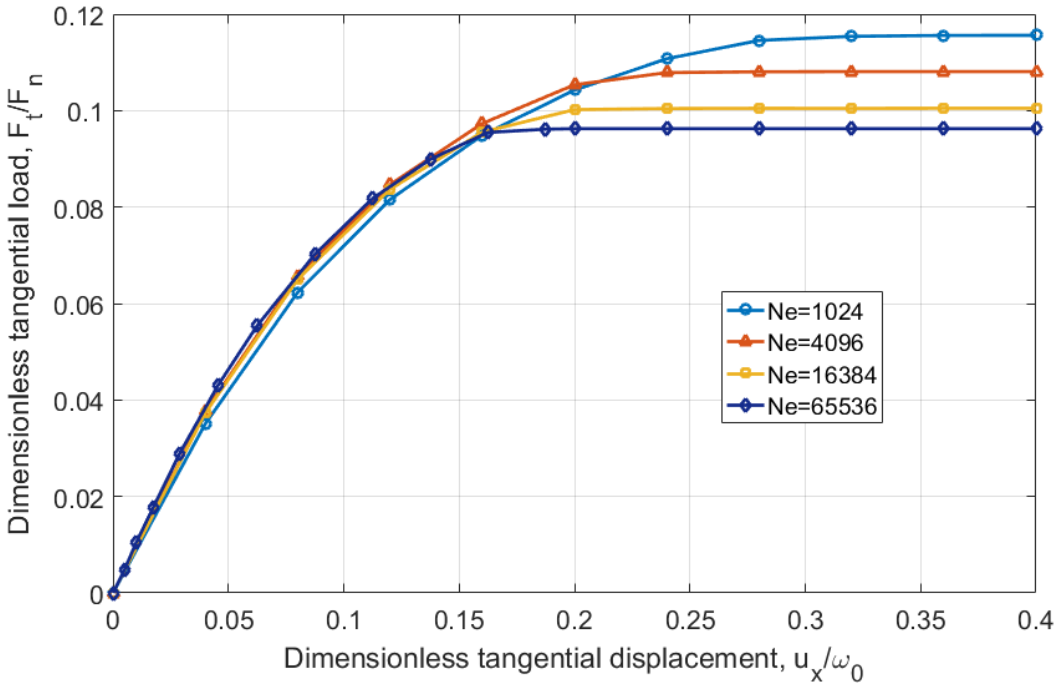

Fig. 5.27. Dimensionless tangential load versus dimensionless tangential displacement for the surfaces with various numbers of contact elements.

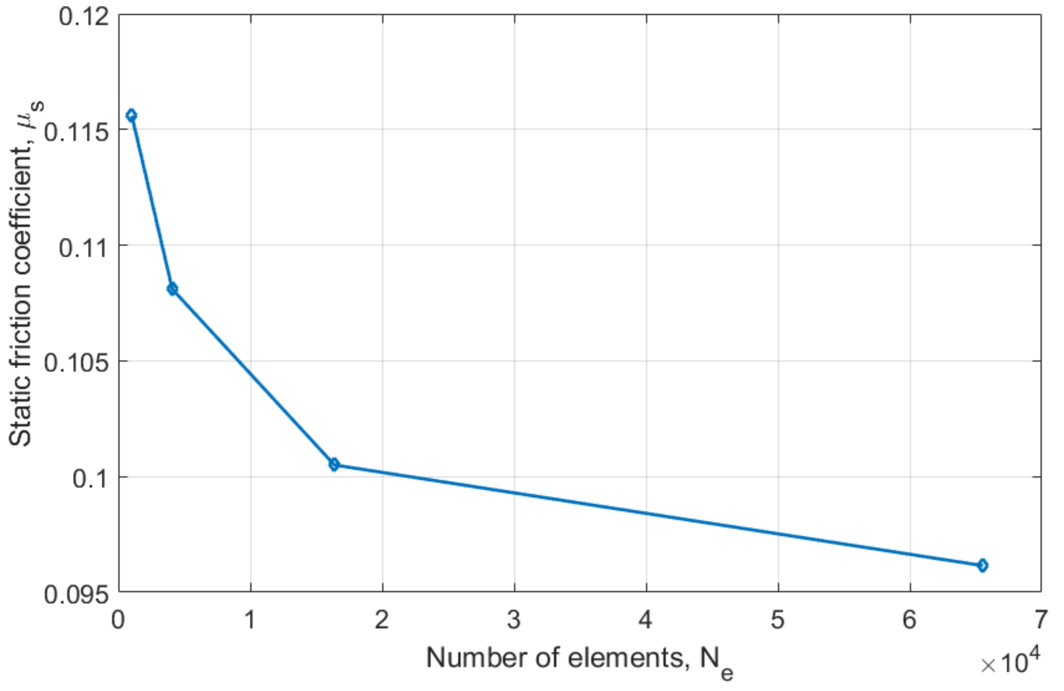

Fig. 5.28. Number of contact elements versus static friction coefficient.

Fig. 5.27 shows the dimensionless tangential force versus the dimensionless tangential displacement. At lower dimensionless tangential loads, (around 0.16), there is not too much difference between the cases with different resolutions (number of contact elements). As the tangential displacement continues to increase, the dimensionless tangential force increases a asymptotically to a constant value, and the tangential stiffness eventually approaches zero last. At that moment, the dimensionless tangential load is the static friction coefficient, μ_s . The static friction coefficients are extracted from the figure and plotted in Fig. 5.28. As can be seen from Fig. 5.28, as the resolution decreases (i.e. number of contact elements increases), the static friction coefficient decreases. Therefore, spectral interpolation and smoothing of the surfaces trends to decrease the friction.

5.3.3. The effect of tangential loading

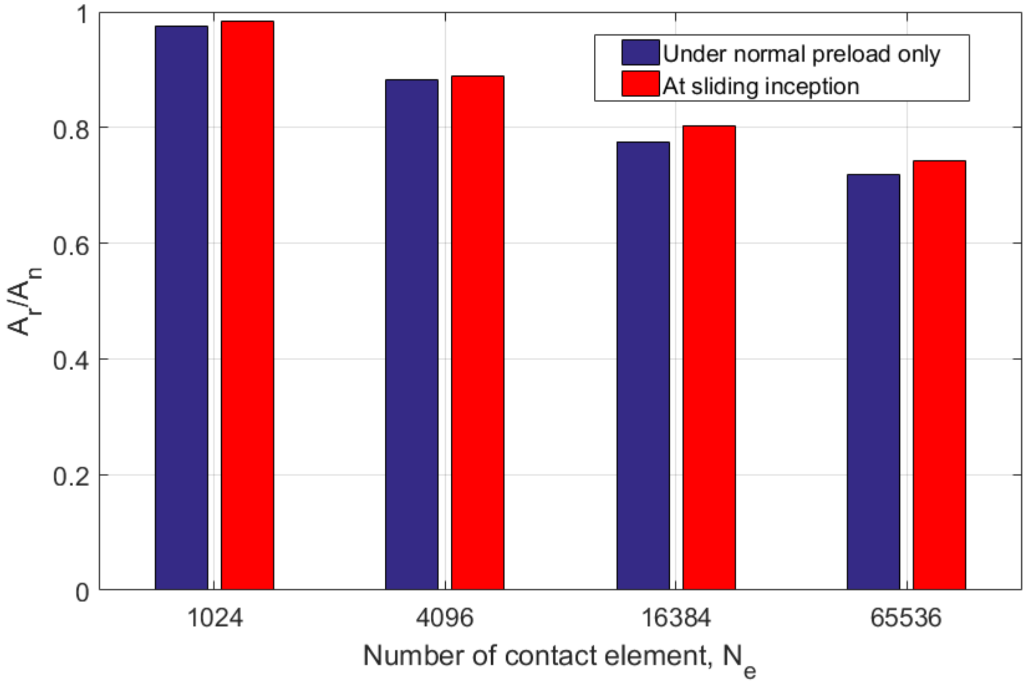

Fig. 5.29. The comparison of contact area ratio between under normal preload and at sliding inception with various numbers of contact elements.

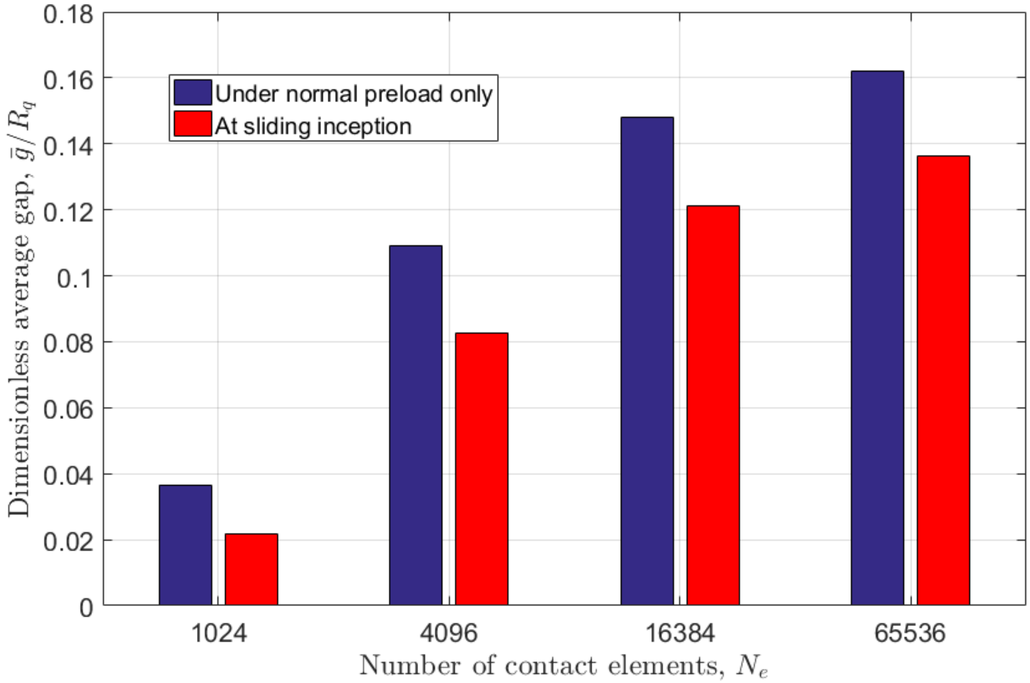

Fig. 5.30. The comparison of dimensionless displacement between under normal preload and at sliding inception with various numbers of contact elements.

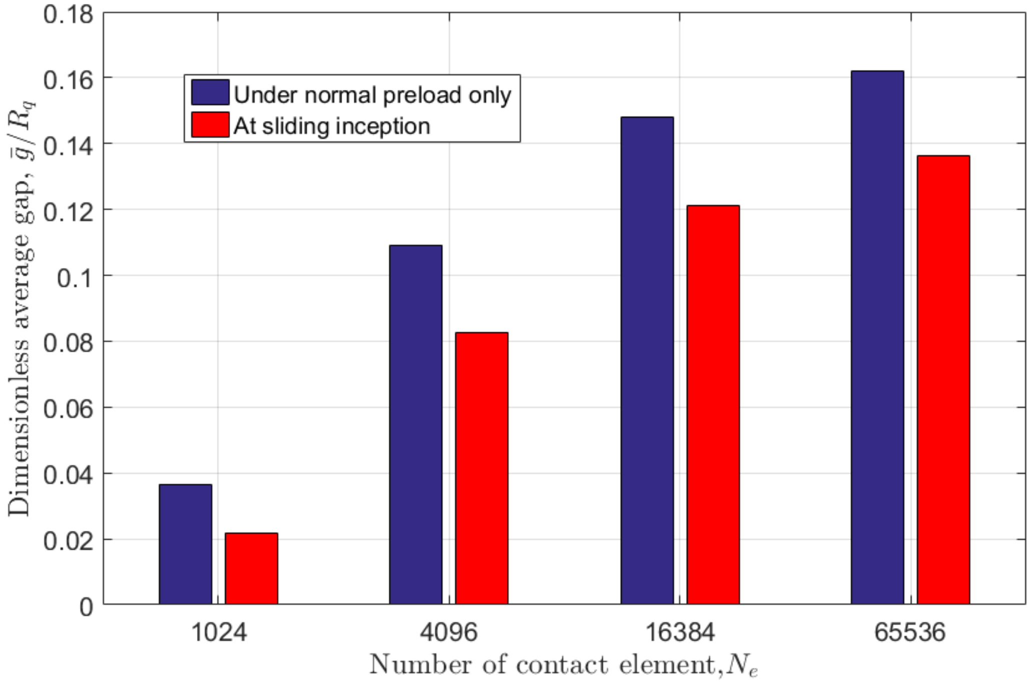

Fig. 5.31. The comparison of dimensionless average gap between under normal preload and at sliding inception with various numbers of contact elements.

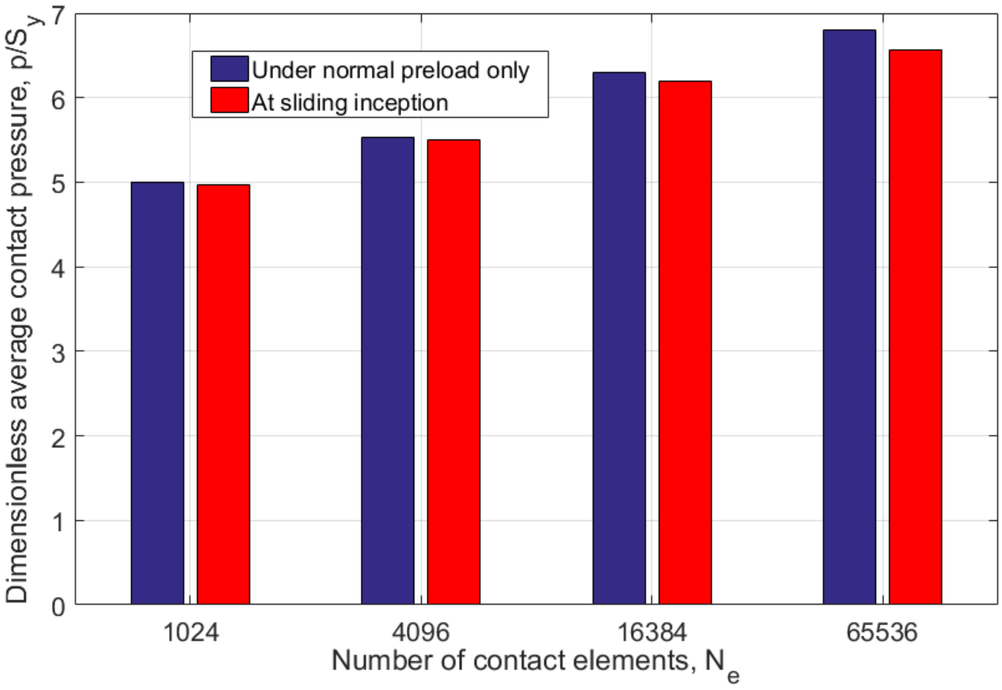

Fig. 5.32. The comparison of dimensionless contact pressure between under normal preload and at sliding inception with various numbers of contact elements.

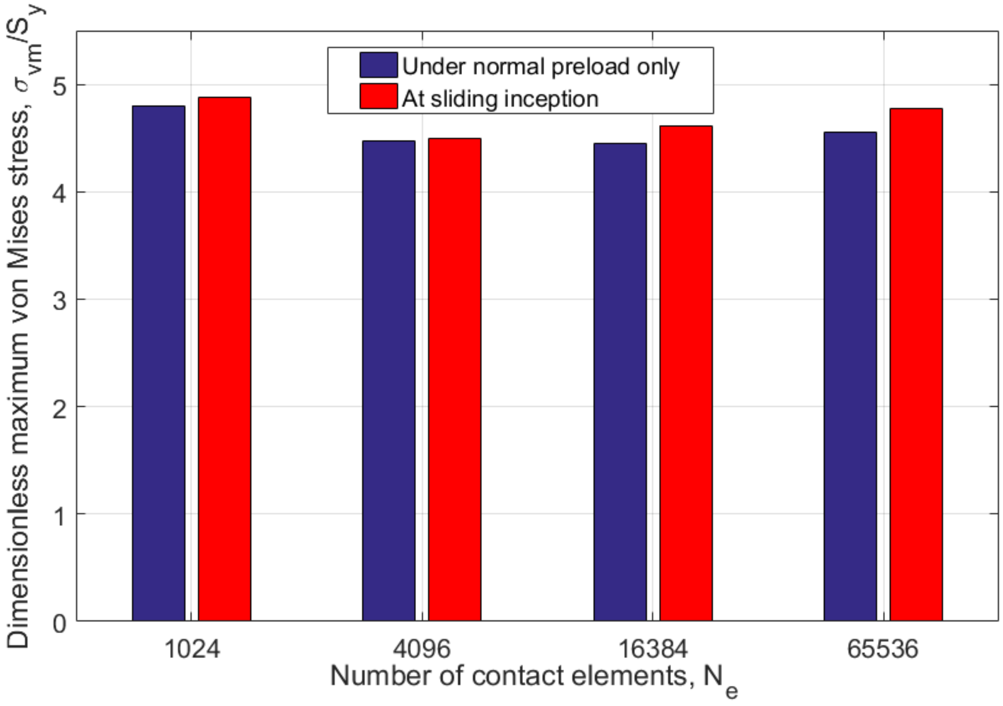

5.33. The comparison of dimensionless maximum von Mises stress between under normal preload and at sliding inception with various numbers of contact elements.

The contact parameters for both the normal preload and at sliding inception cases for different resolutions are presented in Figs. 5.29 - 5.33. As can be seen from Fig. 5.29, the contact area ratio at sliding inception are greater than its corresponding value under normal preload only for all the resolutions (Number of contact element). It can be said that the tangential load can increase the contact area. This increase is called junction growth, as we mentioned in Chapter 4. From Figs. 5.30 and 5.31, the dimensionless displacement of the rigid flat at sliding inception is greater than the value under the normal preload only, while the dimensionless average gap at sliding inception is less than the value under normal preload for each case. Therefore, the tangential load can increase the displacement and reduce the average gap. From Fig. 5.32, the dimensionless average contact pressure at the sliding inception is less than the value under normal preload only, but the difference is relatively small. The tangential force can decrease the average contact pressure, because the normal preload is fixed, and the tangential force can increase the contact area. This results in the average contact pressure decreasing. From Fig. 5.33, the maximum von Mises stress becomes larger due to the tangential force for all the cases regardless of the resolution.

5.4. Conclusion

In this chapter, the deterministic elastic-plastic contact between rough surfaces and a rigid flat under normal and tangential loading was studied by using FEM. The effect of resolution and tangential load on several contact parameters are analyzed. From the analysis, we found that: as the resolution decreases, the contact area ratio and dimensionless displacement decreases, while the dimensionless average gap and dimensionless contact pressure increases for both the normal preload and at sliding inception cases. We also found the tangential force can increase the contact area ratio, dimensionless displacement and dimensionless maximum von Mises stress, and decrease the dimensionless average gap and dimensionless contact pressure.

CHAPTER 6. ELASTIC-PLASTIC ROUGH SURFACE CONTACT UNDER COMBINED NORMAL AND TANGENTIAL LOADING

6.1. Introduction

6.1.1. Normal Loading

A number of models that attempt to solve the normal contact between rough surfaces have been developed. One of the most widely used are statistical models. In this approach, the rough surfaces are assumed to consist of *N* asperities, whose heights, z, above a mean level follow probability density function, such as the Gaussian distribution or exponential distribution. In 1966, Greenwood and Williamson [93] developed a statistical rough surface contact model, in which the surface is considered isotropic. The asperity scale contacts are assumed to have no lateral interaction between them, and only the asperities deform during the loading processing. Then, Greenwood and Tripp [94] suggested that two rough surfaces in contact can be simplified as one equivalent rough surface contacting a rigid flat. Based on their work, Chang, Etsion and Bogy [7] presented an elastic-plastic asperity model for analyzing the contact of rough surfaces, which is based on the volume conservation of an asperity during plastic deformation. After that, many researchers model elastic-plastic contact by using more advanced models, Kogut and Etsion (KE) [95] developed an elastic-plastic contact model for the rough surface based on the FEM results of a single asperity in [96]. They provided an empirical equation for the real contact area as a function of plasticity index and normal load. However, the plasticity index is limited to 8. Jackson and Green [74] extend the KE model to higher indices by considering full plastic deformation based on their single elastic-plastic asperity model [97]. In these rough surface contact models, the finite element results of a single asperity are incorporated into a statistical representation of surface roughness to analyze the elastic-plastic contact between two rough surfaces.

Archard [16] developed the first multi-scale elastic rough surfaces contact model that considered multi-scale features. The structure of the rough surfaces used in Archard's model is described as "protuberances on protuberances”. He used the concept of stacking smaller and smaller asperities in order to capture the multiscale nature of surface roughness. After Archard’s work, truncation and fractal surface characterization were used to model contact between rough surfaces by Majumdar and Bhushan [98]. Majumdar and Bhushan used the asperity wavelength and amplitude to calculate the radius of curvature of the asperities, and concluded that the real contact area has a power law relationship with the applied normal load. Later, using the same stacked asperity assumption proposed by Archard, Ciavarella et al. [17] analyzed the elastic contact between a rigid flat and a Weierstrass-Mandelbrot (W-M) fractal surfaces. Wu [99] proposed a method based on the Fast Fourier Transform (FFT) to generate three-dimensional rough surfaces. Much later, Jackson and Streator [19] proposed a contact model between rough surfaces that considered asperities using a sinusoidal geometry, and proposed a rough surface multi-scale model based on an FFT for elastic, elastic-plastic and full plastic contact. They used stacked sinusoids to model the multiple scales of roughness. Gao and Bower [20] presented a 2D multi-scale stacked contact model by including plastic deformation based on their single asperity contact model [78]. Then, considering the stacked rough surface contact model in [19] , Wilson et al. [21] analyzed the surface separation and contact resistance for elastic-plastic multi-scale contact.

However, both statistical summation and multi-scale models provide a technique to bridge length scales between asperity level and macroscale level. A more direct way is to model actual rough surfaces in a finite element framework. This is known as a deterministic model. Hence, lots of deterministic models have been developed. Most of the surfaces that were mainly considered are the following three types: a.) Gaussian random surfaces, b.) fractal surfaces and c.) real measured surfaces.

Considering generated random rough surfaces with Gaussian distributions, different aspects of contact were studied by many researchers. Peng and Bhushan [100] developed a model for the layered elastic-plastic half space in contact with another rough surface. In their work, the effects of stiffness, and thickness of the substrate and layer are studied, and optimum parameters are provided. Considering the rough surfaces with both isotropic and anisotropic Gaussian distributions, the thermomechanical contact homogenization was studied by Temizer [101].

Megalingam and Mayuram [102] analyzed the contact model between a rigid flat and a deformable rough surface, which is with a Gaussian distribution. In addition, they also compared the results between deterministic, simplified multi-asperity and modified statistical contact models. They show that these models are in good agreement. Recently, Song et al. [103] analyzed elastic-plastic contact between a rigid flat and a solid body with a rough surface by using conventional mechanism-based strain gradient plasticity (CMSGP) theory, they found that the contact pressure in the CMSGP is higher than its corresponding value according to the J_2 plasticity. They found that the highest contact pressure locates at the edge of the contact in the GMSGP model, while the highest contact pressure shifts from the edge to the center with increasing load in the J_2 model.

Fractal geometry can be used to characterize the multi-scale nature of rough surfaces. Considering elastic contact, in 2005 Ciavarella et al. [104] developed a “discrete” GW model, and took the generated fractal rough surface data into the simulation. Then, this method was used to calculate electrical contact resistance by Ciavarella et al. [105].

Some probabilistic self-affine fractal surfaces, which exhibit different scaling normal to the interface than along it, were considered by many researchers. The elastic contact between a rigid flat and a generated self-affine fractal rough surface was analyzed by Hyun et al. [106] using finite element. In their work, the real contact area, contact pressure distribution and contact morphology were analyzed. Later, Hyun et al. [107] analyzed the effect of cutoffs in the surface roughness at small and large length-scales. They found that a small-scale cutoff lowers the probability of both low and high pressures while a large-scale cutoff has little effect on the pressure distribution. Considering elastic-plastic contact, Pei et al. [108] analyzed the contact area, local contact pressure, and the subsurface deformation. Both elastic and elastic-plastic contacts with different fractal dimensions and fractal roughness parameters were studied by Sahoo and Ghosh [109] again using finite element. The effect of strain hardening on the contact behaviors was also studied by Sahoo and Ghosh.

Some researchers used input data for simulations directly from the real measured rough surfaces into the FE model. Kwon et al. [89] examined the effect of surface smoothing and mesh density for real surfaces, which were measured from a standard micro comparator. They found that the mesh density has a significant effect on the maximum contact pressure and maximum equivalent stress under low loads, and that the smoothing has no significant for all the parameters.

Considering a CrN coating surface, the effect of surface roughness on the indentation results on the nanoindentation was studied by Walter and Mitterer [110]. They found that the roughness evaluated elastic modulus is underestimated due to roughness. Thompson [90] discussed some techniques and considerations associated with the incorporation of measured surfaces in FE models. Yastrebov et al. [111] analyzed elastic-plastic contact between deformable rough surfaces and a rigid flat by using a reduced model and an FE model. Poulios and Klit [112] carried out a few simulations of rough surfaces in contact, in which both generated Gaussian distribution and real rough surfaces were considered. They analyzed the contact pressure and real contact area and compared the results with GW contact model.

6.1.2. Combined Normal and Tangential Loading

The contact between rough surfaces under combined normal and tangential loading has been investigated by many researchers. In 1988, based on the principles of Tabor and Bowden[5], Chang, Etsion, and Bogy (CEB) [7] created one of the first elastic-plastic asperity contact models and included it in a statistical model of rough surface contact (Greenwood and Williamson [93]). They found the effect of adhesion on the maximum tangential load is significant. They used a statistical representation of surface roughness. The surfaces are modeled by a collection of spherical asperities with a Gaussian height distribution, for which the asperity height probability density, $\phi(z)$, is given by:

$$\phi(z) = \frac{1}{\sqrt{2\pi}\sigma_s} exp\left[-0.5\left(\frac{z}{\sigma_s}\right)^2\right] \tag{6.1}$$

where σ_s is the standard derivation on the asperity heights.

In their model, the inception of slip occurred at the first yielding (also yield inception) of the surface in the contact (considering shear and normal load). Hence, the maximum tangential force that all the contacting asperities can support was assumed to be the static friction of the contacting rough surfaces, and it can be calculated by the von Mises criterion. The static friction coefficient is given in the form:

$$\mu_s = \frac{(F_t)_{max}}{F_{ext}} = \frac{(F_t)_{max}}{F_n - F_s} \tag{6.2}$$

where $(F_t)_{max}$ is the tangential force needed to shear the junctions, F_n is the normal force, and F_s is the adhesion force.

Based on the analysis of metallic surfaces, they found that the smooth surfaces and the harder material can support more shear force, while in contrast the static friction coefficient decreases as both the plasticity index and the dimensionless external force increase. The effect of small normal loads on the static friction coefficient was experimentally investigated, and then found that the static friction coefficient decreases as the normal load increases [81].

The FEM results of a single asperity contact can be incorporated into a statistical model to represent the rough surfaces in the elastic-plastic or fully plastic regimes. Several models to predict the static friction for rough surfaces in contact were developed. Kogut and Etsion (KE) [95] presents a model that incorporates the results of finite element results in [8] into a statistical representation of surface roughness. They suggested that the CEB failure criterion used in [7] underestimated the tangential force needed to shear the junctions, because the elastic region surrounded the single plastic spot can support additional tangential load. They analyzed the effects of the tangential force, nominal contact area, plasticity index,Ψ, and adhesion parameter, θ, on the static friction coefficient. Much later, Cohen et al. analyzed the static friction coefficient [13] and junction growth [14] under the full stick condition. They incorporated the finite element results [9] in a statistical representation of surface roughness to predict the statistic friction between rough surfaces. The dimensionless real contact area in Cohen et al. [13] is given by:

$$A_0^* = \frac{A_0}{A_n} = \left(0.36 + \frac{0.41}{\psi}\right)(F_n^*)^{[0.97 - 0.1\,\exp(-\psi^{1.5})]} \tag{6.3}$$

where F_n^* is the dimensionless normal load, and given by:

$$F_n^* = \frac{F_n}{A_n S_y} \tag{6.4}$$

By using two of the same governing equations in the GW model, the normal load F_n and maximum friction force, $(F_t)_{max}$, can be expressed as:

$$F_n = \eta A_n \int_{d^*}^{\infty} \bar{F}(\omega^*)\, \phi^*(z^*) dz^* \tag{6.5}$$

$$(F_t)_{max} = \eta A_n \int_{d^*}^{\infty} (\bar{F_t})_{max}(\omega^*)\, \phi^*(z^*) dz^* \tag{6.6}$$

By solving Eq. (6.6) and finding a best fit curve to the results, the dimensionless static friction $(F_t)^*_{max}$ is given by:

$$(F_t)^*_{max} = \left(0.26 + \frac{0.43}{\psi}\right) (F_n^*)^{(0.0095\psi+0.91)} \tag{6.7}$$

Hence, the static friction coefficient is given by:

$$\mu_s = \frac{(F_t)^*_{max}}{F_n^*} = \left(0.26 + \frac{0.43}{\psi}\right) (F_n^*)^{(0.0095\psi-0.09)} \tag{6.8}$$

where the plasticity index, ψ, is given by:

$$\psi = \frac{2E'}{\pi C S_y} \sqrt{\frac{\sigma_s}{R}} \tag{6.9}$$

where σ_s is the standard deviation of the asperity heights, and given by McCool as

$$\sigma_s = \left(1 - \frac{0.8968}{\alpha}\right)^{0.5} m_0^{0.5} \tag{6.10}$$

where α is the bandwidth parameter:

$$\alpha = \frac{m_0 m_4}{m_2^2} \tag{6.11}$$

The spectral moments m_0, m_2, and m_4 are the variance of heights, mean square slope, and the mean square curvature, respectively. They are all given by McCool [113] as

$$m_0 = \frac{1}{N}\sum_{n=1}^{N}[z(x)]_n^2 \tag{6.12}$$

$$m_2 = \frac{1}{N}\sum_{n=1}^{N}\left(\frac{dz}{dx}\right)_n^2 \tag{6.13}$$

$$m_4 = \frac{1}{N}\sum_{n=1}^{N}\left(\frac{d^2z}{dx^2}\right)_n^2 \tag{6.14}$$

The asperity height standard deviation then can be given as

$$R = 0.375\ \left(\frac{\pi}{m_4}\right)^{0.5} \tag{6.15}$$

However, the plasticity index is also dependent on multi-scales of roughness [92]. Jackson and Green [114] proposed an alternative formulation based on the multiscale rough surface contact method:

$$\psi = \frac{B_{max}}{B_c} \tag{6.16}$$

However, the theoretical equation for static friction in Cohen et al. [13] is not valid for plasticity indices above 8. Li, Etsion, and Talke [15] extended the model to higher plasticity indices by incorporating the FEM results that considering the large (full plasticity) deformation of Jackson and Green [97]. The empirical expressions of plasticity values in the range of $0 < \psi \leq 32$, were derived [15].

The dimensionless contact area under normal preload only is given by the curve fit equation [15]

$$A_0^* = \frac{A_0}{A_n} = [0.47 + 0.57\exp(-1.2\psi^{0.93})](F_n^*)^{[1-0.27\exp(-1.43\psi^{0.41})]} \tag{6.17}$$

and the dimensionless static friction $(F_t)_{max}^*$ is given by [15]:

$$(F_t)_{max}^* = [0.26 + 0.32\exp(-0.34\psi^{1.19})](F_n^*)^{[1-\exp(-1.9\psi^{0.4})]} \tag{6.18}$$

Hence, the static friction coefficient is given by [15]:

$$\mu_s = \frac{(F_t)^*_{max}}{F^*_n} = [0.26 + 0.32\exp(-0.34\psi^{1.19})](F^*_n)^{[-\exp(-1.9\psi^{0.4})]} \tag{6.19}$$

Several experimental studies were performed by many researchers. The effects of skewness and kurtosis on the original CEB statistical static friction model [7]was investigated by Tayebi and Polycarpou [115]. In 2007, Lee and Polycarpou [116] sought to verify the statistical based static friction models by using a precision experimental apparatus. They made comparisons to the measurements using the static friction model derived by Kogut and Etsion [4], which also includes the effects of adhesion. Recently, Lee et al. [117] also examined the effect of non-Gaussian or asymmetric asperity height distributions on the statistical static friction models and compared the predictions to experimental measurements. They found that the model developed by Cohen et al. [13] predicts higher friction coefficients, and the model provided by Kogut and Etsion [4] with the Pearson distribution has a good agreement with the experimental results. Later, Ibrahim-Dickey et al. [118] used an experimental method to measure the static friction between tin surfaces. The experimental results have a reasonable agreement with the theoretical model given by Li et al. [15].

6.2. Surface Modeling Approach

6.2.1. Real measured surfaces

As shown in Fig. 5.2, the surfaces of 2L, 8L, and 32G are adopted for the simulations. In this study, we used a 128 by 128 grid of measured surface data to model the rough surfaces. The RMS and plasticity index values for these surfaces are listed in Table 6.1. m_{2x}, m_{4x}, R_x, σ_{sx}, ψ_x are the parameters for each line profile in the x direction, and m_{2y}, m_{4y}, R_y, σ_{sy}, ψ_y are the parameters for each line profile in the y direction. Smoother surfaces have smaller plasticity indices, and the rougher surfaces have large plasticity indices. However, the plasticity index of existing models is limited to 32, and the only surface available in that range in the comparator is the 2L surface. The surface 2L data is used in this chapter, and the other 2 surfaces (8L, 32G) are investigated in the next chapter. The parameters of surface 2L are listed in Table 6.1. The three-dimensional rendering and contour are plotted in Figs. 6.1- 6.2, respectively.

Table 6.1. Numerical values of parameters for Eqs. (6.9) - (6.15)

Parameters	Unit	2L	8L	32G
R_q	m	2.04e-7	5.58e-7	1.126e-6
R_{qx}	m	2.027e-7	5.493e-7	8.901e-7
R_{qy}	m	1.654e-7	5.22e-7	1.117e-6
m_0	m^2	4.161e-14	3.115e-13	1.268e-12
m_2	1	0.055	0.435	1.6
m_4	m^{-2}	1.639e11	1.205e12	5.271e12
R	m	1.642e-06	6.055e-7	2.895e-7
σ_s	m	1.580e-07	4.132e-7	9.12e-7
ψ_x	1	25.174	71.563	146.245
ψ_y	1	28.05	65.998	152.347
ψ	1	26.612	68.781	149.296

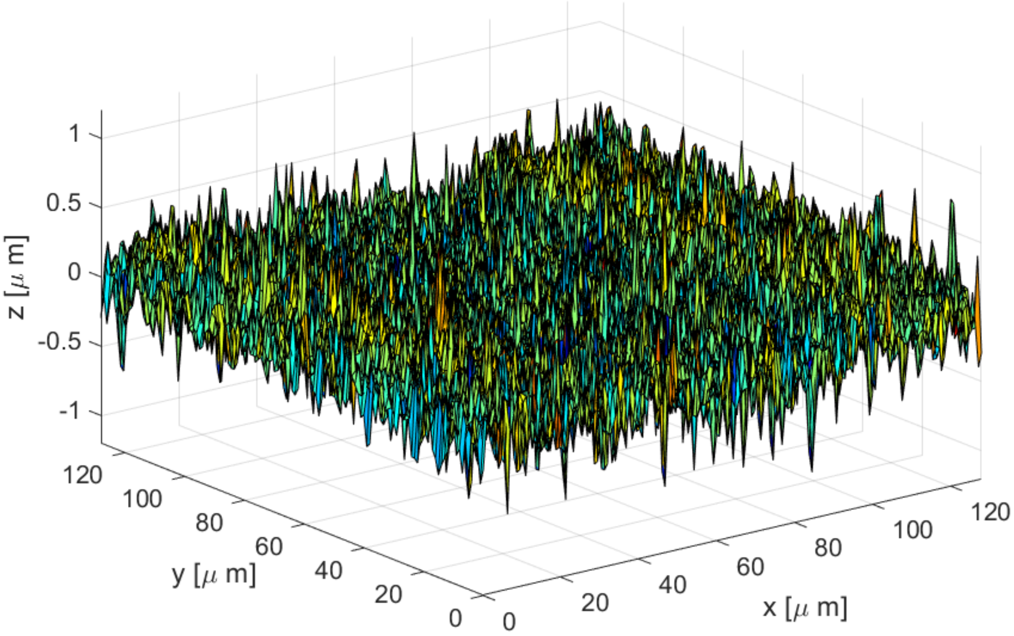

Fig. 6.1. The three-dimensional plot of the surface 2L.

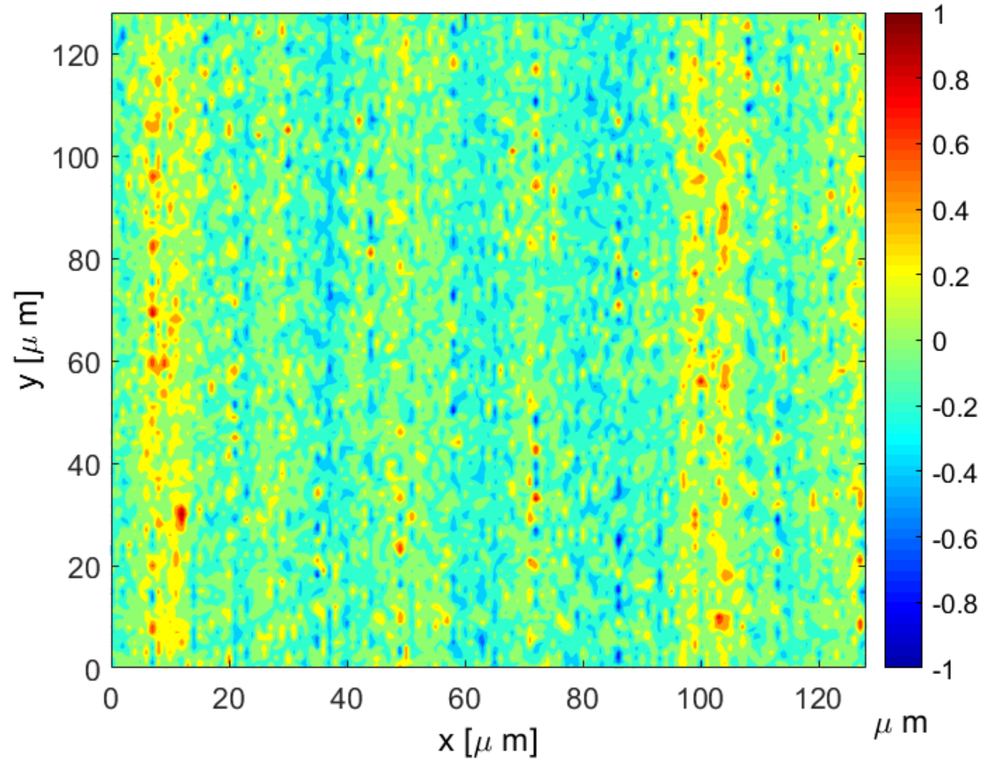

Fig. 6.2. Topographical contour plot of the surface 2L.

6.2.2. Generated Surfaces

Since the roughness of the surfaces measured is in the range of 0.204 to 1.126 μm, some smoother surfaces are needed to investigate the rough surface contact over a wide range. Hence, two kinds of smooth surfaces are generated: self-affine generated rough surface and random Gaussian rough surface.

a.) Self-affine generated rough surface

First, a self-affine generated fractal rough surface is considered. Commonly, a fractal geometry should be continuous, non-differentiable and statistically self-affine. A 3D fractal surface topography using a modified two-variable Weierstrass -Mandelbrot function can be written as [119]

$$h(x,y) = L\left(\frac{G}{L}\right)^{D-2}\left(\frac{\ln\gamma}{M}\right)^{1/2}\sum_{m=1}^{M}\sum_{n=1}^{n'_{max}}\gamma^{(D-2)n}\left\{\cos(\phi_{m,n}) - \cos\left[\frac{2\pi\gamma^{n}(x^2+y^2)^{1/2}}{L}\cos\left(\tan^{-1}\left(\frac{y}{x}\right)-\frac{\pi m}{M}\right)+\phi_{m,n}\right]\right\}, 2 \leq D \leq 3 \tag{6.20}$$

where D is the fractal dimension. $\phi_{m,n}$ is a random phase, n is the frequency level, n'_{max} is the maximum frequency level, given by $n'_{max} = int(\log(L/L_s)/\log(\gamma))$, L is sampling length, L_s is the sampling resolution, γ is the scaling parameter that controls the density of frequency. M is the number used to construct the surfaces. The same rough surface data in Xu's thesis [120] is used. In the following part, we call this generated surface F1, and the parameters are listed in the table 6.2. The roughness calculated is equal to 0.006 μm. The three-dimensional plot and contour are plotted in Figs. 6.3 - 6.4, respectively.

Table 6.2. The parameters used for surface G1

Parameter	$G(\mu m)$	D	$L_x\ (\mu m)$	$L_y\ (\mu m)$	$L_{sx}\ (\mu m)$	$L_{sy}\ (\mu m)$
Value	9.46×10^{-8}	2.44	16	16	0.125	0.125

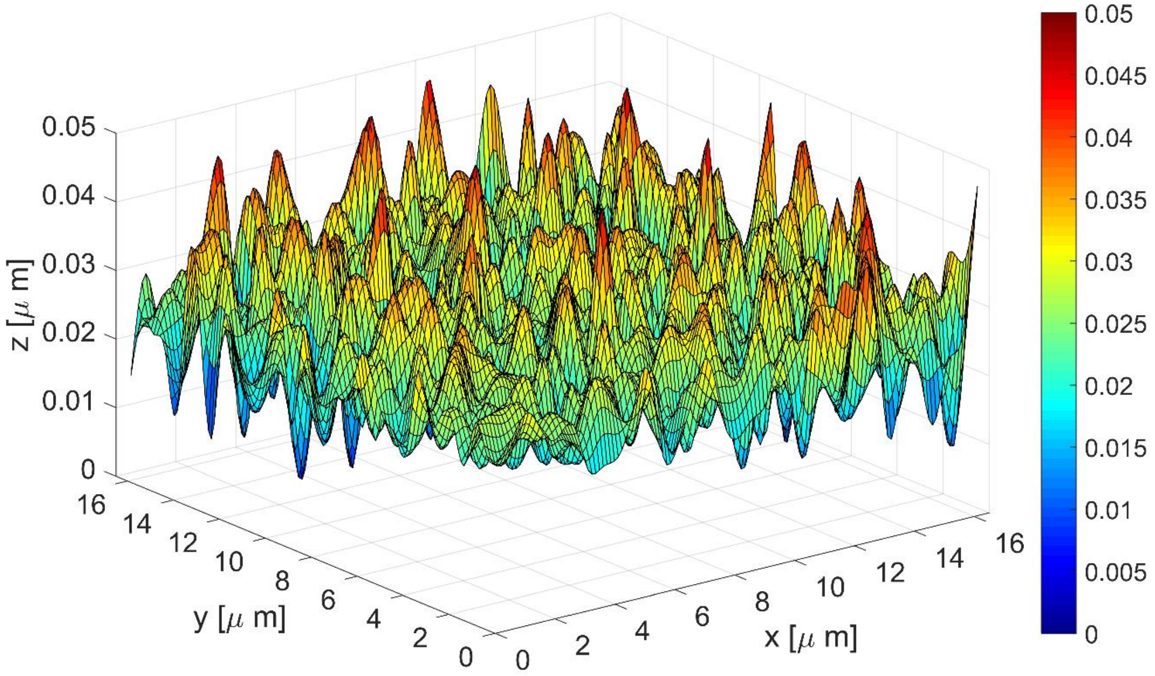

Fig. 6.3. The three-dimensional plot of the generated surface in ref. [120].

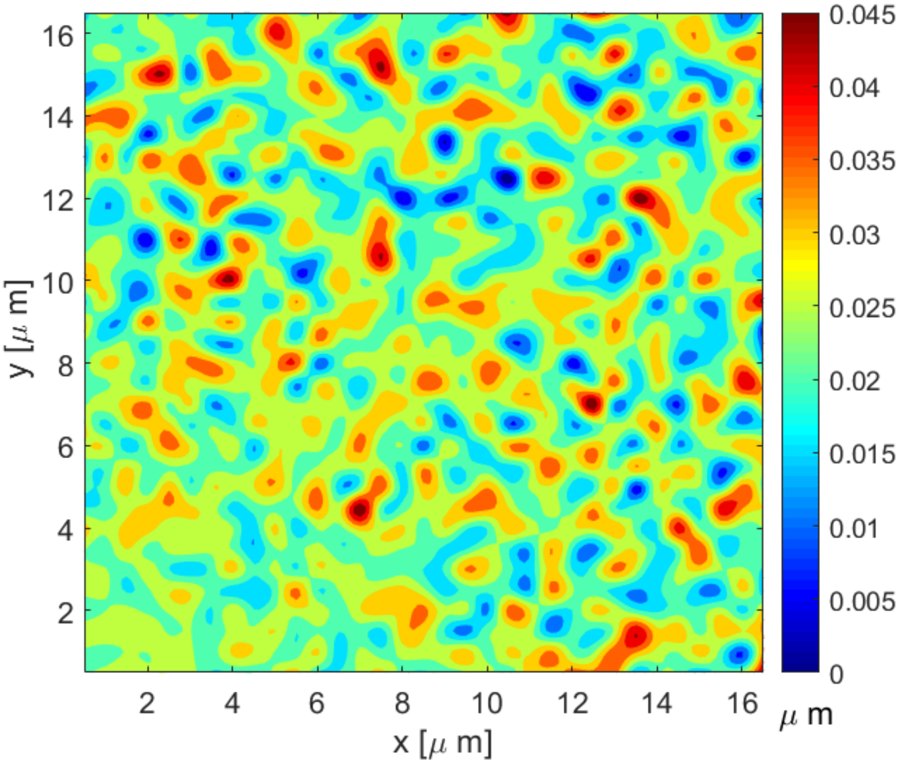

Fig. 6.4. Topographical contour plot of the surface F1.

b.) Random Gaussian Rough Surface

In statistical contact models, the asperity heights of a rough surface are described by a Gaussian distribution for the rough surfaces, although some engineering surfaces follow a non-Gaussian distribution. Note that surface height and asperity heights are different. The surface heights are the data collected from a profilometer. Whereas asperity heights are calculated from the definition of the asperity, which is the surface points taller than their surrounding points. As suggested in [117, 121, 122], it is reasonable that the surface height and asperity height have similar behaviors.

In order to compare the FEM results with the statistical models, 9 rough surfaces with nominally Gaussian distributions are generated by using MATLAB. The average value of the surface heights is set to zero, and the standard deviation of surface heights is varied from 0.01

to 0.2 μm, which are call G1 to G9. The RMS height and plasticity index are listed in Table 6.3. In this chapter, Firstly, the generated Gaussian surface G5, is used to investigate the effect of the normal force on the static friction coefficient. The rough surface plot and contour are shown in Fig. 6.5 and Fig. 6.6, respectively. Then, all the rest of the generated random surfaces are considered to investigate the effect of the plasticity index on the static friction coefficient in the following parts.

Table 6.3. The RMS height and plasticity index of generated Gaussian surfaces

Surface name	**RMS height (μm)**	ψ_x	ψ_y	ψ
Gaussian G1	0.01	1.32	1.32	1.32
Gaussian G2	0.025	3.33	3.33	3.33
Gaussian G3	0.05	6.63	6.61	6.62
Gaussian G4	0.075	10.03	10.05	10.04
Gaussian G5	0.1	13.21	13.18	13.20
Gaussian G6	0.125	16.63	16.55	16.59
Gaussian G7	0.15	19.75	19.77	19.76
Gaussian G8	0.175	23.19	23.04	23.11
Gaussian G9	0.2	26.27	26.07	26.17

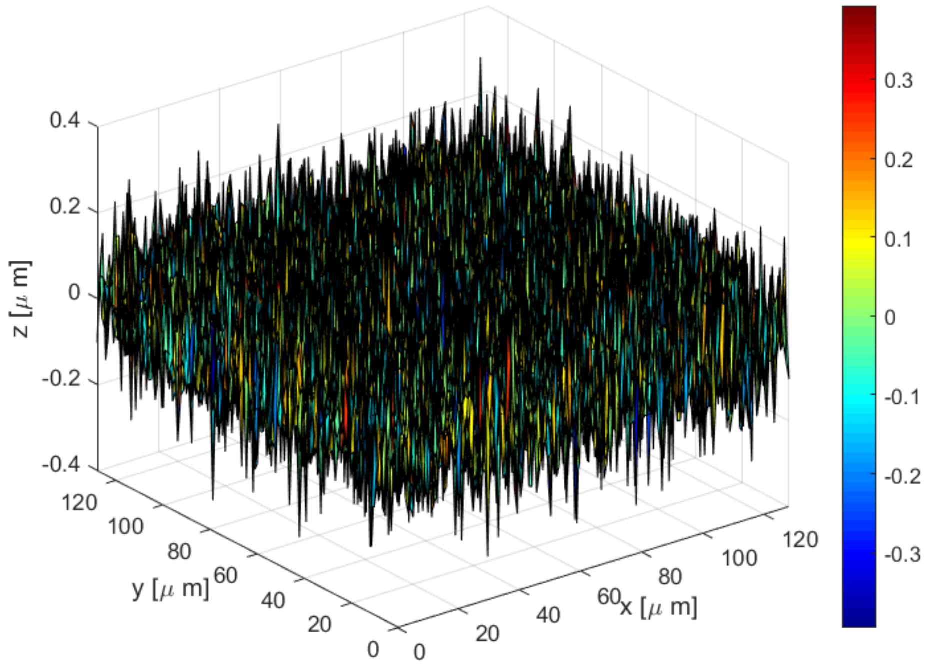

Fig. 6.5. The three-dimensional plot of Gaussian surface G5.

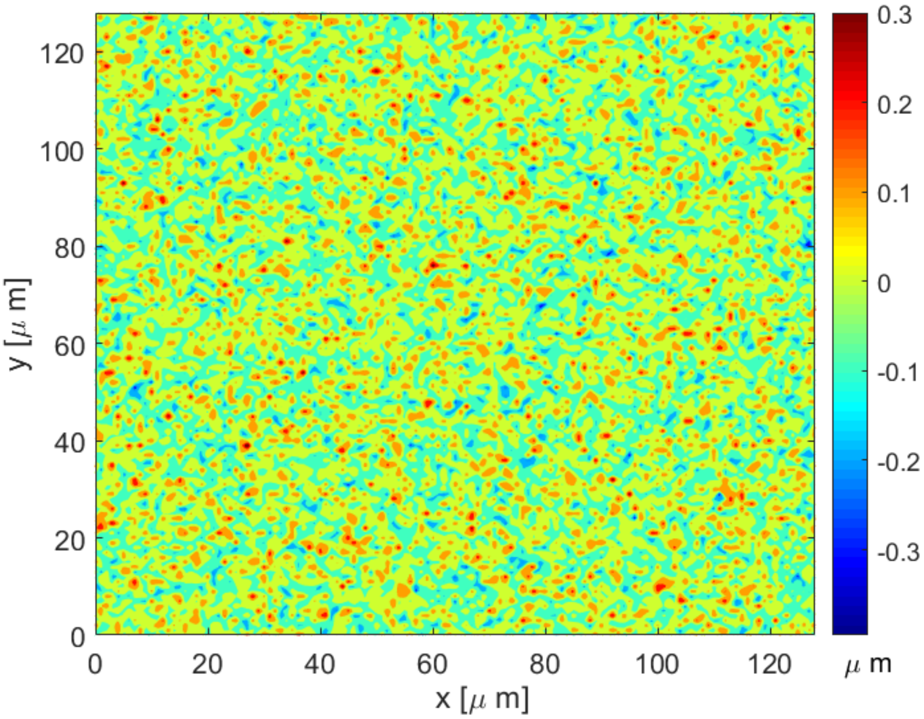

Fig. 6.6. Topographical contour plot of Gaussian surface G5.

6.2.3. Rough Surface Height Distribution

It is necessary to consider the rough surface distribution for the chosen rough surfaces. In Fig. 6.7, the surface distribution is plotted, and a symmetric Gaussian distribution is fitted to the data for comparison. Note that the points with positive values are on the contact side.

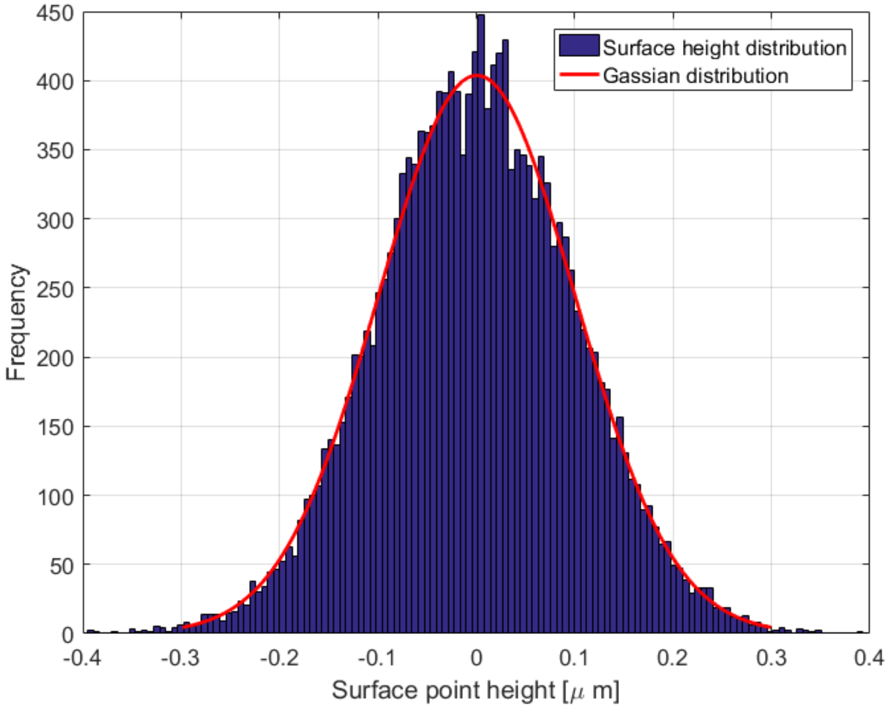

Fig. 6.7. The surface height distribution of Gaussian surface G5.

The MATLAB command “Histogram” is used to plot Fig. 6.7. This command creates a histogram plot of surface heights. The histogram function uses an automatic binning algorithm that returns bins with a uniform width, chosen to cover the range of elements in X and reveal the underlying shape of the distribution. Histogram displays the bins as rectangles such that the height of each rectangle indicates the number of elements in the bin. The width of the bines are used the default values.

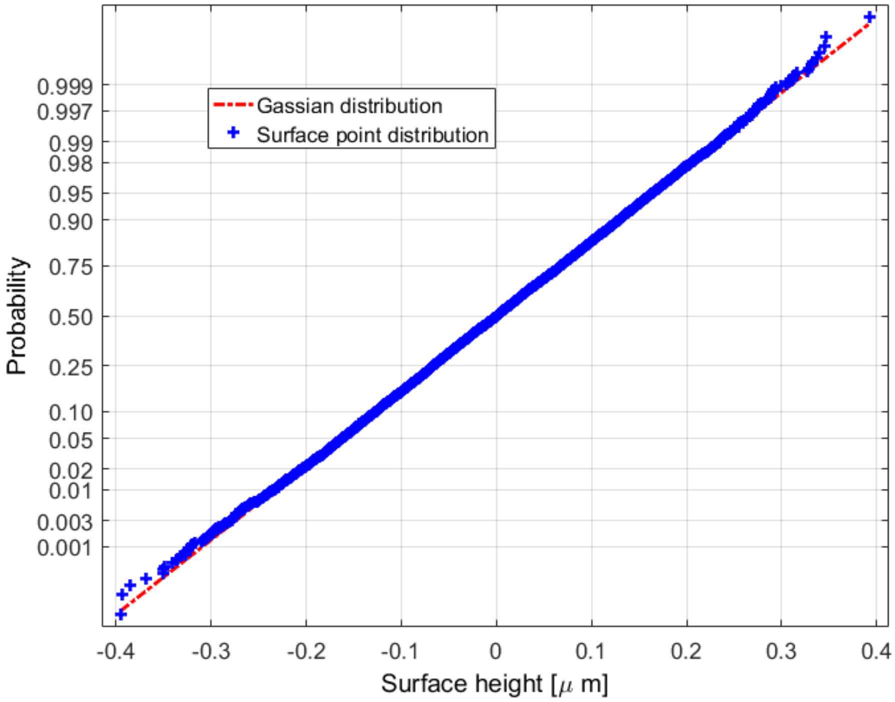

Fig. 6.8. Normal probability plot of Gaussian surface G5.

The normal probability plot is used to check whether the surface height conforms to a normal distribution. The cumulative distribution of generated surface data for surface G5 and the theoretical cumulative Gaussian distribution are plotted in Fig. 6.8. The MATLAB command “normplot” is used to plot Fig. 6.8. This command displays a normal probability plot of the surface heights. Use a normal probability plot to assess visually whether the sample data in x comes from a population with a normal distribution. If the sample data has a normal distribution, then the data appears along the reference line. Distributions other than normal can introduce curvature in the plot. As seen from Fig. 6.8, most of the surface data are located on the line of the Gaussian distribution, and it could be represented by a Gaussian distribution. The surface height roughness histogram and probability for the surface 2L are plotted in Fig. 6.9 - 6.10, respectively. Similarly, the surface height roughness histogram and probability for the surface 2L are plotted in Fig. 6.11

- 6.12, respectively. As can be seen from Figs. 6.10 and 6.12, the height distributions of surface 2L and surface F1 are not Gaussian.

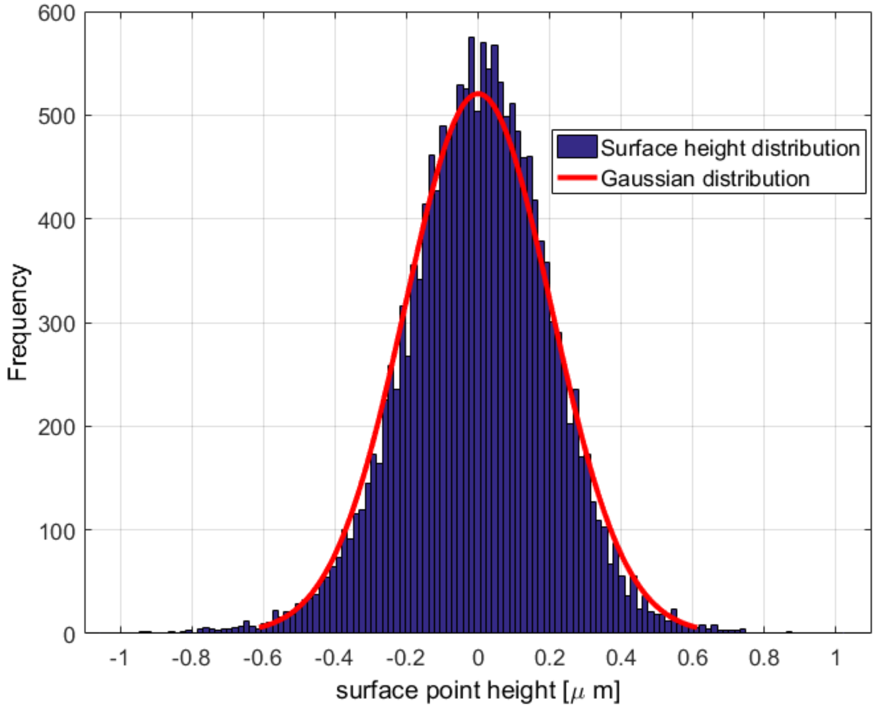

Fig. 6.9. The surface height distribution of the surface 2L.

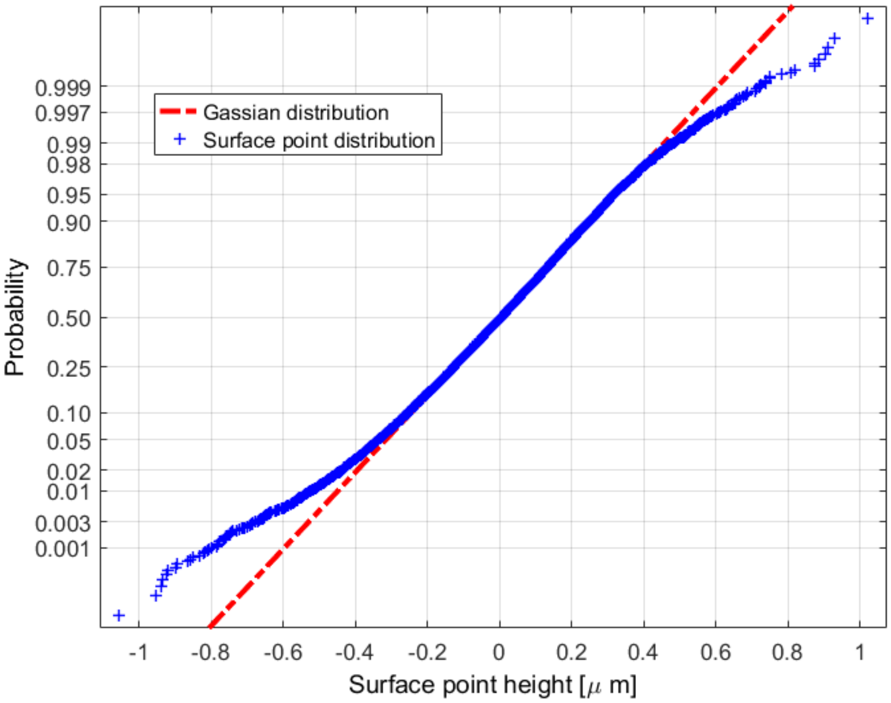

Fig. 6.10. Normal probability plot of surface 2L.

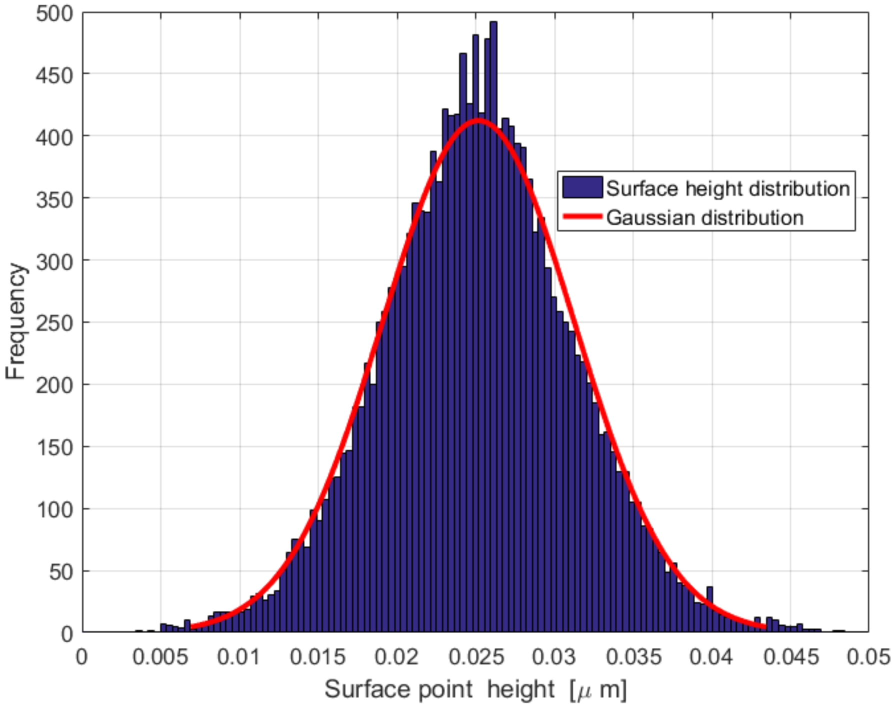

Fig. 6.11. The surface height distribution of the surface F1.

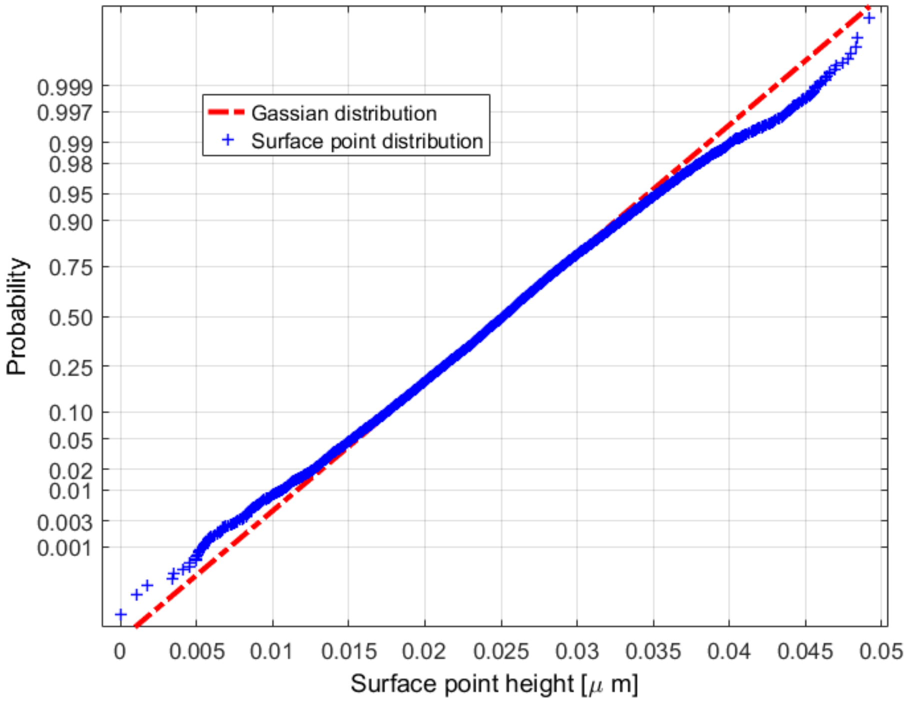

Fig. 6.12. Normal probability plot of surface F1.

6.3. Finite Element Model

The finite element model and boundary conditions in Chapter 5 are used, (see Fig. 5.10). Again, the 8-node brick element solid 185 is used to model the solid substrate. Targe 170 and Conta 173 are used to form the contact pair. Considering computing time, 129×129 array surface points are considered. One line is added in the *x* and *y* directions to guarantee the two side surfaces of solid body have the same deformation. The rough surface was a uniform mesh formed by a 128×128 array of element. The bottom surfaces are fixed in all directions, and the *xz* surfaces are restrained in the y direction, and the *yz* surfaces are coupled to enforce periodicity. The normal force is applied on the rigid flat, and then the normal preload is held constant while a tangential displacement is applied on the rigid flat. The critical interfacial shear strength is set to $S_y/\sqrt{3}$. The sliding occurs when the shear stress of all the elements reach that value. Then gross sliding occurs, and the stiffness vanishes at that moment.

6.4. Results and Conclusion

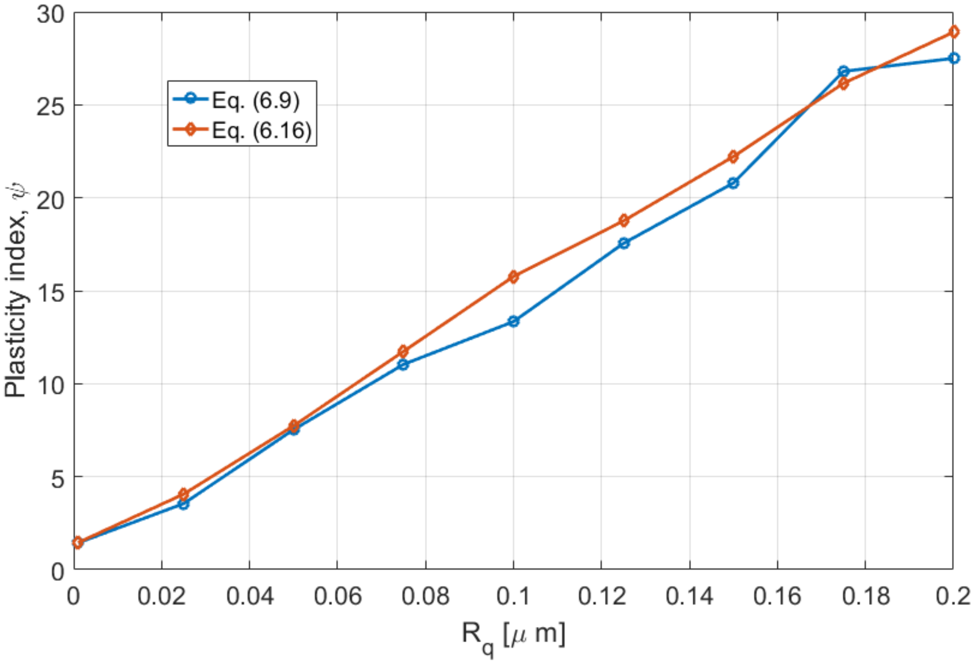

Fig. 6.13. Comparison of formula of plasticity index in Eqs. (6.9) and (6.16).

The plastic index can be calculated either from Eq. (6.9) or Eq. (6.16). A comparison of these two formulas is plotted in Fig. 6.12. From Fig. 6.12, the values predicted by the Eq. (6.9) and (6.16) do not always have a good agreement. Eq. (6.16) might be better than Eq. (6.9). In order to compare the results with the models in [13] and [15], the Eq. (6.9) is used to calculate plastic index, since it is more common in the literature. The FEM simulations are employed by using the fractal rough surface F1, Gaussian surfaces G1, G2, G6, G9 and real measured rough surface 2L, in order of increasing roughness. The plasticity indices are 2.39, 1.32, 3.33, 16.59, 26.17, and 26.61 respectively.

6.4.1. Effects on Contact Area under Normal Preload

The material parameters of a typical steel are chosen: $E = 200$ GPa, $\nu = 0.3$, $S_y = 1$ GPa, and $E_t = 4$ GPa. In order to be consistent with the models in [13] and [15], the upper limit of the normalized contact normal load, $F_n/(A_n S_y)$, is set to 0.3. The contact condition is the full stick condition under normal loading and the critical shear strength criterion is used to determine the sliding inception under combined normal and tangential loading. In the subsection 6.4.1.1, the results of the first loading step (under only normal loading) are analyzed. In the subsection 6.4.1.2, the results of the first loading step (under combined normal and tangential loading) are analyzed.

6.4.1.1. The Effect of Normal Load on The Contact Area

First, the fractal rough surface F1 is used in the simulation. Fig. 6.14. presents the comparison of the contact area under the normal preload only as predicted by the FEM, CKE model and LET model. From Fig. 6.14, they all show the same trend. As the dimensionless normal load increases, the contact area increases. The values of the FEM contact areas are higher than the values predicted by the CKE model and LET model.

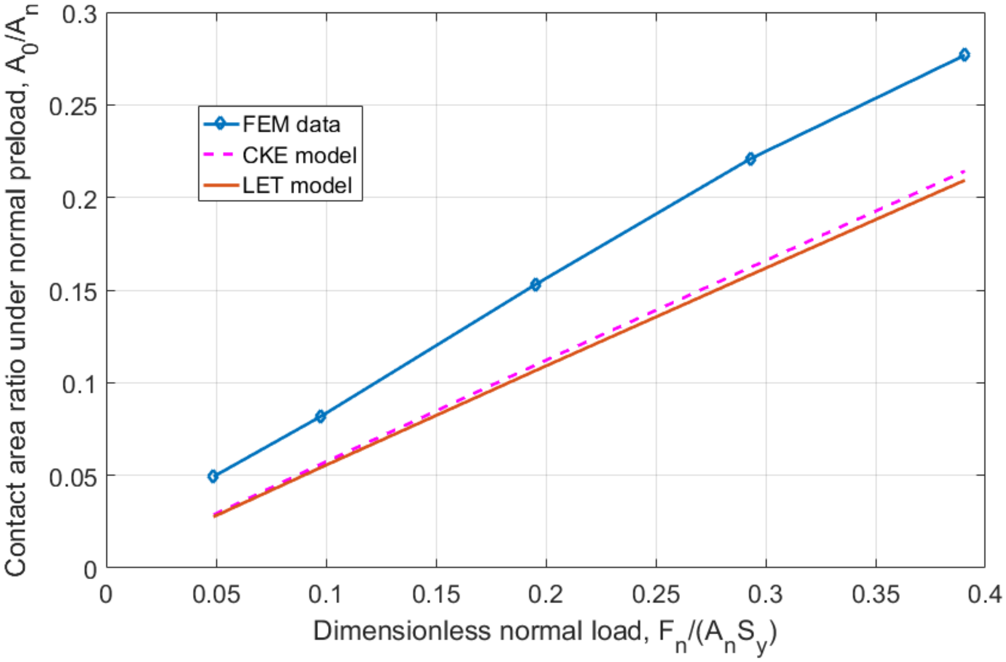

Fig. 6.14. Comparison of contact area between the FEM data and statistical models on for surface F1.

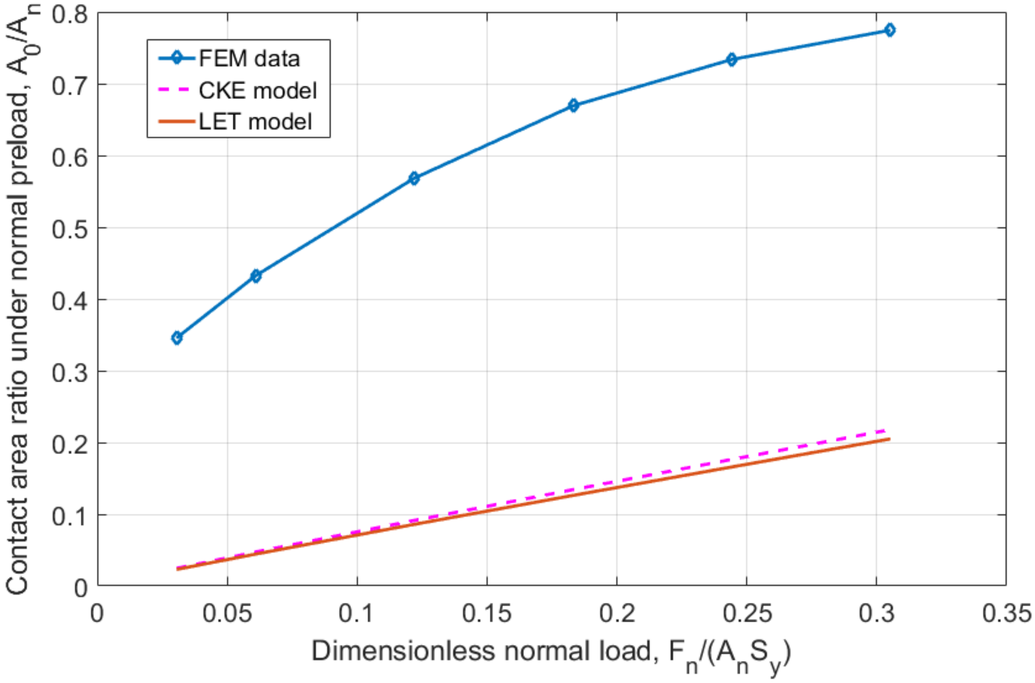

Fig. 6.15. Comparison of contact area between the FEM data and statistical models for the surface G1.

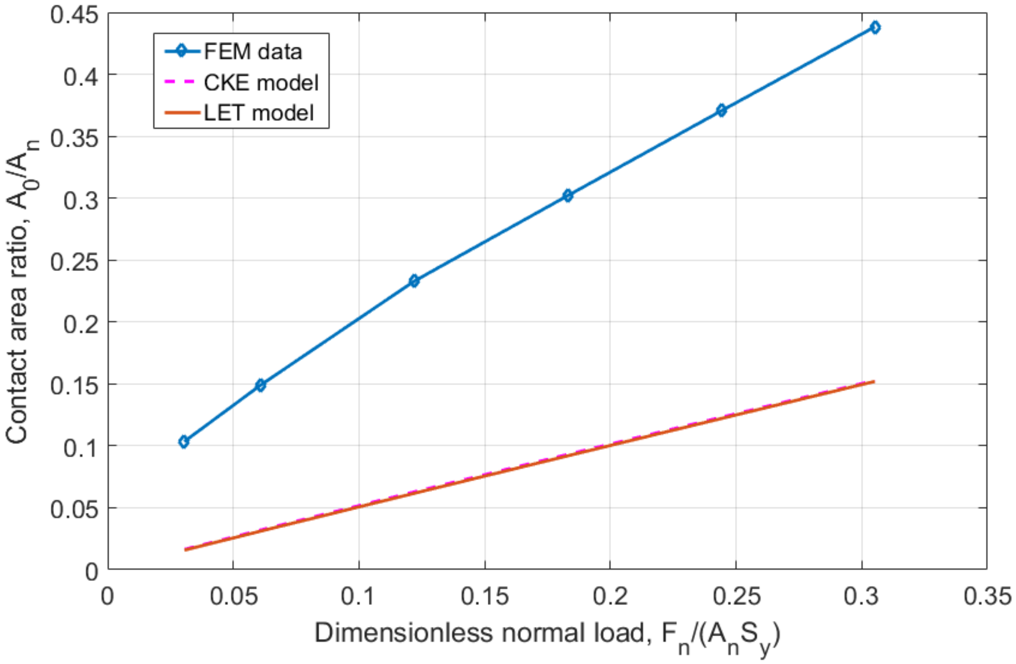

Fig. 6.16. Comparison of contact area between the FEM data and statistical models for the surface G2.

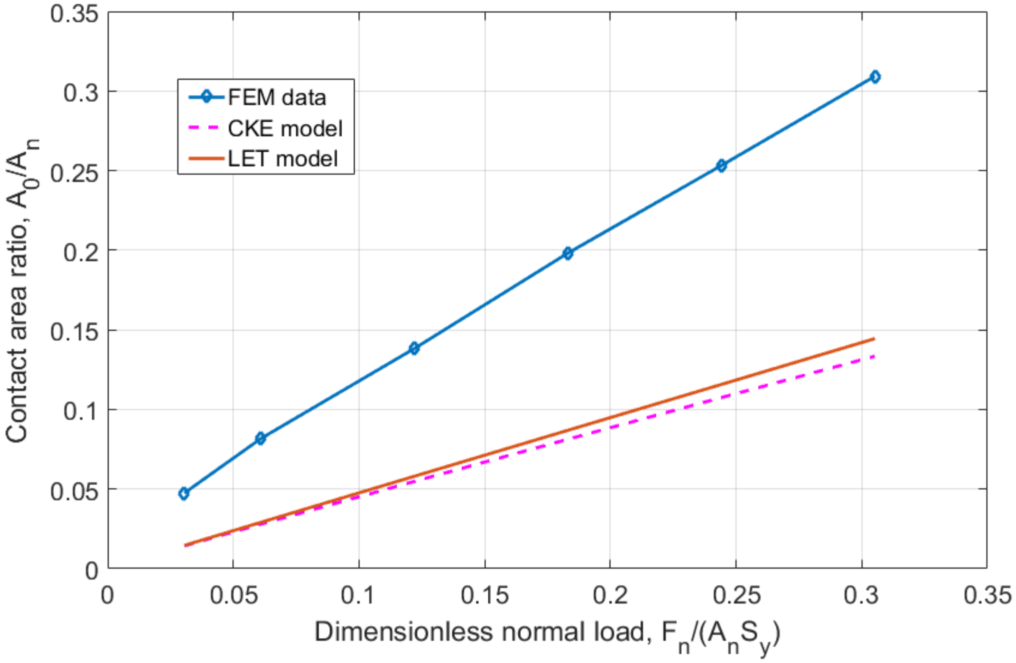

Fig. 6.17. Comparison of contact area between the FEM data and statistical models for the surface G3.

Similar to the fractal rough surface, from Fig. 6.15 - 6.17, Surfaces G1, G2 and G3 show the same trend, as the dimensionless normal load increases, the contact area increases for the generated Gaussian rough surfaces. The values of contact area of the FEM results are higher than the values predicted by the CKE model and LET model. The values of the contact area predicted by the LET model are lower than the values predicted by CKE model except for the case of surface G3.

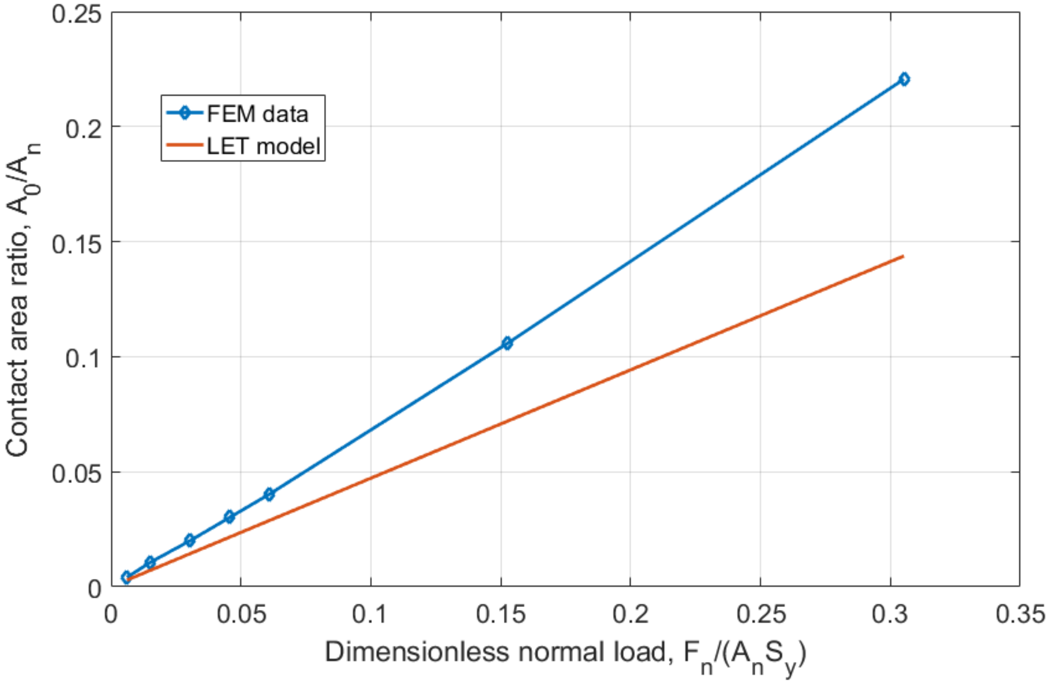

Fig. 6.18. Comparison of contact area between the FEM data and statistical models for the surface G5.

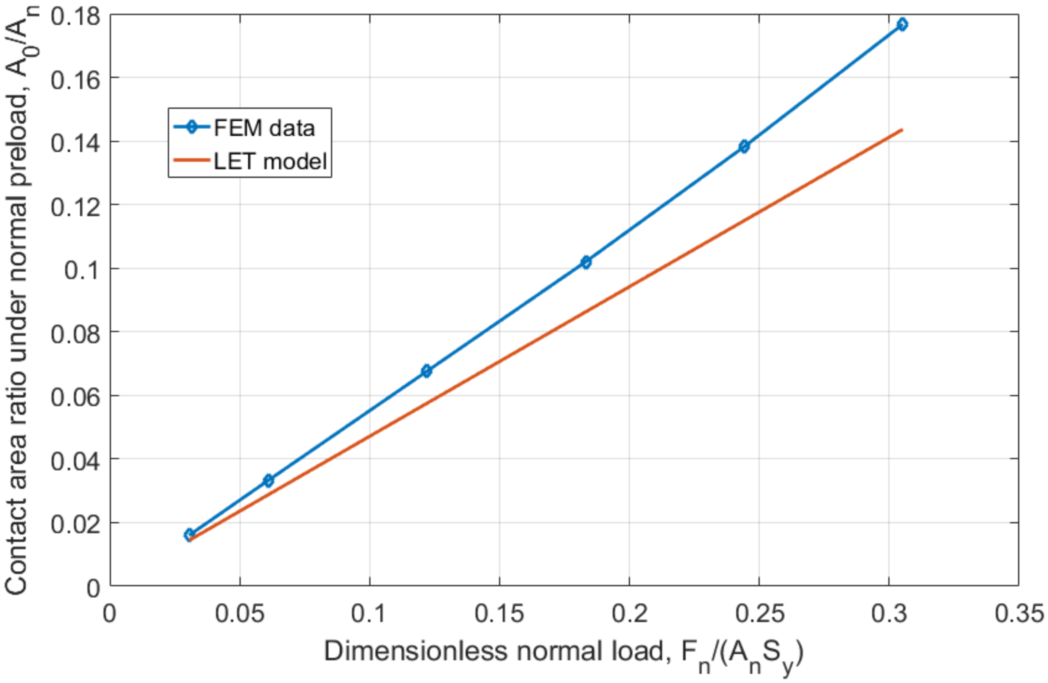

Fig. 6.19. Comparison of contact area between the FEM data and statistical models for surface 2L.

Then, a generated Gaussian rough surface with a higher plasticity index and a real measured rough surface 2L are used in the simulation. The plasticity index for these two surfaces are 13.2 and 26.61 respectively. Since the CKE model is not valid when the plasticity index is larger than 8, only the LET model is compared with the FEM results. As expected, they show the same trend, as the dimensionless normal load increases, the contact area increases. It is also shown that, as the dimensionless normal load increases, that the difference of contact area between the FEM results and the LET model become larger.

6.4.1.2. The Effect of Plasticity Index on the Contact Area

Sometimes, sharp asperities would deform plastically even under relatively low loads, while blunt asperities would deform elastically even under heavier loads. the parameter most used to evaluate this behavior is the plasticity index, ψ, whose equation is given in Eq. (6.9). The 9 generated Gaussian distribution rough surfaces are used in the FEM model to investigate the effect of plasticity index on the contact area. The roughness, R_q, of these surfaces are varied from 0.01 to 0.2 μ m, and the plasticity index, ψ, are varied from 1.32 to 26.2.

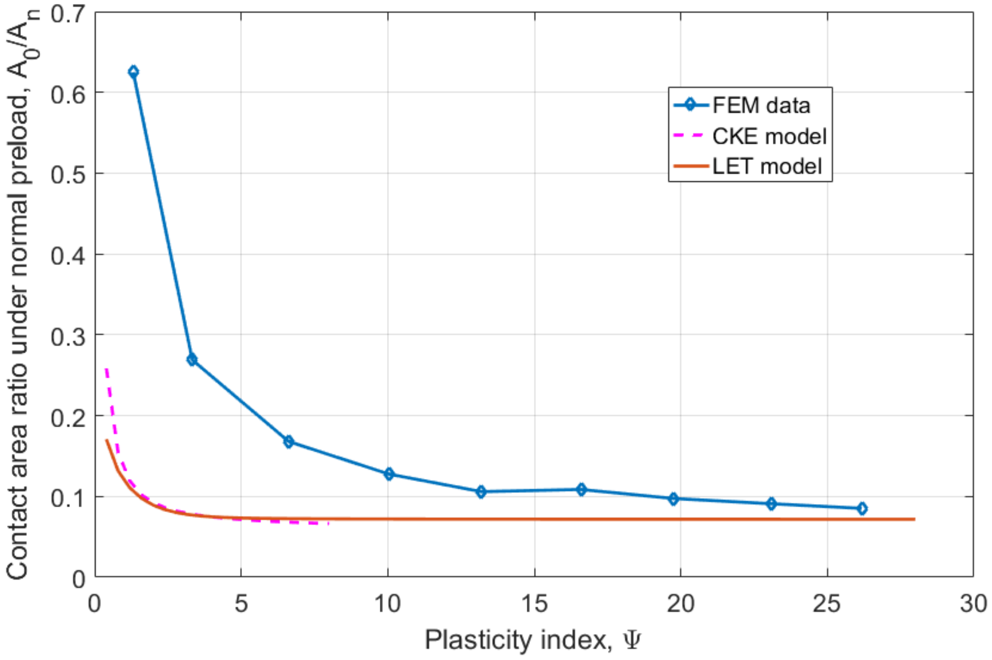

Fig. 6.20. Comparison of contact area between the FEM data and statistical models for generated surfaces with different plasticity index indices.

Fig. 6.20 presents a comparison of the FEM predicted contact area with the statistical model predictions for generated Gaussian surfaces (G1 to G9). Both of the FEM results and the statistical models show the same trend: as the plastic index increases, the contact area increases, and the FEM results approach to the LET model. This suggests that additional plasticity tends to lessen differences in the theories.

6.4.2. Effects on Static Friction Coefficient

The effects of normal load and plasticity index on the static friction coefficient are investigated in this subsection. The results are extracted from FEM model in the second loading step (combined normal and tangential loading) in the same simulation of Section 6.4.1.

6.4.2.1. The Effect of Normal Load on the Static Friction Coefficient

In this section, the surface F1 is used in the simulation. The dimensionless tangential load versus dimensionless tangential displacement with different normal preloads are plotted in Fig. 6.21. The maximum tangential force is obtained when the stiffness reaches zero for each case, and the static friction coefficient is calculated by dividing the maximum tangential load by the normal force. As can be seen from Fig. 6.21, the higher dimensionless normal load can support less maximum dimensionless tangential load. This is because less yielding has already occurred due to normal loading.

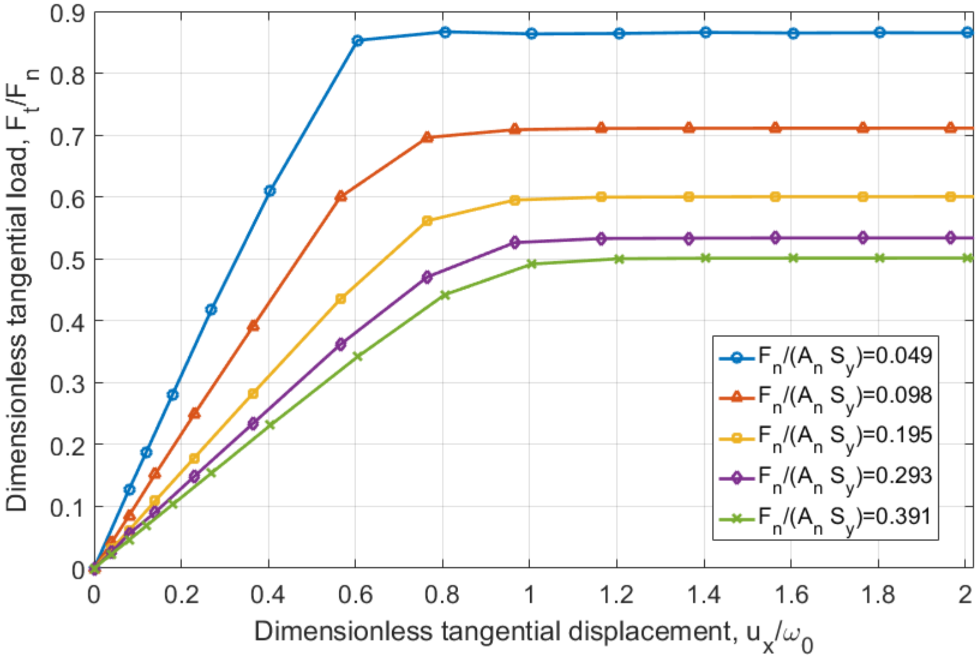

Fig. 6.21. The dimensionless tangential load versus dimensionless tangential displacement under different normal load for surface F1.

Again, the static friction coefficients are obtained by choosing the dimensionless tangential load when the stiffness becomes zero. The static friction coefficient for different normal preloads are extracted from Fig. 6.21. and plotted in Fig. 6.22. The static friction coefficients predicted by the CKE model (Eq. (6.7)) and LET model (Eq. (6.16)) are also plotted for comparison. As can be seen from Fig. 6.22, both the CKE model and the LET model predict the same trend as the FEM results. As the dimensionless normal load increases, the static friction coefficient decreases. However, both the CKE model and the LET model predict a lower value than the FEM data.

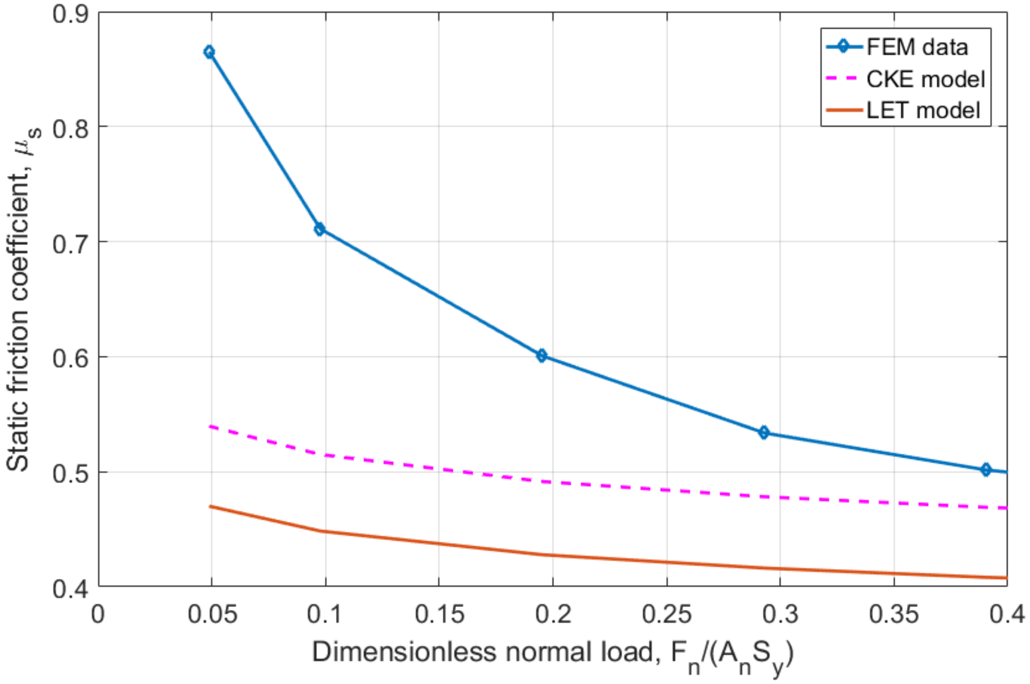

Fig. 6.22. Comparison of static friction coefficient between the FEM data and statistical models for surface F1.

Second, the generated Gaussian surfaces (G1, G2, G3) with different plasticity indices are analyzed. The static friction coefficient of the surfaces with $\Psi = 1.32, \Psi = 3.33, \Psi = 6.62$ are plotted in Figs. 6.23 - 6.25. Again, the FEM results are compared with the static friction models.

In Figs. 6.23 - 6.25, the FEM results show the same trend as the CKE model and LET model. However, the FEM static friction results are higher than what the statistical models predicted.

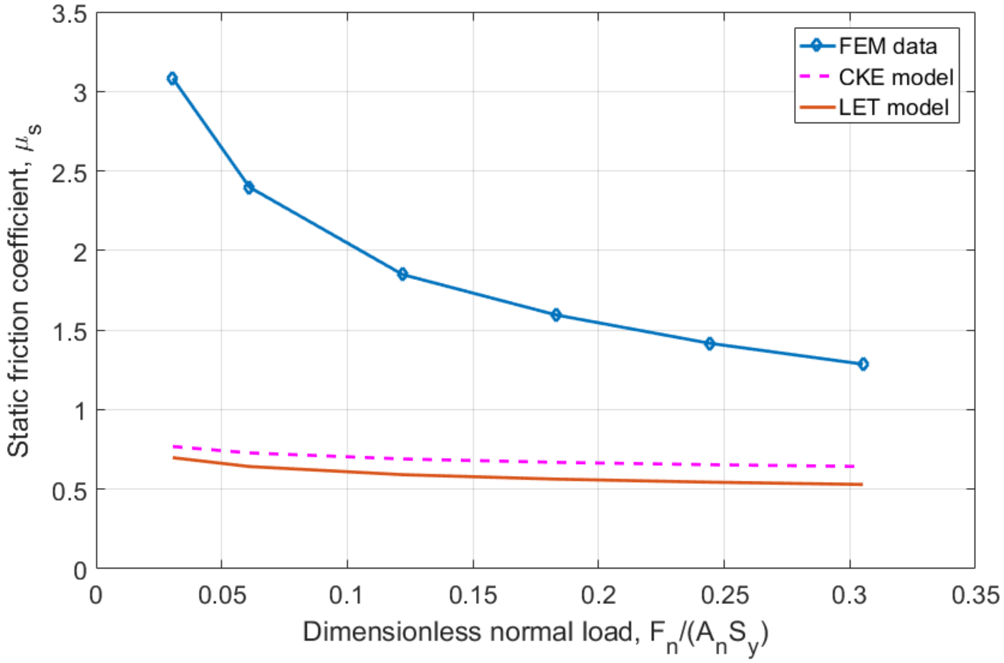

Fig. 6.23. Comparison of static friction coefficient between the FEM data and the statistical models for the surface G1.

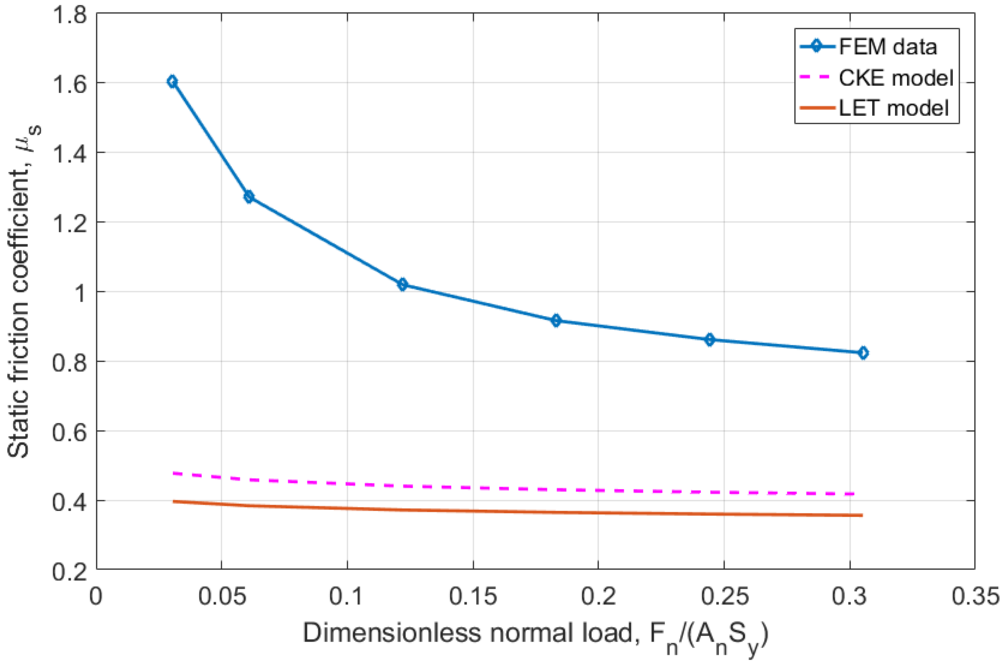

Fig. 6.24. Comparison of static friction coefficient between the FEM data and the statistical models for the surface G2.

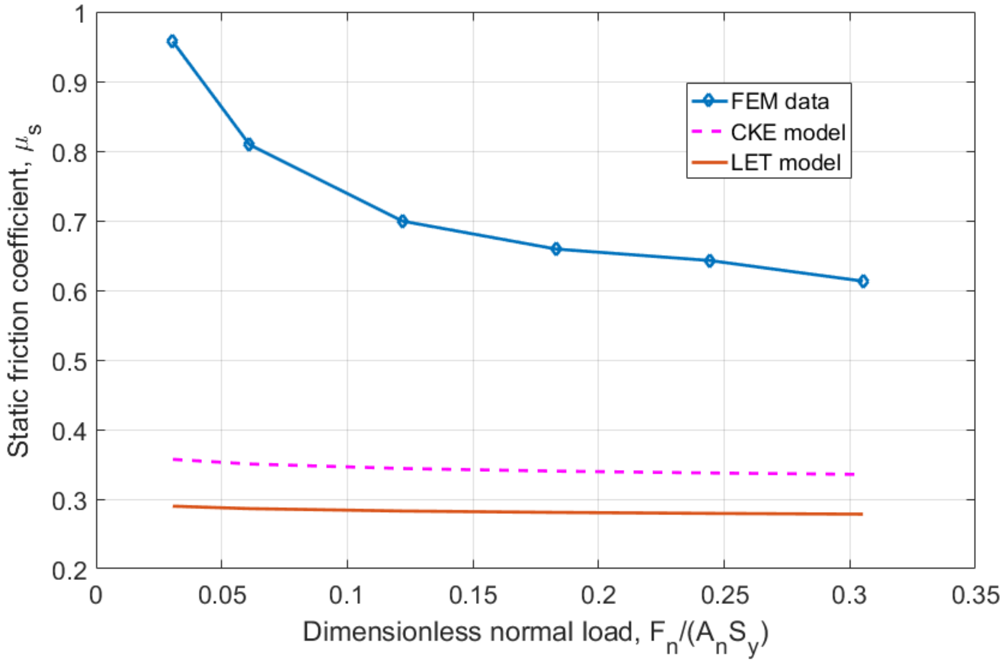

Fig. 6.25. Comparison of static friction coefficient between the FEM data and the statistical models for the surface G3.

Then, the static friction coefficient of rough surfaces with high plasticity indices are analyzed. Again, since the plasticity indices, ψ, are larger than 8, the CKE model is not considered here. Fig. 6.26 presents the comparison of the CKE model for the FEM results for generated rough surface G5 and Fig. 6.27 presents the comparison of the CKE model to the FEM results surface 2L.

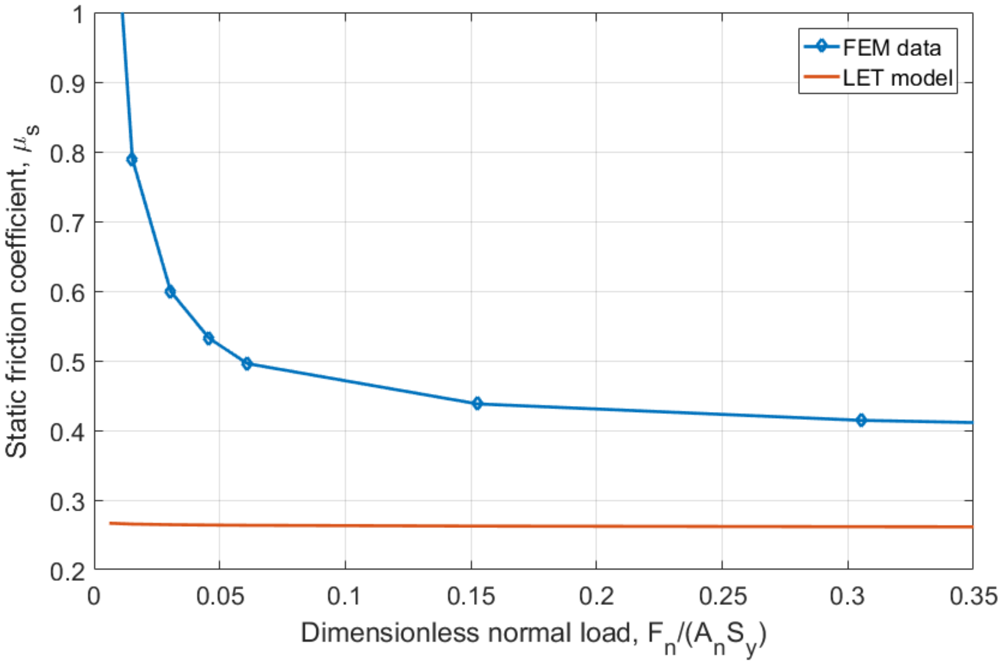

Fig. 6.26. Comparison of static friction coefficient between the FEM data and the statistical models for the surface G5.

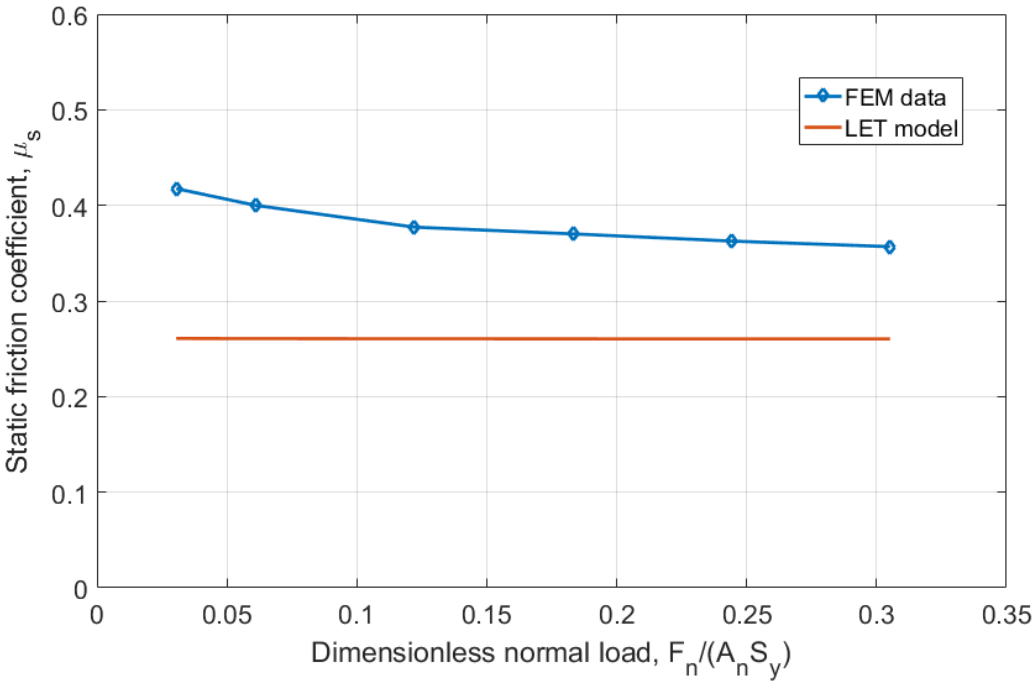

Fig. 6.27. Comparison of static friction coefficient between the FEM data and the statistical models for surface 2L.

The static friction coefficient predicted by the LET is a nearly constant value, 0.26, when $\psi > 8$. As can be seen in Fig. 6.26 and 6.27, the FEM results are greater than what is predicted by the LET model (Eq. (6.17)). As the dimensionless normal preload increases, the static friction coefficient of the FEM results decreases and approach but do not reach the value predicted by LET model, which is approximately 0.26.

6.4.2.2. The Effect of Plasticity Index on Static Friction Coefficient

Just as in subsection 6.4.1.2, the results of the 9 rough surfaces extracted from the FE model are analyzed here**.** The dimensionless tangential load versus dimensionless tangential displacement is plotted in Fig. 6.28, and the static friction coefficient as a function of plasticity index is plotted in Fig. 6.29. As shown in Fig. 6.29, as the plasticity index increases, the static friction coefficient decreases. Both the CKE model and the LET model show the same trend as the FEM results, and the static friction coefficients predicted by these two models are lower than the FEM data.

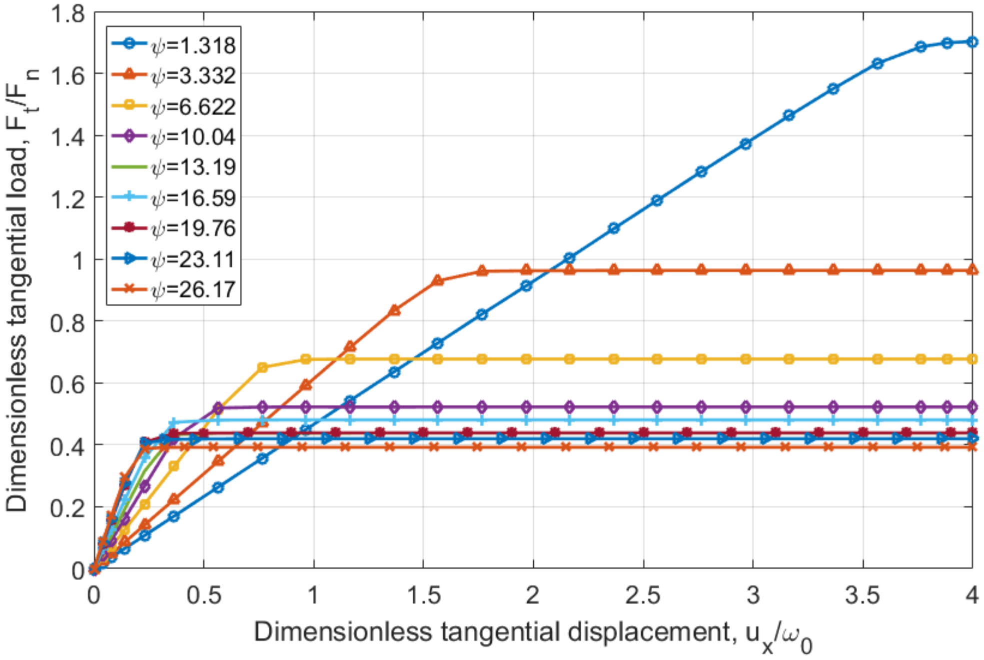

Fig. 6.28. The dimensionless tangential load versus dimensionless tangential displacement for the surfaces with different plasticity indices.

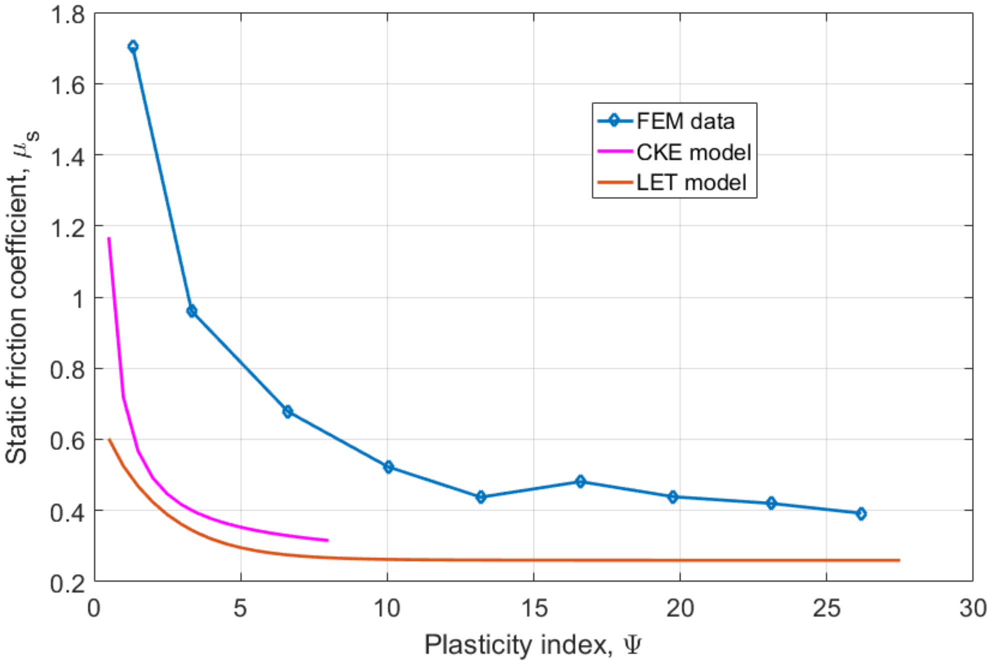

Fig. 6.29. Comparison of static friction coefficient between the FEM data and statistical models for generated surfaces with different plasticity index indices.

6.4.3. The Effect of Strain Hardening on Static Friction Coefficient

The material of the solid body with rough surfaces are considered as elastic-plastic linear isotropic hardening with a tangent modulus, E_t. The results considered so far are for the case of bilinear hardening with $E_t = 2\%\ E$. The schematic of the material model was shown in Fig. 5.13 in Chapter 5. The simulations are now carried out by using the same material properties except for the tangent modulus. The tangent modulus is set now to $E_t = 0$. By removing the influence of hardening, its effect can be observed.

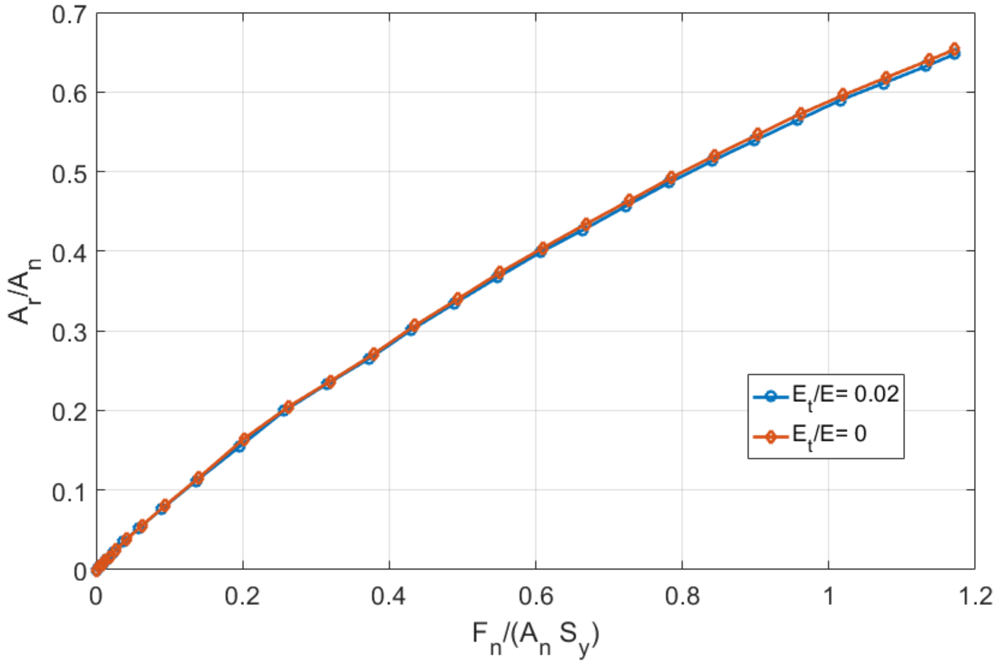

Fig. 6.30. The effect of strain hardening on the contact area considering different normal loads for Surface F1.

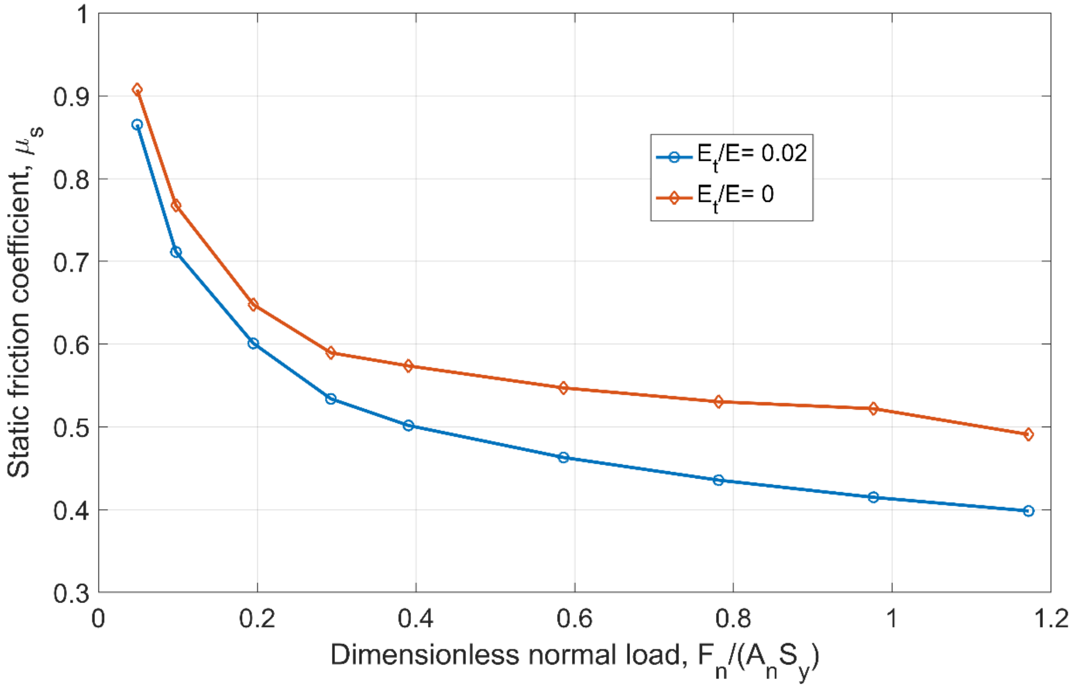

Fig. 6.31. The effect of strain hardening on the static friction coefficient considering different normal loads for Surface F1.

First, the fractal rough fractal surface F1 is used in the simulation. The results of contact area and static friction coefficient with a 2% tangent modulus and without any tangent modulus are plotted in Figs. 6.30 and 6.31, respectively. Both contact area and static friction coefficient without strain hardening are greater than the corresponding values with strain hardening. For this fractal rough surface, the impact of the strain hardening on contact area is not obvious. This is mainly because fractal surface F1 is so smooth, the roughness is only 0.006 μm and the plasticity index is 2.38. Interestingly, as can be seen from Fig. 6.31, the bilinear stain hardening clearly has an influence on the static friction coefficient, and this effect increases as the dimensionless normal load increases.

Then, the effect of strain hardening on the contact area of surfaces with different roughness are analyzed. As can be seen from Fig. 6.32, the effect of strain hardening on contact area becomes more significant for the rougher surfaces.

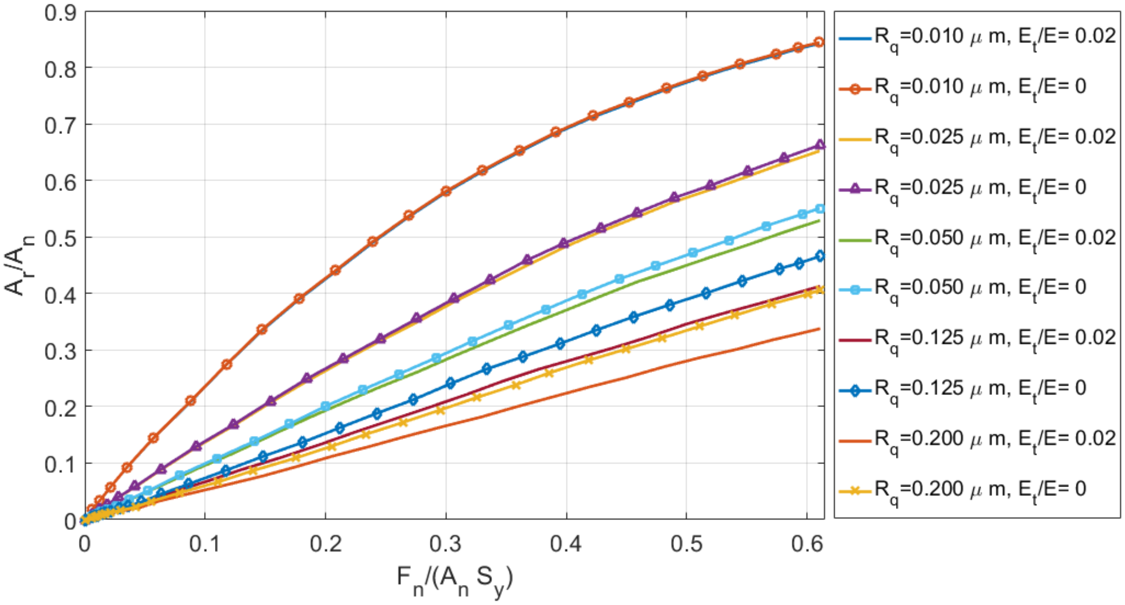

Fig. 6.32. The effect of strain hardening on the static friction coefficient considering different normal loads for surfaces G1, G2, G3, G6 and G9.

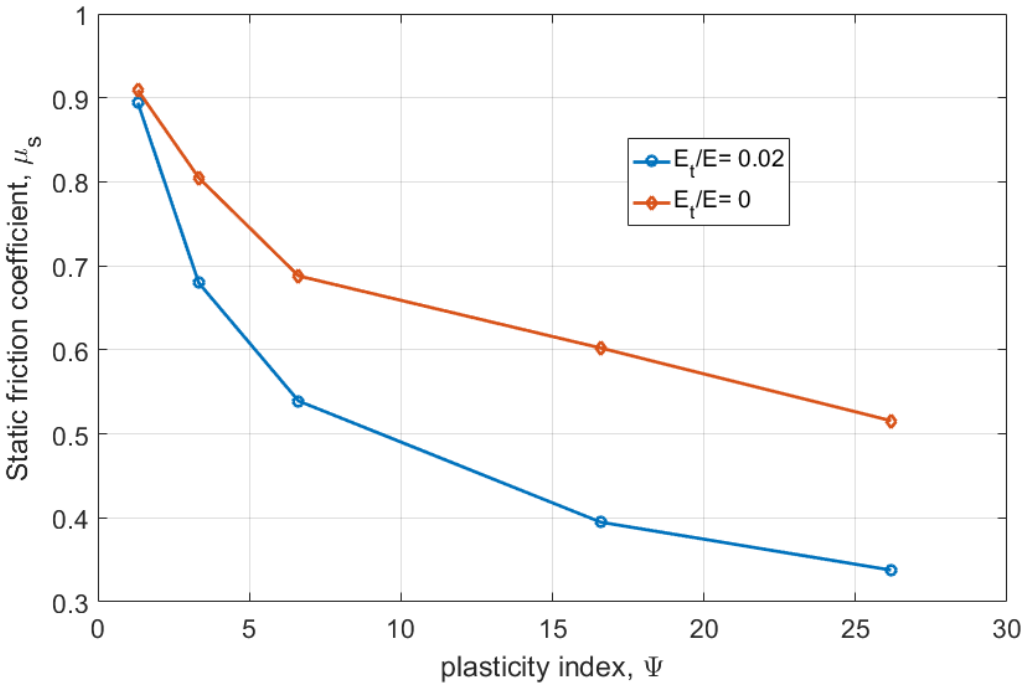

Fig. 6.33. The effect of strain hardening on the static friction coefficient for various values of plasticity index.

The static friction coefficient versus platicity index for the cases with and without strain hardening are plotted in Fig. 6.33. As can be seen from Fig. 6.33, the effect of strain hardening on static friction coefficient is significant for the surfaces with larger plasticity indices.

6.4.4. Elastic Perfect Plastic Rough Surface Contact with High Plasticity Index

As can be seen from the literature review and previous study in the above sections, the statistical models and FEM results mentioned previously only considered bilinear strain hardening materials. Nevertheless, the dimensionless normal load is limited to 0.3 and the plastic index is limited to 32. Very little work has been done considering the elastic-perfectly plastic contact of rough surfaces with very high plasticity indices under higher normal loads.

In this subsection, the strain hardening is not considered, the elastic perfect plastic contact is analyzed. The same material properties were used except for the tangent modulus, E_t, and it is set to zero. The static friction coefficient is investigated over a wide range of dimensionless normal loads $0.98 \leq F_n/(A_n S_y) \leq 2.93$, which are much larger than the dimensionless normal load in [13, 15], 0.3. The plasticity index is varied from 26.6 to 134.2.

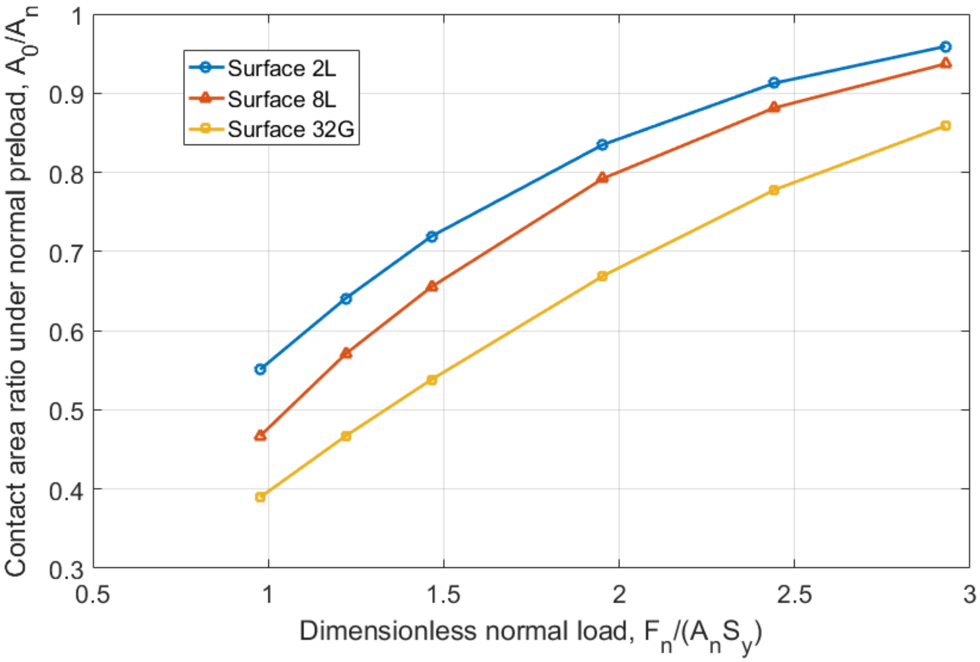

Fig. 6.34. Contact area as a function of dimensionless normal load for the different rough surfaces with no strain hardening.

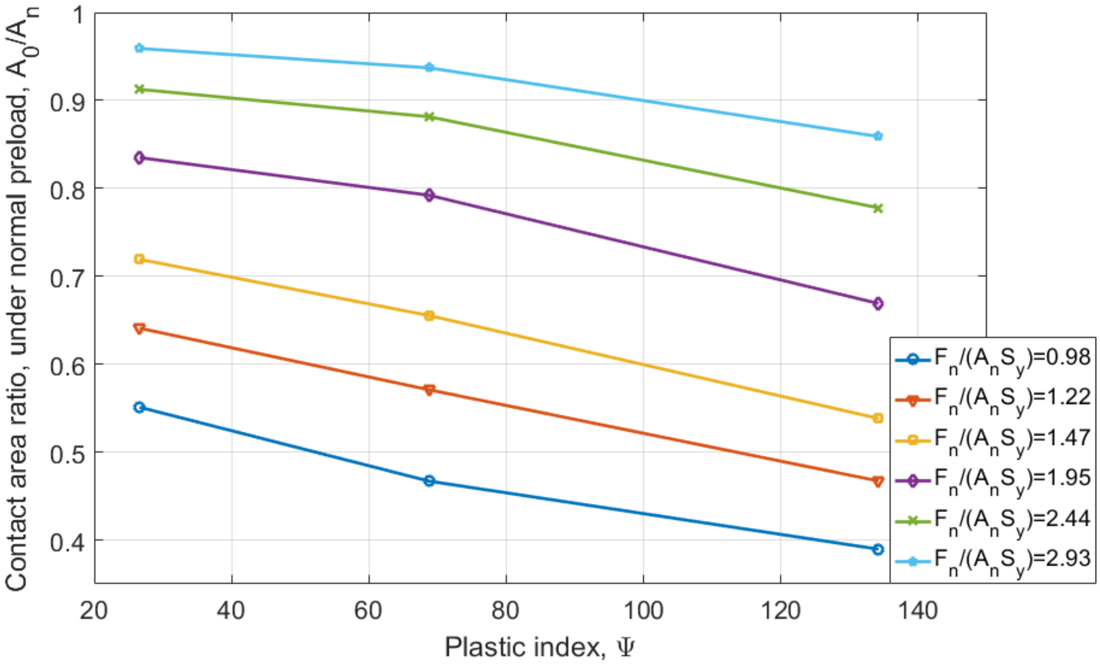

Fig. 6.35. Contact area as a function of plasticity index for the different rough surfaces with no strain hardening.

Fig. 6.34 presents the contact area versus dimensionless normal load. The three surfaces show the same trend: as the dimensionless normal load increases, the contact area increases for all the three surfaces. The same result set are plotted as a function as the plasticity index in Fig. 6.35. From Fig. 6.35, as the plastic index increases, the contact area decreases. This is similar to the behavior for the cases with strain hardening under lower loads.

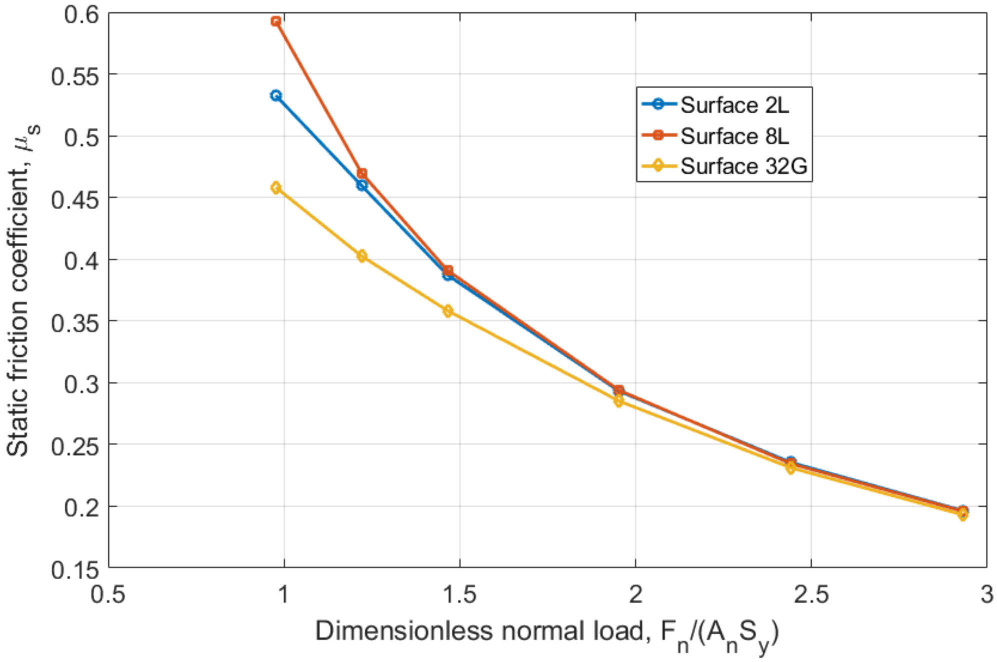

Fig. 6.36. Static friction coefficient versus dimensionless normal load for Surface 2L, 8L and 32G with no strain hardening.

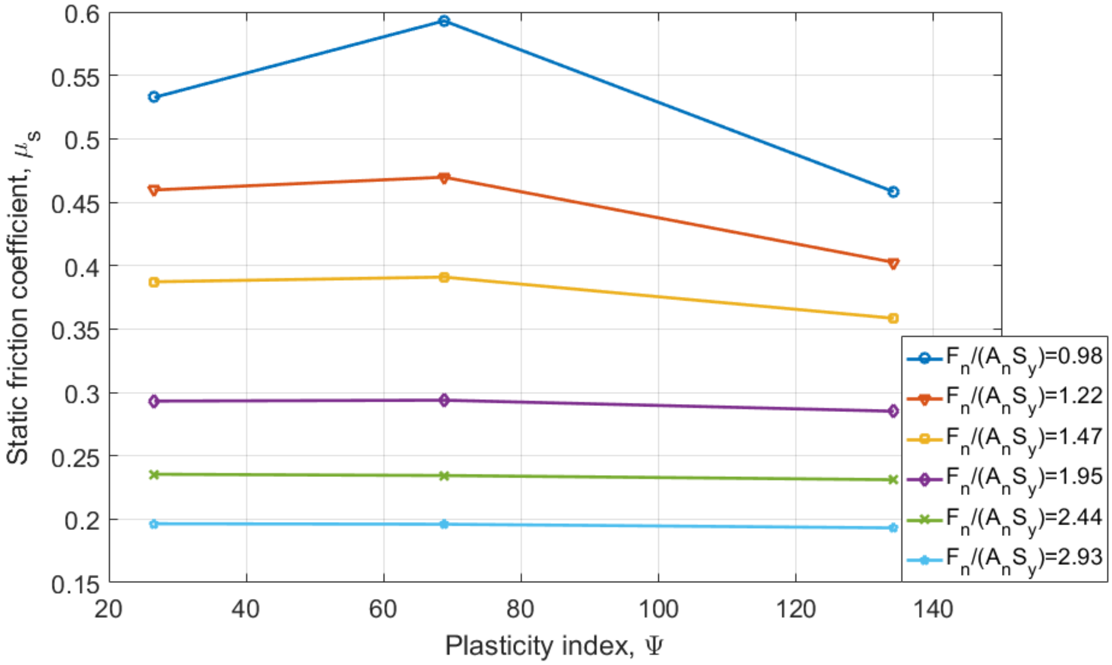

Fig. 6.37. Static friction coefficient versus plasticity index for Surface 2L, 8L and 32G with no strain hardening.

Then, the static friction coefficient versus normal load is plotted in Fig. 6.36. As expected, these surfaces show the same trend: the static friction coefficient decreases as the dimensionless normal load increases. From Fig. 6.36, under very high loads, these curves become very close. The same data set is plotted in Fig. 6.37. Fig. 6.37 shows that the static friction coefficient as a function of the plasticity index under different normal loads. As we found in the section 6.4.2, for the low plasticity indices with bilinear strain hardening material, the static friction coefficient decreases with increasing plasticity index (see Fig. 6.29). As can be seen from Fig. 6.37, which is very different from those cases, for very high loads, the static friction decreases very slowly and is nearly a constant. This trend agrees with the LET model. But for lower loads, the static friction coefficient for the surface with higher plasticity indices can be less than, equal to or greater than the static friction coefficient of the surface with lower plasticity indices.

6.5. Conclusion

A finite element model was used to simulate the sliding inception of a rigid flat loaded against a deformable solid with different rough surfaces under combined normal and tangential loading. The effects of different parameters on the contact area and static friction coefficient were studied. It is observed that the static friction coefficient decreases as the dimensionless normal load and plasticity index increases. The FEM results were compared with several statistical static friction models, and confirm their trends on the prediction of static friction coefficient. However, the quantitative predictions are rather poor for some cases. In most cases, the statistical model predictions of contact area and static friction are lower than the FEM predictions. In this study, we also found that the strain hardening considered by the tangent modulus, E_t, can increase the contact area and decrease the static friction coefficient. Considering the material without strain hardening, the contact area and static friction of rough surfaces with higher plasticity indexes under high loads were investigated. The static friction coefficient for the surface with higher plasticity indices can be greater or less than the static friction coefficient with lower plasticity indices for some cases, it depends on the normal load. However, the difference is not significant.

CHAPTER 7. A MULTI-SCALE ROUGH SURFACE STATIC FRICTION MODEL

7.1. Introduction

Considering the influence of multi-scale structure, Archard [16] suggested that the asperities of rough surfaces can be modeled as “protuberance up on protuberance”. By using a similar idea as Archard’s, Ciavarella modeled rough surface contact using the two-dimensional elastic sinusoidal solution given by Westergaard [18]. Also based on Archard’s work, Jackson and Streator (JS) [19] developed a non-statistical multi-scale model of normal contact between rough surfaces. They used a stacked 3D sinusoidal geometry to represent the asperities in contact at each level of the surface, and predicted the real contact area as a function of the normal contact load. The central idea of the JS model is that a surface can be decomposed into stacks of sinusoidal waves with different amplitudes and wavelengths, as shown in Fig. 7.1. Each frequency is considered a scale or layer of asperities which are stacked iteratively upon each other. The Fourier transform was used to convert the data into a series of stacked sine and cosine waves. The amplitudes at each frequency are calculated from the complex terms and their conjugates from the Fourier transform.

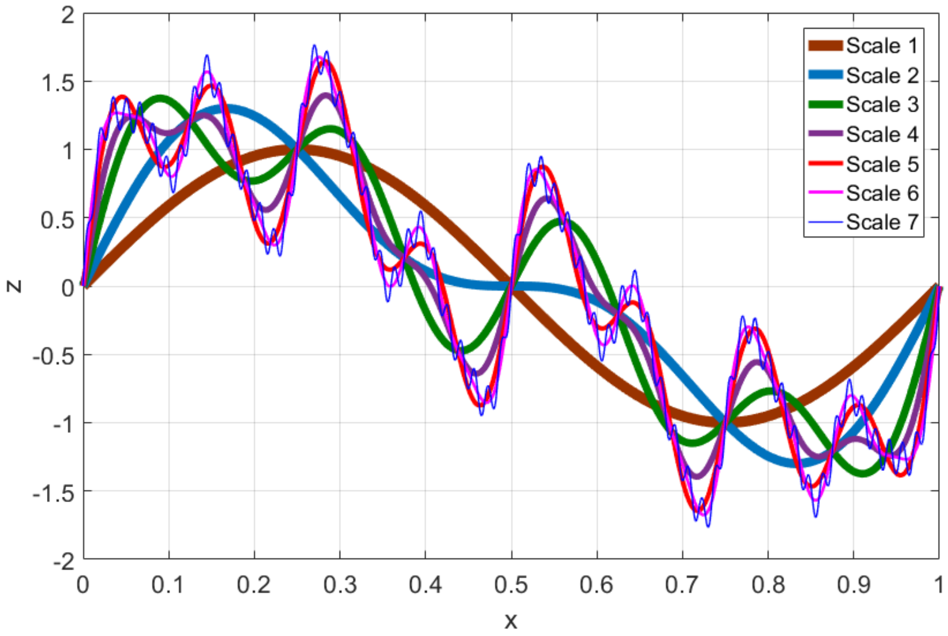

Fig. 7.1. A schematic depicting the decomposition of a surface into superimposed sine waves.

The basic assumptions of the JS multi-scale model are:

(1.) Smaller asperities are located on top of the larger asperities.

(2.) Each scale level of asperities carries the same total normal load

(3.) At each scale level, all the asperities at this level shares equally the normal load equally.

(4.) The contact area at a given scale level cannot be greater than the contact area at a larger scale.

Based on the assumptions, each frequency level of asperities carries the same total load, and the load at each scale level is sheared equally among all the asperities at that level. Following this, the contact area is then calculated iteratively using the factorial equation:

$$A_r = \left(\prod_{i=1}^{i_{max}} \bar{A}_i \eta_i \right) A_n \tag{7.1}$$

where A_r is the real area of contact, $\bar{A}$ is the contact area of a single asperity on a certain scale of roughness, η is the real asperity density, A_n is the nominal contact area, and the subscript i denotes a specific asperity scale level, with i_{max} denoting the smallest scale level considered. Since each scale shares the same the total load, F_n, the single asperity load at the i_{th} scale can be related to the total load by

$$F_n = \overline{F}_{n_i} \eta_i A_{i-1} \tag{7.2}$$

The parameters in Eq. (7.2) can be obtained after performing the fast Fourier transform, where η is the asperity areal density and given by

$$\eta_i = 2/\lambda_i^2 \tag{7.3}$$

Each frequency level is modeled using a sinusoidal contact model, for elastic contact, the JGH model (Eqs. (3.2) and (3.3)) and the fitted equations (Eqs. (3.4) and (3.5))) are used. For elastic-plastic contact, the FEM based equations in [48, 58] can be used.

Since the JS model needs solving numerically by multiple interactions, Jackson simplified it to a closed form equation for the rough surface contact [49]. He assumed that the real contact pressure is equal to the maximum complete contact pressure of the surface. If the contact pressure is less than the complete contact pressure, ($p^* or\ p_{ep}^*$), at a particular scale, this scale will reduce the contact area. As the scales are included, the contact pressure will keep on increasing until it overcomes the complete contact pressure at the remaining smaller scales. He found the real contact area is related to the ratio of the maximum amplitude to the wavelength ratio found for the spectrum of the surface, which is derived from Eq. (3.13)

$$B_c = \frac{\sqrt{2} S_y}{\pi E' \left[3e^{-2(\nu+1)/3} + 2\left(\frac{1-2\nu}{1-\nu}\right) \right]} \tag{7.4}$$

and when $B < B_c$ the contact is in the elastic range, the contact area can be obtained by the equation

$$(A_r)_{elastic} = \frac{F_n}{\sqrt{2}\pi E' B_{max}} \tag{7.5}$$

where B_{max} is the maximum value of the ratio of amplitude over wavelength, Δ/λ.

when $B > B_c$ the contact is in the elastic-plastic range, and the contact area can be obtained by the equation

$$\mathrm{A_r} = \frac{F_n}{\left(p_{ep}^*\right)_{B_{max}}} = \frac{F_n}{\sqrt{2}\pi E' B_{max} \cdot 0.992^{\left\{\left(\frac{B_{max}}{B_c}\right)^{\left[\frac{10}{3}\left(\frac{B_{max}}{B_c}\right)^{-0.39} + \frac{9}{4}\nu^4 + 0.64\right]_{-1}}\right\}}} \tag{7.6}$$

with B_c being given by Eq. (7.4). Here, $B_{max}$is the maximum ratio of amplitude to wavelength.

7.2. Multi-scale Contact Model

7.2.1 Methodology

As discussed previously, the rough surface data set used for this model is converted into a serious of stacked sine waves using the Fourious Transfrom. All calculations for the model are then made based on the amplitude and wavelength of these sinusoidal waves.

The MATLAB command “fft2 (z, $\mathrm{N}_x, \mathrm{N}_y$)” is used to perform the Fourier transform. This command is the two-dimensional Fourier transform of a matrix using a fast Fourier transform algorithm. N_x and N_y are the number of the points in the *x* or *y* directions. The FFT converts the surface height matrix into a complex-valued matrix. i.e. $z_f = \text{fft2 }(\mathrm{z}, \mathrm{N}_x, \mathrm{N}_y)/(4\mathrm{N}^2)$. The amplitude of the matrix can be obtained from $\Delta = abs(z_f)$ or $\Delta = z_f \cdot \mathrm{conj}(z_f)$. However, the method to obtain the amplitudes discussed in the section 7.1 is just for a 2D profile. A single amplitude for each scale level is required while multiple amplitudes will result for a 3D surface.

An equivalent 2D equivalent amplitude was calculated by using a two-sided amplitude spectrum method developed by Rostami and Streator [123]. A single-side spectral method is found more convenient to calculate amplitude. The equivalent amplitude can be obtained by the expression:

$$\Delta_k = \frac{1}{2}\left[\sqrt{\sum_{k_x=1}^{N_x/2}\left|z_f(K_x, K)\right|^2} + \sqrt{\sum_{k_y=1}^{N_y/2}\left|z_f(K, K_y)\right|^2}\right] \tag{7.7}$$

The wavelength can be obtained by: $\lambda_k = L/k$, where L is the scan length. For example, the wavelengths of the first and second scale level are L and $L/2$, respectively. The surface 2L is used to develop the friction model. The scan lengths in the x and y directions are both 127 μm, and the total number of the points in the area is 16384 (128 points in each direction) The resulting amplitude versus wavelength curve is plotted in Fig. 7.2. and the resulting amplitude to wavelength ratio versus wavelenth is plot in Fig. 7.3. From Fig. 7.3, the effective amplitude is normalized by the wavelength. The amplitude to wavelength ratio has a decreasing trend with the increasing wavelength. This trend is what is expected for a self-affine multi-scale surface structure, as discussed in Jackson [49].

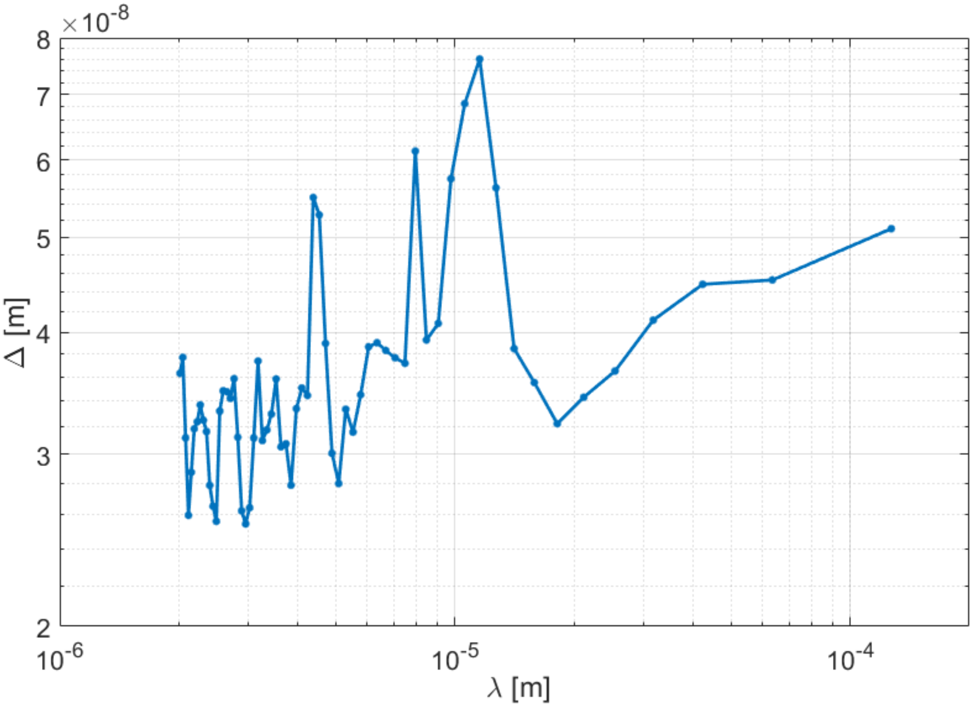

Fig. 7.2. Resulting amplitude versus wavelength for the surface 2L.

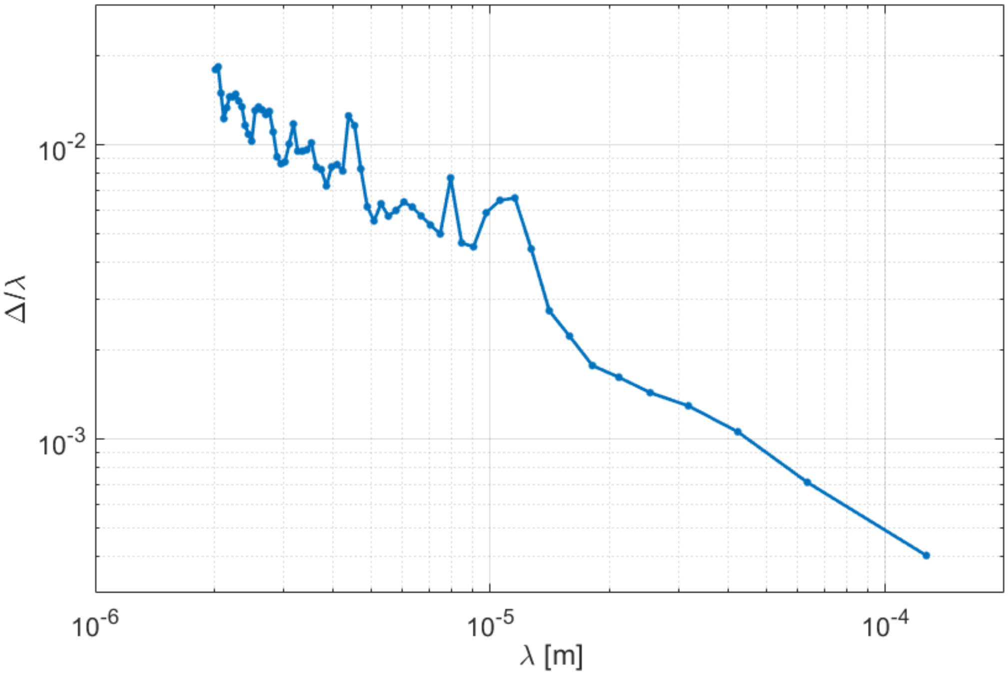

Fig. 7.3. Resulting amplitude/wavelength versus wavelength for the surface 2L.

7.2.2. Results and Discussion

Again, there are two loading steps: first, a normal preload was applied on the rigid flat; Then normal load is held constant, and a lateral displacement is applied and increased gradually. In the first normal loading step, the same assumptions in [19] are used and noted. Based previously on the frame work [19] discussed in the section 7.1, the real contact area of the rough surface can be obtained as a function of the normal load. While initially neglect frictional load, for the elastic contact, the JGH model (Eq. (3.2) and (3.3)) and fitted equation equations (Eq. (3.4) and (3.5)) are used to predict the contact area on each frequency level. For the elastic-plastic contact, the multi-scale framework incorporates the KJ model [58], Jackson et al. [48] and Ghaednia et al. [55] analysis to consider the asperity contact on each scale level.

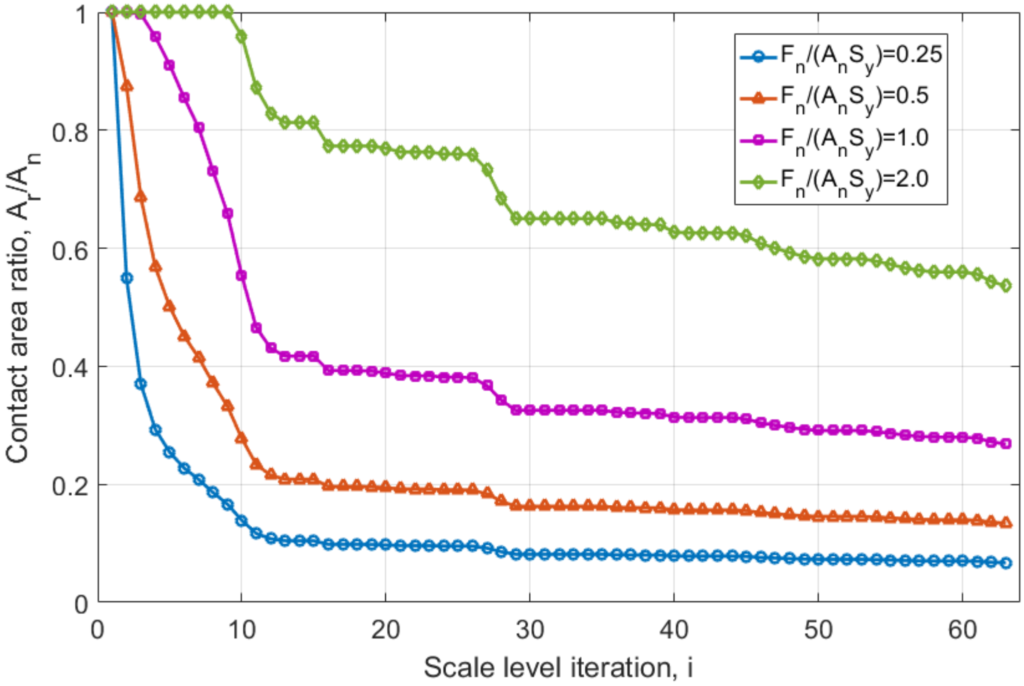

Fig. 7.4. Predicted contact area as a function of considered scale levels under different contact normal loads for surface 2L.

In order to verify the multi-scale model, the contact area predicted by the model as a function of scale level interation under different normal loads is plotted in Fig. 7.5. Fig. 7.5 shows that the scale levels cause contact area to decrease. At the same scale level, contact area increaes as the dimensionless normal load increases. For the surface 2L, the contact scale is at the smallest scale.

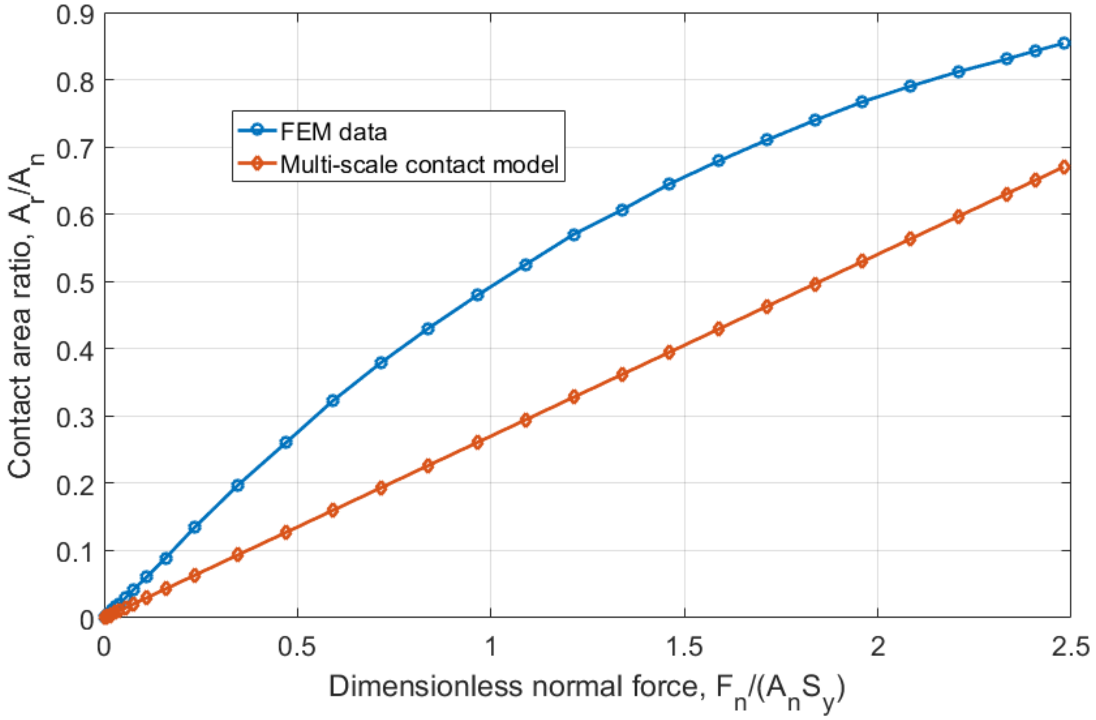

Fig. 7.5. Comparison of contact area between FEM results and the multiscale contact model for surface 2L.

The prediction of contact area are then compared with FEM results for under only normal preload, the multi-scale model is compared with the FEM results of rough surface 2L that was obtianed in Chapter 6 for elastic-plastic contacts. As discussed in Chapter 6, the employed material properties are an elastic modulus, E, of 200 GPa, Poisson's ratio, ν, of 0.3, yield strengh, S_y, of 1 GPa and a tanget modulus, E_t, of 2% of the elastic modulus. The comparison between the multi-scale model and FEM results are plotted in Fig. 7.6. They show a similar trend, and are in reasonable agreement. However, the multi-scale model predicts a more linear relationship between contact area and pressure than the FEM results.

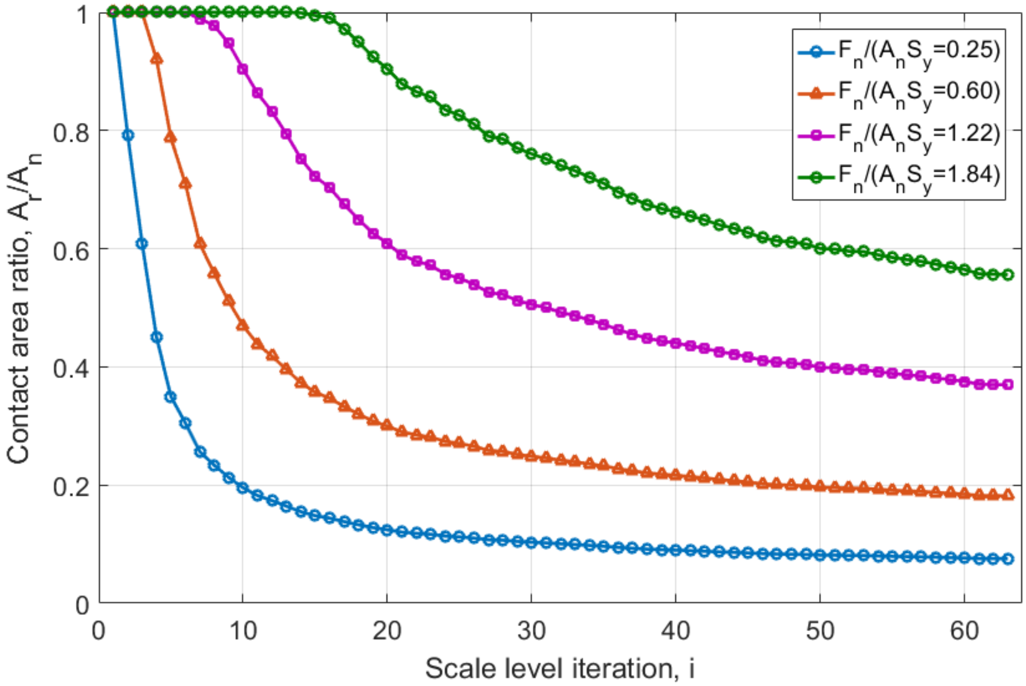

Fig. 7.6. Predicted contact area as a function of considered scale levels under different normal loads for Surface G5.

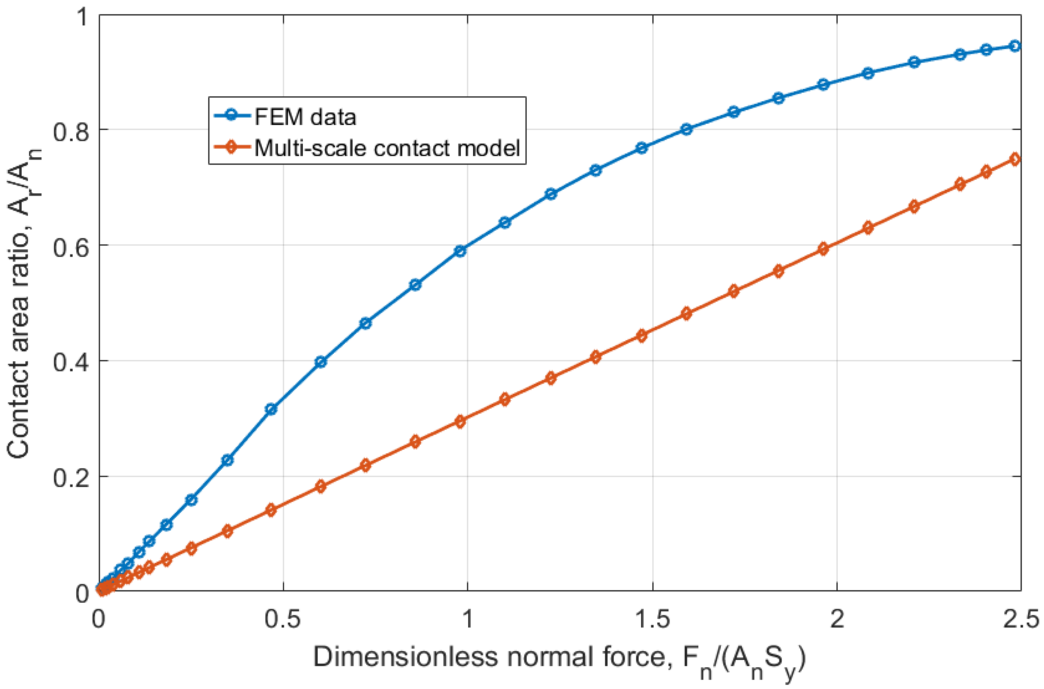

Fig. 7.7. Comparison of contact area between FEM results and the multiscale contact model for surface G5.

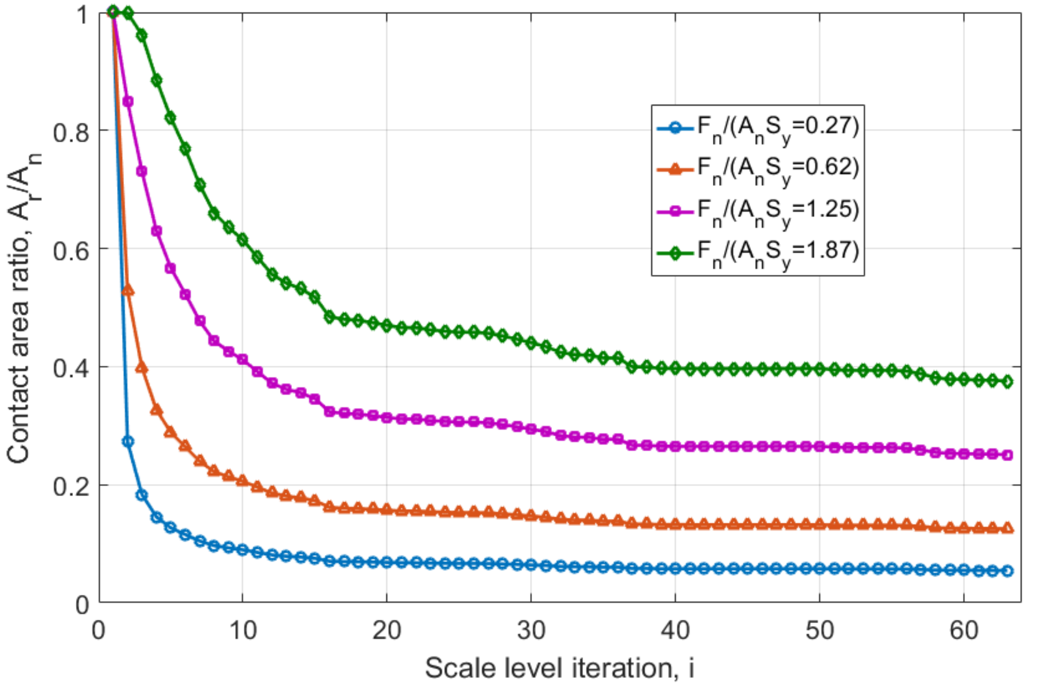

Fig. 7.8. Predicted contact area as a function of considered scale levels under different contact normal loads for surface 8L.

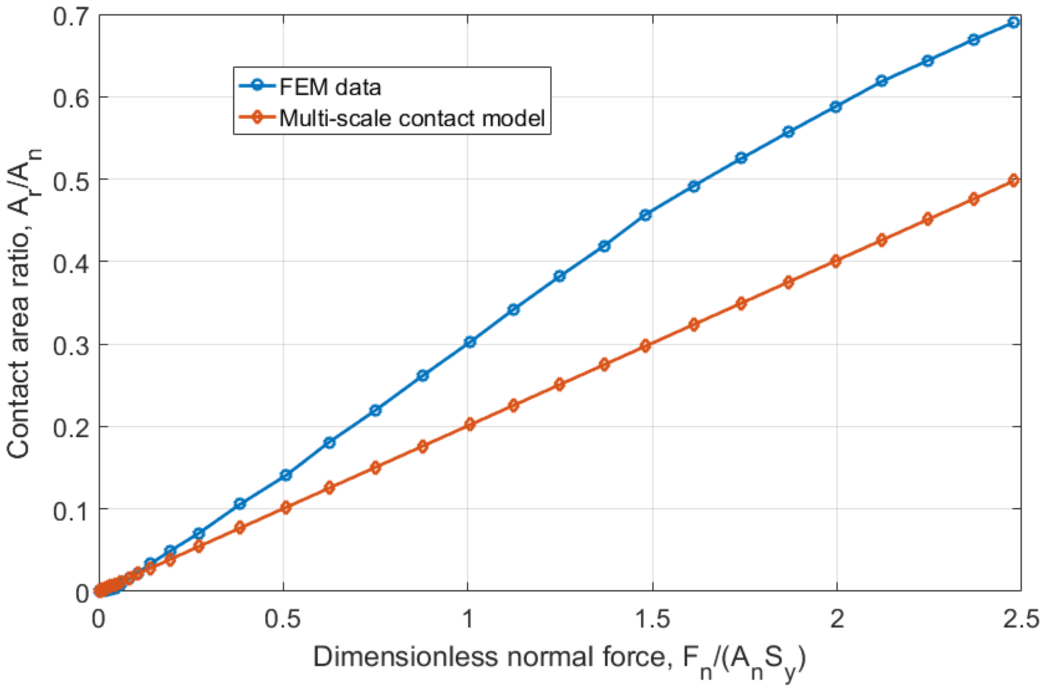

Fig. 7.9. Comparison of contact area between FEM results and the multiscale contact model for surface 8L.

Surface G5 and 8L are also used to compare the predicted results for only a normal load as well. The contact area decreases as the iteration increases, and converges to a constant value (see Fig. 7.6 and Fig. 7.8). As expected, the comparison between the multi-scale model and FEM results show that the FEM results and multi-scale models show a similar trend, and are in a reasonable agreement (see Fig. 7.7 and Fig. 7.9). However, they still have some differences. The FEM results are higher than the predictions of the multi-scale model except lower loads.

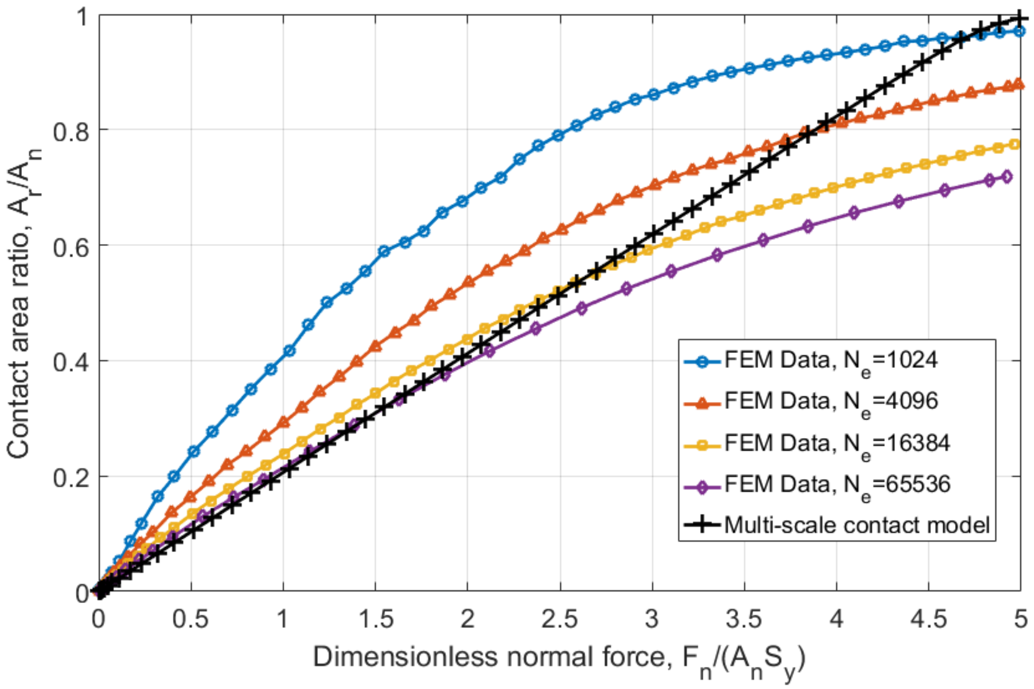

Fig. 7.10. Comparison of contact area between FEM results and the multiscale contact model for surface 63M and interpolated surfaces.

The elastic-plastic contact of both the original surface and interpolated surfaces from surface 63M are investigated. The applied load varied over a wide range. The the multi-scale model are compared to FEM results, and are plotted in Fig. 7.10. As can be seen from Fig. 7.10, as the number of contact elements increases, the results approaches the multi-scale model at loads $F_n/(A_nS_y) \leq 2.2$. The multi-scale matches the FEM results for $N_e = 65536$ the best.

7.3. Multi-scale Stactic Friction Model

The following will describe how the JS multi-scale model is modified to predict the effect of tangential load and friction. The maximum shear stress criterion is used to determine the sliding inception. As discussed in Chapter 4, when the frictional shear stress on one asperity in contact reaches the critical interfacial shear strength, local sliding occurs. Once all the asperities in contact slide, the entire surface starts sliding. Considering junction growth, the contact area at sliding inception at each scale are analyzed, and the sliding contact area at sliding inception of the rough surface can be obtained.

7.3.1. Methodology

In the second loading step, based on the assumptions of the normal stacked friction model, two assumptions are added:

(5.) Each scale level of asperities carries the same tangential total load.

(6.) At each scale level, all the asperities at this level shared the load equally.

(7.) The shear stress at a given scale level cannot be less than the shear stress at a larger scale.

To illustrate in more detail how the multi-scale driction model is used to model static friction, a flow chart is given in Fig. 7.11.

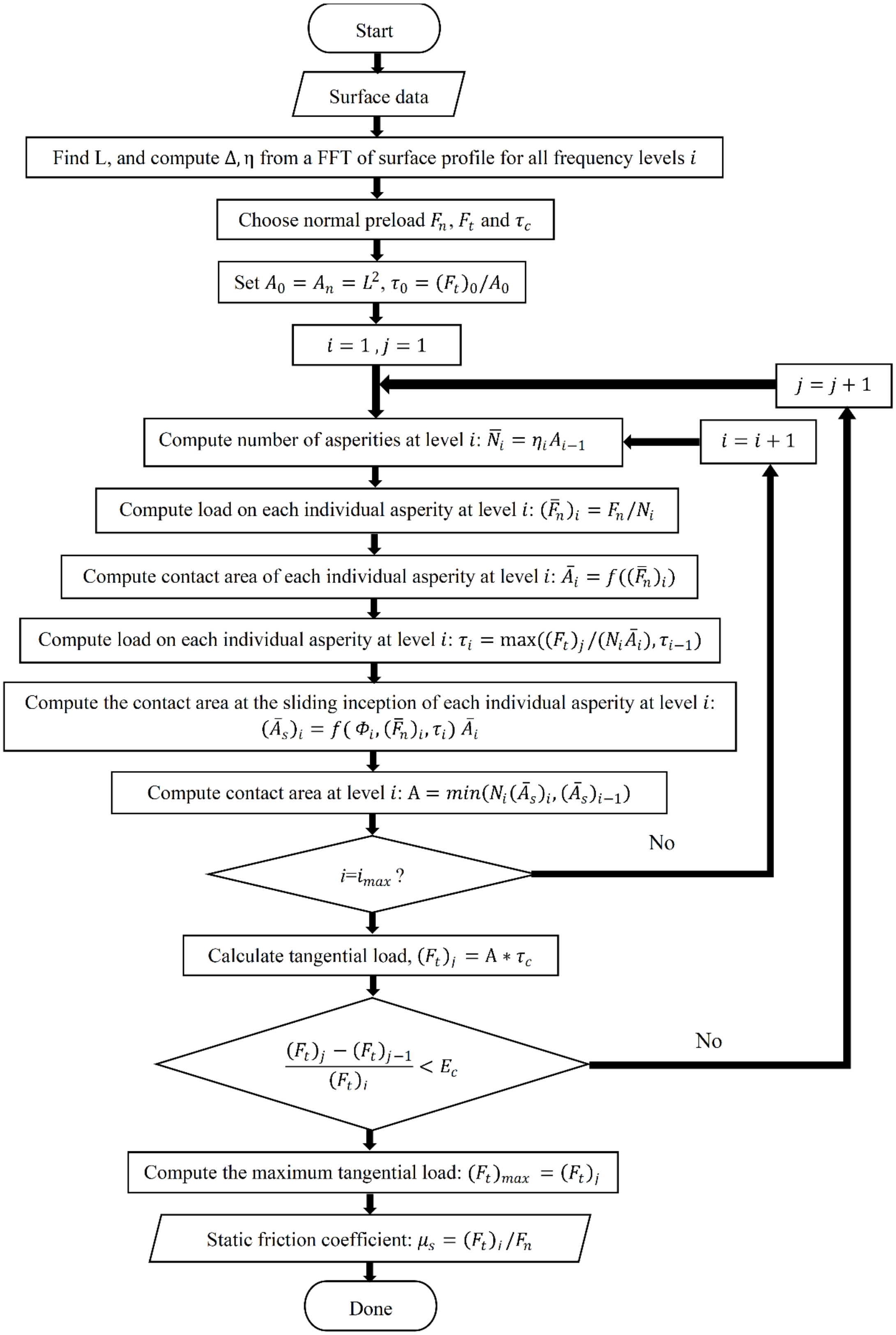

Fig. 7.11. Flow chart of the proposed multi-scale friction model.

The main procedure is listed below:

1.) Praparation. Select and scan the rough surface data, and perform an FFT.

2.) Find the parameters required at each scale level. Find the scan length for the x and y directions, L, calculate equivalent amplitude, Δ, using Eq. (7.8). Calculate asperity density, η, using Eq. (7.3).

3.) Apply a normal force, F_n and tangential shear stress, τ.

4.) Set the initial values: nominal contact area, A_n and critical shear strength, τ_c.

5.) Iterates to find the contact area at sliding inception

- Start interation from $j = 1$.
- Start interation from $i = 1$.
- Compute the number of asperities at scale level 1.
- Compute the normal force applied on each asperity at scale level 1. The total normal load is divided evenly among all the asperities of this level.
- Compute contact area of each individual asperity at level 1 by using Eqs. (3.12) - (3.17) for elastic-plastic contact. The single contact area is determined by a given load, geometric parameter and set of material properties.
- Compute shear stress at level 1, keeping with assumption #7, the shear stress at scale level 1 can be obtained by $\tau_1 = \max((F_t)_0/A_1, (F_t)_0/A_n)$.
- Compute the contact area, $(A_s)_1$, at the sliding inception of each individual asperity at level 1 using Eq. (4.12). This step considers junction growth.
- Updata contact area at level 1, keeping with assumption #4, make guarantee that the contact area at a given scale level could not be greater than the values of the larger scales below it. i.e. choose the small values. $A_1 = \min((A_s)_1, A_0)$.

- End current iteration and start the next interation for $i = 2$, calculate contact area at scale level 2.
- Repeat iteration untile the scale number reaches i_{max}.
- keeping with assumption #5 and assumption #6, tangential load at each scale level are the same, so it is enough to calculate the tangetial force at the contacting scale, by using contact area times critical shear strength.
- Start next iteration for $j = 2$.
- Repeat these procedures iteratively until the $((F_t)_j - (F_t)_{j-1})/(F_t)_j$ is below a small constant value E_c. At that moment, the tangential load is the maximum tagnential load.

6.) Compute the static friction coefficient of the rough surface, $\mu_s = (F_t)_j/F_n$.

7.3.2. Results and Discussion

Based on the procedure introduced in Section 7.3.1, the contact area is investigated firstly. Again, the surface 2L under dimensionless normal load $F_n/(A_n S_y) = 0.5$ is considered. The predicted contact areas at each scale under only normal load and at sliding inception are plotted in Fig. 7.12. As can be seen from Fig. 7.12, the contact area for both cases, the contact area decreases as the scale becomes samaller, and the differences are the junction growth for each scale.

Considering the assumption 5, each scale level of asperities carries the same tangential total load. The larger scales have smaller contact areas, and lower shear stresses. The predicted shear stress is plotted in Fig. 7.13. The pridicted shear stress increases until it reaches the critical shear strength. The lower scales have smaller shear stress, because the tangetial force is certain, the lower scales have larger contact areas and the resulting lowers stresses. The tangential load causes the junction growth. The increased contact area need more tangential force to overcome the friction. after a few iterations, the tangential force will converge to a constant value (see figure 7.14).

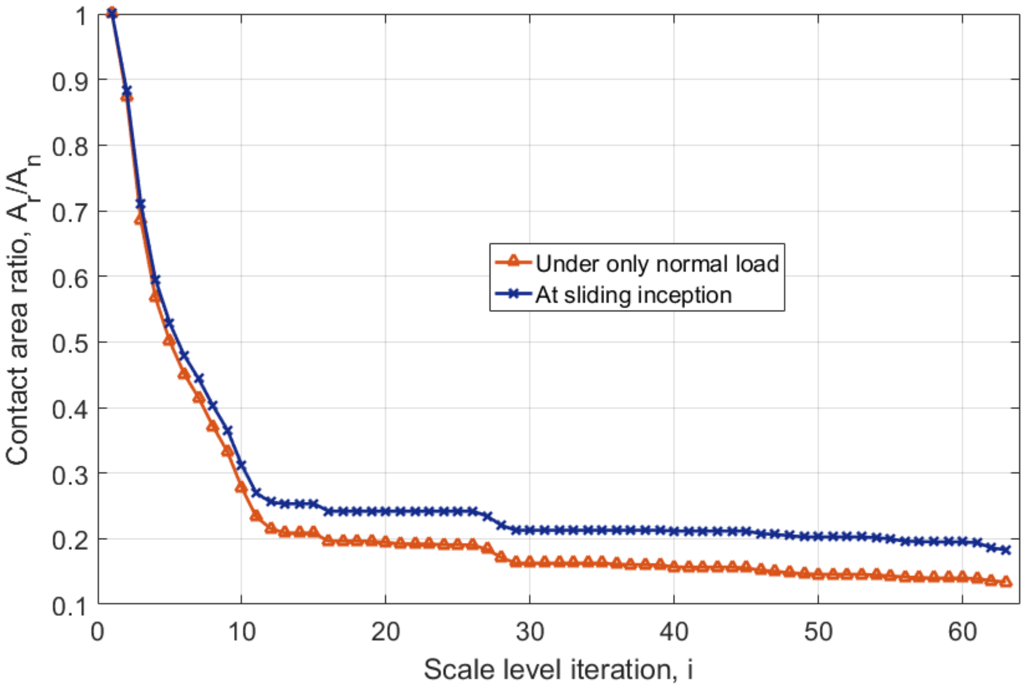

Fig. 7.12. Predicted static friction coefficient as a function of considered scale levels under only normal load and at sliding inception for surface 8L.

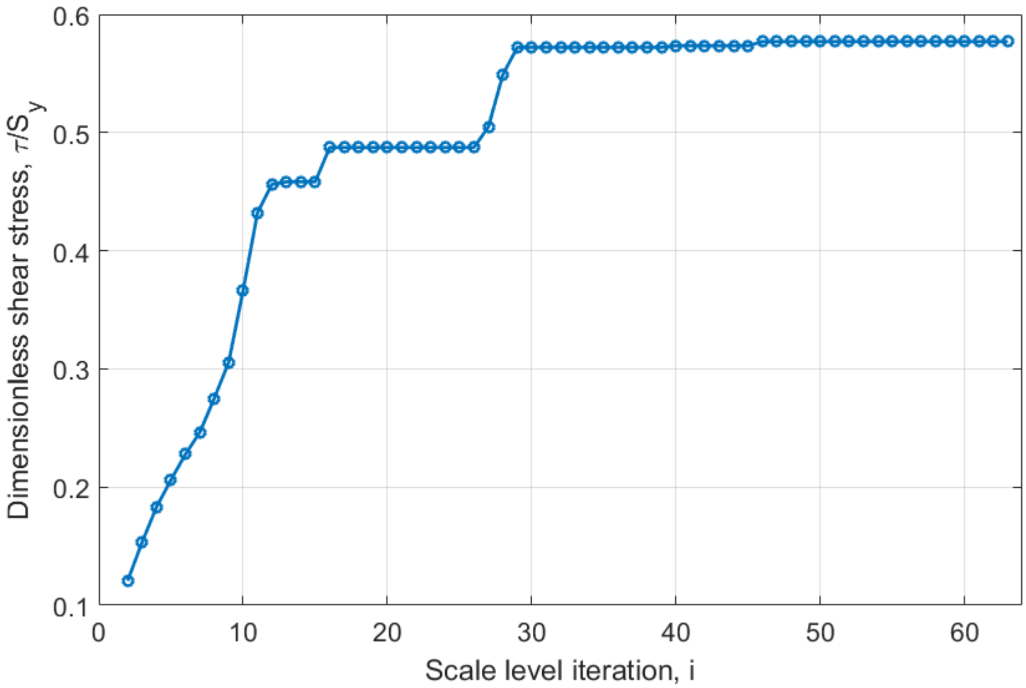

Fig. 7.13. Predicted shear stress as a function of considered scale levels under a dimensionless normal load $F_n/(A_n S_y) = 0.5$ for surface 2L.

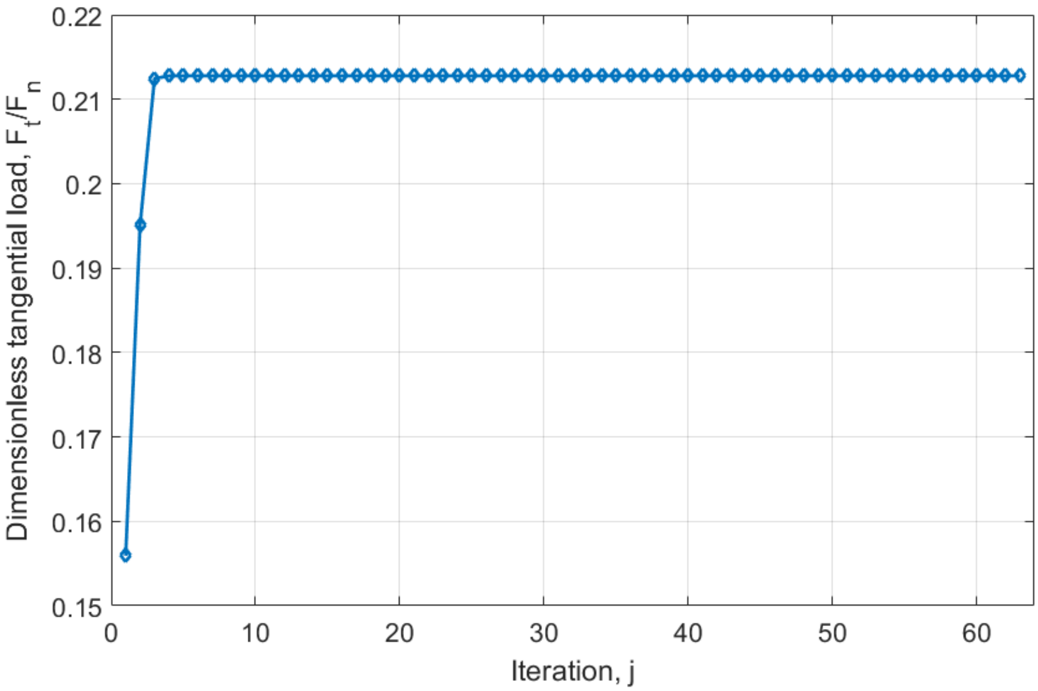

Fig. 7.14. Predicted dimensionless tangential load under a dimensionless normal load, $F_n/(A_n S_y) = 0.5$ for surface 2L.

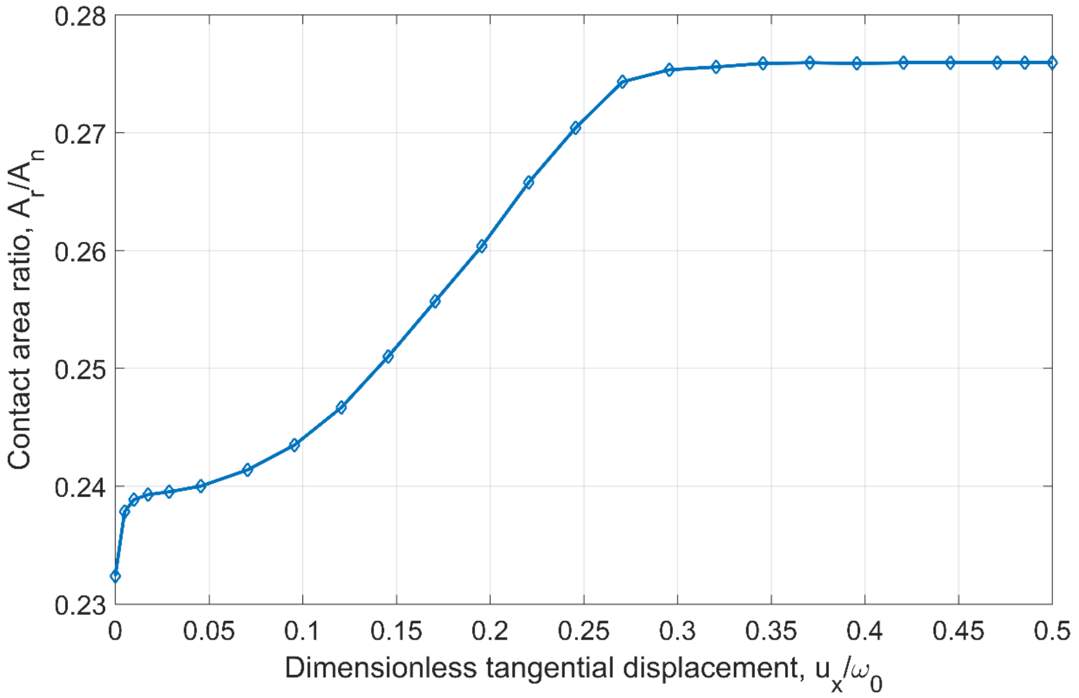

Fig. 7.15. FEM data of contact area evolution under combiend normal and tangential loading for surface 2L.

From the FEM results, the junction growth phenomenon for this case can be observed. As can be seen from Fig. 7.15, as dimensionless tangential displacement increases, the contact area ratio increases, and converge to a constant value at the sliding inception. For this case the increased contact area ratio is 18.75%.

The results produced by the proposed model using the KJ model at the asperity level are compared. A comparison of the predicted static friction coefficient as a function of dimensionless normal load, $F_n/(A_n S_y)$, is made between the proposed multi-scale friction model, the CKE model, LET model and FEM results. As can be seen from Fig. 7.16, the FEM results show a decreasing trend, while the proposed model and the LET model predicts a nearly constant relasionship. The LET model is only valid for lower loads. As the dimensionless normal load increases, the FEM data approaches the proposed model.

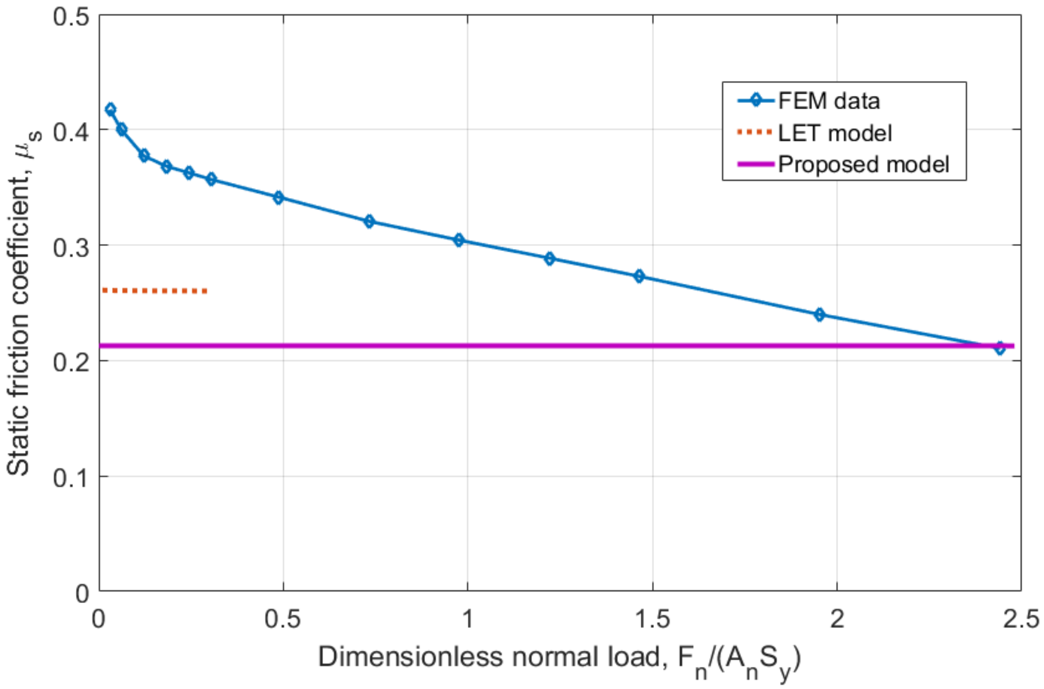

Fig. 7.16. Comparison of static friction coefficient between FEM results, LET model and the proposed multiscale friction model for surface 2L.

The comparison between proposed model FEM results and the LET model for surface G5 and 8L are plotted in Fig. 7.17 and Fig. 7.18, respectively. Intresting, both the proposed model and statistical model predict a constant friction coefficient for the surface G5 and surface 8L. The static friction coefficients predicted by the proposed model fall below the FEM results the LET model. They do not always show the same trend or have a good agreement. This is mainly because the spectrum method decreases the contact area with load. However the FEM results and proposed model predictions are fairly close under heavy normal loads.

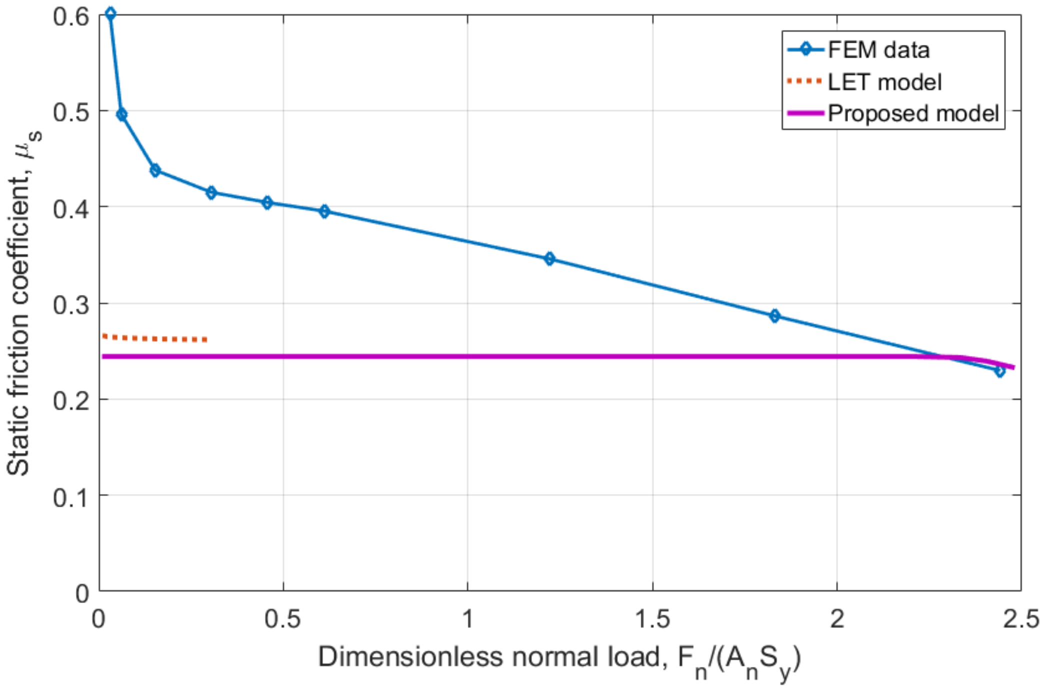

Fig. 7.17. Comparison of static friction coefficient between FEM results, LET model and proposed multiscale friction model for surface G5.

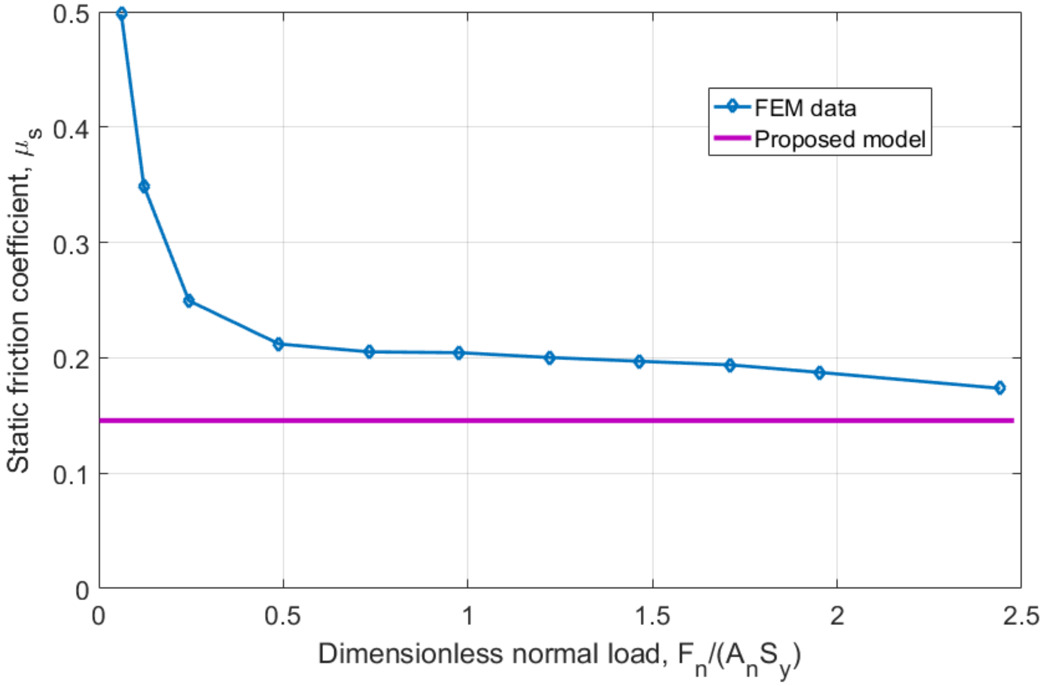

Fig. 7.18. Comparison of static friction coefficient between FEM results, LET model and the proposed multiscale friction model for surface 8L.

In order to investigate the effect of plasticity index on static friction coefficient, the generated Gaussian surfaces G1 to G9 are used in the simulations. The contact area under only normal loading are plotted in Fig. 7.19. As can be seen from Fig. 7.19, under the same normal load, the surfaces with larger plasticity have lower contact area ratios in most of cases. Under the dimensionless nornal load $F_n/(A_nS_y) = 1.86$, the smoothest one (surface G1) has reached the complete contact ($A_r/A_n = 1$).

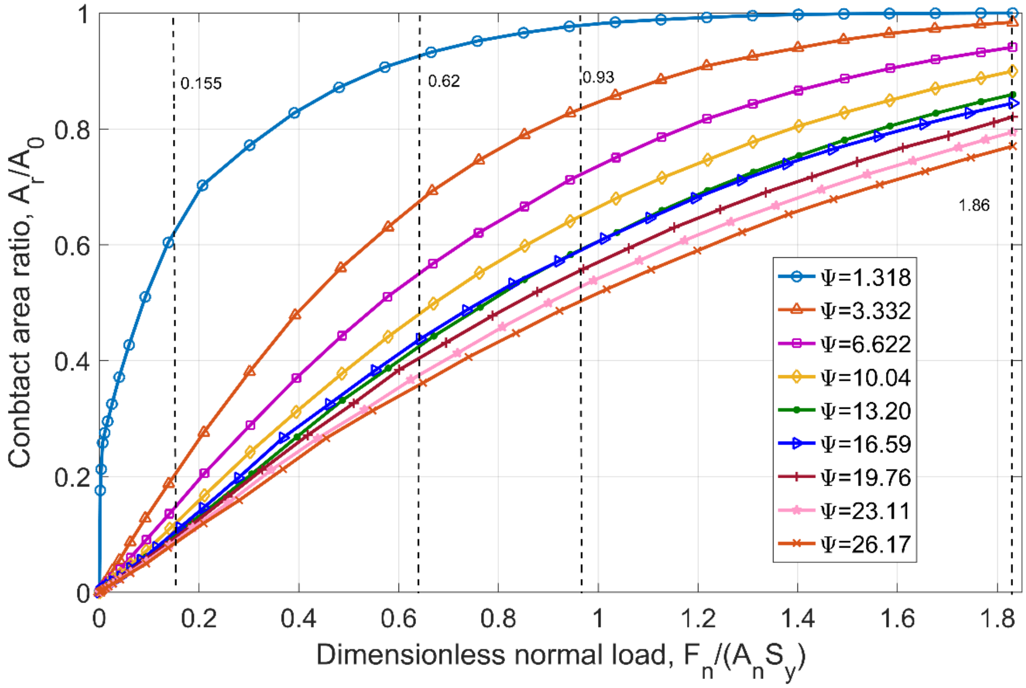

Fig. 7.19. Contact area ratio versus dimensionless normal load for the various surfaces with different plasticity indices.

Fig. 7.20 shows the comparison of static friction coefficient, μ_s, as a function of plasticity index, Ψ, between the proposed model, the CKE model, LET model and FEM results. This case is under low load ($F_n/(A_nS_y) = 0.155$). All of them show the same trend, that the static friction coefficient decreases as plasticity index increases. Note that the static friction coefficient of the surface with $\Psi = 16.59$ is higher than the static friction coefficient of the surface with $\Psi = 16.59$.

Recall that the contact area of the surface with $\Psi = 16.59$ is higher than the contact area of the surface with $\Psi = 13.20$ under dimensionless contact pressure ($F_n/(A_n S_y) = 0.155$) in Fig. 7.19. This confirms that the static friction coeffcient is related to the contact area. The proposed static friction model predictions are lower than the FEM results and higher than or close to the CKE model and LET model for the surfaces with lower plasticity indices (roughly $\Psi \leq 11$). Under high loads, the static friction coefficient becomes below the LET model slightly, and it is still lower than the FEM predictions. Howerver, the proposed multi-scale friction model predictions are less than the FEM results especially under low normal loads.

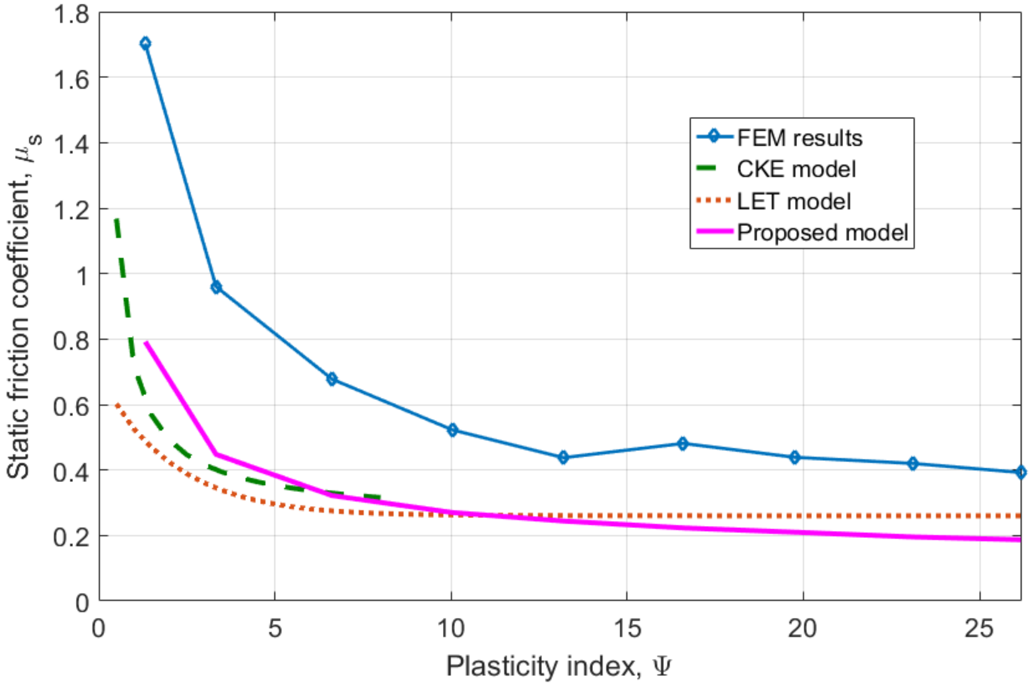

Fig. 7.20. Comparison of static friction coefficient for surfaces with various plasticity indices under a dimensionless normal load $F_n/(A_n S_y) = 0.155$.

Next, the effect of static friction coefficient under heavy loads $F_n/(A_n S_y) = 0.62$ is investigated. Fig. 7.21 shows the comparison of static friction coefficient, μ_s, as a function of plasticity index, Ψ, between the proposed model and FEM results under various normal loads for the surfaces G1 to G9. Under the normal preload $F_n/(A_nS_y) = 0.62$, the multi-scale friction model predicts lower values than the FEM data.

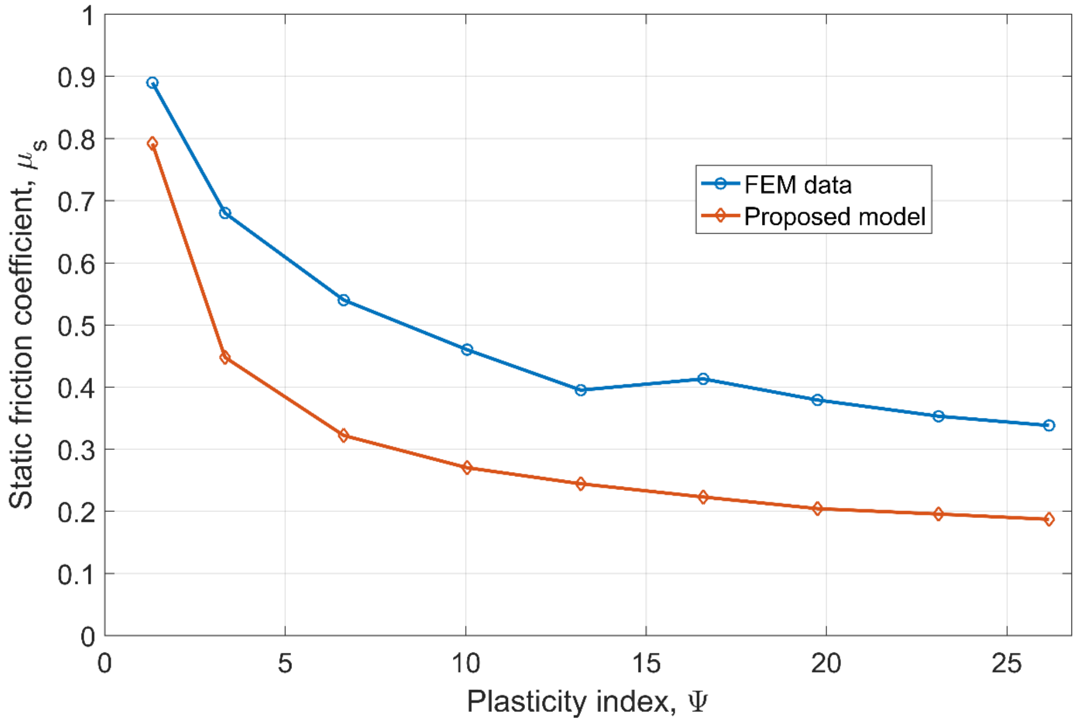

Fig. 7.21. Comparison of static friction coefficient between FEM data and the proposed model for surfaces with various plasticity indices under a dimensionless normal load $F_n/(A_nS_y) = 0.62$.

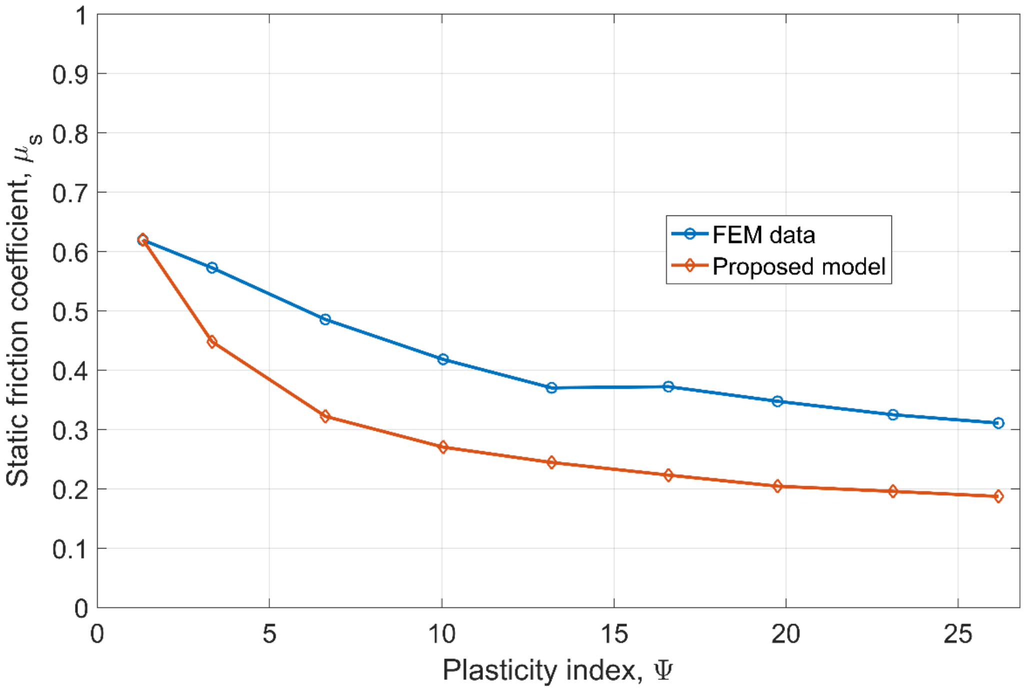

Fig. 7.22. Comparison of static friction coefficient between FEM data and the proposed model for surfaces with various plasticity indices under a dimensionless normal load $F_n/(A_nS_y) = 0.93$.

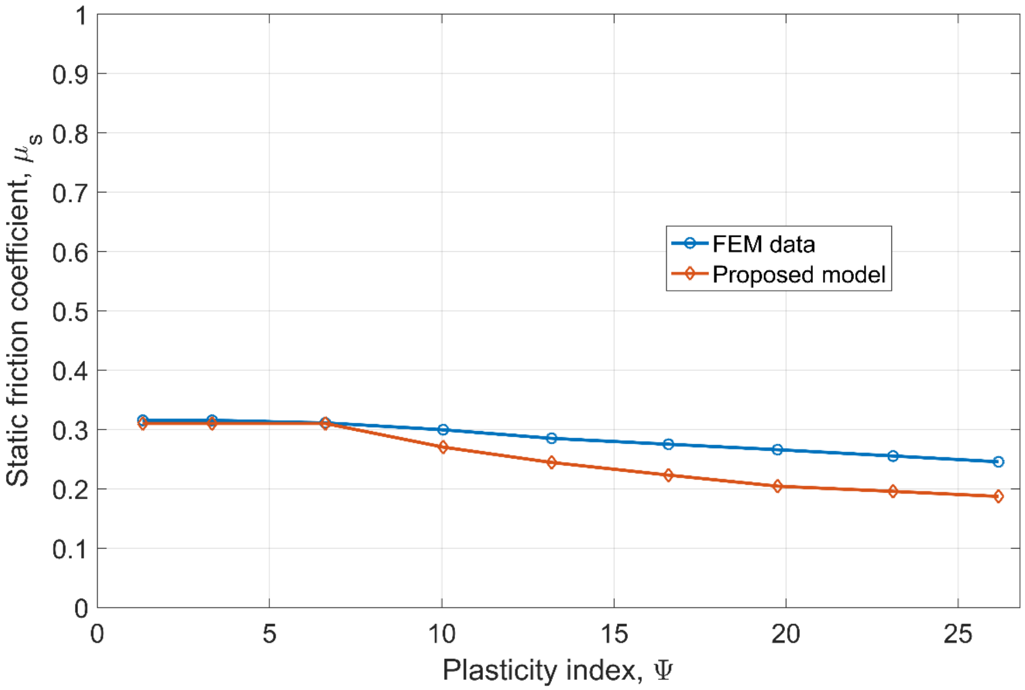

Fig. 7.23. Comparison of static friction coefficient between FEM data and the proposed model for surfaces with various plasticity indices under a dimensionless normal load $F_n/(A_nS_y) = 1.86$.

Much higher loads than in Fig. 7.21 are also applied. The dimensionless normal preload $F_n/(A_nS_y) = 0.93$ is applied firstly. As cen be seen from Fig. 7.22, the multi-scale friction model predicts lower values of the static friction coefficient than the FEM data except for the first point. That is because the contact area of the G1 surface under normal loading is greater than 90%, due to junction growth, the complete contact might be reached. Under the normal preload $F_n/(A_nS_y) = 1.86$, as can be seen from Fig. 7.23, excluding the complete contact cases (the surface G1, G2 and G3 are flattened), the proposed static friction model predicts lower values than the FEM data. It also can be seen that, as the dimensionless normal preload increses, the difference between FEM results and proposed model becomes smaller. The multi-scale model can predict the complete contact accurately, and matches fairly well with the FEM data.

The proposed model has the same trend as the FEM model and theoretical models. There are also still some differences between them. The proposed multi-scale friction model predicts lower values than the FEM data. However, as discussed previously the proposed model is not in a good quantititive agreement with FEM results at lower loads (see Figs. 7.15- 7.17). Fig. 7.24 shows the contact area for surface 8L under the normal loads $F_n/(A_nS_y) = 0.06$ and $F_n/(A_nS_y) = 0.12$, respectively. The red color presents the local contact areas. The numbers of local contact areas and contact nodes are plotted in Fig. 7.25. As the dimensionless normal load increases, the numbers of contact nodes increase while the number of local contact area increases until it becomes a nealy constant. Note that the results in Figs 7.25 are not normalized so that the differentces between them can be seen more easily. The ratio of numbers of contact nodes to thelocal contact area is plotted in Fig. 7.26. From Fig. 7.26, as the dimensionless normal load increases, the ratio nealy increases. The ratio is below 4 under the dimensionless lower normal loads 0.06 and 0.12, i.e.

there are only less than 4 contact nodes for each contact area. This probably cause accuracy problem in ANSYS.

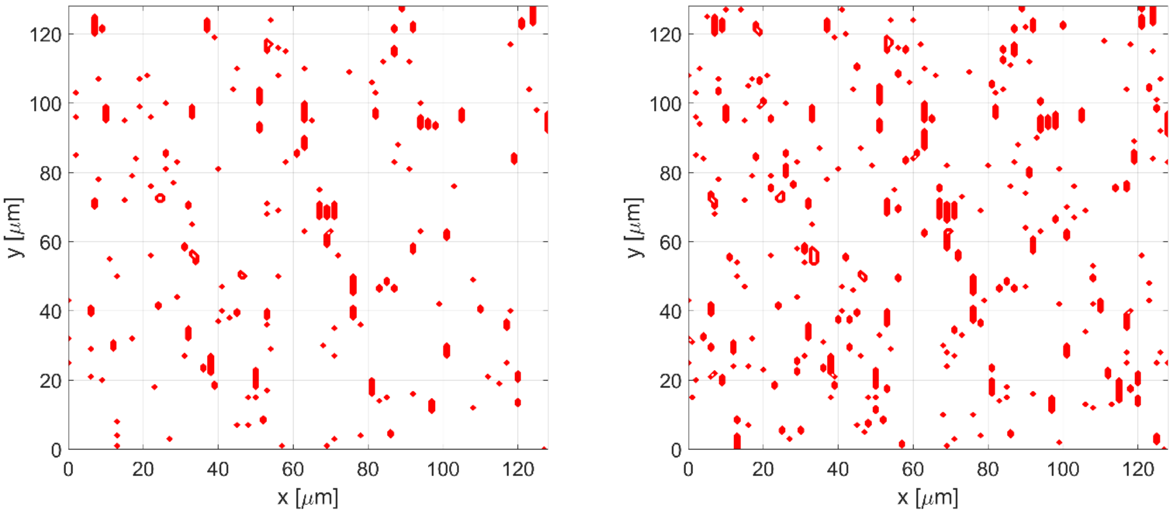

(a) $F_n/(A_n S_y) = 0.06$ (b) $F_n/(A_n S_y) = 0.12$

Fig. 7.24. Contact area under dimensionless normal loads for surface 8L.

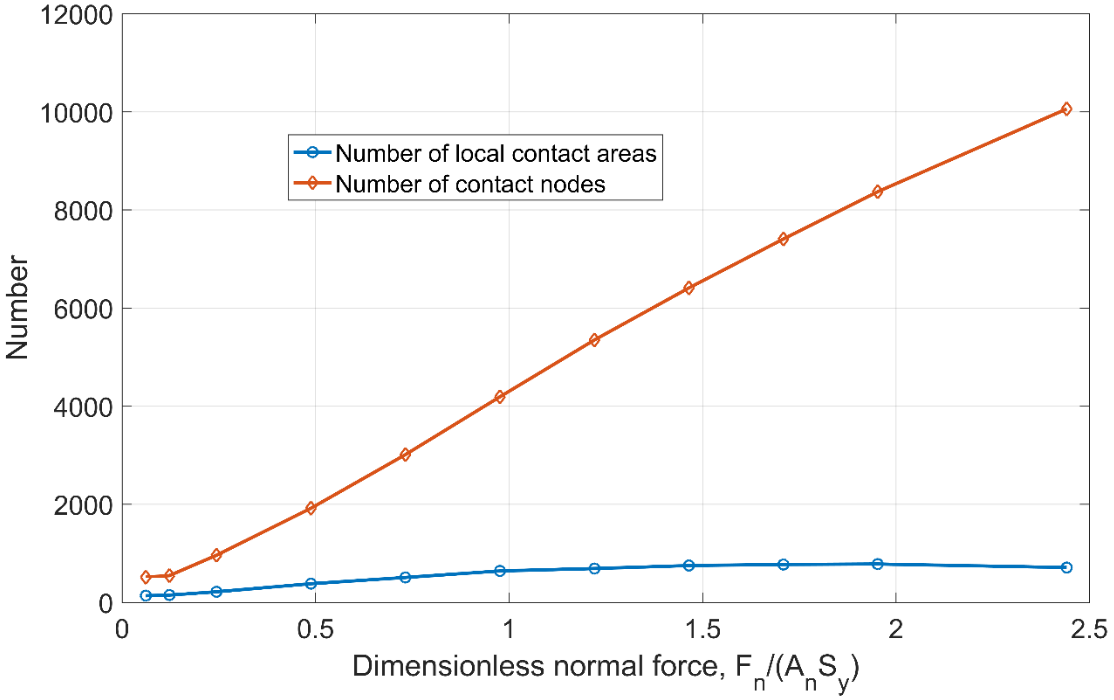

Fig. 7.25. Number of local contact areas and nodes versus dimensionless normal load for surface 8L.

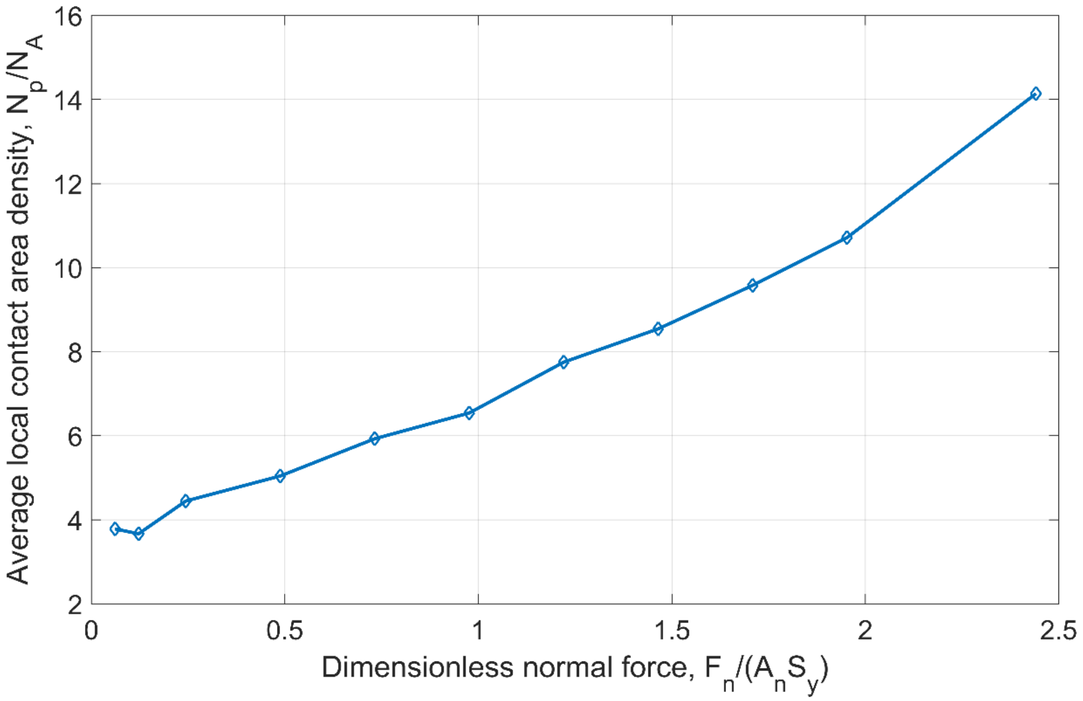

Fig. 7.26. Average local contact area density versus dimensionless normal force for surface 8L.

7.4. Conclusion

Since most existing friction models [13, 15] have limitations on the range of normal load and plasticity: $F_n/(A_n S_y) \leq 0.3$ and $\Psi \leq 32$, a model for the static friction of rough surfaces for a wide range of normal loads and plasticity indices was developed, which an attempt to capture the multi-scale features, and elastic-plastic deformations.

First, the contact area of FEM results, under normal load only are compared with the JS multi-scale contact model. They have the same trend and reasonable agreement. However, they also show some differences. The JS multiscale model predicts lower values than the FEM data.

Next, this study formulates an iterative multi-scale friction model framework for modeling friction between rough surfaces, which uses the Fourier series based representation of the rough surface. Second, the comparison of the predicted static friction coefficient between the proposed model, statistical models and FEM results are made. Firstly, the effect of normal load on the static friction coefficient is analyzed. In this step, the surface 2L, surface G5 and surface 8L were used in the FE models. The FEM results show a decreasing trend, while the proposed friction model and statistical models predict constant values. The proposed model predictions are lower than the FEM results and theoretical models. Then, the effect of plasticity index on the static friction coefficient is analyzed. In this step, 9 generated Gaussian surfaces with various plasticity indices under a wide range of normal loads are used in the simulations. The proposed model shows the same trend as the theoretical models and FEM results: as the plasticity index increases, the static friction coefficient decreases. The proposed model predicts lower static friction coefficients than the FEM results, while the predictions are close to the theoretical models under normal loads. The difference of static friction coefficients between the proposed model and FEM results becomes smaller with increasing normal load.

Overall, the proposed model, theoretical models and FEM results are in a good qualitative agreement, especially for higher loads and higher plasticity indices. The proposed friction model also can predict the complete contact accurately. However, the proposed model and FEM results show a big difference for the cases with lower loads and lower plasticity indices. This might be because of the elaborate problem in the ANSYS.

CHAPTER 8. CONCLUSIONS AND FUTURE WORK

8.1. Summary and Conclusion

Friction is an important and complex physical phenomenon, and modeling friction contacts is a challenge due to the complicated multiple scales of features on surfaces. Many researchers have developed different kinds of models to solve this problem. Most existing friction models are based on a statistical treatment that incorporates the results of a single asperity into a statistical representation of surface roughness. These models can be applied to macroscale rough surfaces after a statistical summation procedure. However, this technique requires the statistical characterization of a surface's roughness and asperity height distribution. Recently, multi-scale models and deterministic models have been developed to analyze the behaviors of elastic-plastic normal contact between rough surfaces. However, very little work has been done by using multi-scale models or deterministic models to predict friction. In this study, the contact between a three-dimensional deformable rough surface and a rigid flat were investigated by using both a multi-scale model and a deterministic model, and the results were compared. However, some intermediate steps are required before reaching this goal.

Firstly, the contact behavior of a single three-dimensional sinusoidal asperity under normal loading were investigated for both elastic and elastic-plastic cases. For the elastic case, the complete contact pressure, general stress distribution, maximum von Mises stress and critical amplitude under the full stick condition were investigated analytically. The analytical equations for complete contact pressure and critical amplitude were provided. For the elastic-plastic case, the effect of contact conditions (perfect slip, full stick) on the complete contact pressure was investigated by using the FEM method. From the results, the effect of contact conditions on contact area does not appear to be significant.

Secondly, the contact behavior of a single elastic-plastic sinusoidal asperity under combined normal and tangential loading was investigated. The effects of the following parameters on the effective static friction coefficient of a single sinusoidal asperity were investigated: material properties (elastic modulus, Poison’s ratio, yield strength), geometry parameters (amplitude/wavelength), contact pressure and the critical interfacial shear strength. We found that the effective static friction coefficient of a single sinusoidal asperity decreases with increasing contact pressure, elastic modulus, Poisson’s ratio, and the ratio of amplitude to wavelength, and increases with increasing yield strength and critical shear strength. Empirical equations of the effective static friction coefficient and junction growth due to tangential load were provided.

Then, this work considers the elastic-plastic contact between deformable rough surfaces and a rigid flat under combined normal and tangential loading. The effect of sampling resolution as controlled by a spectral interpolation method on the contact behaviors was investigated. The first loading step, in which a normal load is applied on the rigid flat, the effects of sampling resolution on the contact area ratio, dimensionless displacement, dimensionless average gap, and maximum von Mises stress were investigated. It was found that: as the resolution decreases, the contact area ratio and dimensionless displacement decreases, while the dimensionless average gap and dimensionless contact pressure increases both under normal preload and at sliding inception. The second step, in which the normal load remains constant and a tangential load is applied and increases gradually, the static friction coefficient was investigated. The effect of tangential load on the contact behaviors were studied as well. We found the tangential force can increase the contact area ratio, dimensionless displacement and dimensionless maximum von Mises stress, and decrease the dimensionless average gap and dimensionless contact pressure.

Next, the effects of the following parameters on the static friction coefficient of rough surfaces were investigated: plasticity index, normal force and tangent modulus. It is observed that the static friction coefficient decreases as the dimensionless normal load and plasticity index increases. The FEM results were compared to the existing statistical models. For some cases, the overall trends of both the FEM results and statistical models are the same; but for a few cases, especially for the rougher surfaces, they are qualitatively different. In most cases the FEM predicts higher friction than the statistical models. We also found that the tangent modulus can decrease the static friction coefficient by hardening the surface.

Finally, a new stacked multi-scale friction model was developed to predict the static friction coefficient of the rough surfaces in contact. The single asperity sinusoidal results in [58] are used within the multi-scale frame work in [19] for the normal loading step to predict real contact area. The multi-scale contact model then was extended to a friction model. The predictions are compared with FEM results and a statistical model. They show the same trend, but they are not in a good qualitative agreement, and this is probably because one or more of the following reasons: the rough surface is not isotropic, the asperity summits have different radii, there is a uncertain interaction between asperities and bulk deformation, the distribution of the asperities are not Gaussian, and the measured nominal contact area is anisotropic and not large enough and not enough nodes in individual asperities in contact in the FE model. This still needs further investigating.

8.2. Recommendation for Future Work

The long-term impact of this research will be to assistant the optimization in the design of surfaces and materials in order to reduce or increase friction. It may be evaluated to increase friction, decrease friction or decrease wear. The developed model can be further incorporated into dynamical system applications, such as cylinder piston systems, and brake systems.

The stacked multi-scale friction model was developed to predict the static friction coefficient, but further effort is still needed to verify the accuracy of this model experimentally. The developed model in this work is only for dry conditions. However, the modeling approach could be applied on the friction with lubrication. The scanning length of the rough surfaces we used in the FE model was limited to just a few hundreds of microns. When developed a microscale model for macroscale contacts, the real rough surfaces that have large nominal areas may contain millions of asperities to model. Hence, one of the major drawbacks is that it needs great computational sources. With the technology developed nowadays, this shortcoming can be overcome later. However, the proposed multi-scale model and existing statistical models can be used without such restrictions.

There are several other aspects of this work that can be extended. The multi-scale friction model for the material without strain hardening still needs to be explored. The stacked multi-scale friction model based on the FFT method could be further extended to analyze the electrical and thermal contact considering tangential load.

REFERENCES

[1] Williams, J., 2005, *Engineering tribology*. Cambridge University Press.

[2] Rabinowicz, E., 1965, *Friction and wear of materials*. Wiley.

[3] Holmberg, K. and Erdemir, A., 2015. *Global impact of friction on energy consumption, economy and environment.* FME Trans, **43**(3), pp. 181-185.

[4] Kogut, L. and Etsion, I., 2004. *A static friction model for elastic-plastic contacting rough surfaces.* Journal of Tribology-Transactions of the ASME, **126**(1), pp. 34-40.

[5] Bowden, F.P.a.T., D., 1954, *Friction and Lubrication of Solids*. Clarendon,Oxford.

[6] Eriten, M., 2012, *Multiscale physics-based modeling of friction*. University of Illinois at Urbana-Champaign.

[7] Chang, W.R., Etsion, I., and Bogy, D.B., 1988. *Static Friction Coefficient Model for Metallic Rough Surfaces.* Journal of Tribology-Transactions of the ASME, **110**(1). pp. 57-63.

[8] Kogut, L. and Etsion, I., 2003. *A semi-analytical solution for the sliding inception of a spherical contact.* Journal of Tribology-Transactions of the ASME, **125**(3), pp. 499-506.

[9] Brizmer, V., Kligerman, Y., and Etsion, I., 2007. *Elastic-plastic spherical contact under combined normal and tangential loading in full stick.* Tribology Letters, **25**(1), pp. 61-70.

[10] Mindlin, R.D., 1949. *Compliance of Elastic Bodies in Contact.* Journal of Applied Mechanics-Transactions of the ASME, **16**(3), pp. 259-268.

[11] Eriten, M., Polycarpou, A.A., and Bergman, L.A., 2010. *Physics-based modeling for partial slip behavior of spherical contacts.* International Journal of Solids and Structures, , **47**(18-19), pp. 2554-2567.

[12] Wu, A.Z., Shi, X., and Polycarpou, A.A., 2012. *An Elastic-Plastic Spherical Contact Model Under Combined Normal and Tangential Loading.* Journal of Applied Mechanics-Transactions of the ASME, **79**(5), p. 051001.

[13] Cohen, D., Kligerman, Y., and Etsion, I., 2008. *A model for contact and static friction of nominally flat rough surfaces under full stick contact condition.* Journal of Tribology-Transactions of the ASME, **130**(3), p. 031401.

[14] Cohen, D., Kligerman, Y., and Etsion, I., 2009. *The Effect of Surface Roughness on Static Friction and Junction Growth of an Elastic-Plastic Spherical Contact.* Journal of Tribology-Transactions of the ASME, **131**(2), p. 021404.

[15] Li, L., Etsion, I., and Talke, F.E., 2010. *Contact Area and Static Friction of Rough Surfaces With High Plasticity Index.* Journal of Tribology-Transactions of the ASME, **132**(3), p. 031401.

[16] Archard, J. 1957. *Elastic deformation and the laws of friction*. in *Proceedings of the Royal Society of London A: Mathematical, Physical and Engineering Sciences*. The Royal Society. **243**(1233), pp.190-205.

[17] Ciavarella, M., et al., 2000. *Linear elastic contact of the Weierstrass profile.* Proceedings of the Royal Society a-Mathematical Physical and Engineering Sciences, **456**(1994), pp. 387-405.

[18] Westergaard, H.M., 1939. *Bearing prssures and cracks.* Journal of Applied Mechanics-Transactions of the ASME, **6**. pp. 49-53.

[19] Jackson, R.L. and Streator, J.L., 2006. *A multi-scale model for contact between rough surfaces.* Wear, **261**(11-12), pp. 1337-1347.

[20] Gao, Y.F. and Bower, A.F., 2006. *Elastic-plastic contact of a rough surface with Weierstrass profile.* Proceedings of the Royal Society a-Mathematical Physical and Engineering Sciences, **462**(2065), pp. 319-348.

[21] Wilson, W.E., Angadi, S.V., and Jackson, R.L., 2010. *Surface separation and contact resistance considering sinusoidal elastic–plastic multi-scale rough surface contact.* Wear, **268**(1), pp. 190-201.

[22] Kuhn, H. and Tucker, A., 1951, *Nonlinear Programming, Second Berkeley Sym-posium of Math. Statistics and Probability*, University of California Press, Berkeley.

[23] Chateauminois, A., Fretigny, C., and Olanier, L., 2010. *Friction and shear fracture of an adhesive contact under torsion.* Physical Review E. **81**(2), p. 026106.

[24] Trejo, M., Fretigny, C., and Chateauminois, A., 2013. *Friction of viscoelastic elastomers with rough surfaces under torsional contact conditions.* Physical Review E, **88**(5), P. 052401.

[25] Prevost, A., Scheibert, J., and Debregeas, G., 2013. *Probing the micromechanics of a multi-contact interface at the onset of frictional sliding.* European Physical Journal E, **36**(2), 17.

[26] Svetlizky, I. and Fineberg, J., 2014. *Classical shear cracks drive the onset of dry frictional motion.* Nature, **509**(7499), pp. 205-208.

[27] Johnson, K.L., 1985, *Contact Mechanics* Cambridge: Cambridge University Press.

[28] Galin, L.A., 1961, *Contact Problems in the Theory of Elasticity*: Department of Mathematics, School of Physical Sciences and Applied Mathematics, North Carolina State College.

[29] Chen, S.H. and Gao, H.J., 2006. *Non-slipping adhesive contact of an elastic cylinder on stretched substrates.* Proceedings of the Royal Society a-Mathematical Physical and Engineering Sciences, **462**(2065), pp. 211-228.

[30] Chen, S. and Gao, H., 2006. *Non-slipping adhesive contact between mismatched elastic spheres: A model of adhesion mediated deformation sensor.* Journal of the Mechanics and Physics of Solids, **54**(8), pp. 1548-1567.

[31] Zhupanska, O.I. and Ulitko, A.F., 2005. *Contact with friction of a rigid cylinder with an elastic half-space.* Journal of the Mechanics and Physics of Solids, **53**(5), pp. 975-999.

[32] Block, J.M. and Keer, L.M., 2008. *Periodic Contact Problems in Plane Elasticity.* Journal of Mechanics of Materials and Structures, **3**(7), pp. 1207-1237.

[33] Goodman, L., 1962. *Contact stress analysis of normally loaded rough spheres.* Journal of applied mechanics, **29**(3), pp. 515-522.

[34] Mossakovskii, V., 1954. *The fundamental mixed problem of the theory of elasticity for a half-space with a circular line separating the boundary conditions.* Prikl. Mat. Mekh, **18**, pp. 187-196.

[35] Mossakovskii, V., 1963. *Compression of elastic bodies under conditions of adhesion (axisymmetric case).* Journal of Applied Mathematics and Mechanics, **27**(3), pp. 630-643.

[36] Spence, D.A., 1968. *Self Similar Solutions to Adhesive Contact Problems with Incremental Loading.* Proceedings of the Royal Society of London Series a-Mathematical and Physical Sciences, **305**(1480), pp. 55-80.

[37] Spence, D.A., 1968. *A Wiener-Hopf Equation Arising in Elastic Contact Problems.* Proceedings of the Royal Society of London Series a-Mathematical and Physical Sciences, 1968. **305**(1480), pp. 81-92.

[38] Borodich, F.M., 1993. *The Hertz Frictional Contact between Nonlinear Elastic Anisotropic Bodies (the Similarity Approach).* International Journal of Solids and Structures, 1993. **30**(11), pp. 1513-1526.

[39] Borodich, F.M. and Keer, L.M., 2004. *Contact problems and depth-sensing nanoindentation for frictionless and frictional boundary conditions.* International Journal of Solids and Structures, 2004. **41**(9-10), pp. 2479-2499.

[40] Conway, H., et al., 1966. *Normal and shearing contact stresses in indented strips and slabs.* International Journal of Engineering Science, **4**(4), pp. 343-359.

[41] Kosior, F., Guyot, N., and Maurice, G., 1999. *Analysis of frictional contact problem using boundary element method and domain decomposition method.* International Journal for Numerical Methods in Engineering, **46**(1), pp. 65-82.

[42] Guyot, N., Kosior, F., and Maurice, G., 2000. *Coupling of finite elements and boundary elements methods for study of the frictional contact problem.* Computer Methods in Applied Mechanics and Engineering, **181**(1-3), pp. 147-159.

[43] Chen, W.W. and Wang, Q.J., 2008. *A numerical model for the point contact of dissimilar materials considering tangential tractions.* Mechanics of Materials, **40**(11), pp. 936-948.

[44] Gallego, L., Nelias, D., and Deyber, S., 2010. *A fast and efficient contact algorithm for fretting problems applied to fretting modes I, II and III.* Wear, **268**(1-2), pp. 208-222.

[45] Greenwood, J.A., 2015, in *Leeds-Lyon Symposium on Tribology*: Leeds, UK.

[46] Johnson, K.L., Greenwood, J.A., and Higginson, J.G., 1985. *The Contact of Elastic Regular Wavy Surfaces.* International Journal of Mechanical Sciences, **27**(6), pp. 383-396.

[47] Saha, S. and Jackson, R. 2016. *Elastic-plastic axisymmetric sinusoidal surface asperity contact*. in *Electrical Contacts (Holm), IEEE 62nd Holm Conference on*. IEEE. pp. 17-24.

[48] Jackson, R.L., Krithivasan, V., and Wilson, W.E., 2008. *The pressure to cause complete contact between elastic-plastic sinusoidal surfaces.* Proceedings of the Institution of Mechanical Engineers Part J-Journal of Engineering Tribology, **222**(J7), pp. 857-863.

[49] Jackson, R.L., 2010. *An Analytical Solution to an Archard-Type Fractal Rough Surface Contact Model.* Tribology Transactions, **53**(4), pp. 543-553.

[50] Zhang, X. and Jackson, R.L. 2014. *The Influence of Multiscale Roughness on the Real Contact Area and Contact Resistance between Real Reference Surfaces*. in *ICEC; The 27th International Conference on Electrical Contacts; Proceedings of*. VDE.

[51] Timoshenko, S. and Goodier, J. *Theory of elasticity. 1951.* New York.

[52] Tripp, J.H., et al., 2003. *Frequency response functions and rough surface stress analysis.* Tribology Transactions, **46**(3), pp. 376-382.

[53] Green, I., 2005. *Poisson ratio effects and critical valus in spherical and cylindrical Hertzian contacts.* APPLIED MECHANICS AND ENGINEERING, **10**(3), pp. 451-462.

[54] Wang, X.Z., Xu, Y., and Jackson, R.L., 2017. *Elastic Sinusoidal Wavy Surface Contact Under Full Stick Conditions.* Tribology Letters, **65**(4). p. 156.

[55] Ghaednia, H., Wang, X.,Saha, S., Jackson, R.L., Xu, Y., Sharma,A., 2017. *A Review of Elastic-Plastic Contact Mechanics.* Applied mechanics reviews, **69**(6), p. 060804.

[56] Brizmer, V., Kligerman, Y., and Etsion, I., 2006. *The effect of contact conditions and material properties on the elasticity terminus of a spherical contact.* International Journal of Solids and Structures, **43**(18-19), pp. 5736-5749.

[57] Zait, Y., Kligerman, Y., and Etsion, I., 2010. *Unloading of an elastic-plastic spherical contact under stick contact condition.* International Journal of Solids and Structures, **47**(7-8), pp. 990-997.

[58] Krithivasan, V. and Jackson, R.L., 2007. *An analysis of three-dimensional elasto-plastic sinusoidal contact.* Tribology Letters, **27**(1), pp. 31-43.

[59] Rostami, A. and Jackson, R.L., 2013. *Predictions of the average surface separation and stiffness between contacting elastic and elastic-plastic sinusoidal surfaces.* Proceedings of the Institution of Mechanical Engineers Part J-Journal of Engineering Tribology, **227**(12), pp. 1376-1385.

[60] Jackson, R.L., et al., 2012. *A Closed-Form Multiscale Thermal Contact Resistance Model.* Ieee Transactions on Components Packaging and Manufacturing Technology, **2**(7), pp. 1158-1171.

[61] Jackson, R.L., Bhavnani, S.H., and Ferguson, T.P., 2008. *A multiscale model of thermal contact resistance between rough surfaces.* Journal of Heat Transfer-Transactions of the ASME, **130**(8), p. 081301.

[62] Jackson, R.L., Krithivasan, V., and Wilson, W.E., 2008. *The pressure to cause complete contact between elastic—plastic sinusoidal surfaces.* Proceedings of the Institution of Mechanical Engineers, Part J: Journal of Engineering Tribology, **222**(7), pp. 857-863.

[63] Mindlin, R.D. and Deresiewicz, H., 1953. *Elastic Spheres in Contact under Varying Oblique Forces.* Journal of Applied Mechanics-Transactions of the ASME, **20**(3), pp. 327-344.

[64] Keer, L.M., Ahmadi, N., and Mura, T., 1984. *Tangential Loading of Elastic Bodies in Contact.* Computers & Structures, **19**(1-2), pp. 93-101.

[65] Hamilton, G.M., 1983. *Explicit Equations for the Stresses beneath a Sliding Spherical Contact.* Proceedings of the Institution of Mechanical Engineers Part C-Journal of Mechanical Engineering Science, **197**(Mar), pp. 53-59.

[66] Hills, D.A. and Sackfield, A., 1985. *Sliding Contact between Dissimilar Elastic Cylinders.* Journal of Tribology-Transactions of the ASME, **107**(4), pp. 463-466.

[67] Bowden, F.P. and Tabor, D., 1964, *The friction and lubrication of solids. Vol. 2*: OUP.

[68] Courtneypratt, J.S. and Eisner, E., 1957. *The Effect of a Tangential Force on the Contact of Metallic Bodies.* Proceedings of the Royal Society of London Series a-Mathematical and Physical Sciences, **238**(1215), pp. 529-550.

[69] Tabor, D., 1959. *Junction Growth in Metallic Friction - the Role of Combined Stresses and Surface Contamination.* Proceedings of the Royal Society of London Series a-Mathematical and Physical Sciences, **251**(1266), pp. 378-393.

[70] Brizmer, V., Kligerman, Y., and Etsion, I., 2007. *A model for junction growth of a spherical contact under full stick condition.* Journal of Tribology-Transactions of the Asme, **129**(4), pp. 783-790.

[71] Zolotarevskiy, V., Kligerman, Y., and Etsion, I., 2011. *The Evolution of Static Friction for Elastic-Plastic Spherical Contact in Pre-sliding.* Journal of Tribology-Transactions of the Asme, **133**(3), p. 034502.

[72] Patil, D.B. and Eriten, M., 2014. *Effects of Interfacial Strength and Roughness on the Static Friction Coefficient.* Tribology Letters, **56**(2), pp. 355-374.

[73] Mulvihill, D.M., et al., 2011. *An elastic-plastic asperity interaction model for sliding friction.* Tribology International, **44**(12), pp. 1679-1694.

[74] Jackson, R.L. and Green, I., 2006. *A statistical model of elasto-plastic asperity contact between rough surfaces.* Tribology International, **39**(9), pp. 906-914.

[75] Persson, B.N.J., 2001. *Elastoplastic contact between randomly rough surfaces.* Physical Review Letters, **87**(11),

[76] Persson, B.N.J., Bucher, F., and Chiaia, B., 2002. *Elastic contact between randomly rough surfaces: Comparison of theory with numerical results.* Physical Review B, **65**(18), p. 184106.

[77] Jackson, R.L., Crandall, E.R., and Bozack, M.J., 2015. *Rough surface electrical contact resistance considering scale dependent properties and quantum effects.* Journal of Applied Physics, **117**(19).

[78] Gao, Y.F., et al., 2006. *The behavior of an elastic-perfectly plastic sinusoidal surface under contact loading.* Wear, **261**(2), pp. 145-154.

[79] Eriten, M., et al., 2012. *Influence of friction and adhesion on the onset of plasticity during normal loading of spherical contacts.* Mechanics of Materials, **48**, pp. 26-42.

[80] Wang, X., Xu, Y., and Jackson, R.L., 2017. *Elastic–Plastic Sinusoidal Waviness Contact Under Combined Normal and Tangential Loading.* Tribology Letters, **65**(2), p. 45.

[81] Etsion, I. and Amit, M., 1993. *The Effect of Small Normal Loads on the Static Friction Coefficient for Very Smooth Surfaces.* Journal of Tribology-Transactions of the ASME, **115**(3), pp. 406-410.

[82] Ovcharenko, A., Halperin, G., and Etsion, I., 2008. *Experimental study of adhesive static friction in a spherical elastic-plastic contact.* Journal of Tribology-Transactions of the ASME, **130**(2), p. 120401.

[83] Etsion, I., 2010. *Revisiting the Cattaneo-Mindlin Concept of Interfacial Slip in Tangentially Loaded Compliant Bodies.* Journal of Tribology-Transactions of the ASME, **132**(2), p. 020801.

[84] Zhang, X.H., Xu, Y., and Jackson, R.L., 2017. *An analysis of generated fractal and measured rough surfaces in regards to their multi-scale structure and fractal dimension.* Tribology International, **105**, pp. 94-101.

[85] Zhang, X. and Jackson, R.L., 2017. *An Analysis of the Multiscale Structure of Surfaces with Various Finishes.* Tribology Transactions, **60**(1), pp. 121-134.

[86] Demirci, I., et al., 2014. *Multiscale Analysis of the Roughness Effect on Lubricated Rough Contact.* Journal of Tribology-Transactions of the ASME, **136**(1),

[87] Yastrebov, V.A., Anciaux, G., and Molinari, J.F., 2017. *On the accurate computation of the true contact-area in mechanical contact of random rough surfaces.* Tribology International, **114**, pp. 161-171.

[88] Kwon, O.H., Thompson, J.M., and Thompson, M.K. 2009. *The effect of surface smoothing and mesh density for real surfaces in contact*. in *Proceedings of the International Conference on Surface Metrology*.

[89] Kwon, O.H. and Thompson, M.K. 2009. *The effect of surface smoothing and mesh density for single asperity contact*. in *Proceedings of the International Conference on Surface Metrology*.

[90] Thompson, M.K. and Thompson, J.M., 2010. *Considerations for the Incorporation of Measured Surfaces in Finite Element Models.* Scanning, **32**(4), pp. 183-198.

[91] Majumdar, A. and Tien, C.L., 1990. *Fractal Characterization and Simulation of Rough Surfaces.* Wear, **136**(2), pp. 313-327.

[92] Kogut, L. and Jackson, R.L., 2006. *A comparison of contact modeling utilizing statistical and fractal approaches.* Journal of Tribology-Transactions of the ASME, **128**(1), pp. 213-217.

[93] Greenwood, J. and Williamson, J.P. 1966. *Contact of nominally flat surfaces*. in *Proceedings of the Royal Society of London A: Mathematical, Physical and Engineering Sciences*. The Royal Society. **295**(1443), pp. 300-319.

[94] Greenwood, J. and Tripp, J., 1970. *The contact of two nominally flat rough surfaces.* Proceedings of the institution of mechanical engineers, **185**(1), pp. 625-633.

[95] Kogut, L. and Etsion, I., 2003. *A finite element based elastic-plastic model for the contact of rough surfaces.* Tribology Transactions, **46**(3), pp. 383-390.

[96] Kogut, L. and Etsion, I., 2002. *Elastic-plastic contact analysis of a sphere and a rigid flat.* Journal of Applied Mechanics-Transactions of the ASME, **69**(5), pp. 657-662.

[97] Jackson, R.L. and Green, I., 2005. *A finite element study of elasto-plastic hemispherical contact against a rigid flat.* Journal of Tribology-Transactions of the ASME, **127**(2), pp. 343-354.

[98] Majumdar, A. and Bhushan, B., 1990. *Role of Fractal Geometry in Roughness Characterization and Contact Mechanics of Surfaces.* Journal of Tribology-Transactions of the ASME, **112**(2), pp. 205-216.

[99] Wu, J.J., 2000. *Simulation of rough surfaces with FFT.* Tribology International, **33**(1), pp. 47-58.

[100] Peng, W. and Bhushan, B., 2001. *A numerical three-dimensional model for the contact of layered elastic/plastic solids with rough surfaces by a variational principle.* Journal of Tribology-Transactions of the ASME, **123**(2), pp. 330-342.

[101] Temizer, I., 2011. *Thermomechanical contact homogenization with random rough surfaces and microscopic contact resistance.* Tribology International, **44**(2), pp. 114-124.

[102] Megalingam, A. and Mayuram, M.M., 2012. *Comparative Contact Analysis Study of Finite Element Method Based Deterministic, Simplified Multi-Asperity and Modified Statistical Contact Models.* Journal of Tribology-Transactions of the ASME, **134**(1), p. 014503.

[103] Song, H., Van der Giessen, E., and Liu, X., 2016. *Strain gradient plasticity analysis of elasto-plastic contact between rough surfaces.* Journal of the Mechanics and Physics of Solids, **96**, pp. 18-28.

[104] Ciavarella, M., Delfine, V., and Demelio, G., 2006. *A "re-vitalized" Greenwood and Williamson model of elastic contact between fractal surfaces.* Journal of the Mechanics and Physics of Solids, **54**(12), pp. 2569-2591.

[105] Ciavarella, M. and Leoci, F., 2006. *An assessment of the Greenwood-Williamson and other asperities models, with special reference to electrical conductance.* Journal of Tribology-Transactions of the ASME, **128**(1), pp. 10-17.

[106] Hyun, S., et al., 2004. *Finite-element analysis of contact between elastic self-affine surfaces.* Physical Review E, **70**(2). 026117.

[107] Hyun, S. and Robbins, M.O., 2007. *Elastic contact between rough surfaces: Effect of roughness at large and small wavelengths.* Tribology International, **40**(10-12), pp. 1413-1422.

[108] Pei, L., et al., 2005. *Finite element modeling of elasto-plastic contact between rough surfaces.* Journal of the Mechanics and Physics of Solids, **53**(11), pp. 2385-2409.

[109] Sahoo, P. and Ghosh, N., 2007. *Finite element contact analysis of fractal surfaces.* Journal of Physics D-Applied Physics, **40**(14), pp. 4245-4252.

[110] Walter, C. and Mitterer, C., 2009. *3D versus 2D finite element simulation of the effect of surface roughness on nanoindentation of hard coatings.* Surface & Coatings Technology, **203**(20-21), pp. 3286-3290.

[111] Yastrebov, V.A., et al., 2011. *Rough surface contact analysis by means of the Finite Element Method and of a new reduced model.* Comptes Rendus Mecanique, **339**(7-8), pp. 473-490.

[112] Poulios, K. and Klit, P., 2013. *Implementation and applications of a finite-element model for the contact between rough surfaces.* Wear, **303**(1-2), pp. 1-8.

[113] Mccool, J.I., 1987. *Relating Profile Instrument Measurements to the Functional Performance of Rough Surfaces.* Journal of Tribology-Transactions of the ASME, **109**(2), pp. 264-270.

[114] Jackson, R.L. and Green, I., 2011. *On the Modeling of Elastic Contact Between Rough Surfaces.* Trib. Trans., **54**(2), pp. 300-314.

[115] Tayebi, N. and Polycarpou, A.A., 2004. *Modeling the effect of skewness and kurtosis on the static friction coefficient of rough surfaces.* Tribology International, **37**(6), pp. 491-505.

[116] Lee, C.H. and Polycarpou, A.A., 2007. *Static friction experiments and verification of an improved elastic-plastic model including roughness effects.* Journal of Tribology-Transactions of the ASME, **129**(4), pp. 754-760.

[117] Lee, C.H., Eriten, M., and Polycarpou, A.A., 2010. *Application of Elastic-Plastic Static Friction Models to Rough Surfaces With Asymmetric Asperity Distribution.* Journal of Tribology-Transactions of the ASME, **132**(3), p. 031602.

[118] Dickey, R.D.I., Jackson, R.L., and Flowers, G.T., 2011. *Measurements of the Static Friction Coefficient Between Tin Surfaces and Comparison to a Theoretical Model.* Journal of Tribology-Transactions of the ASME, **133**(3), p. 031408.

[119] Yan, W. and Komvopoulos, K., 1998. *Contact analysis of elastic-plastic fractal surfaces.* Journal of Applied Physics, **84**(7), pp. 3617-3624.

[120] Xu, Y., 2012, *An Analysis of Elastic Rough Contact Models*. Department of Mechanical Engineering, Samuel Ginn College of Engineering, Auburn university.

[121] Ning, Y. and Polycarpou, A.A., 2004. *Extracting summit roughness parameters from random Gaussian surfaces accounting for asymmetry of the summit heights.* Journal of Tribology-Transactions of the ASME, **126**(4), pp. 761-766.

[122] Yu, N. and Polycarpou, A.A., 2004. *Combining and contacting of two rough surfaces with asymmetric distribution of asperity heights.* Journal of Tribology-Transactions of the ASME, **126**(2), pp. 225-232.

[123] Rostami, A. and Streator, J.L., 2015. *Study of liquid-mediated adhesion between 3D rough surfaces: A spectral approach.* Tribology International, **84**, pp. 36-47.

APPENDIX A

!****An Elastic-plastic Sinusoidal Model Under Combined Normal Loading ****!

```
! Length unit: mm
/FILNAME,SD0.02,1          ! Name the current job
!**************************Preprocessor****************************!
/prep7                               ! Preprocessor
/NUMBER,-1
/PNUM,ELEM,0
!------------------------Choose element type --------------------------!
ET, 1, SOLID186         ! Solid 186 (20-node brick element)
ET, 2, TARGE170       ! Type 2 = 4-node target element
ET, 3, CONTA174       ! Type 3 = 8-node contact element
!------------------------Set the element keyoptions --------------------------!
KEYOPT,2,2,1            ! Boundary conditions for rigid target nodes: Specified by user.
KEYOPT,3,1,0            ! Degree of Freedom: UX,UY,UZ (default)
KEYOPT,3,2,0            ! Contact algorithm: Augmented LaGrangian (default)
KEYOPT,3,4,0            ! Location of contact detection point: normal to target surface
KEYOPT,3,5,1            ! CONF/ICONT automated adjustment: close gap with auto CNOF
KEYOPT,3,6,1            ! Contact stiffness variation: make a normal refinement
KEYOPT,3,7,0            ! Element level time incrementation control: no control (default)
KEYOPT,3,8,0            ! Asymmetric contact selection: No action (default)
KEYOPT,3,9,1            ! Effect of initial penetration or gap: Exclude both
KEYOPT,3,10,2           ! Contact stiffness update: Each iteration
```

```
KEYOPT,3,11,0         ! Shell thickness effect: Exclude
KEYOPT,3,12,3         ! Behavior of contact surface: Bonded (stick condition)
KEYOPT,3,14,0         ! Behavior of fluid penetration load: various during iterations (default)
!-------------------------Set real constant ---------------------------!
R,1,0,0,10, 0.1,0,0    ! Set normal penalty stiffness factor and penalty stiffness 0.01
RMORE,,,, ,,
RMORE,,,, ,,
RMORE,,,, ,,
RMORE,,,,,,
!-------------------------set the material property ---------------------------!
MP, EX, 1, 200E3       ! Elastic modulus [N/mm^2]
MP, NUXY, 1, 0.3       ! Poisson's ratio
TB, BISO               ! Bilinear isotropic material model
TBDATA, 1, 1e3         ! Yield stress [N/mm^2]
TBDATA, 2, 4e3         ! Tangent modulus [N/mm^2]
!-----------------------Set the number of the Kpts and geometric parameters -------------------------!
*SET, N, 65                        ! Number of nodes in a and y direction
*DIM, XX, ARRAY, 2*N-1             ! Array of nodes in x direction
*DIM, YY, ARRAY, N                 ! Array of nodes in y direction
*SET, DELTA, 0.02                  ! Amplitude [mm]
*SET, LAMBDA, 1                    ! Wavelength in x and y direction
*SET, DEPTH, 30*DELTA                    ! Depth of the substrate [mm]
*SET, DELXY, LAMBDA/(2*N-2)  ! The mesh interval in x and y directions [mm]
*SET, PI, 3.14159265D0
!-------------------------Create the Keypoints---------------------------!
*DO, I, 1, 2*N-1                              ! Nodal coordinate in the x direction
*SET, XX(I), LAMBDA/(2*N-2)*(I-1)
*ENDDO
```

```
*DO, I, 1, N                                ! Nodal coordinate in the y direction
*SET,YY(I), LAMBDA/2/(N-1)*(I-1)
*ENDDO
*DIM, ZZ, ARRAY, 2*N-1, N        ! Sinusoidal surface height matrix
*DO, I, 1, 2*N-1                           ! Calculate the sinusoidal surface height
*DO, J, 1, N
*SET, ZZ(I,J) , DELTA*( 1 - COS(2*PI*XX(I))*COS(2*PI*YY(J)) ) + DEPTH
*ENDDO
*ENDDO
*DO, I, 1, 2*N-1
*DO, J, 1, N
K, (I-1)*N + J, XX(I), YY(J), ZZ(I,J)
*ENDDO
*ENDDO
!-------------------------Create the lines---------------------------!
*DO, J, 1, 2*N-1                              ! Connecting the neighboring key points along y axis
*DO, I, 1, N-1
L, (J-1)*N + I, (J-1)*N + I + 1
*ENDDO
*ENDDO
*DO, I, 1, 2*N -2                              ! Connecting the neighboring key points along x axis
*DO, J, 1, N
L, (I-1)*N + J, (I-1)*N + J + N
*ENDDO
*ENDDO
!-------------------------Create the sinusoidal surface---------------------------!
*DO, I, 1, 2*N-2                               ! Creating area element through the neighboring lines
*DO, J, 1, N-1
```

```
LSEL, S, LOC, X, XX(I) - 1/8*DELXY, XX(I+1) + 1/8*DELXY

LSEL, R, LOC, Y, YY(J) - 1/8*DELXY, YY(J+1) + 1/8*DELXY

AL, ALL

ALLSEL

*ENDDO

*ENDDO

CM, SINUSOIDAL, AREA          ! Creating the sinusoidal surface by combining the small area

!------------------------Create the volume--------------------------!

K,N*(2*N-1)+1,0,0,0

K,N*(2*N-1)+2,0,LAMBDA/2,0

K,N*(2*N-1)+3,LAMBDA,0,0

K,N*(2*N-1)+4,LAMBDA,LAMBDA/2,0           ! Creating keypoints

L,N*(2*N-1)+1,N*(2*N-1)+2

L,N*(2*N-1)+3,N*(2*N-1)+4

L,N*(2*N-1)+1,N*(2*N-1)+3

L,N*(2*N-1)+2,N*(2*N-1)+4

L,1,N*(2*N-1)+1

L,N,N*(2*N-1)+2

L,N*(2*N-2)+1,N*(2*N-1)+3

L,N*(2*N-1),N*(2*N-1)+4                               ! Creating lines for the solid body!

AL,N*(2*N-2)+(N-1)*(2*N-1)+1,N*(2*N-2)+(N-1)*(2*N-1)+3,N*(2*N-2)+(N-1)*(2*N-1)+2,N*(2*N-2)+(N-1)*(2*N-1)+4

ASEL, S, AREA, ,(N-1)*(2*N-2)+1

CM, Bottom_surface, AREA                           ! Creating the bottom surface

ALLSEL

LSEL, S, LOC, X, 0*LAMBDA - 1/8*DELXY, 0*LAMBDA + 1/8*DELXY

AL,ALL

ASEL, S, AREA, ,(N-1)*(2*N-2)+2

CM, Left_surface, AREA                             ! Creating the left-side surface
```

```
ALLSEL

LSEL, S, LOC, X, 1*LAMBDA - 1/8*DELXY, 1*LAMBDA + 1/8*DELXY

AL,ALL

ASEL, S, AREA, ,(N-1)*(2*N-2)+3

CM, Right_surface, AREA                ! Creating the right-side surface

ALLSEL

LSEL, S, LOC, Y, 0*LAMBDA - 1/8*DELXY, 0*LAMBDA + 1/8*DELXY

AL,ALL

ASEL, S, AREA, ,(N-1)*(2*N-2)+4

CM, Front_surface, AREA                ! Creating the front surface

ALLSEL

LSEL, S, LOC, Y, (1/2)*LAMBDA - 1/8*DELXY, (1/2)*LAMBDA + 1/8*DELXY

AL,ALL

ASEL, S, AREA, ,(N-1)*(2*N-2)+5

CM, Back_surface, AREA                 ! Creating the back surface

ALLSEL

ASEL, S, AREA, ,SINUSOIDAL

ASEL, A, AREA, ,Bottom_surface

ASEL, A, AREA, ,Left_surface

ASEL, A, AREA, ,Right_surface

ASEL, A, AREA, ,Front_surface

ASEL, A, AREA, ,Back_surface

VA,ALL                                ! Creating the volume by the six surfaces

WPOFFs,,,DEPTH + 2*DELTA              ! Working coordinate system with the peak of the sinusoidal

RECTING, -LAMBDA/32, LAMBDA+LAMBDA/8, -LAMBDA/32,
LAMBDA/2+LAMBDA/32                    ! Rectangular surface (X1, X2, Y1, Y2)

!------------------------Mesh the volume--------------------------!

! mesh the target surface

LESIZE, N*(2*N-2)+(N-1)*(2*N-1)+8+1,,, 1       ! Meshing target surface
```

```
LESIZE, N*(2*N-2)+(N-1)*(2*N-1)+8+2,,, 1
LESIZE, N*(2*N-2)+(N-1)*(2*N-1)+8+3,,, 1
LESIZE, N*(2*N-2)+(N-1)*(2*N-1)+8+4,,, 1
ASEL, S,,, (N-1)*(2*N-2)+5+1
TYPE, 2                               ! Select target 170
AMESH, ALL                            ! Meshing area
ESURF, ALL, REVERSE                   ! Reverse normal direction of element target 170
ALLSEL
LESIZE, N*(2*N-2)+(N-1)*(2*N-1)+4+1 ,,, 16, 14
! Divided four vertical lines element into 16 sections, ratio 14
LESIZE, N*(2*N-2)+(N-1)*(2*N-1)+4+2 ,,, 16, 14
LESIZE, N*(2*N-2)+(N-1)*(2*N-1)+4+3 ,,, 16, 14
LESIZE, N*(2*N-2)+(N-1)*(2*N-1)+4+4 ,,, 16, 14
ASEL,S,AREA, ,SINUSOIDAL  ! Select all areas
LSLA, S                                  ! Select lines contained in the current area set
LESIZE, ALL, , , 1                       ! Divided the line elements on the sinusoidal surface
ALLSEL
VSWEEP, 1                                ! Meshing the only volume through sweep method
!-------------------------CONTACT PAIR CREATION---------------------------!
ASEL, S, AREA, , SINUSOIDAL    ! Select all the area elements on the sinusoidal surface
NSLA, S, 1                              ! Select all the nodes attached to the area
TYPE, 3                                ! Select contact 174
ESLN, S, 0                              ! Select all the area elements on the areas
ESURF                                  ! Laying element contac 174 on the meshed top surface
ALLSEL
REAL, 1                               ! Creating a pilot node on the rigid flat
TYPE, 2
TSHAP, PILO
```

```
N, 1E8 ,-LAMBDA/32, -LAMBDA/32, DEPTH+2*DELTA
E, 1E8
NSEL, S , , , 1E8                    ! Select the newly created node
CM, PILOT, NODE
ALLSEL
!------------------------Redefine element number for postprocessing--------------------------!
*SET,I1 , 0
*SET,II1 , 0
*DIM, CONTNOD, ARRAY, (2*N-1)*N                    ! Create and store contact nodes
ESEL, S, TYPE,,3
NSLE, S, ALL
*DO, I, 1, 2*N-1
  *DO, J, 1, N
    I1 = NODE( XX(I), YY(J), ZZ(I,J) )
   II1 = (I-1)*N + J
   CONTNOD(II1) = I1
  *ENDDO
*ENDDO

*DIM, CONTELE, ARRAY, (2*N-2)*(N-1)                    ! Create and store contact elements
*DO, I, 1, 2*N-2
  *DO, J, 1, N-1
    ESEL, S, TYPE, , 3
    NSLE, S, ALL
    NSEL, R, LOC, X, XX(I) - DELXY/8, XX(I+1) + DELXY/8
    NSEL, R, LOC, Y, YY(J) - DELXY/8, YY(J+1) + DELXY/8
    ESLN, S, 1
    *GET, II1, ELEM, 0, NUM, MAX
```

```
    *SET, I1 , (I-1)*(N-1) + J
    *SET, CONTELE(I1), II1
    ALLSEL
  *ENDDO
*ENDDO
!********************************Solution*********************************!
!------------------------Boundary Conditions-------------------------!
/SOL                                    ! Solution processor
ASEL, S, AREA, , Bottom_surface         ! Select the bottom surface
NSLA, S, 1                              ! Select the nodes associated with the bottom surface
D, ALL, ALL, 0
ALLSEL
ESEL, S, TYPE,,1
ESEL, A, TYPE,,3
NSLE, S, ALL
CPCYC, ALL,,,LAMBDA,0,0
ALLSEL
ASEL, S, AREA,  , Front_surface          ! Select the front surfaces
ASEL, A, AREA,  , Back_surface           ! Select the back surfaces
NSLA, S, 1                               ! Select the nodes associated with the areas
D, ALL, UY, 0                            ! Define the DOF in Y direction
ALLSEL
SAVE, 'Boundary_D', 'db'
! -----------------------------* Apply the normal force on the rigid flat *------------------------------!
/SOLU
! 1ST LOADING STEP
ANTYPE, 0                                ! Static
LUMPM, 0                                 ! No lump mass
```

```
NLGEOM, 1                          ! NON-LINEAR ANALYSIS
KBC, 0                             ! RAMP LOADING
AUTOTS, 1                          ! Do not Use automatic loading steps
NSUBST,100,10000,25
Time, 100                           ! Time at the end of the first loading step
NEQIT, 30                           ! Number of maximum equilibrium iteration
RESCONTROL, ,ALL,LAST,200           ! Write the restart file .RNNN at every substep
OUTRES, ALL, ALL                    ! Output results of each substep
D, PILOT, UX, 0                     ! X displacement of the Pilot node
D, PILOT, ROTX, 0                   ! X rotation of the Pilot node
D, PILOT, UY, 0                     ! Y displacement of the Pilot node
D, PILOT, ROTY, 0                   ! Y rotation of the Pilot node
F, PILOT, FZ, -101.5                ! Z load of the Pilot node
D, PILOT, ROTZ, 0                  ! Z rotation of the Pilot node

CNCHECK, AUTO


SOLVE
SAVE
```

APPENDIX B

```
! ********************Elastic-plastic Rough Surface Contact*********************!
! Length unit: mm
! Meshing of rough surfaces is achieved by moving the nodes belong to the top surface of cubic
! by the amount of surface height by three steps


/FILNAME,2L_NP128,1          ! Name the current job
!****************************** Preprocessor ******************************!
/PREP7                                  ! Enter preprocessor
!-------------------------Choose element type ---------------------------!
ET, 1, SOLID185                    ! Solid 185 (8-node brick element)
ET, 2, TARGE170                   ! Type 2 = 4-node target element
ET, 3, CONTA173                  ! Type 3 = 8-node contact element
!-------------------------Set the element keyoptions ---------------------------!
KEYOPT,2,2,0            ! Boundary conditions for rigid target nodes: Specified by user.
KEYOPT,3,1,0            ! Degree of Freedom: UX,UY,UZ (default)
KEYOPT,3,2,0            ! Contact algorithm: Augmented Lagrangian (default)
KEYOPT,3,4,0            ! Location of contact detection point: normal to target surface
KEYOPT,3,5,1            ! CONF/ICONT automated adjustment: close gap with auto CNOF
KEYOPT,3,6,1            ! Contact stiffness variation: make a normal refinement
KEYOPT,3,7,0            ! Element level time incrementation control: no control (default)
KEYOPT,3,8,0            ! Asymmetric contact selection: No action (default)
KEYOPT,3,9,1            ! Effect of initial penetration or gap: Exclude both
KEYOPT,3,10,2           ! Contact stiffness update: Each iteration
```

```
KEYOPT,3,11,0          ! Shell thickness effect: Exclude
KEYOPT,3,12,3          ! Behavior of contact surface: Bonded (stick condition)
KEYOPT,3,14,0          ! Behavior of fluid penetration load: various during iterations (default)
!------------------------Set real constant ---------------------------!
R,1,0,0,10, 1,0,0    ! Set normal penalty stiffness factor 10 and penalty stiffness 0.1
RMORE,,,, ,,
RMORE,,,, ,,
RMORE,,,, ,,
RMORE,,,,,,
!------------------------Set the material property ---------------------------!
MP, EX, 1, 200E3        ! Elastic modulus [N/mm^2]
MP, NUXY, 1, 0.3        ! Poisson's ratio
TB, BISO                ! Bilinear isotropic material model
TBDATA, 1, 1e3          ! Yield stress [N/mm^2]
TBDATA, 2, 4e3          ! Tangential modulus [N/mm^2]
! -------------------------* READ ROUGH SURFACE DATA *-------------------------!
/INPUT, READ_SURFACE_DATA, TXT             ! Read external file
DEL_X = L/(NP-1)
DEL_Y = L/(NP-1)
*SET, N_END, 5                              ! Number of node on the lines of bottom surface
*SET, NLAYERO, 5                            ! Original planned layer number
*SET, H_BOTTOM, DEL_X*2**(NLAYERO)      ! The length of the lines on bottom surface
*DIM, H_BSAE, ARRAY, NLAYERO      ! Height of each layer (in z direction)
*DO, I, 1,NLAYERO
  H_BSAE(I) = DEL_X*2**(NLAYERO-I)
*ENDDO
!------------------------------------Base set--------------------------------------
NLAYER_B=2*NLAYERO                          ! TOTAL NUMBER OF BASE LAYER
```

```
*DIM, LDEPTH, ARRAY, NLAYER_B
LDEPTH(1)=H_BOTTOM                    ! DEPTH IN Z AXIS
*DO, I, 2,NLAYER_B
  LDEPTH(I) = LDEPTH(I-1)+H_BSAE(NINT((I-1)/2))
*ENDDO
!--------------------------------------Surface set----------------------------------------!
*SET, NLAYER_S, 3                            ! Three layers for the rough surface
R_S=4
*IF, DEL, GE, DELL, THEN
DEL_S=DEL
*ELSE
DEL_S=DELL
*ENDIF
*SET, H_SURFACE, 1.5*DEL+DEL_S/R_S
*SET, H_INCREASE, (1.5*DEL_S)/(NLAYER_S-1)
*DIM, LDEPTH_T, ARRAY, NLAYER_S
*DO, I, 1,NLAYER_S
*IF, I, EQ, 1, THEN
 LDEPTH_T(I) = LDEPTH(NLAYER_B)+DEL_S/R_S
*ELSE
 LDEPTH_T(I) = LDEPTH(NLAYER_B)+DEL_S/R_S+(I-1)*H_INCREASE
*ENDIF
*ENDDO
LDEPTH_TOP=LDEPTH_T(NLAYER_S)
!------------------------------------Create volume --------------------------------------!
*DO, I, 1, NLAYER_B
   *IF, I, EQ, 1, THEN
      BLC5, L/2, L/2, L, L, LDEPTH(I)
```

```
    WPOFFS, 0, 0, LDEPTH(I)
  *ELSE
    BLC5, L/2, L/2, L, L, LDEPTH(I) - LDEPTH(I-1)
    WPOFFS, 0, 0, LDEPTH(I) - LDEPTH(I-1)
  *ENDIF
*ENDDO

*DO, I, 1, NLAYER_S
  *IF, I, EQ, 1, THEN
    BLC5, L/2, L/2, L, L, DEL_S/R_S
    WPOFFS, 0, 0, DEL_S/R_S
  *ELSE
    BLC5, L/2, L/2, L, L, LDEPTH_T(I) - LDEPTH_T(I-1)
    WPOFFS, 0, 0, LDEPTH_T(I) - LDEPTH_T(I-1)
  *ENDIF
*ENDDO
VGLUE, ALL                              ! Glue volumes
NUMCMP, VOLU                            ! Renumber the volume entities
! ---------------------------------- Mesh substrate -------------------------------
! DIVIDING LINE ELEMENTS ON BOTTOM SURFACE
ASEL, S, LOC, Z, -DEL_X/10, DEL_X/10
LSLA, S
LESIZE, ALL,,,(N_END-1)
ALLSEL
! DIVIDING LINE ELEMENTS ON EACH LAYERS OF BASE
*DO, I, 1, NLAYER_B
  ASEL, S, LOC, Z, LDEPTH(I) - DEL_X/10, LDEPTH(I) + DEL_X/10
  LSLA, S
```

```
  LESIZE, ALL,,, 2**(NINT((I-1)/2))*(N_END-1)
  ALLSEL
*ENDDO
*DO, I, 1, NLAYER_S
  ASEL, S, LOC, Z, LDEPTH_T(I) - DEL_X/10, LDEPTH_T(I) + DEL_X/10
  LSLA, S
  LESIZE, ALL,,, (NP-1)
  ALLSEL
*ENDDO
!------------------------------Premesh lines on side surfaces-------------------------------!
*DO, I, 2, NLAYER_B
  KSEL, S, LOC, Z, LDEPTH(I-1)-DEL_X/10, LDEPTH(I) + DEL_X/10
  LSLK, S, 1
  LESIZE, ALL,,,1                  ! Dividing line element on side surface (base)
  ALLSEL
*ENDDO
ALLSEL
*DO, I, 2, NLAYER_S
  KSEL, S, LOC, Z, LDEPTH_T(I-1)-DEL_X/10, LDEPTH_T(I) + DEL_X/10
  LSLK, S, 1
  LESIZE, ALL,,,1                  ! Dividing line element on side surface (surface layers)
  ALLSEL
*ENDDO
ALLSEL
KSEL, S, LOC, Z, LDEPTH(NLAYER_B)-DEL_X/10, LDEPTH(NLAYER_B+1)+ DEL_X/10
KSEL, A, LOC, Z, -DEL_X/10, LDEPTH(1) + DEL_X/10
LSLK, S, 1
LESIZE, ALL,,,1            ! Dividing line element on side surface (top surface and bottom surface)
```

```
ALLSEL
!-------------------------------------MESH-----------------------------------!
TYPE, 1                                   ! Solid 174
MAT, 1                                    ! Material
MSHAPE, 0, 3D                             ! Element shape: 3D brick
MSHKEY,1                                  ! Mapped meshing
VSEL,S,VOLU, ,NLAYER_B+1,NLAYER_B + NLAYER_S        ! Mesh surface
MOPT, PYRA, ON                             ! Turn on pyramid element
MSHAPE, 1, 3D                              ! Element shape: 3D tetrahedral
MSHKEY,0                                   ! Free meshing
VSEL,S,VOLU, ,1,NLAYER_B                   ! Mesh base
VMESH, ALL                                  ! Mesh the volume
! ------------------------------------ Model rigid flat---------------------------------------
ASEL, U, AREA, , ALL
ESEL, U, ELEM, , ALL
NSEL, U, NODE, , ALL
*SET,DEL_L , 0
K, 1001, -L/32, -L/32, LDEPTH_TOP+ DEL-DEL_L            ! Target surface
K, 1002, -L/32, L+L/32, LDEPTH_TOP + DEL-DEL_L
K, 1003, L+L/8, L+L/32, LDEPTH_TOP + DEL-DEL_L
K, 1004, L+L/8, -L/32, LDEPTH_TOP + DEL-DEL_L
A, 1001, 1004, 1003, 1002
CM, RIGID_FLAT, AREA                                    ! Create rigid flat area
WPOFFS, 0, 0, DEL-DEL_L
ALLSEL
! ------------------------------Identify contact pair -------------------------------------
ASEL,S,AREA, ,RIGID_FLAT
LSLA
```

```
LESIZE, ALL,,, 1                              ! Meshing target surface with one target 170
ASEL,S,AREA, ,RIGID_FLAT
TYPE, 2                                       ! Select target 170
AMESH, ALL                                   ! Mesh area
ESURF, ALL, REVERSE                          ! Reverse normal direction of element target 170
! ---------------------------- Define Pilot node -------------------------------!
TSHAP, PILO
N, 1E8 ,-L/32, -L/32, LDEPTH_TOP+ DEL-DEL_L
E, 1E8
NSEL, S , , , 1E8                           ! Select the newly created node
CM, PILOT, NODE
ALLSEL
! ------------------------------* Meshing contact *-------------------------------!
NSEL, S, LOC, Z, LDEPTH_TOP - DEL_X/10, LDEPTH_TOP + DEL_X/10
TYPE, 3                              ! Select Conta174
MAT, 1
ESLN, S, 0                           ! Select element on the select set
ESURF                               ! Laying element Conta 174 on the meshed top surface
ALLSEL
! --------------------------------- Moving nodes-----------------------------------!
/NUMBER,-1
/PNUM,ELEM,0
!------------------------------------Define components -------------------------------!
NSEL, S, LOC, Z, LDEPTH_T(1) - DEL_X/10, LDEPTH_T(1) + DEL_X/10
CM, SURFACE_TOP1, NODE
ALLSEL
NSEL, S, LOC, Z, LDEPTH_T(2) - DEL_X/10, LDEPTH_T(2) + DEL_X/10
CM, SURFACE_TOP2, NODE
```

```
ALLSEL
NSEL, S, LOC, Z, LDEPTH_T(3) - DEL_X/10, LDEPTH_T(3) + DEL_X/10
CM, SURFACE_TOP3, NODE
ALLSEL
*SET,NUM_NODE,NP*NP
*DIM, NODE_LIST_A1,ARRAY,NUM_NODE     ! Node number vector (surface 1)
*DIM, NODE_LIST_A2,ARRAY,NUM_NODE     ! Node number vector (surface 2)
*DIM, NODE_LIST_A3,ARRAY,NUM_NODE     ! Node number vector (surface 3)
*DIM, NODE_LOCX_A1,ARRAY,NUM_NODE  ! Initialize nodal x location vector (surface 1)
*DIM, NODE_LOCX_A2,ARRAY,NUM_NODE  ! Initialize nodal x location vector (surface 2)
*DIM, NODE_LOCX_A3,ARRAY,NUM_NODE  ! Initialize nodal x location vector (surface 3)
*DIM, NODE_LOCY_A1,ARRAY,NUM_NODE  ! Initialize nodal y location vector (surface 1)
*DIM, NODE_LOCY_A2,ARRAY,NUM_NODE  ! Initialize nodal y location vector (surface 2)
*DIM, NODE_LOCY_A3,ARRAY,NUM_NODE  ! Initialize nodal y location vector (surface 3)
*DIM, NODE_LOCZ_A1,ARRAY,NUM_NODE  ! Initialize nodal z location vector (surface 1)
*DIM, NODE_LOCZ_A2,ARRAY,NUM_NODE  ! Initialize nodal z location vector (surface 2)
*DIM, NODE_LOCZ_A3,ARRAY,NUM_NODE  ! Initialize nodal z location vector (surface 3)
*DIM, NODE_ROUGHNESS_A1,ARRAY,NUM_NODE     ! Surface height vector (surface 1)
*DIM, NODE_ROUGHNESS_A2,ARRAY,NUM_NODE     ! Surface height vector (surface 2)
 *DIM, NODE_ROUGHNESS_A3,ARRAY,NUM_NODE    ! Surface height vector (surface 3)
!---------------------------- Moving nodes on the surfaces ------------------------
MODMSH, DETACH               ! Deattach the elements and nodes with solid
SHPP,OFF                     ! Terminate element checking
!--------------------------- Moving nodes on the surfaces 3------------------------
ALLSEL
NSEL, S, NODE,  , SURFACE_TOP3                   ! Select the front surfaces
*VGET,NODE_LIST_A3,NODE, ,NLIST                 ! Get the node number on the surface 3
*DO, I, 1, NUM_NODE
```

```
   *GET, NODE_LOCX_A3(I), NODE, NODE_LIST_A3(I), LOC, X
   *GET, NODE_LOCY_A3(I), NODE, NODE_LIST_A3(I), LOC, Y
   *GET, NODE_LOCZ_A3(I), NODE, NODE_LIST_A3(I), LOC, Z
   *SET,X3,NODE_LOCX_A3(I)
   *SET,Y3,NODE_LOCY_A3(I)
   *SET,Z3,NODE_LOCZ_A3(I)
   INDEX_X3 = X3/DEL_X+1
   INDEX_Y3 = Y3/DEL_Y+1
   *SET, NODE_ROUGHNESS_A3(I),ZZ(INDEX_X3, INDEX_Y3)
   NMODIF,NODE_LIST_A3(I),X3,Y3,Z3+(3/3)*NODE_ROUGHNESS_A3(I)
*ENDDO
!---------------------------- Moving nodes on the surfaces 2-----------------------
ALLSEL
NSEL, S, NODE,  , SURFACE_TOP2                    ! Select the front surfaces
*VGET,NODE_LIST_A2,NODE, ,NLIST    ! Get the node number on the surface 2
*DO, I, 1, NUM_NODE
   *GET, NODE_LOCX_A2(I), NODE, NODE_LIST_A2(I), LOC, X
   *GET, NODE_LOCY_A2(I), NODE, NODE_LIST_A2(I), LOC, Y
   *GET, NODE_LOCZ_A2(I), NODE, NODE_LIST_A2(I), LOC, Z
   *SET,X2,NODE_LOCX_A2(I)
   *SET,Y2,NODE_LOCY_A2(I)
   *SET,Z2,NODE_LOCZ_A2(I)
   INDEX_X2 = X2/DEL_X+1
   INDEX_Y2 = Y2/DEL_Y+1
   *SET, NODE_ROUGHNESS_A2(I),ZZ(INDEX_X2, INDEX_Y2)
   ! OR NODE_ROUGHNESS_A2(I) = ZZ(INDEX_X2, INDEX_Y2)
   NMODIF,NODE_LIST_A2(I),X2,Y2,Z2+(2/3)*NODE_ROUGHNESS_A2(I)
*ENDDO
```

```
!------------------ MOVINGN NODES ON THE SURFACE 1-----------------------
ALLSEL
NSEL, S, NODE,  , SURFACE_TOP1                         ! Select the front surfaces
*VGET,NODE_LIST_A1,NODE, ,NLIST
*DO, I, 1, NUM_NODE
   *GET, NODE_LOCX_A1(I), NODE, NODE_LIST_A1(I), LOC, X
   *GET, NODE_LOCY_A1(I), NODE, NODE_LIST_A1(I), LOC, Y
   *GET, NODE_LOCZ_A1(I), NODE, NODE_LIST_A1(I), LOC, Z
   *SET,X1,NODE_LOCX_A1(I)
   *SET,Y1,NODE_LOCY_A1(I)
   *SET,Z1,NODE_LOCZ_A1(I)
   INDEX_X1 = X1/DEL_X+1
   INDEX_Y1 = Y1/DEL_Y+1
   *SET, NODE_ROUGHNESS_A1(I),ZZ(INDEX_X1, INDEX_Y1)
   NMODIF,NODE_LIST_A1(I),X1,Y1,Z1+(1/3)*NODE_ROUGHNESS_A1(I)
*ENDDO
! -----------------------------* Create components *------------------------------!
ALLSEL
ESEL, S, TYPE, , 3
CM, ROUGH_SURFAEC_ELEM, ELEM                           ! Rough surface element
ALLSEL
ESEL, S, TYPE, , 2
NSLE, S, ALL
CM, TARGE_SURFACE, NODE                                ! Target surface nodes
ALLSEL
NSEL, S, LOC, Z, -DEL_X/10, DEL_X/10                   ! Bottom surface nodes
CM, BOTTOM_SURFACE, NODE                               ! Nodes on surface of the substrate
ALLSEL
```

```
NSEL, S, LOC, Y, -DEL_X/10, DEL_X/10                ! Front surface nodes
CM, FRONT_SURFACE, NODE
ALLSEL
NSEL, S, LOC, Y, L-DEL_X/10, L+DEL_X/10          ! Back surface nodes
CM, BACK_SURFACE, NODE
ALLSEL
NSEL, S, LOC, X, -DEL_X/10, +DEL_X/10              ! Left surface nodes
CM, LEFT_SURFACE, NODE
ALLSEL
NSEL, S, LOC, X, L-DEL_X/10, L+DEL_X/10         ! Right surface nodes
CM, RIGHT_SURFACE, NODE
ALLSEL
! ------------------------------ Redefine element number type two -------------------------------!
*SET, NCONTN, NP*NP
*SET, NCONTE, (NP-1)*(NP-1)
*DIM, NODE_LIST,ARRAY,NCONTN
*DIM, ELEM_LIST,ARRAY,NCONTE
*DIM, NODE_LOCX,ARRAY,NCONTN
*DIM, NODE_LOCY,ARRAY,NCONTN
*DIM, NODE_LOCZ,ARRAY,NCONTN
ESEL, S, TYPE, , 3
NSLE, S, ALL
*VGET,NODE_LIST,NODE, ,NLIST
*DO, I, 1, NCONTN
   *GET, NODE_LOCX(I), NODE, NODE_LIST(I), LOC, X
   *GET, NODE_LOCY(I), NODE, NODE_LIST(I), LOC, Y
   *GET, NODE_LOCZ(I), NODE, NODE_LIST(I), LOC, Z
*ENDDO
```

```
ALLSEL
ESEL, S, TYPE, , 3
*VGET,ELEM_LIST,ELEM, ,ELIST
ALLSEL
! ----------------------------- X, Z and node number at front Section -----------------------------!
  ESEL, S, TYPE,,1
  NSLE, S, ALL
  NSEL, R, LOC, Y, -DEL_X/10, DEL_X/10
  *VGET, LIST_FRONT, NODE, , NLIST
  *GET, NUM_FRONT,NODE,  , COUNT
  *DIM, X_FRONT, ARRAY, NUM_FRONT
  *DIM, Z_FRONT, ARRAY, NUM_FRONT
  *DO, J, 1, NUM_FRONT
   *GET, CX1, NODE, LIST_FRONT(J), LOC, X
   *SET, X_FRONT(J), CX1
   *GET, CZ1, NODE, LIST_FRONT(J), LOC, Z
   *SET, Z_FRONT(J), CZ1
  *ENDDO
ALLSEL
! ------------------------------- Boundary conditions --------------------------------!
/SOL                                        ! Solution processor
!Step 1. Bottom surface
NSEL, S, NODE, , BOTTOM_SURFACE
D, ALL, ALL, 0                              ! Displacement in all directions are zero
ALLSEL
! Step 2. Two side surfaces
NSEL, S, NODE, , LEFT_SURFACE               ! Select the nodes associated with the left surface
NSEL, A, NODE, , RIGHT_SURFACE              ! Select the nodes associated with the right surface
```

```
CPCYC, ALL,1.0E-6,,XX(NP)-XX(1),0,0   ! Couple all the nodes on the side surfaces
ALLSEL


NSEL, S, NODE,  , FRONT_SURFACE        ! Select the nodes on front surface
NSEL, A, NODE,  , BACK_SURFACE         ! Select the nodes on back surface
D, ALL, UY, 0                          ! Define the DOF in Y direction
ALLSEL
SAVE, 'Boundary', 'db'
! ----------------------------- Apply the normal force on the rigid flat -------------------------------!
/SOLU
ANTYPE, 0                              ! Static
LUMPM, 0                               ! No lump mass
NLGEOM, 1                              ! Non-linear analysis
KBC, 0                                 ! Ramp loading
AUTOTS, 1                              ! Use automatic loading steps
NSUBST,100,10000,50                    ! Initial 100, maximum 10000, minimum 50
Time, 100                              ! Time at the end of the first loading step
NEQIT, 100                             ! Maximum number of iteration
RESCONTROL, ,ALL,1,200                 ! Write the restart file .RNNN at every substep
OUTRES, ALL, ALL                       ! Output all results of each substep
D, PILOT, UX, 0                        ! X displacement of the Pilot
D, PILOT, ROTX, 0                      ! X rotation of the Pilot
D, PILOT, UY, 0                        ! Y displacement of the Pilot
D, PILOT, ROTY, 0                      ! Y rotation of the Pilot
F, PILOT, FZ, -20                      ! Z load of the Pilot
D, PILOT, ROTZ, 0                      ! Z rotation of the Pilot
CUTCONTROL,PLSLIMIT,0.3
CNVTOL, F, , 0.025, 2, 1e-4            ! Set convergence value based on force
```

```
CNVTOL, U, , 0.025, 0, 1e-4                    ! Set convergence value based on displacement
CNCHECK,AUTO
SOLVE
!************************Post Processor***************************!
/POST1
SET, 1
*GET, NSUBSTEP1, ACTIVE, 0, SOLU, NCMSS
*DIM, CONPRESS, ARRAY, NSUBSTEP1*NCONTE
*DIM, ESTATUS, ARRAY, NSUBSTEP1*NCONTE
*DIM, REACT_FZ_ARRAY, ARRAY, NSUBSTEP1
*DIM, UZP_ARRAY, ARRAY, NSUBSTEP1
*DIM, UZN_ARRAY, ARRAY, NSUBSTEP1*NCONTN
*DIM, VM_FRONT, ARRAY, NUM_CROSS*NSUBSTEP1
*DIM, PSN_FRONT, ARRAY, NUM_CROSS*NSUBSTEP1
*SET, REACT_FZ, 0
*SET, CONSTATUS, 0
*SET, U_ZP, 0
*SET, U_ZN, 0
*SET, PRESSURE, 0
*SET, VM1, 0
*SET, PSN1, 0
!-----------------------------------------------Target------------------------------------------------------
ALLSEL
*DO, I, 1, NSUBSTEP1
   SUBSET, 1, I
   *GET, U_ZP, NODE, 1E8, U, Z
   *SET, UZP_ARRAY(I), U_ZP
*ENDDO
```

```
!---------------------------------------------------------Contact------------------------------------------------------------
ALLSEL
ESEL, S, TYPE, , 3
NSLE, S, ALL
*DO, I, 1, NSUBSTEP1
   SUBSET, 1, I
   ETABLE, CONPRES, CONT, PRES                    ! CONTACT PRESSURE
   ETABLE, CONSTAT, CONT, STAT                    ! CONTACT STATUS
*ENDDO
  *DO, II, 1, NCONTE
   *GET, PRESSURE, ETAB, 1, ELEM, ELEM_LIST(II)
   *SET, CONPRESS((I-1)*NCONTE + II) , PRESSURE
   *GET, CONSTATUS, ETAB, 2, ELEM, ELEM_LIST(II)
   *SET,ESTATUS((I-1)*NCONTE + II) , CONSTATUS
  *ENDDO
    FSUM, RSYS, CONT
   *GET, REACT_FZ, FSUM, 0, ITEM, FZ              ! REACTION FORCE IN Z DIRECTION
    REACT_FZ = -REACT_FZ
   *SET, REACT_FZ_ARRAY(I), REACT_FZ
*ENDDO
*DO, I, 1, NSUBSTEP1
   SUBSET, 1, I
  *DO, II, 1, NCONTN
   *GET, U_ZN, NODE, NODE_LIST(II), U, Z
   *SET,UZN_ARRAY((I-1)*NCONTN + II) , U_ZN     !DISPLACEMTN IN Z DIRECTION
  *ENDDO
*ENDDO
!---------------------------------------------------------Solid--------------------------------------------------------------
```

```
ALLSEL
ESEL, S, TYPE, , 1
NSLE, S, ALL


*DO, I, 1, NSUBSTEP1
    SUBSET, 1, I
   *DO, J, 1, NUM_FRONT
    *SET, III, (I-1)*NUM_FRONT + J
    *GET, VM1, NODE, LIST_FRONT(J), S, EQV              ! VON MISES STRESS AT THE
CREOSS SECTION
    *SET, VM_FRONT(III), VM1
   *ENDDO
*ENDDO
*DO, I, 1, NSUBSTEP1
    SUBSET, 1, I
   *DO, J, 1, NUM_FRONT
    *SET, III, (I-1)*NUM_FRONT + J
    *GET, PSN1, NODE, LIST_FRONT(J), EPPL, EQV         ! PLASTIC STRAIN AT THE
CREOSS SECTION
    *SET, PSN_FRONT(III), PSN1
   *ENDDO
*ENDDO
/INPUT, WRITE_RESULTS, txt
```

APPENDIX C

% Fourier Interpolation Method MATLAB Code

```
clc; clear; close all

load X_63M_N32.txt;
load Y_63M_N32.txt;
load Z_63M_N32.txt;

X0=X_63M_N32;
Y0=Y_63M_N32;
Z0=Z_63M_N32;.

Interval_x=X0(2)-X0(1);  % interval between two adjacent pints in x direction
Interval_y=Y0(2)-Y0(1);  % interval between two adjacent pints in y direction

NP0=32;                  % Number of points for the original data
NP1=64;                  % Number of points on each line after first interpolation
NP2=128;                 % Number of points on each line after second interpolation

R1=2;                    % Amplitude ratio for the original data
R2=4;                    % Amplitude ratio after first interpolation
R3=8;                    % Amplitude ratio after second interpolation


X1=(0:NP1-1)*(Interval_x/2^1);
Y1=(0:NP1-1)*(Interval_y/2^1);

X2=(0:NP2-1)*(Interval_x/2^2);
Y2=(0:NP2-1)*(Interval_y/2^2);

% _______________________First interpolation (64*64)_________________________

ZZ1=fftshift(fft2(ifftshift(Z0)));          % complex
ZZ2=zeros(NP1,NP1);
ZZ2((NP1/2)-NP0/2+1:(NP1/2)+NP0/2,(NP1/2)-NP0/2+1:(NP1/2)+NP0/2)=ZZ1;
% complex after adding zero
Z1=fftshift(ifft2(ifftshift(ZZ2)));         % IFFT transform
```

```
Z1_1=R1^2*real(Z1);

figure (1)
plot(X0,Z0(:,1))
hold on
plot(X1,Z1_1(:,1));
grid on
title('First interpolation of one line in x direction');
xlabel('x [\mu m]');
ylabel('z [\mu m]');
legend('Original surface','Surface after second interpolation'

% __________________Second interpolation (128*128)____________________

ZZ3=fftshift(fft2(ifftshift(Z1_1)));        % first fourier transform
ZZ4=zeros(NP2,NP2);
ZZ4((NP2/2)-NP1/2+1:(NP2/2)+NP1/2,(NP2/2)-NP1/2+1:(NP2/2)+NP1/2)=ZZ3;
Z2=fftshift(ifft2(ifftshift(ZZ4)));
Z2_1=2^2*real(Z2);

Z2_0=reshape(Z2_1,1,NP2^2);
sigma2=sqrt(1/(NP2)^2*sum((Z2_0-mean(Z2_0)).^2));


figure (2)
plot(X0,Z0(:,1))
hold on
plot(X2,Z2_1(:,1));
grid on
title('Second interpolation of one line in x direction');
xlabel('x [\mu m]');
ylabel('z [\mu m]');
legend('Original surface','Surface after second interpolation')
```

APPENDIX D

Finite Element Method Results

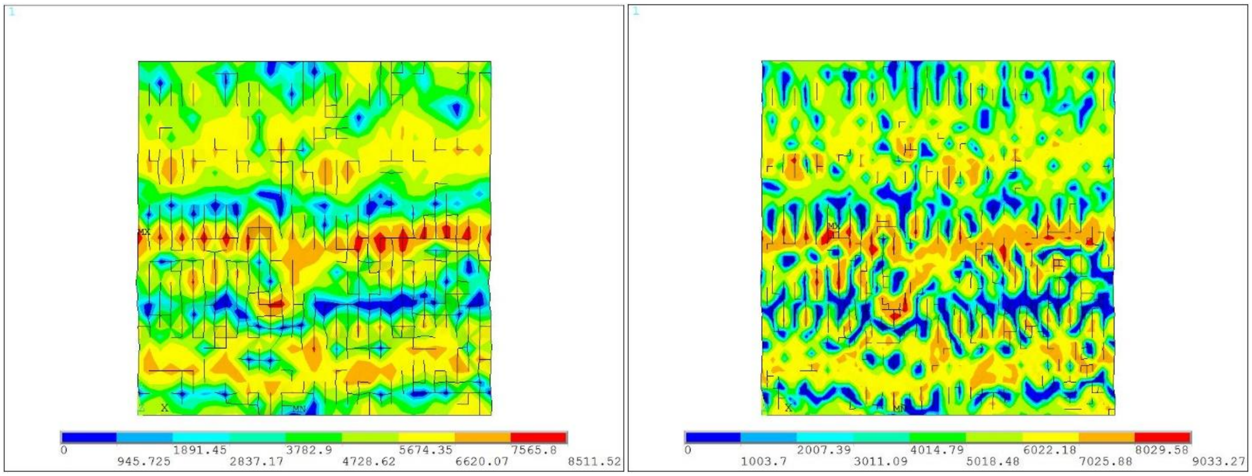

(a) $N_e = 1024$ (b) $N_e = 4096$

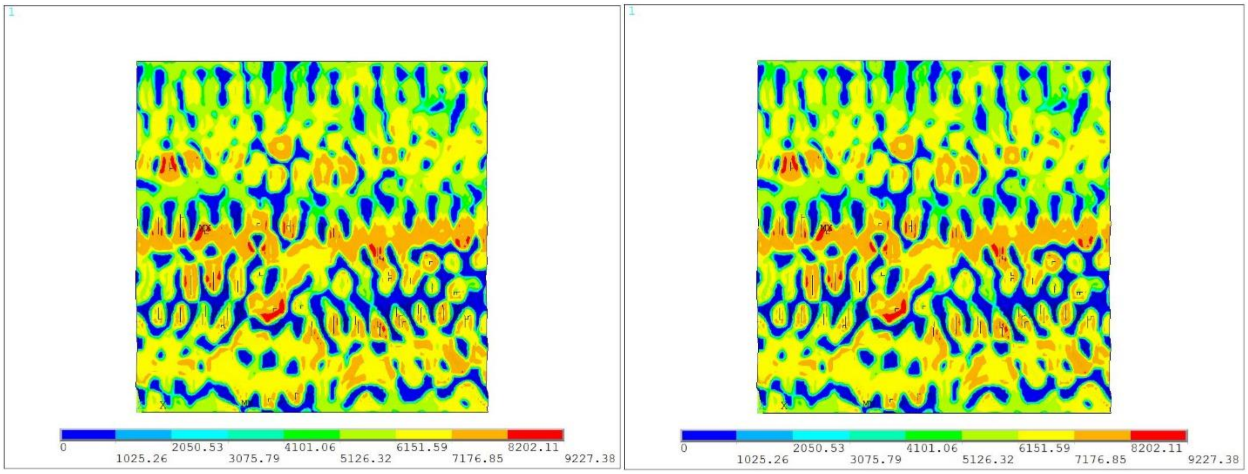

(c) $N_e = 16384$ (d) $N_e = 65536$

Fig. B1. Contact pressure for original surface 63M and interpolated surfaces under normal loading only

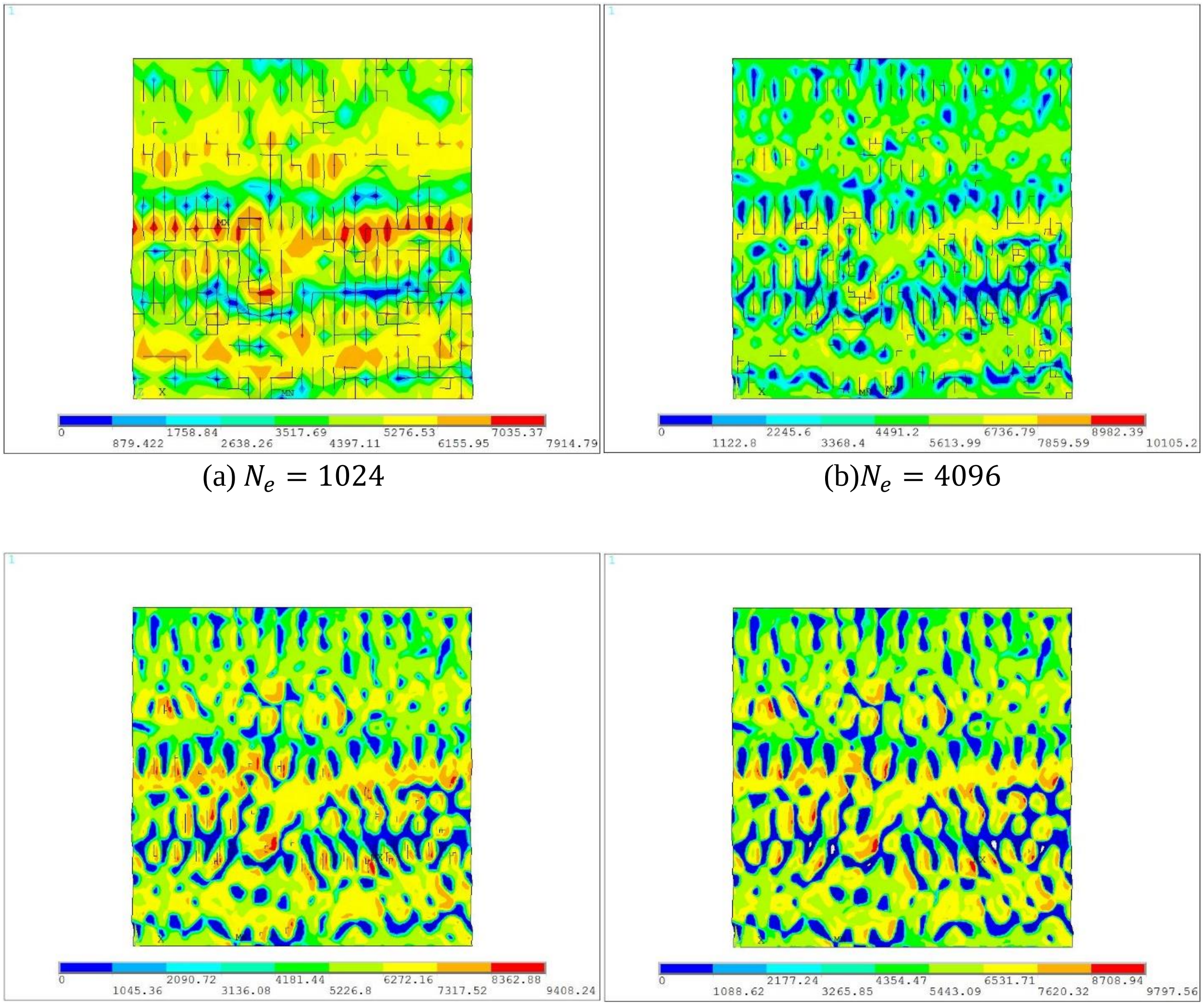

(a) $N_e = 1024$ (b)$N_e = 4096$

(c)$N_e = 16384$ (d)$N_e = 65536$

Fig. B2. Contact pressure for original surface 63M and interpolated surfaces at sliding inception

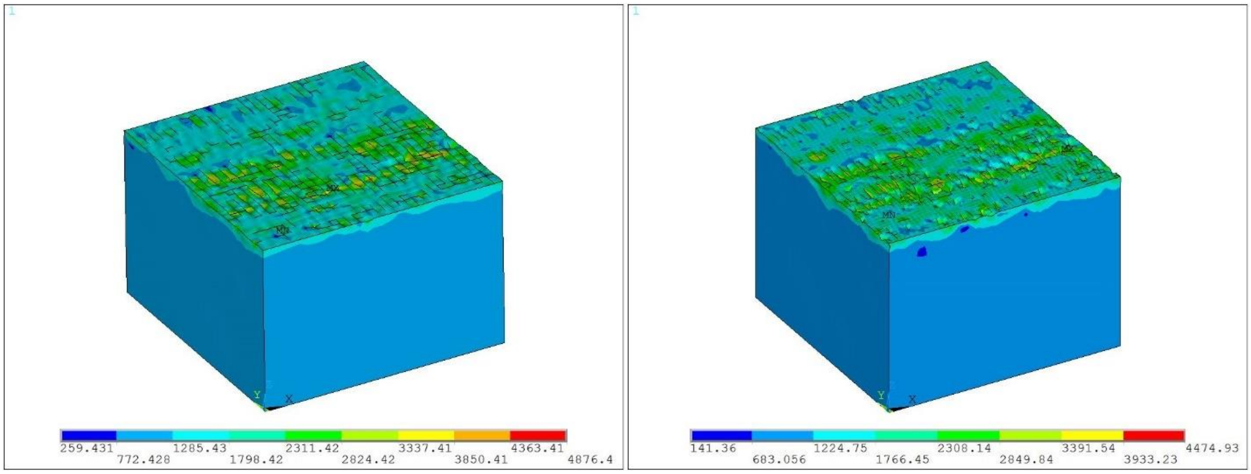

(a) $N_e = 1024$ (b)$N_e = 4096$

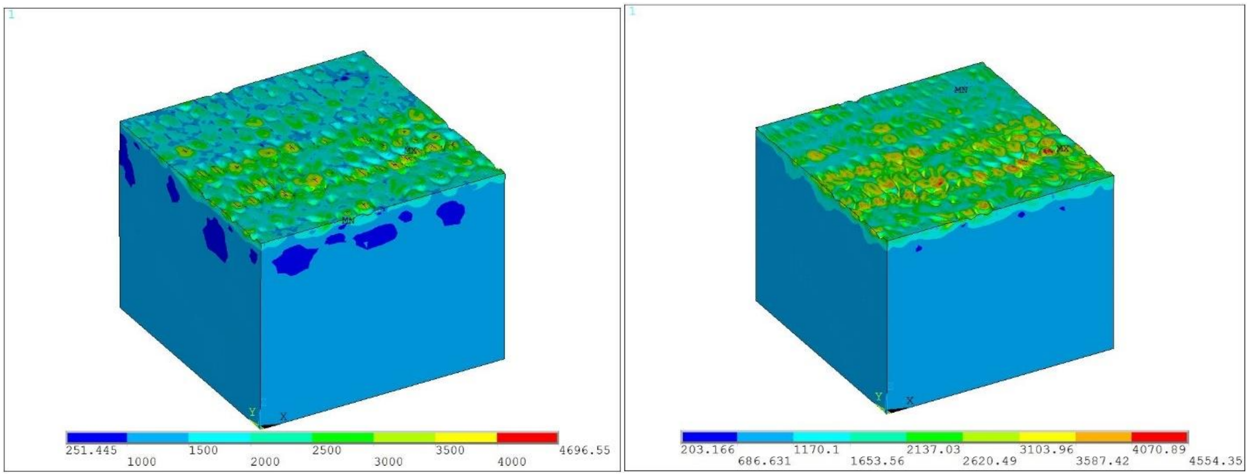

(c)$N_e = 16384$ (d)$N_e = 65536$

Fig. B3. Contact pressure for original surface 63M and interpolated surfaces under normal loading only

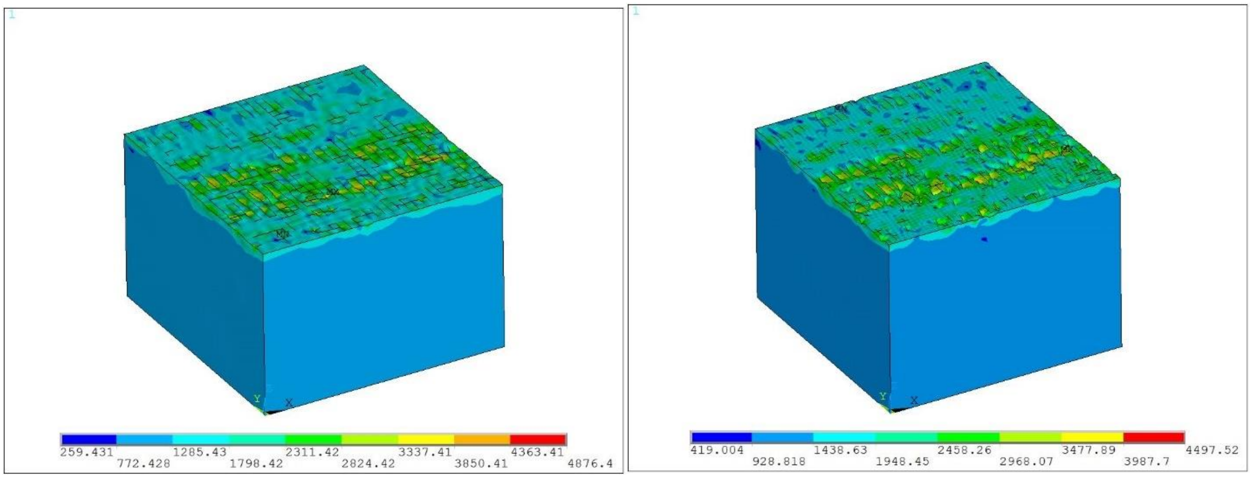

(a) $N_e = 1024$

(b) $N_e = 4096$

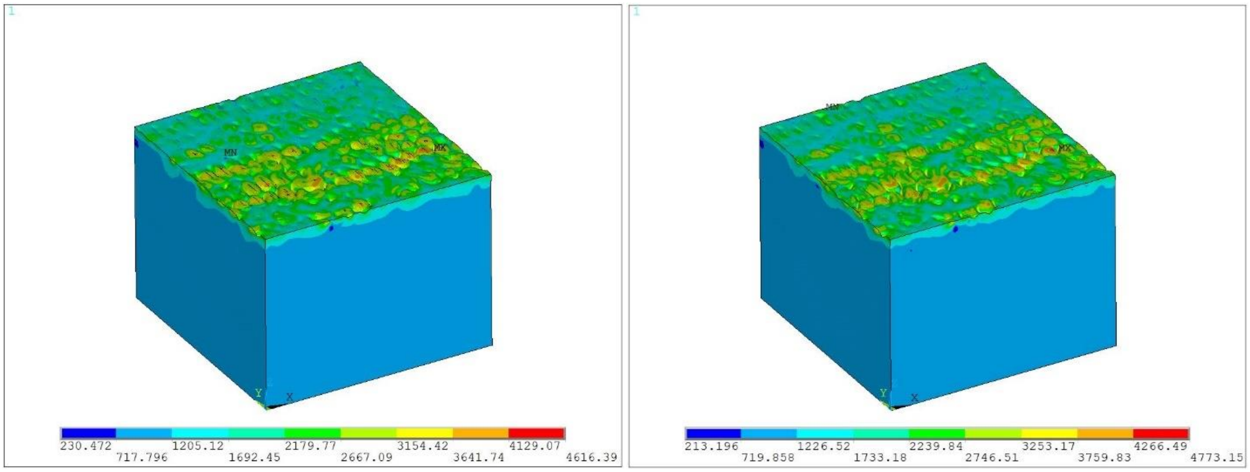

(c) $N_e = 16384$

(d) $N_e = 65536$

Fig. B4. Von Mises stress for original surface 63M and interpolated surfaces at sliding inception

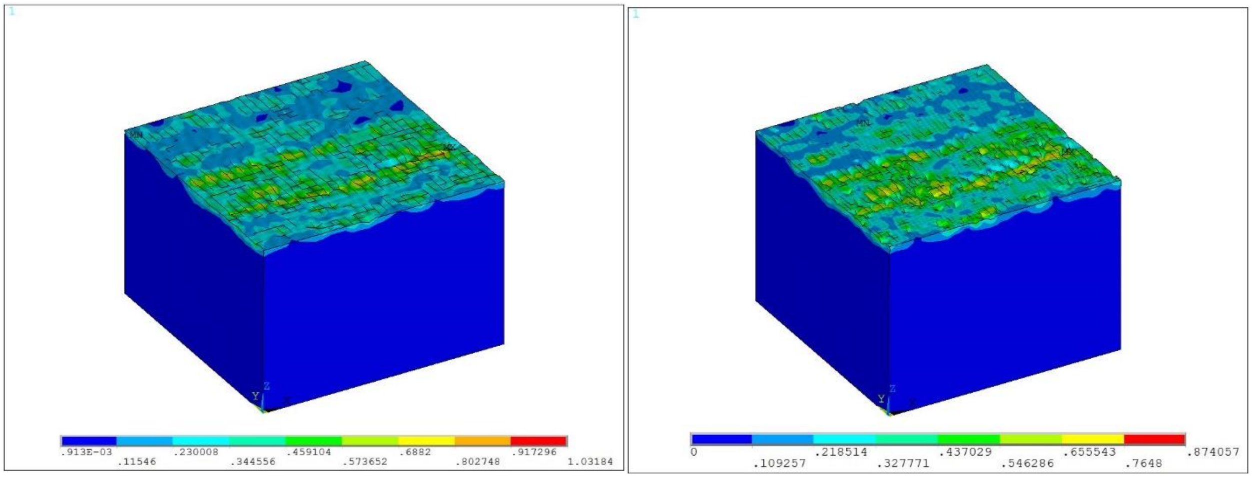

(a) $N_e = 1024$ (b)$N_e = 4096$

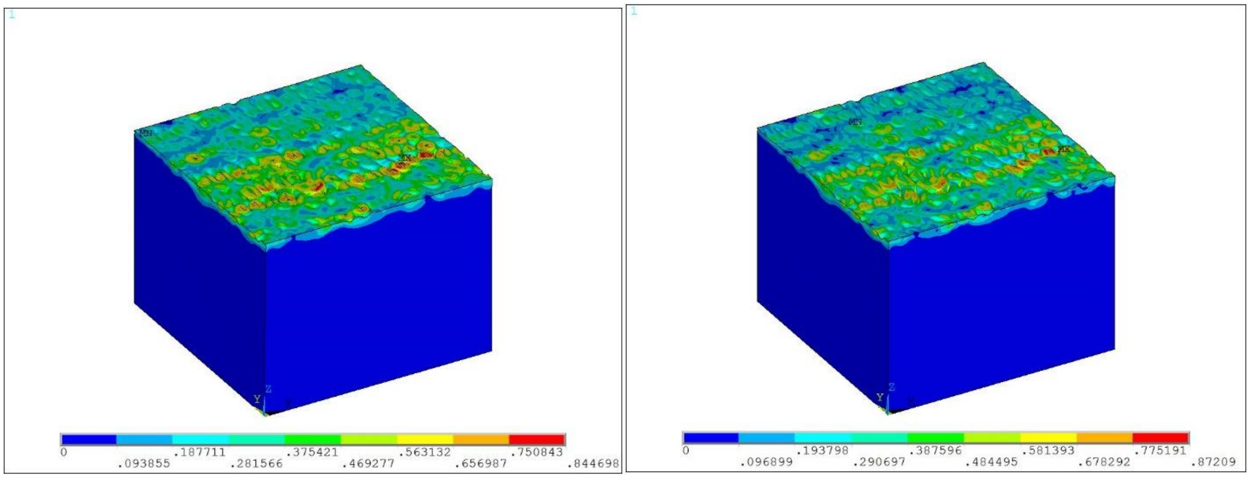

(c)$N_e = 16384$ (d)$N_e = 65536$

Fig. B5. Equivalent plastic strain for original surface 63M and interpolated surfaces under normal loading only

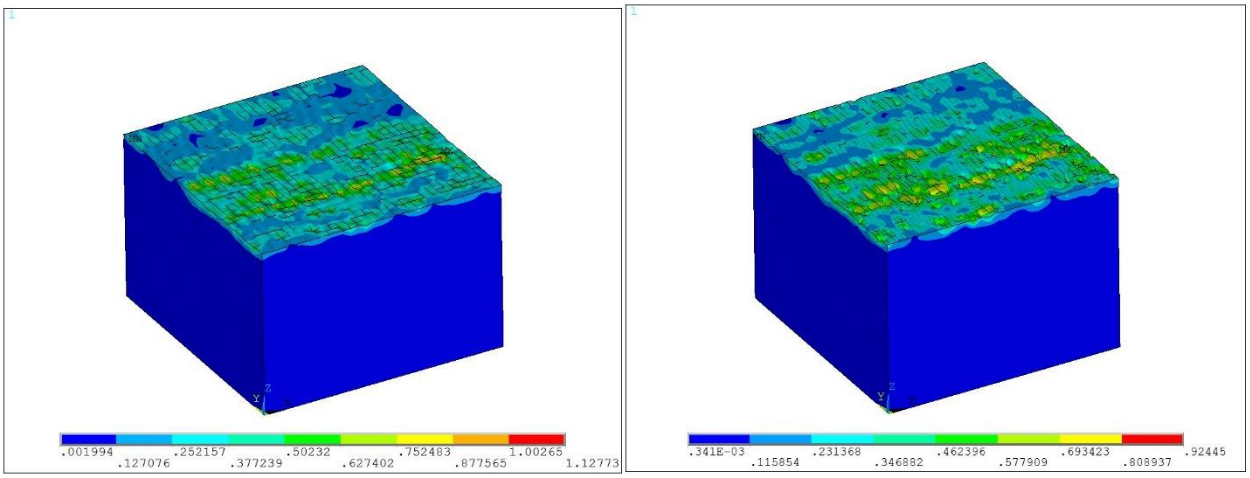

(a) $N_e = 1024$ (b)$N_e = 4096$

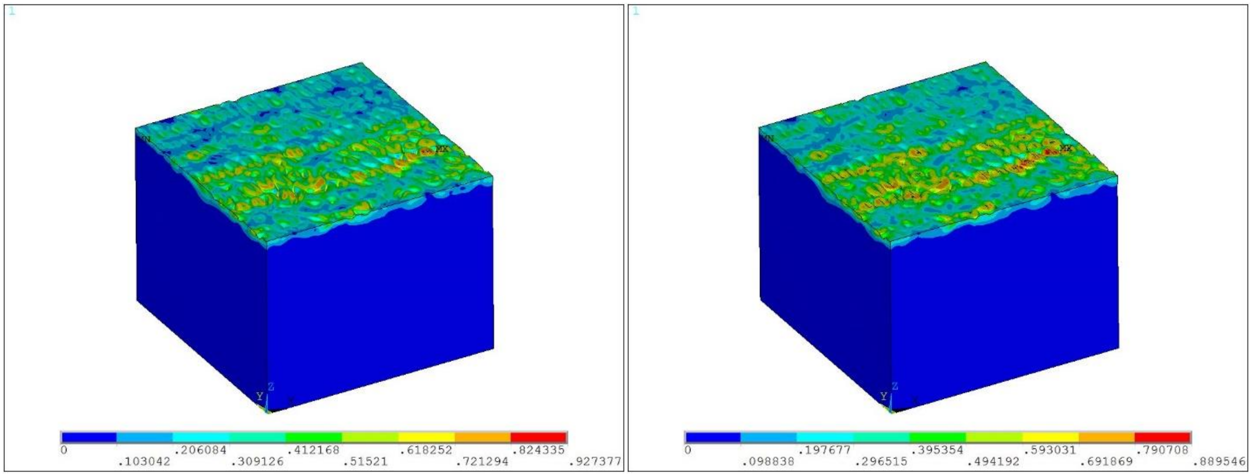

(c)$N_e = 16384$ (d)$N_e = 65536$

Fig. B6. Equivalent plastic strain for original surface 63M and interpolated surfaces at sliding inception